

CORE-SHELL NANOPARTICLES AS A  
PLATFORM TECHNOLOGY FOR THE  
TREATMENT OF PROLIFERATIVE OCULAR  
DISEASES



Dissertation to obtain the Degree of Doctor of Natural Sciences  
(Dr. rer. nat.)  
from the Faculty of Chemistry and Pharmacy  
University of Regensburg

Presented by  
**Sebastian Beck**  
from Saalburg (Thuringia/ Germany)

May 2022









*To Helen and my Family*

---



“Bevor du jemanden heilst, frage ihn, ob er bereit ist aufzugeben, was ihn krank macht.”

**Hippokrates**



# Contents

	Page
<b>I Main Part</b>	<b>1</b>
<b>1 General Introduction</b>	<b>3</b>
1.1 Vision and the Human Eye . . . . .	4
1.1.1 Following the Pathway of Light . . . . .	4
1.1.2 Ocular Fundus . . . . .	5
1.2 Supply of Retinal Tissue . . . . .	8
1.2.1 Choroidal Vasculature . . . . .	9
1.2.2 Retinal Vasculature . . . . .	9
1.2.3 Pericytes - the Vascular Companions . . . . .	12
1.3 Blood-Retinal Barrier . . . . .	13
1.3.1 Outer Blood-Retinal Barrier . . . . .	14
1.3.2 Inner Blood-Retinal Barrier . . . . .	16
1.4 Ocular Diseases . . . . .	18
1.4.1 Age-related Macular Degeneration . . . . .	19
1.4.2 Diabetic Retinopathy . . . . .	25
1.5 The Need for an Adaptable Platform Technology . . . . .	30
1.6 References . . . . .	31
<b>2 Goals of the Thesis</b>	<b>49</b>
2.1 Concept . . . . .	50
2.1.1 Considerations about a Nanoparticulate Platform . . . . .	50
2.1.2 Pre-Clinical Testing . . . . .	51
2.1.3 EXP3174 - A Promising Pharmacon . . . . .	51
2.2 Goals of the Thesis . . . . .	52
2.3 References . . . . .	53
<b>3 The Building Blocks for Nanoparticle Manufacturing</b>	<b>57</b>
3.1 Introduction . . . . .	58
3.2 Material and Methods . . . . .	60
3.2.1 Material . . . . .	60
3.2.2 Synthesis of Block-co-Polymers . . . . .	60
3.2.3 Analytics of Block-co-polymers . . . . .	60
3.2.4 Synthesis of Losartan Carboxylic Acid . . . . .	61
3.2.5 Analytics of Losartan Carboxylic Acid . . . . .	61
3.2.6 Coupling of EXP3174 to Block-Co-Polymer . . . . .	62

3.2.7	Analytics of EXP3174-PEG-PLA . . . . .	63
3.2.8	Purity of Nanoparticle Dispersions . . . . .	64
3.2.9	Labeling of PLGA . . . . .	64
3.3	Results and Discussion . . . . .	65
3.3.1	Block-co-Polymers . . . . .	65
3.3.2	Losartan Carboxylic Acid . . . . .	68
3.3.3	EXP3174-PEG-PLA Block-co-Polymer . . . . .	70
3.3.4	PLGA . . . . .	73
3.4	Conclusion . . . . .	73
3.5	References . . . . .	74
<b>4</b>	<b>Nanoparticle Manufacturing and Analytical Methods with special Focus on the Particle Number Concentration</b>	<b>77</b>
4.1	Introduction . . . . .	78
4.2	Material and Methods . . . . .	80
4.2.1	Material . . . . .	80
4.2.2	Manufacturing of Nanoparticles . . . . .	80
4.2.3	Dynamic Light Scattering . . . . .	81
4.2.4	Nano Tracking Analysis . . . . .	82
4.2.5	Determination of Total Polymer Content . . . . .	82
4.2.6	TEM Images and Size Analysis . . . . .	83
4.2.7	Quantification of EXP3174 . . . . .	83
4.3	Results and Discussion . . . . .	83
4.3.1	Nanoparticle Analysis . . . . .	84
4.3.2	Nanoparticle Concentration . . . . .	86
4.3.3	Further Consideration to the PEG Shell . . . . .	95
4.3.4	Ligand Density . . . . .	99
4.4	Conclusion . . . . .	101
4.5	References . . . . .	102
<b>5</b>	<b>Nanoparticle Stability and Freeze Drying</b>	<b>107</b>
5.1	Introduction . . . . .	108
5.2	Material and Methods . . . . .	109
5.2.1	Material . . . . .	109
5.2.2	Manufacturing and Quality of Nanoparticle Dispersions	109
5.2.3	Nanoparticle Size Characterization . . . . .	110
5.2.4	Freeze-Thaw . . . . .	110
5.2.5	Lyophilization Process . . . . .	111
5.2.6	Radioligand Binding Studies . . . . .	111
5.3	Results and Discussion . . . . .	111
5.3.1	Nanoparticle Stability . . . . .	111
5.3.2	Freeze-Thaw . . . . .	114
5.3.3	Freeze-Drying of Model Nanoparticles . . . . .	118
5.3.4	Freeze-Drying of Targeted Core-Shell Nanoparticles . .	120
5.4	Conclusion . . . . .	122
5.5	References . . . . .	125



<b>6</b>	<b>Design of Antagonistic Nanoparticles with Sub-Nanomolar Avidity</b>	<b>131</b>
6.1	Introduction . . . . .	132
6.2	Material and Methods . . . . .	133
6.2.1	Material . . . . .	133
6.2.2	Manufacturing and Characterization of Nanoparticles . . . . .	133
6.2.3	Cell Culture . . . . .	134
6.2.4	Transfection of Rat Mesangial Cells . . . . .	134
6.2.5	Flow Cytometry . . . . .	134
6.2.6	Calcium Mobilization Assay . . . . .	135
6.2.7	Radioligand Binding Experiment . . . . .	136
6.2.8	Confocal Laser Scanning Microscopy . . . . .	138
6.3	Results and Discussion . . . . .	139
6.3.1	Milestone in Nanoparticle Development . . . . .	139
6.3.2	Ligand-Decorated Nanoparticles with a Sub-Nanomolar Avidity . . . . .	141
6.3.3	Localization of Binding Nanoparticles . . . . .	147
6.3.4	Nanoparticle Avidity to Cells with High Receptor Density . . . . .	148
6.4	Conclusion . . . . .	152
6.5	References . . . . .	152
<b>7</b>	<b>Number of Binding Ligands</b>	<b>157</b>
7.1	Introduction . . . . .	158
7.2	Material and Methods . . . . .	159
7.2.1	Material . . . . .	159
7.2.2	Manufacturing Gold-Tagged Nanoparticles . . . . .	159
7.2.3	Analytics of the Nanoparticle Dispersions . . . . .	159
7.2.4	Cell Culture . . . . .	160
7.2.5	Ligand-Receptor Complexes per Nanoparticle . . . . .	161
7.3	Results and Discussion . . . . .	162
7.3.1	Theoretical Background . . . . .	162
7.3.2	Experimental . . . . .	164
7.3.3	Number of Binding Ligands . . . . .	166
7.4	Conclusion . . . . .	166
7.5	References . . . . .	168
<b>8</b>	<b>Nanoparticles to Target Retinal Vessels</b>	<b>171</b>
8.1	Introduction . . . . .	172
8.2	Material and Methods . . . . .	173
8.2.1	Material . . . . .	173
8.2.2	Nanoparticle Stability Study . . . . .	173
8.2.3	Biodistribution Study . . . . .	174
8.2.4	Nanoparticle Tracing in Retinal Vasculature . . . . .	175
8.3	Results and Discussion . . . . .	176
8.3.1	Nanoparticle Stability in Human Serum . . . . .	176
8.3.2	Biodistribution of Core-Shell Nanoparticles . . . . .	180
8.3.3	Nanoparticle Tracing in Ocular Vasculature . . . . .	184
8.4	Conclusion and Outlook . . . . .	188
8.5	References . . . . .	189

<b>9 Overall Summary</b>	<b>195</b>
<b>II Supplement</b>	<b>203</b>
<b>III Appendix</b>	<b>211</b>
<b>Abbreviations</b>	<b>213</b>
<b>Curriculum Vitae</b>	<b>219</b>
<b>List of Publications</b>	<b>221</b>
<b>Acknowledgments</b>	<b>223</b>
<b>Declaration in Lieu of Oath</b>	<b>225</b>

**Part I**

**Main Part**



## **Chapter 1**

# **General Introduction**

## 1.1 Vision and the Human Eye

Vision is a complex interplay of a multitude of highly specialized cells. Basically, the eye captures optical stimuli and translates them into biochemical signals. These signals are conducted via the optic nerve fibres to dedicated areas in the brain, where the images are assembled.

The human eye is able to detect electromagnetic radiation within a wavelength of approximately 400 to 700 nm. This is the range of visible light. The gross anatomy of a human eye is illustrated in figure 1.1. The diameter of an adult human eyeball is not ideally spherical. Its dimensions are approximately 24.2 mm (horizontal), 23.7 mm (vertical) and 22.0 mm to 24.8 mm (axial) [1].

### 1.1.1 Following the Pathway of Light

Incoming light passes the transparent and avascular cornea (refer to **a** in figure 1.1) first. Thereby light encounters the multilayered corneal epithelium, BOWMAN'S layer (a basal membrane), the corneal stroma, the DESCEMENT'S membrane (another basal membrane) and the monolayered corneal endothelium [2]. At about 90% of its thickness, the stroma is the main part of the cornea. It comprises keratocytes as the major apparent cell type, embedded in lamellar, highly uniform collagen fibrils and a complex extracellular matrix (proteoglycans) [3]. These components are precisely organized in order to maintain the corneal transparency. The collagen fibrils have a diameter of approximately 32 nm and a center-to-center interfibrillar spacing of 62 nm [4], so that light scattering effects are negligible. However, the cornea blocks most of the harmful ultraviolet radiation in order to protect the retina (refer to **j** in figure 1.1) [5].

Subsequently, remaining light passes the anterior chamber (refer to **b** in figure 1.1) until they reach the lens (refer to **g** in figure 1.1). Thereby, the amount of entering light is regulated by the iris (refer to **c** in figure 1.1). The iris carries pigmented cells blocking excessive incoming light like a shutter. The pupil is the central opening of the iris. Its size can be adjusted by dilation or restriction of the iris, so that the amount of incoming light is finally regulated [5]. The lens has a remarkable refractive index and focusses the incoming light onto the retina. In the lens only a monolayer of epithelial cells show proliferative activity. These cells migrate over the lens equator and differentiate into lens fiber cells. The fiber cells build the dense layer-like lens structure [6]. They accumulate proteins called crystallins, which are responsible for the remarkable high refractive index [7]. Their dense and organized packaging is the origin of the transparency of the lens similarly to the transparency of the cornea [5]. The lens is a polar structure. Its growth is precisely balanced by a complex interplay with retinal and corneal cells. Soluble factors like the fibroblast growth factor migrate across the vitreous (refer to **h** in figure 1.1) and the aqueous humor (anterior and posterior chamber - **b** and **d** in figure 1.1). While the epithelial cells are exposed to the aqueous humor, the fiber cells are in contact with the vitreous humor. Inhere the lens equator is the border [6]. Consequently, the lens is not comparable to a rigid glass lens of optical instruments.

The ciliary zonule (refer to **f** in figure 1.1) build the lens suspension. They are originating at the ciliary body (refer to **e** in figure 1.1) and hold the lens in place.

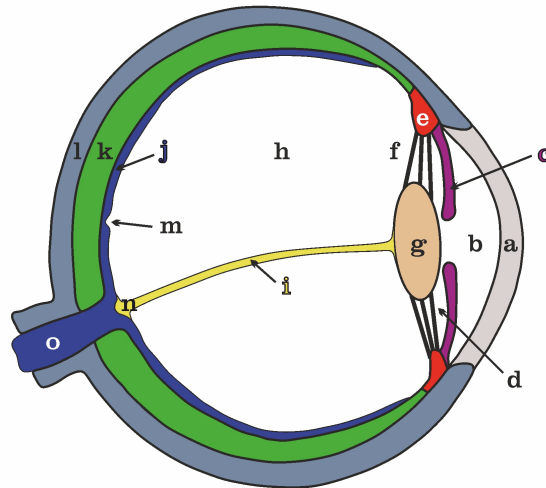


Figure 1.1: Gross anatomy of the human eyeball: Cornea (a), Anterior chamber (b), Iris (c), Posterior chamber (d), Ciliary body (e), Ciliary zonule (f), Lens (g), Vitreous humor (h), Residual hyaloid canal (i), Retina (j), Choroid (k), Sclera (l), Fovea (m), Optic disc (n) and Optic nerve (o).

The ciliary body consists of a double-layer epithelium, ciliary muscles and the already mentioned ciliary zonule. The outer epithelium cell layer of the ciliary body is a prolongation of neuronal retinal cells, while the subordinated layer is the direct prolongation of the retinal pigment epithelium (RPE) cells. The contraction of the ciliary muscles occurs coincidentally with a diminution of the zonular fibre tension, changing the flatten lens shape into a bulbar lens shape. So light originating from objects below a distance of 6 m can be focused onto the retina [5]. This process is called accommodation. It adjusts the degree of refraction and enables sharp vision for different object distances.

### 1.1.2 Ocular Fundus

As already mentioned above, incoming light is cleared of the harmful, ultra-violet share, regulated with respect to its intensity and focussed on the fovea. The fovea is a small avascular pit (refer to **m** in figure 1.1) in the centre of the *macula lutea*. The macula lutea is the location of the sharpest vision within the retina (refer to **j** in figure 1.1). Within the retinal tissue incoming light is translated into biochemical signals. These signals are transmitted via ganglion cells and the optic nerve (refer to **o** in figure 1.1) to the brain. The retina comprises a unique and complex cytoarchitecture that is schematically depicted in figure 1.2 (left side).

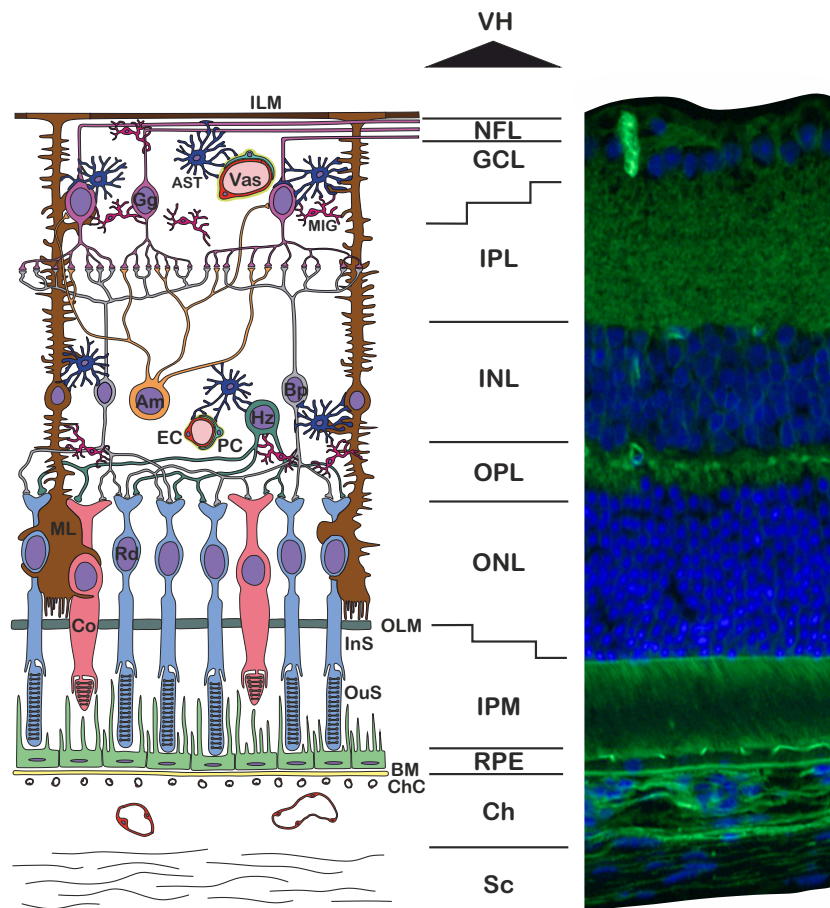


Figure 1.2: **Left:** Schematic drawing of the ocular fundus. **Right:** Cross-section through the retinal fundus of an adult murine eye. [Vitreous humor(VH), Nerve fiber layer (NFL), Ganglion cell layer (GCL), Inner plexiform layer (IPL), Inner nuclear layer (INL), Outer plexiform layer (OPL), Outer nuclear layer (ONL), Interphotoreceptor layer (IPM), Retinal pigment epithelium (RPE), Choroid (Ch), Sclera (Sc), Inner limiting membrane (ILM), Astrocyte (Ast), Vasculature (vas), Ganglion cell (Gg), Microglial cell (MIG), Amacrine cell (Am), Bipolar cell (Bp), Horizontal cell (Hz), Endothelial cell (EC), Pericyte (PC), Mueller cell (ML), Rod (Rd), Cone (Co), Outer limiting membrane (OLM), Inner segment (InS), Outer segment (OuS), BRUCH's membrane (BM) and Choriocapillaris (ChC)]



### Retinal Pigment Epithelium

The outer distal layer of the human retina is built by RPE cells, appearing with a hexagonal tile-shape (plan view). They are densely packed forming a tight monolayer. The cell density is decreasing from the foveal area ( $4220 \pm 727$  cells /mm<sup>2</sup>) to the periphery ( $1600 \pm 411$  cells /mm<sup>2</sup>) [8]. This means that the size of RPE cells increases to the periphery as well. An adult eyeball comprises approximately  $3.5 \times 10^6$  RPE cells [8]. At the retina's periphery the RPE cells merge directly into the subordinated epithelium cell layer of the ciliary body. RPE cells absorb light via melanin that is enriched in melanosomes [9]. These pigments capture scattered light and protect the photoreceptors from excessive light exposure. On the apical side, RPE cells form long microvilli surrounding the light sensitive outer segment of the photoreceptors as it is illustrated in figure 1.2. This increases the cell surface tremendously and enables the exchange of nutrients, water, ions, oxygen, retinol and any other essential biomolecule. Moreover, RPE cells have a unique barrier function, which is discussed in section 1.3.

### Retinal Neurons

There are two types of photoreceptors, that are embedded into the RPE microvilli:

- rods and
- cones.

The retina of a human eye hosts round about  $120 \times 10^6$  rods and  $10 \times 10^6$  cones [5]. Rods are extremely sensitive to light and enable light-dark vision. On the contrary, cones are mainly situated in the central retina. There are three types of cones responding to different wavelength ranges and facilitating the color vision. However, cones need a higher light amount, so that the color vision is better working during day time. For both types of photoreceptors the vitamin-A-derivative 11-*cis*-retinal translates incoming photons into biochemical signals. 11-*cis*-retinal is associated to a heptahelical, transmembrane G-protein called opsin. Once a photon hits a 11-*cis*-retinal molecule, the transferred energy can cause the transformation to all-*trans*-retinal and initiates a signalling cascade [10]. Subsequently, there is a couple of intermediates until light-sensitive 11-*cis*-retinal is recovered. RPE cells are indispensable in this regeneration (*retinoid cycle*). Opsin is a generic term covering a family of proteins. For instance rhodopsin is an opsin that is present in rods, while cones host photopsins (S-, M- or L-photopsin). Opsins respond to different wavelength ranges, they are located in the membrane of stacked discs inside the photoreceptors. Since the mentioned regeneration cycle requires the interplay with RPE cells, the stacked discs are basically situated in the distal photoreceptor part (outer segment of the photoreceptors). The corresponding retinal layer is termed interphotoreceptor layer. It is clearly segregated by the outer limiting membrane (refer to figure 1.2).

The overlying layer is the outer nuclear layer that is dominated by the photoreceptors' nuclei. This is very characteristic and can be easily recognized in

a microscopic image as it is depicted in figure 1.1 (right side). The generated signals are vertically transmitted through bipolar cells in the inner nuclear layer to the ganglion cells (refer to figure 1.2). The ganglion cells generate action potentials that are conducted via the nerve fibers. Eventually, the nerve fibers merge to form the optic nerve when they exit the eye and conduct the action potentials to the brain. In the region where outer nuclear layer and inner nuclear layer as well as inner nuclear layer and ganglion cell layer are approximating, their synaptic connections arise. These connective regions are the plexiform layers, namely outer and inner plexiform layer. Aside, the vertical signal transduction, amacrine cells and horizontal cells mediate a horizontal signal transduction. The role of these cells is not absolutely unveiled, but they are modifying the generated signals. For instance, it is known that horizontal cells give a negative feedback to photoreceptors, while amacrine cells are adjusting the retinal light sensitivity during the circadian cycle [11, 12]. Hence, the horizontal signal transduction is similarly important as the vertical one.

### **Retinal Glia**

Beyond retinal neurons, there are a multitude of glial cells taking supporting and protecting functions. The principal glial cells are the Mueller cells. Their nuclei are situated in the inner nuclear layer while their dendrites span almost all retinal layers (refer to figure 1.2). Mueller cells form the core of radial organizational units comprising photoreceptors and retinal neurons [13]. They encompass photoreceptors tightly to control the supply of nutrients and the elimination of waste products. Mueller cells regulate the electrolyte homeostasis in the extracellular fluid and support the synaptic activity by recycling of neurotransmitters [14–17]. Furthermore, researchers report additional functions like light-guiding properties, mechanical strength, viscoelasticity, autocrine functions and regenerative potentials [18–21].

Astrocytes are preferentially located around retinal blood vessels [22]. They support the development of retinal vasculature and even emerge in species possessing retinal angiogenesis [23]. Moreover, astrocytes control the transport of biomolecules from the retinal capillaries to the retinal neurons and clear metabolites in turn [13]. Mueller cells and astrocytes correspond to the macroglia.

Apart from that, microglial cells are distributed in the human retina between the nerve fiber layer and the outer nuclear layer. They originate from hematopoietic progenitor cells and migrate into the retina during early embryonic phases. Microglial cells are macrophage-like cells defending against pathogens and degrading apoptotic neurons as well as cellular debris. Furthermore, microglial cells support the sculpturing of neuronal and vascular architecture. Inhere the synaptic refinement is particularly important [24–26].

## **1.2 Supply of Retinal Tissue**

In general, the human retina is supplied by the choroidal and the retinal vasculature. The choroidal vessels are situated beneath the retina in the choroid

as it is indicated in figure 1.1 k. The choroid supplies the outer retina. On the contrary, retinal vessels grow through the hyaloid of the optic nerve, enter the vitreous body and migrate alongside the inner limiting membrane to the periphery. Thereof, they sprout vertically to reach and supply the inner retina. Retinal vessels do not sprout beyond the outer plexiform layer under physiological conditions [27]. The retinal vessel density is raised in specific layers and form several plexuses as it is depicted in figure 1.3.

### 1.2.1 Choroidal Vasculature

Choroidal vessels form a network of capillaries closely beneath the retina. This is the choriocapillaris, predominantly delivering outer retina with essential biomolecules (e.g. oxygen, water, ions, nutrients and retinol). Furthermore, waste products and metabolites are cleared through the choriocapillaris into the systemic circuit. The innerphotoreceptor layer is an avascular area, that is separated from the choriocapillaris by the outer blood-retinal barrier (oBRB). The oBRB controls the exchange of every biomolecule or metabolite passing this barrier. It is extensively discussed in section 1.3. The tissue-weighted blood perfusion in the choriocapillaris accounts  $14\,000\text{ ml min}^{-1}\text{ kg}^{-1}$  [9]. This is 3.5 times the blood perfusion of the kidneys [30]. Such an outstanding high blood perfusion indicates the extreme metabolic rate in the photoreceptors that follows the rapid aging of strongly light exposed tissue. Furthermore, the high blood perfusion is necessary to cool the retinal tissue and maintain the homeostasis. Interestingly, the oxygen saturation in the choriocapillaris is 90%, whereas it accounts only 45% in the retinal vasculature [9]. This means that the oxygen consumption is clearly higher in the retinal vasculature.

### 1.2.2 Retinal Vasculature

Retinal vessels appear with a completely different architecture. Retinal vessels originate from the optical nerve disc, where vascular endothelial cells (ECs) migrate to the retinal periphery. Nowadays, it is known that ECs are not passive gatekeepers, but tissue-specific conductors playing a key role in the tissue regeneration and the homeostasis. Capillary ECs secrete and respond to a multitude of angiocrine factors [31]. Vascular endothelial growth factor (VEGF) is the most prominent one. Through the migration towards the retinal periphery, ECs form the primary plexus. The primary plexus is running between the inner limiting membrane and the nerve fiber layer [23]. The migration of vascular ECs follows a complex signalling cascade. Retinal ganglion cells sense hypoxia and start secreting platelet derived growth factor alpha ( $\text{PDGF}\alpha$ ), that attracts astrocytes. Astrocytes in turn secrete VEGF inducing vascular EC migration. The ECs sprout alongside the astrocyte template, since astrocytes produce extracellular matrix (ECM) biomolecules (e.g. fibronectin and heparan sulfate) guiding endothelial tip cells. Furthermore, endothelial tip cells are able to sense and follow VEGF gradients. Therefore astrocytes are essential for the sprouting of vessels into the retina. In turn, the astrocytes respond to the vascular ECs, downregulate VEGF secretion and stop EC migration. This negative feedback is amplified by the raising supply of oxygen through the developing

## 1.2. SUPPLY OF RETINAL TISSUE

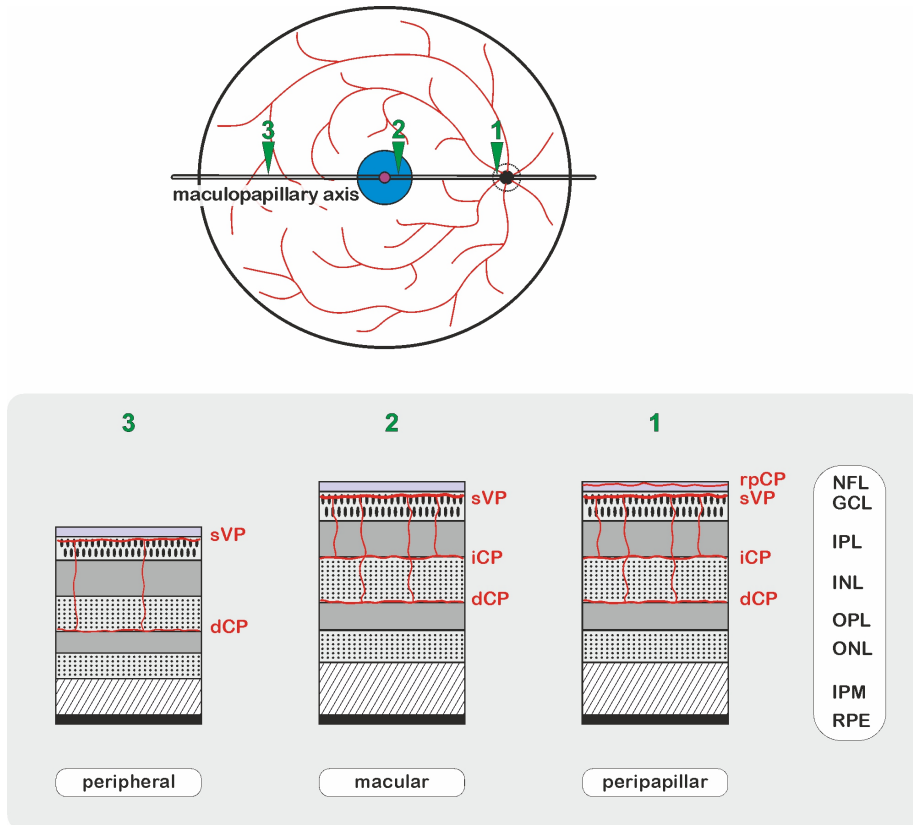


Figure 1.3: Localisation of the retinal vasculature [28, 29]. **Top:** Frontal view onto the ocular fundus. The retinal vasculature enters the eyeball through the optical disc (solid black sphere), which is surrounded by the peripapillary region (dotted circle). The fovea is located in the centre of the ocular fundus (purple) and surrounded by the macular region (blue sphere). **Bottom:** Illustration of the vertical blood supply (red) in the inner retina at essential retinal regions alongside the maculopapillary axis. **1:** peripapillar - four vascular plexuses; **2:** macular - three vascular plexuses; **3:** peripheral - two vascular plexuses. [**Retinal plexuses:** radial peripapillary capillary plexus (rpCP), superficial vascular plexus (sVP), intermediate capillary plexus (iCP) and deep capillary plexus (dCP); **Retinal layers:** Nerve fiber layer (NFL), Ganglion cell layer (GCL), Inner plexiform layer (IPL), Inner nuclear layer (INL), Outer plexiform layer (OPL), Outer nuclear layer (ONL), Interphotoreceptor layer (IPM) and Retinal pigment epithelium (RPE)]

vessels [23]. Originating from the developed primary plexus, vascular ECs are migrating into the inner retina. It is not surprising that VEGF again plays a key role, but transforming growth factor beta (TGF- $\beta$ ) and Norrin are assumed to guide the vessels' branches [23, 32]. These factors are secreted by Mueller cells [33], so that they guide vertical angiogenesis in the retina [28]. The cytokine Norrin is a protein that activates the  $\beta$ -catenin signaling cascade. Therefore, a complex interplay of the target receptor Frizzled-4, the co-receptor low-density lipoprotein receptor-related protein 5 and the co-activator tetraspanin 12 is necessary [34–38]. Subsequently,  $\beta$ -catenin accumulates in the cytoplasm and connects the cytoskeleton with membrane-presented proteins like claudin 5, cadherins and plasmalemma vesicle-associated protein. The latter proteins are essential for the formation of tight cell-cell contacts as it is the case in the blood-retinal barrier (BRB) [39–41].

Nascent vessels are labile. Either they differentiate into stable, mature vessels or they are pruned by EC regression. Blood perfusion and shear stress control the lateral EC migration. This was evidenced in the work of Chen et. al. [42]. They used micro-beads to reduce the blood flow in certain vessels and demonstrated their pruning. On the contrary, the noradrenergic elevation of blood flow impeded pruning.

Campbell et. al. investigated the ocular blood perfusion in nine healthy humans (mean age  $30.2 \pm 7.4$  years) by projection-resolved optical coherence tomography (OCT) [29], which is a refinement development of the OCT method. Projection-resolved OCT enables a 3D-*in vivo*-visualization of the choroidal and retinal vessel density with an axial resolution of a few micrometers. They presented cross-sectional images along the maculopapillary axis at different regions (peripapillary, parafoveal, perifoveal and peripheral) and determined the capillary density for each region in regard to the retinal layers. Therewithin, they identified four retinal plexuses[29]:

- (1) Radial peripapillary capillary plexus
- (2) Superficial vascular plexus
- (3) Intermediate capillary plexus
- (4) Deep capillary plexus

In general, the retinal vasculature pervades the entire inner retina. Whereas capillary density peaks mainly occur in three regions: the outer ganglion cell layer, the interphase between inner plexiform layer and inner nuclear layer as well as the interphase between the inner nuclear layer and the outer plexiform layer. These maxima are termed superficial vascular plexus, intermediate capillary plexus and deep capillary plexus [29]. In addition, there is another locally limited capillary plexus, the radial peripapillary capillary plexus. As indicated by the name "peripapillary", it is predominantly situated in the surrounding area of the optical disc and running above the superficial vascular plexus. But the radial peripapillary capillary plexus nearly disappears beyond a lateral reach of approximately 3 mm [29]. For better understanding, the vascular architecture of the human retina is illustrated in figure 1.3. In essence, the central, avascular fovea is widely surrounded by retinal regions, developing three vascular plexuses (superficial vascular plexus, intermediate capillary

plexus and deep capillary plexus).

This complex retinal vasculature pervades and supplies the entire inner retina. However, biomolecules and metabolites are not freely exchanged between the retinal neurons and the retinal vasculature. Every exchange is strictly controlled by the inner blood-retinal barrier (iBRB), which is outlined in section 1.3.

### 1.2.3 Pericytes - the Vascular Companions

Pericytes (PCs) are individual globular cells periodically situated abluminal of vascular ECs, wrapping capillaries and microvessels in a finger-like structure [43]. PCs and ECs are closely interconnected and even share the same basement membrane (BSM) [44, 45]. Gap junctions enable direct exchange of biomolecules, while adhesion plaques, integrins and N-cadherin underpin the tight connection [44, 46]. PCs can be found in a multitude of organs like pancreas, lung, skeletal muscle, gut, bone marrow and many more [47]. However, PCs are also present in the central nervous system (CNS) and the retina. In these privileged sites, PCs possess an outstanding importance, since their dysfunction leads to a decline of fundamental barriers like the blood-brain barrier (BBB) as well as the BRB. In the CNS the EC/PC ratio is 1:1-3:1, indicating a higher PC density with regard to the human skeletal muscle (where EC/PC ratio was assumed between 10:1 and 100:1) [44, 48]. In general, it can be deduced that the PC coverage is higher around vascular ECs with barrier properties.

Earlier, PCs were only associated with blood flow regulation properties, since they can reduce the cross-sectional vessel lumen by contraction and therefore enhance the blood flow. Kureli et. al. found F-actin and alpha smooth muscle actin ( $\alpha$ -SMA) in retinal PCs demonstrating the relation to smooth muscle cells (occurring in arteries) [49].

Nowadays, PCs are getting more and more attention, since they are crucially involved in physiological and pathophysiological angiogenesis [46, 47, 50, 51]. In the previous section 1.2.2 the growth of retinal vasculature during prenatal and early development was discussed. The mentioned stabilization of immature vessels is supported by PCs. PCs express platelet derived growth factor receptor beta (PDGF-R $\beta$ ) (another similarity to smooth muscle cells), so that they are attracted by EC-secreted platelet derived growth factor beta (PDGF $\beta$ ) [43, 45, 50]. Park et. al. determined the highest PDGF $\beta$  expression in the vascular front region, recruiting PCs to the vascular ECs [52]. Subsequently, PCs are essential for the development of the BRB [53]. An inadequate PC coverage leads to hemorrhages, disrupted plexus formation, inflammation, increased EC apoptosis and extreme hypoxia [52]. Therefore, PCs are also essential for the development, maturation and stabilization of retinal capillaries [53]. On the contrary, PCs are dispensable for the maintenance of iBRB integrity during adulthood. After the complete establishment of the iBRB, they seem to lose their importance. But this is definitely not the case. Human vasculature is further subjected to a continuous remodelling depending on the tissue-specific oxygenation. This angiogenesis remodelling is incredibly complex in privileged sites like the brain and the retina since the BBB respectively the BRB must be continuously sustained. If a stabilized retinal capillary is needed to

sprout in a certain direction, PCs must be detached from the vascular EC first. Therefore, VEGF and matrix metalloproteases (MMPs) induce the degradation of the BSM, so that PCs can detach in a locally restricted vessel section. Subsequently, PCs secrete angiopoietin 1 that activates EC-presented Tie-2 receptor mediating the proliferation of the effected EC (tip cell). In that way, ECs start sprouting and build a nascent vessel (stalk cells). These nascent ECs in turn secrete angiopoietin 2 that is a partial antagonist for EC-presented Tie-2. As long as PCs secrete angiopoietin 1, angiopoietin 2 acts as an antagonist and reduces vascular sprouting. Tie-2 is also weakly expressed by PCs. The regulation details are not absolutely clear so far, but the angiopoietin/Tie-2 signalling and the angiopoietin 1/angiopoietin 2 balance are crucial for the vascular remodelling [45, 54]. Then the ECs of nascent vessels again attract PCs by the expression of PDGF $\beta$ , that are necessary to become a mature vessel [50].

Additionally, it becomes more and more evident that PCs own regenerative properties like parenchymal stem cells [44, 46, 50]. So they express several stem cell markers primarily CD34 and CD133 [50, 55]. For example, Stebbins et. al. generated PC-like cells from human pluripotent stem cells in order to induce BBB-properties in brain microvascular endothelial cells [56]. Vice versa there are first achievements in reprogramming. So Karow et. al. successfully converted brain PCs into neurons [57]. On this basis, PCs have the ability to repair or renew cells that are activated due to an injury. A representative example therefore, is the PC-mediated tissue repair after ischemic stroke [58] or the crucial role of PCs in myofibroblast wound healing [59]. These are only a few examples why PCs are focussed in current research. Since PCs are involved in neuronal disorders like diabetic retinopathy (DR) [60], Alzheimer's disease [61], multiple sclerosis [62] and CADASIL [63], they are becoming a promising target for new therapeutic approaches of various diseases [64].

Eventually, PCs fulfill very important functions not only in the retina: (1) regulation of the capillary blood flow, (2) stabilization and maturation of capillaries and microvessels, (3) contribution to the construction of physiological barriers like the BRB, (4) control of capillary angiogenesis and (5) tissue regeneration. They seem to play a key role in physiological vasculature homeostasis while their imbalance can trigger or at least contribute to pathological states. A really prominent example therefore is the decline of the iBRB following DR (refer to section 1.3 and 1.4.2).

## 1.3 Blood-Retinal Barrier

The human blood circuit is a complex network of blood vessels spanning the whole body. With an increasing distance to the heart, the vessels are massively branching to reach all peripheral tissue. Leaky capillaries enable the exchange of nutrients and metabolites. In privileged areas, this exchange is strongly regulated by a cellular barrier. Such barriers are constructed by a densely packed cell layer demarcating the privileged area and the vasculature. The most prominent example is the blood-brain barrier (BBB), protecting the CNS. Since the retina is an outgrowth of the neuroectoderm of the diencephalon [65], the retinal neurons correspond to such a privileged area as well. The retinal

neurons are demarcated by the BRB. It is splitted into two parts:

- the oBRB and
- the iBRB.

Both parts are essential for the retinal neurons. They are discussed in the following subsections.

### 1.3.1 Outer Blood-Retinal Barrier

The choriocapillaris is a fenestrated capillary network supplying the photoreceptors in the outer retina. Both tissues are segregated by RPE cells and the BRUCH's membrane (BM) (refer to figure 1.2). They control any metabolic exchange and form the oBRB. Hence, the oBRB is the physiological barrier between the choroidal vasculature and the outer retina.

The BM is a stable pentalamellar acellular sheet of the ECM. It is 2  $\mu\text{m}$  to 4  $\mu\text{m}$  thick [66], while its thickness raises during ageing by a few micrometres [67]. BM is maintained from both adjacent tissues - the RPE cells and the fenestrated capillary ECs of the choriocapillaris. The structure and the lead components of the BM are already known [65, 68–70]. The five layers and the comprising biomacromolecules are outlined in histological order in table 1.1.

Table 1.1: Structure and components of pentalamellar BM [65, 68–70].

Layer	Structure
BSM <sup>(1)</sup>	RPE synthesized <b>proteins</b> (collagen type IV) and <b>glycoproteins</b> (laminin and fibronectin), as well as proteoglycans of heparan-, chondroitin- and dermatan sulphate
ICL <sup>(2)</sup>	Collagen grid (collagen type I, III and V) embedded into glycosaminoglycan matrix (comprising hyaluronic acid, chondroitin- and dermatan sulphate)
EL <sup>(3)</sup>	Elastin fibres embedded in collagen type VI and fibronectin
OCL <sup>(4)</sup>	Widely similar to ICL
BSM <sup>(5)</sup>	Interrupted BSM composed of proteins (collagen type IV, V and VI), glycoproteins (laminin) and proteoglycans predominantly of heparan sulfate

<sup>(1)</sup> Basement membrane of RPE cells    <sup>(2)</sup> Inner collagen layer    <sup>(3)</sup> Elastin layer

<sup>(4)</sup> Outer collagen layer    <sup>(5)</sup> Basement membrane of choriocapillaris

The BM acts like a molecular sieve allowing the passing of biomolecules like nutrients, pigment precursors, vitamin A and antioxidants to the photoreceptors. The removal of metamolites like oxidized lipids and oxidized cholesterol works reversely [9, 65, 71]. Lee et. al. determined a molecular weight (MW) exclusion limit of  $150 \pm 40$  kDa [66]. Moreover, BM restricts choroidal as well as retinal cell migration. Already years ago, this cell migration restriction was associated with collagen type IV [65, 72, 73]. Nowadays it becomes apparent,



### 1.3. BLOOD-RETINAL BARRIER

---

that collagen type IV and laminins cause the high stiffness of 250 to 500 GPa that impedes cell migration [74]. Collagen type IV is a lead component in the BSMs of the human eye and essential for its structural stability [75, 76].

After passing the BM, biomolecules reach the RPE cells. The RPE is a continuous monolayer, whose hexagonal cells are densely packed and connected via tight junctions. Hence, a diffusion through the paracellular space is strongly impeded. That's why a couple of specialized transport mechanisms control the exchanges of biomolecules. Rizzolo et. al. categorized these transport mechanisms into five pathways[77]:

- (1) Para-cellular Diffusion
- (2) Facilitated Diffusion
- (3) Active Transport
- (4) Transcytosis
- (5) Solute Modification

As already mentioned above, *para-cellular diffusion* is strongly limited by tight junctions. Furthermore, this barrier is indispensable for the manifestation of RPE polarity and the establishment of concentration gradients [71, 77, 78].

*Facilitated diffusion* covers passive diffusion via specialized transporters along the concentration gradient. For instance, this is the case for the transport of glucose via GLUT-1 transporters [79, 80].

*Active transport* predominantly includes the pumping of ions through the basolateral and/or apical plasma membrane against a concentration gradient. The process is energy driven meaning that it consumes adenosine triphosphate (ATP) [71].

*Transcytosis* is absolutely indispensable for the functionality of photoreceptors. Light passes the approximately 800 to 2000 discs per photoreceptor[81] and the opsins collect the majority of the incident photons. The discs are permanently exposed to light in a high oxygen environment, so that they are aging very rapidly and must be renewed continuously. The disc formation is a complex process. There is more and more evidence that the discs evolve from ciliary ectosome release [81, 82]. The discs are produced at the proximal photoreceptor base of the outer segment and shedded at their distal tip [81]. The shed is subsequently phagocytosed by RPE cells, transferring and releasing the shed metabolites at the basolateral plasmamembrane [83, 84]. RPE cells maintain the degradation of the shed during its journey from the apical to the basolateral [85, 86]. Therefore the shedding of photoreceptors' outer segment illustrates exemplary, that engulfed cargo can be transported through the oBRB via transcytosis.

Lastly, *solute modification* is another prominent transport mechanism. RPE cells receive exhausted light-insensitive all-*trans*-retinal, transfer it enzymatically into 11-*cis*-retinal (isomerization) and re-deliver it to the photoreceptors [9, 10, 87]. This is one part of the retinoid cycle, where the solute all-*trans*-retinal, delivered from the apical direction, is enzymatically modified and re-directed to the photoreceptors. Retinol (vitamin A) is also delivered by the choroidal capillaries. After enzymatic modification to 11-*cis*-retinal in the RPE cells it enters the retinoid cycle as well [9, 87]. Another example is the elimination of carbondioxide through the RPE that is converted into hydrogencarbonate.

Inhere carbondioxide is also modified and transferred through the RPE [88].

In addition to the above mentioned five pathways, Fields et. al. introduced a sixth pathway [78]:

#### (6) Exosomes

*Exosomes* are extracellular nanovesicles that are released by most cell types. The RPE cells receive lipoprotein particles from the choroidal capillaries (basolateral) and release exosomes filled with lipids and proteins on the apical side. Klingeborn et. al. identified a few hundreds of proteins in total, that are delivered by RPE cells in both directions (apical as well as basolateral) [89].

Summing up, BM and RPE cells possess a couple of highly specialized features and transfer mechanisms to control the cargo exchange. Furthermore, they are specialized for the recycling and removal of retinal metabolites. Consequently, the functionality of the oBRB is absolutly essential for vision.

### 1.3.2 Inner Blood-Retinal Barrier

While the oBRB demarcates the choroidal vasculature and the outer retina, the inner blood-retinal barrier (iBRB) is analogously the physiological barrier between the retinal vasculature and the inner retina. Basically, the iBRB offers a similar concept for the protection of retinal tissue. In both barriers highly specialized transport mechanisms control the inflow and outflow of biomolecules and metabolites. Nevertheless, the cellular architecture is completely different. In the iBRB, the vascular EC are tightly connected by tight junctions impeding para-cellular diffusion. In comparison the vascular ECs in the oBRB are fenestrated and the actual barrier is built by the BM and the RPE cells. Accordingly, the specialized transport mechanisms are located in the RPE cells and not in the choroidal ECs. For the iBRB these specialized transport mechanisms are located in the ECs of the retinal vessels itself. The tightness of the ECs plays a key role for the iBRB integrity. The ECs accompanying PCs are maintaining this tightness and regulate the iBRB. PCs and retinal ECs are embedded in the same BSM as it is extensively discussed in section 1.2.3. Additionally, astrocytes, Mueller cells and microglial cells are in contact with the BSM of the PC-EC-unit. Collectively this cell assembly is termed the neovascular unit [90, 91]. In the neovascular unit, astrocytes maintain the homeostatic regulation and especially support the development of tight junction. Mueller cells give structural stability and enable the communication between vasculature and neurons [92]. Microglial cells represent the retina-resident macrophages facillitating the main immunological response after injuries or in pathological circumstances. The interplay within the neovascular unit is absolutely essential for the integrity of the iBRB [91, 93].

However, the mentioned specialized transport mechanisms of the ECs in the retinal vasculature are the key feature of the iBRB. Hereinafter, the classification of Diaz-Coránguez et. al. [27] was harmonized with regard to the classification of Rizzolo et. al. [77]:

#### (1) Para-cellular Diffusion

### 1.3. BLOOD-RETINAL BARRIER

---

- (2) Passive Diffusion
- (3) Facilitated Diffusion/ Carrier-mediated Transporters
- (4) Active Transport
- (5) Transcytosis

*Para-cellular diffusion* is strongly limited, since tight junctions between the vascular ECs are maintaining an effective sealing. This is necessary to control biomolecule exchange and the establishment of concentration gradients as well as an polarization of the barrier. A prominent tight junction representative is Claudin-5. It is a highly important protein to maintain the iBRB. Deficiencies in claudin-5 expression raises the iBRB permeability [27]. Furthermore, some claudins connect vascular ECs and enable the selective horizontal transfer of different ions at once. However, there are numerous further proteins involved in the maintenance of the barrier function. Occludin is therefore another important example. Low levels of occludin go along with an increased permeability as well. Liu et. al. identified the occludin S490 phosphorylation as a trigger for VEGF-induced neovascularization [94]. They gave evidence that the substitution of S490 with an alanin completely inhibited the VEGF-induced neovascularization. Further important proteins are JAM (junctional adhesion molecule) and adherens junctions predominantly built of VE-cadherins connected to  $\beta$ -catenins (already mentioned in section 1.2.2). All these tight connections of vascular ECs are essential for the integrity of the iBRB.

*Passive diffusion* is the gradient-driven diffusion of lipophilic small molecules through the iBRB without energy consumption.

*Facillitated diffusion* covers highly specialized transmembrane proteins selectively transporting certain substrates along a concentration gradient. This is the case for hydrophilic substances that cannot directly pass the iBRB. The most prominent example inhere is the GLUT1-transporter, facilitating the supply of retinal tissue with glucose as it was previously reported for the oBRB. In addition several further carriers for dehydroascorbic acid, different aminoacids, choline, adenosine, sucrose or mannitol are reported [95].

*Active transport* covers the energy-driven transport of substrates against a concentration gradient. In order to perpetuate the homeostasis and the cellular functionality, for example transporters are pumping ions like sodium and potassium against a concentration gradient under the consumption of ATP. Another example are efflux pumps like the very prominent P-glycoprotein (P-gp). If a substrate for P-gp enters the EC it is actively cleared to the luminal direction, so that it can not pass the iBRB. This is really useful for the protection of retinal tissue, but in can also hinder the delivery of therapeutic drugs [95–98]. P-gp corresponds to the adenosin triphosphate binding cassette superfamily covering further well-known efflux pumps like multidrug resistance protein and breast cancer resistance protein.

*Transcytosis* describes the transport of biomolecules through a cell via plasmamembrane invaginations. Thereto, some cargo binds to surface presented receptors that mediate the recruitment of proteins to the plasmamembrane (*receptor-mediated transport*). The recruited proteins induce a membrane curvature until the cargo is fully invaginated. Then the vesicle can pinch off the plasmamembrane, travel through the cell und fuse with the opposite plasmamembrane in order to release their cargo. Transcytosis is especially downregulated in cells maintaining a barrier-function. A prominent exam-

ple is the caveolin mediated endocytosis pathway [99], that is also expressed in the BBB [100]. It is named after caveolin-1, which is a membrane-bound protein facilitating the plasmamembrane curvature. Examples for caveolin mediated endocytosis transported cargo are transferrin, insulin, albumin, high density lipoprotein (HDL) particles and low density lipoprotein (LDL) particles, interleukin-1, platelet derived growth factor (PDGF), VEGF and TGF- $\beta$  [27]. Apart from the receptor-mediated transport there are also *pinocytic vessels* especially transporting plasma proteins. This mechanism does not involve specialized receptors selecting for the intended cargo. In general, transcytosis is strongly regulated in cellular barriers like the iBRB. This especially becomes apparent in pathophysiological states, where transcytosis is upregulated and the permeability raises dramatically as it is the case in DR [99, 101–103].

## 1.4 Ocular Diseases

The World Health Organization (WHO) estimated in their World Report on Vision that approximately 2.2 billion people suffered from vision impairment in 2019 [104]. The contributing ocular diseases are listed in table 1.2.

Table 1.2: Global magnitude of vision impairment in 2019 [104].

Ocular Disease	Sufferers (millions)
Presbyopia	1.800
Unaddressed refractive error	124
Cataract	65
<b>AMD</b>	<b>10</b>
Glaucoma	6
<b>DR</b>	<b>3</b>
Trachoma	2
Others	37
Unknown	189

While presbyopia, refractive errors and cataract can be effectively treated using spectacles, contact lenses or surgery, the other listed diseases mostly need a pharmacological intervention. Trachoma is a bacterial infection and can usually curatively be treated with antibiotics. The treatment of age-related macular degeneration (AMD), glaucoma and DR is widely intended to inhibit progression and prevent blindness. Currently there is no curative therapy available, so that further research is needed.

AMD and DR are ranking among the leading causes of blindness. In 2020, globally at least 33.6 million adults aged 50 years and older suffered from blindness, solely 1.8 millions (5.6 %) are caused by AMD and 0.9 millions (2.5 %) by DR. In comparison to the year 1990, this is a decline of almost 30 % of AMD-caused cases, while the DR-caused cases raised clearly (e.g. 138.3 % for the southern sub-Saharan Africa and more than 90 % for high-income North-America) [105]. The impairment of vision up to the total loss of vision (blindness) is a burden

for every patient. This work is primarily dealing with the proliferative subtypes of AMD and DR. These proliferative subtypes are preliminary stages of blindness that are attributed to the decline of the BRB. Their pathogenesis and current therapeutics will be discussed subsequently. Since the pathogenesis of other main causes of blindness like glaucoma and cataract vary fundamentally, they are not focussed in this work.

### 1.4.1 Age-related Macular Degeneration

#### Epidemiology

The global prevalence of people aged 45 to 85 years suffering from any AMD is approximately 8.7%, whereas the prevalence of early-stage AMD is 8.0% [106]. Worldwide 196 million were estimated to suffer from any AMD in 2020, while 288 millions were projected for 2040 [106, 107]. Thereby, the clearest rise (early-stage and late-stage AMD) was predicted for Asia and Africa [107].

Apart from that, Li et. al. focussed on the situation in Europe. They reported a prevalence of 27.7% [108], that is substantially higher than the European prevalence of 18.3% reported by Wong et. al. [107]. The annual incidence for late-stage AMD in Europe is also remarkable. It accounts 1.4 per 1.000 individuals, that corresponded to about 700.000 new late-stage AMD cases per year [108].

Despite the increase of people diseased with any type of AMD, it must be admitted that the percentage of AMD-caused blindness cases decreased in the last decades [104]. This was allocated with therapeutic efforts in the treatment of wet AMD [109]. But wet AMD effects only about 10% of the individuals suffering from an late-stage AMD, so that further therapeutic improvements are absolutely needed [110].

#### Pathogenesis

AMD is an ocular disease preferentially affecting the central macular region of the retina. It can be differentiated between early-stage AMD and late-stage AMD. Clinical signs of the early-stage AMD are drusen and abnormalities of the RPE that are recognizable via ocular fundus imaging techniques. Late-stage AMD can be further subdivided into the 'wet' or 'neovascular' and the 'dry' or 'atrophic' (non-neovascular) AMD. The visible changes in an advanced dry AMD are termed *geographic atrophy (GA)*. Both subtypes are associated with vision impairment and can progress until total vision loss [111]. The major risk factors are age and smoking [112].

**Early-stage AMD** - The basic diagnosis criterion for an early-stage AMD is the occurrence of drusen larger than 125  $\mu\text{m}$  or pigmentary abnormalities [113, 114]. With increasing age neutral lipids are accumulating in the ECM (e.g. BM) and can impair their functionality. The term *neutral lipids* covers triglycerides, esterified cholesterol and fatty acids. The human fat metabolism is complex. Roughly summarized, dietary lipids are absorbed from the intestine and transported to the peripheral tissue via *chylomicrons*. Through enzymatic

degradation (*lipolysis*) the fatty acids are released and can be further consumed via  $\beta$ -oxidation. The remains of chylomicrons (*chylomicron remnants*) are transported to the liver, that is crucially involved in the human lipid logistics. The liver processes especially cholesterol ensuring its provision to and collection from peripheral tissue as well as its excretion as bile salts. In the context of AMD pathogenesis it is worth focusing on the lipoprotein particles which are transporting water-insoluble lipids through the lymphatic as well as the systemic circulation. Lipoprotein particles (VLDL, LDL, IDL and HDL) comprise a neutral lipid core surrounded by unesterified cholesterol, proteins (apolipoproteins) and phospholipids with varying amounts [115]. Their size cover a wide range of 8 nm to 600 nm (HDL < LDL < IDL < VLDL << chylomicron) [112, 115, 116]. HDL and LDL deliver lipophilic substances like xanthophylls (lutin and zeaxanthin),  $\beta$ -carotinoids (provitamin A) and vitamin A to the retina. Therefore, HDL particles bind to RPE cells via the scavenger receptor class B1 and LDL via the low density lipoprotein receptor (LDL-R) [117]. Xanthophylls are enriched in the macular lutea, facilitating their yellow colorization. Xanthophylls filter excessive light and protect the retina as an antioxidant [117]. Vitamin A is the precursor for 11-*cis*-retinal (retinoid cycle) and therefore essential for vision (refer to section 1.1.2). For the exchange of the latter substances, lipoprotein particles have to travel from the choriocapillaris to the RPE cells and vice versa. On their way they need to pass the BM. This means that the BM pore size is large enough for the passage of particles between 8 nm to 15 nm (HDL) and 18 nm to 24 nm (LDL) [116]. With increasing age lipoprotein particles stick to the pores and occlude the BM step by step. This was demonstrated by Curcio et. al. in a very descriptive way via electron microscopic images [112]. The accumulation occurs during the outward travelling from RPE cells to the choriocapillaris [118]. The deposit is subdivided with regard to the deposit location. It is termed *basal laminar deposit (BlamD)* if it is located between the RPE and its BSM, while it is termed *basal linear deposit (BlinD)* if it is located between the RPE's BSM and the inner collagen layer. Both changes are typical for AMD-diseased eyes. BlinD is commonly known as *lipid wall*. Further accumulation of lipoprotein particles in the lipid wall provokes locally limited protrusion that are termed *druses*. The composition is similar to the lipid wall, but due to their size they can be recognized in ocular fundus imaging. The lead compound of soft druses is esterified cholesterol [119], which could not be detected in eyes from donors under the age of 22 years [112]. This emphasizes the age-related pathogenesis of AMD and elucidate the commonly known BM thickening due to protein and lipid deposition [119].

**Dry AMD** - Drusen, ageing and other factors (e.g. smoking and blue light exposure) enhance the secretion of inflammatory factors that lead to the increase of reactive oxygen species (ROS) from mitochondria [120]. The raising oxidative stress overstrains and damages mitochondria so that resulting mitochondrial desoxyribonucleic acid (mtDNA) fragments further induces the inflammation via factors like nuclear factor kappa-light-chain-enhancer of activated B-cells (NF- $\kappa$ B) [120–123]. However, the inflammation reaction also activates peroxisome proliferator-activated receptor gamma coactivator 1-alpha (PGC-1 $\alpha$ ), a protein interacting with transcription factors that regulate the energy production. PGC-1 $\alpha$  is a protective protein reducing the concentration of mitochondrial ROS [120, 123]. Nevertheless, continuously increasing

oxidative stress, whether related to lifestyle or normal ageing, overcomes the protective capacity at some time. Blasiak et. al. mentioned that impaired autophagy plays an essential role in the regeneration of mitochondria and the rise of oxidative stress [120]. Desoxyribonucleic acid (DNA) damages and mitochondrial decline arrest the cell cycle and cause the shift into senescent RPE cells. Senescence further induces oxidative stress, impairs the autophagy and increases the concentration of oxidized lipoprotein particles. Ultimately this cascade results in the death of the reflected RPE cells [122, 124]. The death of RPE cells is a hallmark in the AMD pathogenesis and characterizes a late-stage dry AMD. Hereinafter, the total cell load (e.g. oxidized lipoprotein particles) is released and enhance the BM deposits (BlamD, BlinD and druses). Initially, RPE gaps can be filled with surrounding RPE cells, but the regeneration capacity is continuously declining.

In addition, the complement system was identified as another important player in the AMD pathogenesis [125, 126]. The complement system is attributed to the innate immune system. They contribute to inflammatory processes and opsonization, support unspecific defences against microbes, but also assist the elimination of cell debris from the host. For instance, activated C3 fragments mark cell debris (opsonization) and attract phagocytic cells, so that they can eliminate the cell debris [125]. Basically, this is a physiological process, protecting ocular tissue. Another example is the complement factor H, a regulatory complement control protein. It binds to various oxidized lipids in order to facilitate their elimination [126, 127]. There is a couple of variants known, lacking the protective properties of native complement factor H. Therefore, anomalies in the gene encoding for complement factor H is reported as a dry AMD risk factor [110, 128]. Interestingly, patients with dry AMD (central GA and inactive choroidal neovascularization) show stronger complement activation than healthy humans and patients with early-stage AMD [126].

However, concurrently to pro-inflammatory processes and raising oxidative stress there is a turnover in the protective function of the complement system. C3a and C3b activate immune cells and trigger inflammation. C5b, C6, C7, C8 and C9 fuse to the membrane attacking complex that build pores in microbes or cells [126]. Oxidized lipids and hydrogen peroxide accumulate and continue to impair the BM. Therefore, the complement system changes from a protective role to a pro-inflammatory factor and progresses AMD pathogenesis. The death of RPE cells entails the loss of choriocapillaris fenestration, so that the supply of the photoreceptors is impaired and trigger their decline as well [129, 130].

**Wet AMD** - The main hallmark of a late-stage wet AMD is choroidal neovascularization. Therewithin, sprouting vessels originate from the choriocapillaris and penetrate through the BM into the outer retina. The growth factor VEGF plays a central role in choroidal neovascularization [131]. It is the target of the actual medicinal gold standard - the anti-VEGF therapeutics. Apart from that, VEGF is primarily an essential signalling protein mediating the fetal and early development of the ocular vasculature (refer to section 1.2). VEGF is physiologically released from RPE cells to maintain the choriocapillaris and its fenestration [132–134]. Accordingly, Shimomura et. al. demonstrated that the anti-VEGF therapeutics also reduce the fenestration of the choriocapillaris [135].

McLeod et. al. imaged the relative RPE area in comparison to the relative choroidal area of human donor eyes diagnosed with wet AMD [129]. They realized that the RPE area over the entire choroid was unaltered, while the choroidal area was extremely decreased to approximately 20 % in the fan-like choroidal neovascularization frontier region [129]. This work demonstrates impressively that in the wet AMD, an ablation of choroidal vessels occurs first. This causes a deficit in the regional supply of the outer retina alongside with an hypoxia. Hypoxia facilitates the release of hypoxia induced factor (HIF), that in turn triggers RPE cells to secrete growth factors like VEGF on their basolateral side [130]. VEGF passes the BM and stimulates ECs to proliferate and migrate towards the outer retina. Vascular ECs and macrophages secrete MMPs to degrade ECM and break through the BM [136]. In addition, HIF induces further growth factors like angiopoietin 2 and PDGF that facilitate the choroidal neovascularization [137]. Moreover, the Renin-Angiotensin-Aldosterone System (RAAS) was also reported to play a role in the choroidal neovascularization. So the expression of angiotensin II receptor type 1 (AT1R), angiotensin II receptor type 2 (AT2R) as well as angiotensin II (Ang II) was proven and especially the inhibition of AT1R decelerated choroidal neovascularization [138]. Yeo et. al. reported that vascular ECs for the newly formed vessels originate from tissue-resident endothelial progenitor cells as well as bone-marrow derived circulating hematopoietic stem cells and endothelial colony-forming cells [130].

Apart from that, TGF- $\beta$  is another signalling peptide involved in the choroidal neovascularization. It is expressed by Mueller cells, microglial cells, RPE cells and in photoreceptors. TGF- $\beta$  suppresses inflammatory actions of microglial cells and supports the survival of RPE. But with the penetration of choroidal vessels through the oBRB, RPE cells lose their polarity and TGF- $\beta$  enhances the transformation of RPE cells into an mesenchymal phenotype [139]. Furthermore, TGF- $\beta$  induces the proliferation and migration of ECs via the activation of ALK1 [139]. Rapidly growing vessels are immature and leaky, so that ruptures lead to the leakage of blood or plasma proteins. Vessel leakage is harmful for photoreceptors and trigger their decline [110]. Ultimately, vision impairment until blindness can occur.

**Condensation** - AMD is a multifactorial ocular disease that arose from a complex interplay of genetic predisposition, lifestyle (e.g. smoking) and regular ageing (e.g. chemical changes in ECM). In a typical AMD progression several pathological processes are crucially involved: (1) damaged vasculature, (2) accumulating lipids in the ECM (BM), (3) mitochondrial dysfunction, (4) misleading complement system, (5) overstressed RPE and (6) chronic inflammation. Although the mechanism of the pathogenesis is not completely clarified, the hallmarks are known. The pathological processes of late-stage AMD subtypes (dry AMD/ GA and wet AMD) are fundamentally different. Nevertheless, both subtypes can ultimately lead to vision impairment and up to total blindness.

#### **Therapeutics**

To this day, there is no treatment for dry AMD available, solely preventive measures can be taken. So the Age Related Eye Disease Study (AREDS)



demonstrated that the oral supplementation of a mixture containing vitamin C, vitamin E,  $\beta$ -carotene and zinc slow down AMD progression [140]. The AREDS2 investigated an additional supplementation with lutein, zeaxanthine and/ or  $\omega$ 3-fatty acids for further reduction of AMD progression. Finally no progress has been made, but the authors recommended to replace  $\beta$ -carotene with lutein, zeaxanthine and  $\omega$ 3-fatty acids. Because this reduces the risk of lung cancer in smokers [141, 142]. Moreover, there are recommendations for the supplementation of vitamin B12, vitamin D and folate [128].

The gold standard for the treatment of wet AMD is the anti-VEGF therapy. This treatment covers the introcular injection of drugs inhibiting the VEGF signalling [143]. The most important drugs are:

- (1) pegaptanib,
- (2) ranibizumab,
- (3) bevacizumab and
- (4) aflibercept.

*Pegaptanib* (Macugen<sup>®</sup>, EyeTech Pharmaceuticals/ Pfizer) is a PEGylated, modified RNA-aptamer against VEGF isoform 165 [144]. A preclinical study in monkeys revealed that the half life of pegaptanib in vitreous humour is 94 h (3.9 days) [145]. The absorption of pegaptanib into the plasma is very slow, so that the application regime defined a 6-week interval between the ocular injections [146]. The main elimination route is renal [144]. Pegaptanib was approved in December 2004 (United States Food and Drug Administration (FDA)) respectively in January 2006 (European Medicines Agency (EMA)) [147]. With the further development of anti-VEGF drugs it lost its clinical relevance.

*Ranibizumab* (Lucentis<sup>®</sup>, Genentech/ Novartis) is a monoclonal antibody fragment (MW 46 kDa) against VEGF-A, which was approved in June 2006 (FDA) respectively in January 2007 (EMA). Animal studies revealed half-life in vitreous humour in the range of 2.6 to 2.8 days [148]. Ranibizumab penetrates directly from the vitreous humour into all retinal layers including RPE cells and even the choriocapillaris [149]. Only less than 0.01 % of the administered dose were found to enter the systemic circulation in an animal model [149]. And in this way systemic side effects could be minimized. A serum half-life of 5.8 days was detected and no accumulation after multi-dose administration could be found [148].

*Bevacizumab* (Avastin<sup>®</sup>, Genentech/ Roche) is a full monoclonal antibody against VEGF-A. Bevacizumab was developed as an oncologic drug and was approved in this context in February 2004 (FDA) respectively January 2005 (EMA). Bevacizumab is also used off-label for wet AMD due to the lower costs per dose, but this is the subject of ongoing debates [150]. Animal studies revealed half-life in vitreous humour in the range of 3.6 to 6.6 days. The serum half-life (humans) was 11.3 days [148].

*Aflibercept* (Eylea<sup>®</sup>, Regeneron/ Bayer) is a recombinant fusion protein (115 kDa) containing domains of vascular endothelial growth factor receptors (VEGF-Rs) (VEGF-R1 and VEGF-R2) fused to the fraction crystallization domain (F<sub>c</sub>) of a human immunoglobulin G (IgG) [151]. The equilibrium dissociation constant of the ligand-receptor complex (K<sub>d</sub>) for VEGF isoform 165 is

lower than 1 pM [151, 152]. It was approved in November 2011 (FDA) respectively November 2012 (EMA). Animal studies revealed a half-life in vitreous humour of 4.9 days. Furthermore, in the administration regime of aflibercept it is possible to extend the injection interval to 12 weeks [152]. Aflibercept differs from the other anti-VEGF-drugs since it is additionally able to bind the placental growth factor (PlGF). The plasma half-life was determined in humans and accounted approximately 1.5 days [148].

The introduction of anti-VEGF therapeutics was a benchmark in the treatment of wet AMD. It stops progression and even alleviate vision impairment for years [153]. This was a true healthcare innovation that reduced the cases of AMD-related blindness clearly [104]. Currently, there are new candidates under investigation in order to reduce the administration frequency (e.g. brolicizumab - antibody fragment with increased half-life, ranibizumab port delivery system) or the advance of the spectrum of addressed growth factors (e.g. facrimab - antibody binding VEGF-A and angiopoietin 2) [152]. Moreover, alternative application routes and several advanced formulation developments (e.g. hydrogels, implants and particulate systems) are under investigation [154]. This is due to the fact that multiple intravitreal injections pose a considerable risk for complications. For one thing, there is the risk of drug-associated side effects like noninfectious uveitis [155, 156]. On the other hand, endophthalmitis (severe complication, incidence: 0.016 % [157]), postinjection intraocular pressure, retinal detachment, subconjunctival or vitreous hemorrhage, lens injury or traumatic cataract are among the rarely observed complications [156, 158–160]. These complications potentially originate from the used devices (e.g. clogging or bending [161], silicone oil droplets [156, 162]), the injection technique (e.g. injury of the lens, application of bubbles [161]) or the application environment [163, 164]. However, the benefit of the anti-VEGF therapy overcomes the rare complication risk.

Nowadays there are a plethora of new therapeutics in the pipeline[143]:

- (1) Inhibitors of the complement system,
- (2) Gene therapeutics,
- (3) RPE transplantation.

The participation of the complement system in the AMD pathogenesis was outlined previously. That's why the complement system is a promising target and a plethora of substances is the subject of current studies. These include APL-2 from Apellis a peptide targeting C3 (Phase III - NCT03525600, NCT0352613) and ARC1905 from IVERIC bio a aptamer-based inhibitor targeting C5 (Phase III - NCT04435366) [126]. Both substances are intended for the dry AMD first. However, there are many other substances under investigation.

Another very interesting approach for the reduction of anti-VEGF administration frequency utilizes gene therapy tools. Reid et. al. introduced the development of recombinant anti-VEGF therapeutics [165]. They used a recombinant adeno-associated virus to apply genes that facilitate the long-term expression of anti-VEGF therapeutics without subsequent intravitreal injections [143, 166].

Since the damage of RPE cells has crucially been involved in the pathogenesis of AMD (especially dry AMD), the transplantation of healthy RPE cells is quite promising. Mandai et. al. used patient material to obtain autologous induced pluripotent stem cell, which were differentiated into RPE cells and transplanted [167]. This is a promising approach because it did not show tumorigenicity in a two years follow up. Nevertheless, it has been an experimental approach so far. But there are even further achievements reported, so that this approach becomes more and more serious [168]. In addition, researchers proved alternative approaches like macular translocation, autologous RPE-choroidal transplantaion or RPE cell suspension injection [143]. But these approaches remain truly challenging with several drawbacks. The outcomes of related studies are eagerly awaited.

### 1.4.2 Diabetic Retinopathy

#### Epidemiology

In 2019, 351.7 million people of working age (20-64 years) suffered from diabetes. The *International Diabetes Foundation* estimates an increase to 417.3 million until 2030 [169]. The prevalence is especially high in middle-income and high-income countries. Among diabetic patients, DR is a major complication that can lead to a complete vision loss. The global prevalence (among diabetic patients) accounted 35.4 % for DR and 7.5 % for the proliferative diabetic retinopathy (PDR) between 1980 and 2008 [170]. The prevalence is higher in those with diabetes mellitus type 1 (T1DM) (DR: 77.3 %, PDR: 32.4 %) than in those with diabetes mellitus type 2 (T2DM) (DR: 25.2 %, PDR: 3.0 %) [170]. This can be explained by the duration of diabetes. Patients with T1DM are getting sick predominantly in childhood or at a younger age, so that they suffer from diabetes for longer periods. This also raises the probability for the occurrence of complications like a DR [90, 171].

Since the life expectancy and the medical care including preventive measures as well as screening methods have constantly been improved, not only the prevalence should be considered but also the incidence. Sabanayagam et. al. systematically reviewed the literature from January 1980 to January 2018 and determined an annual DR incidence ranging between 2.2 % and 22.3 % [172]. The corresponding data pool included 14 population studies worldwide. However, the authors identified a tendential decrease in the annual DR incidence over the reviewed period. Furthermore, they reported that the annual incidence of PDR accounted 0.03 % to 0.72 % [172]. What these annual numbers actually mean for an individual diabetes patient, can be deduced from the work of Klein et. al. They followed 955 insulin-taking T1DM patients, diagnosed before reaching the age of 30 for a period of up to 25 years. Overall 97 % got a DR and even 42 % suffered from a progression to the PDR [171]. These data indicate that the disease duration is an intrinsic risk factor that truly influences the DR severity.

##### Pathogenesis

Diabetic retinopathy (DR) is a severe complication in the course of a diabetes mellitus disease. In general, diabetes mellitus is associated with a long-term, raised blood-glucose level (hyperglycemia). The underlying causes are manifold and complex, so that diabetes mellitus was categorized into different types:

(1) T1DM (2) T2DM (3) Gestational diabetes (4) Others. T1DM is associated with an insufficient or total loss of insulin secretion by the pancreas. It predominantly arises in childhood and can be treated through the administration of insulin. T2DM is the most common form of diabetes. Inhere the somatic cells lose their sensitivity to insulin causing an insufficient uptake of blood-supplied glucose. Gestational diabetes occurs during pregnancy and owns some similarities to T2DM. The reason is not completely clarified, but an insulin resistance following placenta-secreted hormones is assumed. Furthermore, there is a multitude of other reasons that can cause diabetes mellitus. For instance it can be associated with genetic defects, pancreatic diseases, endocrinological defects, infections or drug therapy.

All of these diabetes types is a long-term, elevated blood-glucose level in common. This can subsequently lead to micro- and macroangiopathies. DRs contribute to the microangiopathies located in ocular tissue [93]. With an increasing duration of high blood-glucose levels the probability for the occurrence of DR complications raises dramatically [171] and can finally lead to the loss of vision. Already to the turn of the millenium several pathological pathways were identified [173]. This consideration is still valid and has been investigated up to the present day [174–176]:

- (1) polyol pathway,
- (2) hexosamine pathway,
- (3) increased levels of advanced glycosylation endproducts (AGE) and
- (4) activation of protein kinase C (PKC).

The *Polyol pathway* is known for the NADPH-dependent reduction of carbonyl compounds catalyzed by the enzyme aldose reductase. The affinity of glucose to this enzyme is low, so that glucose is normally metabolized to sorbitol in negligible quantities. However, the metabolic rate increases in intracellular hyperglycemic situations raising the intracellular sorbitol concentration as well [176]. The accumulation of sorbitol causes a hyperosmolarity resulting in damage of retinal vascular ECs, the loss of PCs and the thickening of BSM [60]. Furthermore, it enhances water influx [177]. In adaption to the hyperosmolarity mitochondrial, transcriptional and translational dysfunction occur until cells devolve apoptosis [177, 178]. Moreover, this process claims the aldose reductase and additionally consumes NADPH. As a result the detoxification of reactive aldehyds is interrupted and the concentration of ROS increases [173]. Moreover, sorbitol can be further metabolized to 3-desoxyglucosone that facilitates the production of AGE [177].

Through the *Hexosamine pathway* cells are able to synthesize amino sugars which are the precursors for glycoproteins, glycolipids, proteoglycans and glucosaminoglycans. For one thing the ECM (e.g. BM or the BSM wrapping

ECs and PCs in the retinal vasculature) comprises such substances. Under euglycemic conditions, glucose is metabolized to ATP (energy carrier) and pyruvate. This pathway is commonly known as glycolysis. Fructose-6-phosphate is an intermediate in the glycolysis and concurrently the first substrate in the hexosamine pathway. Fructose-6-phosphate is slowly converted by the fructose-6-phosphate-amido transferase (GFAT) that is the first enzyme in the hexosamine pathway [175]. Therefore, the production of amino sugars is low under euglycemic conditions. However, under hyperglycemic conditions the concentration of Fructose-6-phosphate increases and raises the production of amino sugars accordingly. This results in an excess protein glycosylation disrupting gene expression and cellular functions in the retina. Amongst others it induces the apoptosis of retinal PCs [175].

AGEs originate from the reaction of glucose-derived dicarbonyls like glyoxal, methylglyoxal and 3-deoxyglucosone with amino groups of intracellular and extracellular proteins [179–182]. AGEs can impair intracellular proteins, ECM components (e.g. collagens and laminins) or ECM proteins (e.g. integrins) as well as plasma proteins [173, 183]. With the modification of BSM the connection between PCs and EC is getting lost and ECM-based barriers like BM lose their functionality. Furthermore, AGE-modified plasma proteins like N-carboxymethyl-lysine (CML) are able to activate transcription factors like NF- $\kappa$ B via receptors for advanced glycosylation endproducts (RAGE). This process induces the expression of pathological genes leading to the secretion of signalling proteins like VEGF and tumor necrosis factor alpha (TNF- $\alpha$ ) that subsequently promote the apoptosis of retinal PCs [60, 183–185]. Additionally, the raising amount of AGE claims the aldose reductase (polyol pathway) further and increases the amount of ROS.

PKC is a collective term for a family of serine/threonine kinases that are involved in versatile signalling pathways. Following oxidative stress, the Poly-ADP-ribose polymerase 1 (PARP1) is upregulated under hyperglycemic conditions. PARP1 is an enzyme catalyzing the metabolization of glycerin-aldehyde-3-phosphate (another glycolysis intermediate). This reaction is an alternative pathway yielding in the production of diacyl glycerol (DAG). DAG is a di-ester of glycerol and two fatty acids that upregulates the PKC signalling [60, 174]. The PKC pathway further activates the production of ROS-generating enzymes and enhance the oxidative stress progressively. The PKC isoforms PKC- $\beta$  and PKC- $\delta$  are known for their involvement in the pathogenesis of DR. PKC- $\beta$  induces the release of nitric oxide (NO) and VEGF in ECs, that in turn increase vascular permeability in the retina, decreases the blood flow and lead to macular edema. PKC- $\delta$  stimulates the synthesis of ROS and induces NF- $\kappa$ B that inhibits PDGF. This signalling cascade ultimately leads to PC-loss and microaneurysms [60, 174].

Beyond these four proven pathogenetic pathways another pathway was moving into focus:

##### (5) ocular RAAS

The RAAS is known to regulate the systemic blood flow. The main signalling axis comprises angiotensinogen, angiotensin I (Ang I) and Ang II. Liver-dis-

tributed angiotensinogen can be converted via the kidney-secreted endopeptidase renin into the decapeptide Ang I. Then, the angiotensin converting enzyme (ACE) is able to remove two further aminoacids to yield the octapeptide Ang II. Ang II in turn is able to activate the AT1R that mediates a plethora of signalling pathways that enhance the blood pressure [186, 187]. The RAAS has already been studied exhaustively, so that this main axis was considerably extended and several local RAASs were identified. Local RAAS are able to produce all substances autonomously. A systemic supply is not needed. So there exists an ocular RAAS, too, and it was found to be crucially involved in the development of ocular diseases especially in DR progression [188–190]. Danser et. al. provided evidence that neither systemic supplied angiotensinogen, Ang I nor Ang II is able to enter the eye for the first time [191]. They concluded that all substances must be produced locally. Until today, all substances were verified in several retinal tissues [190, 192, 193]. It is known that ocular Ang II activates inositol-1,4,5-phosphate (IP<sub>3</sub>) as well as DAG/ PKC signalling cascades. This leads to the secretion of growth and transcription factors like VEGF, TGF- $\beta$  and NF- $\kappa$ B. Furthermore, it induces the concentration of AGEs. As a result the activation of the ocular RAAS triggers angiogenesis, vascular inflammation, neuronal dysfunction, matrix accumulation, cell proliferation and apoptosis [190]. Moreover, the RAAS can be upregulated by the hexosamine pathway [194].

These pathways describe different molecular mechanisms, how hyperglycemia impairs ocular vasculature and triggers the development of a DR. However, they cannot be seen as isolated pathways but rather as entangled pathological processes. The DR can be separated into two different stages (1) non-proliferative diabetic retinopathy (NPDR) and (2) PDR. A NPDR becomes clinically significant with the appearance of microaneurysms and intraretinal hemorrhage in ocular fundus imaging. In the further progress cotton wool spots and diabetic macular edema (DME) can be recognized. The oxidative stress, cell death and the hyperglycemic dysregulation of the signalling pathways trigger astrocytes and Mueller cells to secrete inflammatory cytokines, initiate an immune response and facilitate retinal angiogenesis [93, 178, 194, 195]. The milestone in the progression of a NPDR is the occurrence of vascular neovascularization. Neovascularization denotes the progression into a PDR that is associated with vitreous hemorrhage, retinal detachment, iris neovascularization, intraocular pressure elevation (neovascular glaucoma) and ultimately with the loss of vision. A hallmark in a DR-progress is the loss of PC around the retinal vasculature and the neovascular breaking through the BRB [60, 174]. PCs are maintaining the iBRB. Their loss disrupts adherens junctions, induces the permeability and triggers the secretion of growth factors like VEGF [53, 90]. The decline of retinal neurons and glial cells through hyperglycemia-induced changes and local hemorrhages impair the blood supply and induce the expression of HIF that in turn triggers the secretion of VEGF and speeds up the harmful neovascularization [196].

The complex interplay of neuronal, glial, immune and vascular cells is essential to maintain the multitude of biochemical processes that are indispensable for vision. With arising deeper understanding of this complex interplay the term neurovascular unit (NVU) was created. It implies the importance of the regulated interplay between retinal tissue. Any dysregulation or impairment of the

neurovascular unit (NVU) participants contribute to pathological processes as it was outlined in context of the DR.

#### **Therapeutics**

The first-line therapy for the treatment of DME is the aforementioned anti-VEGF medication. It again covers the intravitreal injection of ranibizumab, bevacizumab and aflibercept [174]. All substances seem to improve vision impairment and reduce mean retinal thickness after a two-year treatment [197]. Furthermore, it was reported that aflibercept slightly superior potentially due to its additional inhibition of PIGF [197–199]. However, the long-term effectiveness is still under evaluation [200].

An intravitreal anti-VEGF medication is also recommended for the treatment of a PDR and furthermore there are studies evaluating the effectiveness in NPDR [201]. However, there is no evidence that this therapy is better than pan-retinal photocoagulation therapy so far, although there are several advantages like improved visual acuity and reduced complications [202, 203].

Another therapeutic option for the treatment of DME is the intravitreal application of steroids [174]. Dexamethasone, fluocinolone and triamcinolone (off-label) are among the frequently administered drugs. They reduce pro-inflammatory processes, reduce the thickness of the retina and improve the visual sharpness as well. Additionally, there are application regimes combining anti-VEGF and long-term steroids to improve the therapy of DME [204]. However, the data basis need to be extended. Moreover, it bears the rare risk of complications associated with an intravitreal administration in general. Whereas, the availability of steroid implants reduce the frequency of intravitreal injection clearly [204]. Beyond that, intravitreal steroids also increase the risk of cataract and increase intraocular pressure [174, 205]. All in all, intravitreal steroid application is actually not the first-line therapy, but it is a valuable therapeutic option [206].

Apart from the approved therapeutics for DME and PDR there are many drugs in the pipeline [206, 207]. The concepts range from molecular modifications in order to increase the intravitreal half-life (e.g. brolocizumab - single chain antibody fragment against VEGF-A - NCT03481634 OR abicipar pegol - PEGylated protein binding VEGF-A - NCT02186119), sustained-release anti-VEGF devices (ranibizumab Port Delivery System - NCT04108156) to the development of drugs affecting further pathogenic targets (e.g. faricimab - monoclonal antibody addressing VEGF-A and angiopoetin 2 - NCT03622593 / NCT03622580 OR ALG-1001 - integrin receptor antagonist - NCT02348918 OR THR-317 - antibody targeting PIGF - NCT03499223). The ongoing studies will reveal if these plausible pharmacological interventions are effective for the treatment of DR.

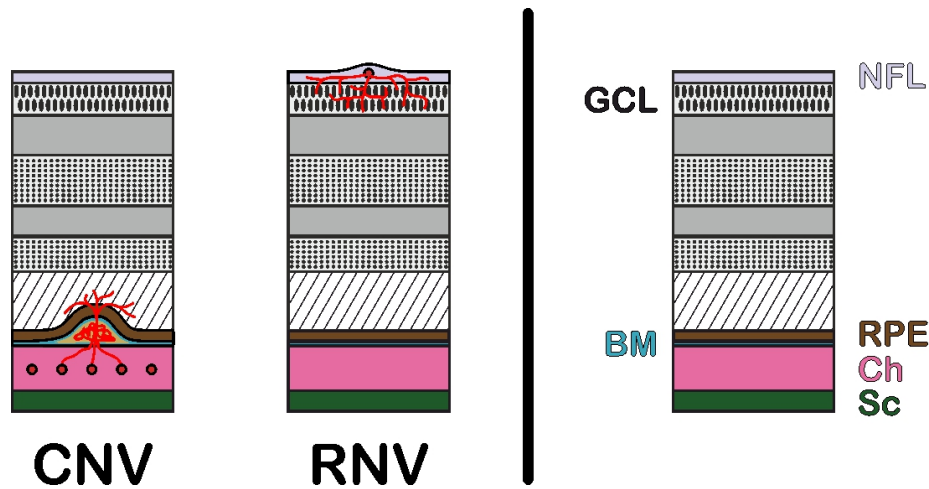


Figure 1.4: Origin of the neovascular sprouts in the course of wet AMD (CNV - choroidal neovascularization) and PDR (RNV - retinal neovascularization) modified from the literature [130, 208, 209] (**left**) in comparison to the physiological situation (**right**). [Nerve fiber layer (NFL), Ganglion cell layer (GCL), Retinal pigment epithelium (RPE), BRUCH's membrane (BM), Choroid (Ch) and Sclera (Sc)]

## 1.5 The Need for an Adaptable Platform Technology

In the previous sections the pathogenesis and the therapeutical options for AMD and DR were discussed in detail. This work focusses on the neovascular forms of AMD (wet AMD) and DR (PDR). The pathological processes are complex and not completely understood so far. But both equally develop a hypoxia-driven neovascularization that involves growth factors like VEGF. Varying are the initial disease triggers and the neovascularization location. As it is illustrated in figure 1.4, in the course of wet AMD vessels sprout from the choroid through the oBRB into the interphotoreceptor layer (**choroidal neovascularization**) while in the course of PDR vessel sprouts originate from the retinal vasculature (**retinal neovascularization**).

That's why the introduction of the anti-VEGF therapy was an unquestionable breakthrough. Eventually, this can be recognized by the reduction of AMD caused blindness. So the age-standardized prevalence globally decreased about 28.7% from 1990 to 2020 [105]. Nevertheless, not every patient can be treated with anti-VEGF therapeutics and additionally not every treated patient responds. Most likely, there are further pathological signalling pathways that are involved. This is in line with the previous achievements and current investigational approaches. So the development started from a highly specialized aptamer (*pegaptanib*) against a single VEGF isoform through antibodies binding all VEGF-A isoforms (bevacizumab and ranibizumab) to a fusion protein binding to all VEGF-A isoforms as well as PlGF (afibercept) [152]. Nowadays, the focus of research is shifting to other pathways. For example, the comple-



ment system is such a target, where promising candidates are already in the pipeline [126].

With respect to this anti-VEGF evolution a novel therapeutic system is supposed to be highly convertible and easily be addressed more than a single target, so that slight modifications allow for the addressing of upcoming targets as well. But in doing so, the pharmacokinetics should not be changed fundamentally, which is certainly challenging.

On closer examination, the approved anti-VEGF therapeutics also show an increase in the mean residence time in the vitreous humor. The researchers aimed to achieve a drug depot in order to extend intravitreal injection intervals. This reduces the frequency of intravitreal injections as well. However, this strategy is limited, so that release systems for a controlled drug release (implants or refillable reservoir [154]) as well as gene therapy options for a permanent local production of anti-VEGF proteins (recombinant adeno-associated viral approach [165]) are under investigation. This is relevant since intravitreal injections bear the risk for rarely but severe complications like endophthalmitis [159]. In addition intravitreal injections must be performed by a health care professional and it is not convenient for the patient. Therefore, an alternative application route (systemic administration) would be preferable for a novel therapeutic system.

After all, there is a considerable need for an highly versatile platform technology, that can be tailored for the targeting of various pathogenetic signalling cascades. Multivalent nanoparticles (NPs) are a great tool for this purpose. It is the aim of this work to forward a promising technique on the road to a true therapeutic option.

## 1.6 References

- [1] Inessa Bekerman, Paul Gottlieb, and Michael Vaiman. "Variations in Eyeball Diameters of the Healthy Adults". In: *Journal of Ophthalmology* (2014). DOI: 10.1155/2014/503645.
- [2] Julie T. Daniels et al. "Corneal Stem Cells in Review". In: *Wound Repair and Regeneration* 9.6 (2001), pp. 483–494. DOI: 10.1046/j.1524-475x.2001.00483.x.
- [3] Myron Yanoff and Jay S. Duker, eds. *Ophthalmology*. Fifth Edition. Amsterdam: Elsevier, 2018.
- [4] James Douth et al. "Light Transmission in the Human Cornea as a Function of Position across the Ocular Surface: Theoretical and Experimental Aspects". In: *Biophysical Journal* 95.11 (2008), pp. 5092–5099. DOI: 10.1529/biophysj.108.132316.
- [5] Jie Zhu, Ellean Zhang, and Katia Del Rio-Tsonis. *Eye Anatomy*. Encyclopedia of Life Sciences. Chichester: John Wiley & Sons, 2012. DOI: 10.1002/9780470015902.a0000108.pub2.
- [6] F. J. Lovicu and J. W. McAvoy. "Growth Factor Regulation of Lens Development". In: *Developmental Biology* 280.1 (2005), pp. 1–14. DOI: 10.1016/j.ydbio.2005.01.020.

## 1.6. REFERENCES

---

- [7] Michael F. Land and Russell D. Fernald. "The Evolution of Eyes". In: *Annual Review of Neuroscience* 15 (1992), pp. 1–29. DOI: 10.1146/annurev.ne.15.030192.000245.
- [8] Songhmitra Panda-Jonas, Jost B. Jonas, and Martha Jakobczyk-Zmija. "Retinal Pigment Epithelial Cell Count, Distribution, and Correlations in Normal Human Eyes". In: *American Journal of Ophthalmology* 121.2 (1996), pp. 181–189. DOI: 10.1016/S0002-9394(14)70583-5.
- [9] Olaf Strauss. "The Retinal Pigment Epithelium in Visual Function". In: *Physiological Reviews* 85.3 (2005), pp. 845–881. DOI: 10.1152/physrev.00021.2004.
- [10] Krzysztof Palczewski. "Chemistry and Biology of Vision". In: *Journal of Biological Chemistry* 287.3 (2012), pp. 1612–1619. DOI: 10.1074/jbc.R111.301150.
- [11] I. Fahrenfort et al. "The Involvement of Glutamate-Gated Channels in Negative Feedback from Horizontal Cells to Cones". In: *Development, Dynamics and Pathology of Neuronal Networks: From Molecules to Functional Circuits*. Ed. by J. van Pelt et al. Vol. 147. Progress in Brain Research. Amsterdam: Elsevier, 2004, pp. 219–229. DOI: 10.1016/S0079-6123(04)47017-4.
- [12] Helga Kolb. "Amacrine Cells of the Mammalian Retina: Neurocircuitry and Functional Roles". In: *Eye* 11.6 (1997), pp. 904–923. DOI: 10.1038/eye.1997.230.
- [13] Andreas Reichenbach and Andreas Bringmann. "Glia of the Human Retina". In: *Glia* 68.4 (2020), pp. 768–796. DOI: 10.1002/glia.23727.
- [14] Serge Poitry et al. "Mechanisms of Glutamate Metabolic Signaling in Retinal Glial (Müller) Cells". In: *Journal of Neuroscience* 20.5 (2000), pp. 1809–1821. DOI: 10.1523/JNEUROSCI.20-05-01809.2000.
- [15] Andreas Bringmann et al. "Müller Cells in the Healthy and Diseased Retina". In: *Progress in Retinal and Eye Research* 25.4 (2006), pp. 397–424. DOI: 10.1016/j.preteyeres.2006.05.003.
- [16] Andreas Bringmann et al. "GABA and Glutamate Uptake and Metabolism in Retinal Glial (Müller) Cells". In: *Frontiers in Endocrinology* 4 (2013). DOI: 10.3389/fendo.2013.00048.
- [17] Elena Vecino et al. "Glia-Neuron Interactions in the Mammalian Retina". In: *Progress in Retinal and Eye Research* 51 (2016), pp. 1–40. DOI: 10.1016/j.preteyeres.2015.06.003.
- [18] Kristian Franze et al. "Müller Cells are Living Optical Fibers in the Vertebrate Retina". In: *Proceedings of the National Academy of Sciences* 104.20 (2007), pp. 8287–8292. DOI: 10.1073/pnas.0611180104.
- [19] Andreas Reichenbach and Andreas Bringmann. "New Functions of Müller cells". In: *Glia* 61.5 (2013), pp. 651–678. DOI: 10.1002/glia.22477.
- [20] Amichai M. Labin et al. "Müller Cells Separate between Wavelengths to Improve Day Vision with Minimal Effect upon Night Vision". In: *Nature Communications* 5 (2014). DOI: 10.1038/ncomms5319.

## 1.6. REFERENCES

---

- [21] Daniel Goldman. “Müller Glial Cell Reprogramming and Retina Regeneration”. In: *Nature Reviews Neuroscience* 15.7 (2014), pp. 431–442. DOI: 10.1038/nrn3723.
- [22] Aruna Jammalamadaka et al. “Characterizing Spatial Distributions of Astrocytes in the Mammalian Retina”. In: *Bioinformatics* 31.12 (2015), pp. 2024–2031. DOI: 10.1093/bioinformatics/btv097.
- [23] Senthil Selvam, Tejas Kumar, and Marcus Fruttiger. “Retinal Vasculature Development in Health and Disease”. In: *Progress in Retinal and Eye Research* 63 (2018), pp. 1–19. DOI: 10.1016/j.preteyeres.2017.11.001.
- [24] Sean M. Silverman and Wai T. Wong. “Microglia in the Retina: Roles in Development, Maturity, and Disease”. In: *Annual Review of Vision Science* 4 (2018), pp. 45–77. DOI: 10.1146/annurev-vision-091517-034425.
- [25] Fenge Li, Danye Jiang, and Melanie A. Samuel. “Microglia in the Developing Retina”. In: *Neural Development* 14 (2019). DOI: 10.1186/s13064-019-0137-x.
- [26] Gurugirijha Rathnasamy et al. “Retinal Microglia - A Key Player in Healthy and Diseased Retina”. In: *Progress in Neurobiology* 173 (2019), pp. 18–40. DOI: 10.1016/j.pneurobio.2018.05.006.
- [27] Mónica Díaz-Coránguez, Carla Ramos, and David A. Antonetti. “The Inner Blood-Retinal Barrier: Cellular Basis and Development”. In: *Vision Research* 139 (2017), pp. 123–137. DOI: 10.1016/j.visres.2017.05.009.
- [28] D. F. Gilmour. “Familial Exudative Vitreoretinopathy and Related Retinopathies”. In: *Eye* 29.1 (2015), pp. 1–14. DOI: 10.1038/eye.2014.70.
- [29] J. P. Campbell et al. “Detailed Vascular Anatomy of the Human Retina by Projection-Resolved Optical Coherence Tomography Angiography”. In: *Scientific Reports* 7 (2017), pp. 1–11. DOI: 10.1038/srep42201.
- [30] L. R. Williams and R. W. Leggett. “Reference Values for Resting Blood Flow to Organs of Man”. In: *Clinical Physics and Physiological Measurement* 10.3 (1989), pp. 187–217. DOI: 10.1088/0143-0815/10/3/001.
- [31] Shahin Rafii, Jason M. Butler, and Bi-Sen Ding. “Angiocrine Functions of Organ-Specific Endothelial Cells”. In: *Nature* 529 (2016), pp. 316–325. DOI: 10.1038/nature17040.
- [32] Roswitha Seitz et al. “Cross-Inhibition of Norrin and TGF- $\beta$  Signaling Modulates Development of Retinal and Choroidal Vasculature”. In: *Investigative Ophthalmology & Visual Science* 59.6 (2018), pp. 2240–2251. DOI: 10.1167/iovs.17-23403.
- [33] Xin Ye et al. “Norrin, Frizzled-4, and Lrp5 Signaling in Endothelial Cells Controls a Genetic Program for Retinal Vascularization”. In: *Cell* 139.2 (2009), pp. 285–298. DOI: 10.1016/j.cell.2009.07.047.
- [34] Yanshu Wang et al. “Norrin/Frizzled4 Signaling in Retinal Vascular Development and Blood Brain Barrier Plasticity”. In: *Cell* 151.6 (2012), pp. 1332–1344. DOI: 10.1016/j.cell.2012.10.042.
- [35] Yulian Zhou et al. “Canonical WNT Signaling Components in Vascular Development and Barrier Formation”. In: *The Journal of Clinical Investigation* 124.9 (2014), pp. 3825–3846. DOI: 10.1172/JCI76431.

## 1.6. REFERENCES

---

- [36] Yanshu Wang et al. "Interplay of the Norrin and Wnt7a/Wnt7b Signaling Systems in Blood-Brain Barrier and Blood-Retina Barrier Development and Maintenance". In: *Proceedings of the National Academy of Sciences* 115.50 (2018), E11827–E11836. DOI: 10.1073/pnas.1813217115.
- [37] Jacob S. Heng et al. "Hypoxia Tolerance in the Norrin-Deficient Retina and the Chronically Hypoxic Brain Studied at Single-Cell Resolution". In: *Proceedings of the National Academy of Sciences* 116.18 (2019), pp. 9103–9114. DOI: 10.1073/pnas.1821122116.
- [38] Chris Cho et al. "Dlg1 Activates Beta-Catenin Signaling to Regulate Retinal Angiogenesis and the Blood-Retina and Blood-Brain Barriers". In: *eLife* 8 (2019). DOI: 10.7554/eLife.45542.
- [39] Ling Guo et al. "Plasmalemma Vesicle-Associated Protein: A Crucial Component of Vascular Homeostasis (Review)". In: *Experimental and Therapeutic Medicine* 12.3 (2016), pp. 1639–1644. DOI: 10.3892/etm.2016.3557.
- [40] Agnieszka Martowicz et al. "Endothelial  $\beta$ -Catenin Signaling Supports Postnatal Brain and Retinal Angiogenesis by Promoting Sprouting, Tip Cell Formation, and VEGFR (Vascular Endothelial Growth Factor Receptor) 2 Expression". In: *Arteriosclerosis, Thrombosis, and Vascular Biology* 39.11 (2019), pp. 2273–2288. DOI: 10.1161/ATVBAHA.119.312749.
- [41] Yanshu Wang et al. "Beta-Catenin Signaling Regulates Barrier-Specific Gene Expression in Circumventricular Organ and Ocular Vasculatures". In: *eLife* 8 (2019). DOI: 10.7554/eLife.43257.
- [42] Qi Chen et al. "Haemodynamics-Driven Developmental Pruning of Brain Vasculature in Zebrafish". In: *Public Library of Science Biology* 10.8 (2012). DOI: 10.1371/journal.pbio.1001374.
- [43] Andrea Trost et al. "Pericytes in the Retina". In: *Pericyte Biology in Different Organs*. Ed. by Alexander Birbrair. Cham (Switzerland): Springer International Publishing, 2019, pp. 1–26. DOI: 10.1007/978-3-030-11093-2-1.
- [44] Annika Armulik, Guillem Genové, and Christer Betsholtz. "Pericytes: Developmental, Physiological, and Pathological Perspectives, Problems, and Promises". In: *Developmental Cell* 21.2 (2011), pp. 193–215. DOI: 10.1016/j.devcel.2011.07.001.
- [45] A. Caporali et al. "Contribution of Pericyte Paracrine Regulation of the Endothelium to Angiogenesis". In: *Pharmacology & Therapeutics* 171 (2017), pp. 56–64. DOI: 10.1016/j.pharmthera.2016.10.001.
- [46] Zi-Sen Zhang et al. "Research Advances in Pericyte Function and their Roles in Diseases". In: *Chinese Journal of Traumatology* 23.2 (2020), pp. 89–95. DOI: 10.1016/j.cjtee.2020.02.006.
- [47] Alexander Birbrair, ed. *Pericyte Biology in Different Organs*. Vol. 1122. Cham (Switzerland): Springer International Publishing, 2019.
- [48] Inês Sá-Pereira, Dora Brites, and Maria Alexandra Brito. "Neurovascular Unit: A Focus on Pericytes". In: *Molecular Neurobiology* 45.2 (2012), pp. 327–347. DOI: 10.1007/s12035-012-8244-2.

## 1.6. REFERENCES

---

- [49] Gulce Kureli et al. "F-Actin Polymerization Contributes to Pericyte Contractility in Retinal Capillaries". In: *Experimental Neurology* 332 (2020). DOI: 10.1016/j.expneurol.2020.113392.
- [50] Andrea Trost et al. "Brain and Retinal Pericytes: Origin, Function and Role". In: *Frontiers in Cellular Neuroscience* 10 (2016). DOI: 10.3389/fncel.2016.00020.
- [51] Alexander Birbrair, ed. *Pericyte Biology in Disease*. Vol. 1147. Advances in Experimental Medicine and Biology. Cham (Switzerland): Springer International Publishing, 2019.
- [52] Do Young Park et al. "Plastic Roles of Pericytes in the Blood-Retinal Barrier". In: *Nature Communications* 8 (2017). DOI: 10.1038/ncomms15296.
- [53] G. S. P. Santos et al. "Role of Pericytes in the Retina". In: *Eye* 32.3 (2018), pp. 483–486. DOI: 10.1038/eye.2017.220.
- [54] Martin Teichert et al. "Pericyte-Expressed Tie2 Controls Angiogenesis and Vessel Maturation". In: *Nature Communications* 8 (2017). DOI: 10.1038/ncomms16106.
- [55] Midori Greenwood-Goodwin et al. "A Novel Lineage Restricted, Pericyte-like Cell Line Isolated from Human Embryonic Stem Cells". In: *Scientific Reports* 6 (2016). DOI: 10.1038/srep24403.
- [56] Matthew J. Stebbins et al. "Human Pluripotent Stem Cell-Derived Brain Pericyte-like Cells Induce Blood-Brain Barrier Properties". In: *Science Advances* 5.3 (2019). DOI: 10.1126/sciadv.aau7375.
- [57] Marisa Karow et al. "Direct Pericyte-to-Neuron Reprogramming via Unfolding of a Neural Stem Cell-Like Program". In: *Nature Neuroscience* 21.7 (2018), pp. 932–940. DOI: 10.1038/s41593-018-0168-3.
- [58] Tomoya Shibahara et al. "Pericyte-Mediated Tissue Repair through PDGFR $\beta$  Promotes Peri-Infarct Astrogliosis, Oligodendrogenesis, and Functional Recovery after Acute Ischemic Stroke". In: *eNeuro* 7.2 (2020). DOI: 10.1523/ENEURO.0474-19.2020.
- [59] Hong Huang, Kai Yin, and Huifang Tang. "Macrophage Amphiregulin-Pericyte TGF- $\beta$  Axis: A Novel Mechanism of the Immune System that Contributes to Wound Repair". In: *Acta Biochimica et Biophysica Sinica* 52.4 (2020), pp. 463–465. DOI: 10.1093/abbs/gmaa001.
- [60] Randa S. Eshaq et al. "Diabetic Retinopathy: Breaking the Barrier". In: *Pathophysiology* 24.4 (2017), pp. 229–241. DOI: 10.1016/j.pathophys.2017.07.001.
- [61] Melanie D. Sweeney, Abhay P. Sagare, and Berislav V. Zlokovic. "Blood-Brain Barrier Breakdown in Alzheimer Disease and Other Neurodegenerative Disorders". In: *Nature Reviews Neurology* 14.3 (2018), pp. 133–150. DOI: 10.1038/nrneuro.2017.188.
- [62] Francisco J. Rivera, Bryan Hinrichsen, and Maria Elena Silva. "Pericytes in Multiple Sclerosis". In: *Pericyte Biology in Disease*. Ed. by Alexander Birbrair. Advances in Experimental Medicine and Biology. Cham (Switzerland): Springer International Publishing, 2019, pp. 167–187. DOI: 10.1007/978-3-030-16908-4<sub>8</sub>.

## 1.6. REFERENCES

---

- [63] Mitrajit Ghosh et al. "Pericytes are Involved in the Pathogenesis of Cerebral Autosomal Dominant Arteriopathy with Subcortical Infarcts and Leukoencephalopathy". In: *Annals of Neurology* 78.6 (2015), pp. 887–900. DOI: 10.1002/ana.24512.
- [64] Abderahim Gaceb et al. "The Pericyte Secretome: Potential Impact on Regeneration". In: *Biochimie* 155 (2018), pp. 16–25. DOI: 10.1016/j.biochi.2018.04.015.
- [65] J. C. Booij et al. "The Dynamic Nature of Bruch's Membrane". In: *Progress in Retinal and Eye Research* 29.1 (2010), pp. 1–18. DOI: 10.1016/j.preteyeres.2009.08.003.
- [66] Christina J. Lee et al. "Determination of Human Lens Capsule Permeability and its Feasibility as a Replacement for Bruch's Membrane". In: *Biomaterials* 27.8 (2006), pp. 1670–1678. DOI: 10.1016/j.biomaterials.2005.09.008.
- [67] M. C. Killingsworth. "Age-Related Components of Bruch's Membrane in the Human Eye". In: *Graefe's Archive for Clinical and Experimental Ophthalmology* 225.6 (1987), pp. 406–412. DOI: 10.1007/BF02334166.
- [68] Daniel Pauleikhoff et al. "Correlation Between Biochemical Composition and Fluorescein Binding of Deposits in Bruch's Membrane". In: *Ophthalmology* 99.10 (1992), pp. 1548–1553. DOI: 10.1016/S0161-6420(92)31768-3.
- [69] R. Guymer, P. Luthert, and A. Bird. "Changes in Bruch's Membrane and Related Structures with Age". In: *Progress in Retinal and Eye Research* 18.1 (1999), pp. 59–90. DOI: 10.1016/S1350-9462(98)00012-3.
- [70] Sabine Aisenbrey et al. "Retinal Pigment Epithelial Cells Synthesize Laminins, Including Laminin 5, and Adhere to Them through  $\alpha$ 3- and  $\alpha$ 6-Containing Integrins". In: *Investigative Ophthalmology & Visual Science* 47.12 (2006), pp. 5537–5544. DOI: 10.1167/iovs.05-1590.
- [71] Nadine Reichhart and Olaf Strauss. "Ion Channels and Transporters of the Retinal Pigment Epithelium". In: *Experimental Eye Research* 126 (2014), pp. 27–37. DOI: 10.1016/j.exer.2014.05.005.
- [72] J. M. Roberts and J. V. Forrester. "Factors Affecting the Migration and Growth of Endothelial Cells from Microvessels of Bovine Retina". In: *Experimental Eye Research* 50.2 (1990), pp. 165–172. DOI: 10.1016/0014-4835(90)90227-L.
- [73] Katarina Wolf et al. "Collagen-Based Cell Migration Models In Vitro and In Vivo". In: *Seminars in Cell & Developmental Biology* 20.8 (2009), pp. 931–941. DOI: 10.1016/j.semcdb.2009.08.005.
- [74] Sjoerd van Helvert, Cornelis Storm, and Peter Friedl. "Mechanoreciprocity in Cell Migration". In: *Nature Cell Biology* 20.1 (2018), pp. 8–20. DOI: 10.1038/s41556-017-0012-0.
- [75] Ernst Pöschl et al. "Collagen IV is Essential for Basement Membrane Stability but Dispensable for Initiation of its Assembly During Early Development". In: *Development* 131.7 (2004), pp. 1619–1628. DOI: 10.1242/dev.01037.

## 1.6. REFERENCES

---

- [76] Willi Halfter et al. “New Concepts in Basement Membrane Biology”. In: *The FEBS Journal* 282.23 (2015), pp. 4466–4479. DOI: 10.1111/febs.13495.
- [77] Lawrence J. Rizzolo et al. “Integration of Tight Junctions and Claudins with the Barrier Functions of the Retinal Pigment Epithelium”. In: *Progress in Retinal and Eye Research* 30.5 (2011), pp. 296–323. DOI: 10.1016/j.preteyeres.2011.06.002.
- [78] Mark A. Fields et al. “Interactions of the Choroid, Bruch’s Membrane, Retinal Pigment Epithelium, and Neurosensory Retina Collaborate to Form the Outer Blood-Retinal-Barrier”. In: *Progress in Retinal and Eye Research* 76 (2020). DOI: 10.1016/j.preteyeres.2019.100803.
- [79] Sofia M. Calado et al. “GLUT1 Activity Contributes to the Impairment of PEDF Secretion by the RPE”. In: *Molecular Vision* 22 (2016), pp. 761–770.
- [80] Guillermo L. Lehmann et al. “Plasma Membrane Protein Polarity and trafficking in RPE Cells: Past, Present and Future”. In: *Experimental Eye Research* 126 (2014), pp. 5–15. DOI: 10.1016/j.exer.2014.04.021.
- [81] William J. Spencer et al. “Photoreceptor Discs: Built Like Ectosomes”. In: *Trends in Cell Biology* 30.11 (2020), pp. 904–915. DOI: 10.1016/j.tcb.2020.08.005.
- [82] Raquel Y. Salinas et al. “Photoreceptor Discs Form Through Peripherin-Dependent Suppression of Ciliary Ectosome Release”. In: *Journal of Cell Biology* 216.5 (2017), pp. 1489–1499. DOI: 10.1083/jcb.201608081.
- [83] Brian M. Kevany and Krzysztof Palczewski. “Phagocytosis of Retinal Rod and Cone Photoreceptors”. In: *Physiology* 25.1 (2010), pp. 8–15. DOI: 10.1152/physiol.00038.2009.
- [84] Omer P. Kocaoglu et al. “Photoreceptor Disc Shedding in the Living Human Eye”. In: *Biomedical Optics Express* 7.11 (2016), pp. 4554–4568. DOI: 10.1364/BOE.7.004554.
- [85] Tim U. Krohne, Frank G. Holz, and Jürgen Kopitz. “Apical-to-Basolateral Transcytosis of Photoreceptor Outer Segments Induced by Lipid Peroxidation Products in Human Retinal Pigment Epithelial Cells”. In: *Investigative Ophthalmology & Visual Science* 51.1 (2010), pp. 553–560. DOI: 10.1167/iovs.09-3755.
- [86] Tina Storm, Thomas Burgoyne, and Clare E. Futter. “Membrane Trafficking in the Retinal Pigment Epithelium at a Glance”. In: *Journal of Cell Science* 133.16 (2020). DOI: 10.1242/jcs.238279.
- [87] Olaf Strauss. “The Retinal Pigment Epithelium”. In: *Webvision: The Organization of the Retina and Visual System*. Ed. by Helga Kolb, Eduardo Fernandez, and Ralph Nelson. Salt Lake City (UT), 1995.
- [88] Jeffrey Adijanto et al. “CO<sub>2</sub>-induced Ion and Fluid Transport in Human Retinal Pigment Epithelium”. In: *Journal of General Physiology* 133.6 (2009), pp. 603–622. DOI: 10.1085/jgp.200810169.
- [89] Mikael Klingeborn et al. “Directional Exosome Proteomes Reflect Polarity-Specific Functions in Retinal Pigmented Epithelium Monolayers”. In: *Scientific Reports* 7 (2017). DOI: 10.1038/s41598-017-05102-9.

## 1.6. REFERENCES

---

- [90] Thomas W. Gardner and Jose R. Davila. "The Neurovascular Unit and the Pathophysiologic Basis of Diabetic Retinopathy". In: *Graefe's Archive for Clinical and Experimental Ophthalmology* 255.1 (2017). DOI: 10.1007/s00417-016-3548-y.
- [91] Natalie Hudson and Matthew Campbell. "Inner Blood-Retinal Barrier Regulation in Retinopathies". In: *Retinal Degenerative Diseases*. Ed. by Catherine Bowes Rickman et al. *Advances in Experimental Medicine and Biology* (Adv Exp Med Biol)Y. Cham: Springer International Publishing, 2019, pp. 329–333.
- [92] Kyle R. Biesecker et al. "Glial Cell Calcium Signaling Mediates Capillary Regulation of Blood Flow in the Retina". In: *Journal of Neuroscience* 36.36 (2016), pp. 9435–9445. DOI: 10.1523/JNEUROSCI.1782-16.2016.
- [93] Shen Nian et al. "Neurovascular Unit in Diabetic Retinopathy: Pathophysiological Roles and Potential Therapeutical Targets". In: *Eye and Vision* 8 (2021). DOI: 10.1186/s40662-021-00239-1.
- [94] Xuwen Liu et al. "Occludin S490 Phosphorylation Regulates Vascular Endothelial Growth Factor-Induced Retinal Neovascularization". In: *The American Journal of Pathology* 186.9 (2016), pp. 2486–2499. DOI: 10.1016/j.ajpath.2016.04.018.
- [95] Ken-ichi Hosoya and Masanori Tachikawa. "Inner Blood-Retinal Barrier Transporters: Role of Retinal Drug Delivery". In: *Pharmaceutical Research* 26.9 (2009), pp. 2055–2065. DOI: 10.1007/s11095-009-9930-2.
- [96] Guillem Pascual-Pasto et al. "Increased Delivery of Chemotherapy to the Vitreous by Inhibition of the Blood-Retinal Barrier". In: *Journal of Controlled Release* 264 (2017), pp. 34–44. DOI: 10.1016/j.jconrel.2017.08.018.
- [97] Karthik Yadav Janga et al. "Retina Compatible Interactions and Effective Modulation of Blood Ocular Barrier P-gp Activity by Third-Generation Inhibitors Improve the Ocular Penetration of Loperamide". In: *Journal of Pharmaceutical Sciences* 107.8 (2018), pp. 2128–2135. DOI: 10.1016/j.xphs.2018.04.008.
- [98] Alejandro Sosnik and Reina Bendayan, eds. *Drug Efflux Pumps in Cancer Resistance Pathways: From Molecular Recognition and Characterization to Possible Inhibition Strategies in Chemotherapy*. 1st ed. Vol. 7. *Cancer Sensitizing Agents for Chemotherapy*. Academic Press, 2020.
- [99] Brian Wai Chow and Chenghua Gu. "Gradual Suppression of Transcytosis Governs Functional Blood-Retinal Barrier Formation". In: *Neuron* 93.6 (2017), pp. 1325–1333. DOI: 10.1016/j.neuron.2017.02.043.
- [100] Benjamin J. Andreone et al. "Blood-Brain Barrier Permeability Is Regulated by Lipid Transport-Dependent Suppression of Caveolae-Mediated Transcytosis". In: *Neuron* 94.3 (2017), pp. 581–594. DOI: 10.1016/j.neuron.2017.03.043.
- [101] Wendy A. Dailey et al. "Norrin Counters VEGFA Induced Expression of Transcytosis Marker PLVAP". In: *Investigative Ophthalmology & Visual Science* 60.9 (2019).



## 1.6. REFERENCES

---

- [102] Zhongxiao Wang et al. “Wnt Signaling Regulates Blood Retinal Barrier Permeability by Suppressing MFSD2A-dependent Vascular Endothelial Transcytosis”. In: *Investigative Ophthalmology & Visual Science* 60.9 (2019).
- [103] Zhongxiao Wang et al. “Wnt Signaling Activates MFSD2A to Suppress Vascular Endothelial Transcytosis and Maintain Blood-Retinal Barrier”. In: *Science Advances* 6.35 (2020). DOI: 10.1126/sciadv.aba7457.
- [104] World Health Organization. *World Report on Vision*. Geneva: World Health Organization, 2019.
- [105] Jaimie D. Steinmetz et al. “Causes of Blindness and Vision Impairment in 2020 and Trends over 30 Years, and Prevalence of Avoidable Blindness in Relation to VISION 2020: the Right to Sight: an Analysis for the Global Burden of Disease Study”. In: *The Lancet Global Health* 9.2 (2021), E144–E160. DOI: 10.1016/S2214-109X(20)30489-7.
- [106] Jost B. Jonas, Chui Ming Gemmy Cheung, and Songhomitra Panda-Jonas. “Updates on the Epidemiology of Age-Related Macular Degeneration”. In: *Asia-Pacific Journal of Ophthalmology* 6.6 (2017), pp. 493–497. DOI: 10.22608/APO.2017251.
- [107] Wan Ling Wong et al. “Global Prevalence of Age-Related Macular Degeneration and Disease Burden Projection for 2020 and 2040: a Systematic Review and Meta-Analysis”. In: *The Lancet Global Health* 2.2 (2014), e106–e116. DOI: 10.1016/S2214-109X(13)70145-1.
- [108] Jeany Q. Li et al. “Prevalence and Incidence of Age-Related Macular Degeneration in Europe: A Systematic Review and Meta-Analysis”. In: *British Journal of Ophthalmology* 104.8 (2020), pp. 1077–1084. DOI: 10.1136/bjophthalmol-2019-314422.
- [109] Rupert R. A. Bourne et al. “Prevalence and Causes of Vision Loss in High-Income Countries and in Eastern and Central Europe in 2015: Magnitude, Temporal Trends and Projections”. In: *British Journal of Ophthalmology* 102.5 (2018), pp. 575–585. DOI: 10.1136/bjophthalmol-2017-311258.
- [110] Jayakrishna Ambati and Benjamin J. Fowler. “Mechanisms of Age-Related Macular Degeneration”. In: *Neuron* 75.1 (2012), pp. 26–39. DOI: 10.1016/j.neuron.2012.06.018.
- [111] Paul Mitchell et al. “Age-Related Macular Degeneration”. In: *The Lancet* 392.10153 (2018), pp. 1147–1159. DOI: 10.1016/S0140-6736(18)31550-2.
- [112] Christine A. Curcio et al. “Aging, Age-Related Macular Degeneration, and the Response-to-Retention of Apolipoprotein B-Containing Lipoproteins”. In: *Progress in Retinal and Eye Research* 28.6 (2009), pp. 393–422. DOI: 10.1016/j.preteyeres.2009.08.001.
- [113] Frederick L. Ferris et al. “A Simplified Severity Scale for Age-Related Macular Degeneration: AREDS Report No. 18”. In: *Archives of Ophthalmology* 123.11 (2005), pp. 1570–1574. DOI: 10.1001/archophth.123.11.1570.

## 1.6. REFERENCES

---

- [114] Ronald Klein et al. "Harmonizing the Classification of Age-related Macular Degeneration in the Three-Continent AMD Consortium". In: *Ophthalmic Epidemiology* 21.1 (2014), pp. 14–23. DOI: 10.3109/09286586.2013.867512.
- [115] Ana Jonas and Michael C. Phillips. "CHAPTER 17 - Lipoprotein Structure". In: *Biochemistry of Lipids, Lipoproteins and Membranes*. Ed. by Dennis E. Vance and Jean E. Vance. San Diego: Elsevier, 2008, pp. 485–506. DOI: 10.1016/B978-044453219-0.50019-2.
- [116] Michael P. Caulfield et al. "Direct Determination of Lipoprotein Particle Sizes and Concentrations by Ion Mobility Analysis". In: *Clinical Chemistry* 54.8 (2008), pp. 1307–1316. DOI: 10.1373/clinchem.2007.100586.
- [117] Sara E. Thomas and Earl H. Harrison. "Mechanisms of Selective Delivery of Xanthophylls to Retinal Pigment Epithelial Cells by Human Lipoproteins". In: *Journal of Lipid Research* 57.10 (2016), pp. 1865–1878. DOI: 10.1194/jlr.M070193.
- [118] Anna C. S. Tan et al. "Calcified Nodules in Retinal Drusen are Associated with Disease Progression in Age-Related Macular Degeneration". In: *Science Translational Medicine* 10.466 (2018). DOI: 10.1126/scitranslmed.aat4544.
- [119] Arthur A. Bergen et al. "On the Origin of Proteins in Human Drusen: The Meet, Greet and Stick Hypothesis". In: *Progress in Retinal and Eye Research* 70 (2019), pp. 55–84. DOI: 10.1016/j.preteyeres.2018.12.003.
- [120] Janusz Blasiak et al. "The Aging Stress Response and Its Implication for AMD Pathogenesis". In: *International Journal of Molecular Sciences* 21.22 (2020). DOI: 10.3390/ijms21228840.
- [121] Paulina Tokarz, Kai Kaarniranta, and Janusz Blasiak. "Role of Antioxidant Enzymes and Small Molecular Weight Antioxidants in the Pathogenesis of Age-Related Macular Degeneration (AMD)". In: *Biogerontology* 14.5 (2013), pp. 461–482. DOI: 10.1007/s10522-013-9463-2.
- [122] Kai Kaarniranta et al. "PGC-1 $\alpha$  Protects RPE Cells of the Aging Retina Against Oxidative Stress-Induced Degeneration through the Regulation of Senescence and Mitochondrial Quality Control. The Significance for AMD Pathogenesis". In: *International Journal of Molecular Sciences* 19.8 (2018). DOI: 10.3390/ijms19082317.
- [123] Kai Kaarniranta et al. "Role of Mitochondrial DNA Damage in ROS-Mediated Pathogenesis of Age-Related Macular Degeneration (AMD)". In: *International Journal of Molecular Sciences* 20.10 (2019). DOI: 10.3390/ijms20102374.
- [124] Janusz Blasiak. "Senescence in the Pathogenesis of Age-Related Macular Degeneration". In: *Cellular and Molecular Life Sciences* 77.5 (2020), pp. 789–805. DOI: 10.1007/s00018-019-03420-x.
- [125] Milosz P. Kawa et al. "Complement System in Pathogenesis of AMD: Dual Player in Degeneration and Protection of Retinal Tissue". In: *Journal of Immunology Research* 2014 (2014). DOI: 10.1155/2014/483960.

## 1.6. REFERENCES

---

- [126] Angela Armento, Marius Ueffing, and Simon J. Clark. "The Complement System in Age-Related Macular Degeneration". In: *Cellular and Molecular Life Sciences* 78.10 (2021), pp. 4487–4505. DOI: 10.1007/s00018-021-03796-9.
- [127] Hongjun Du et al. "Novel Mechanistic Interplay between Products of Oxidative Stress and Components of the Complement System in AMD Pathogenesis". In: *Open Journal of Ophthalmology* 6.1 (2016), pp. 43–50. DOI: 10.4236/ojoph.2016.61006.
- [128] Hanna M. Zajac-Pytrus et al. "The Dry Form of Age-Related Macular Degeneration (AMD): The Current Concepts of Pathogenesis and Prospects for Treatment". In: *Advances in Clinical and Experimental Medicine* 24.6 (2015), pp. 1099–1104. DOI: 10.17219/acem/27093.
- [129] D. Scott McLeod et al. "Relationship Between RPE and Choriocapillaris in Age-Related Macular Degeneration". In: *Investigative Ophthalmology & Visual Science* 50.10 (2009), pp. 4982–4991. DOI: 10.1167/iovs.09-3639.
- [130] Natalie Jia Ying Yeo, Ebenezer Jia Jun Chan, and Christine Cheung. "Choroidal Neovascularization: Mechanisms of Endothelial Dysfunction". In: *Frontiers in Pharmacology* 10 (2019). DOI: 10.3389/fphar.2019.01363.
- [131] Flavia Plastino, Noemi Anna Pesce, and Helder André. "MicroRNAs and the HIF/VEGF Axis in Ocular Neovascular Diseases". In: *Acta Ophthalmologica* 99.8 (2021), E1255–E1262. DOI: 10.1111/aos.14845.
- [132] Alexander G. Marneros et al. "Vascular Endothelial Growth Factor Expression in the Retinal Pigment Epithelium Is Essential for Choriocapillaris Development and Visual Function". In: *The American Journal of Pathology* 167.5 (2005), pp. 1451–1459. DOI: 10.1016/S0002-9440(10)61231-X.
- [133] Magali Saint-Geniez et al. "An Essential Role for RPE-Derived Soluble VEGF in the Maintenance of the Choriocapillaris". In: *Proceedings of the National Academy of Sciences* 106.44 (2009), pp. 18751–18756. DOI: 10.1073/pnas.0905010106.
- [134] G. A. Lutty et al. "Development of the Human Choriocapillaris". In: *Eye* 24.3 (2010), pp. 408–415. DOI: 10.1038/eye.2009.318.
- [135] Yukiko Shimomura et al. "Changes in Choriocapillaris Fenestration of Rat Eyes after Intravitreal Bevacizumab Injection". In: *Graefes Archive for Clinical and Experimental Ophthalmology* 247.8 (2009), pp. 1089–1094. DOI: 10.1007/s00417-009-1054-1.
- [136] Hans E. Grossniklaus and W. Richard Green. "Choroidal Neovascularization". In: *American Journal of Ophthalmology* 137.3 (2004), pp. 496–503. DOI: 10.1016/j.ajo.2003.09.042.
- [137] Peter A. Campochiaro. "Ocular Neovascularization". In: *Journal of Molecular Medicine* 91.3 (2013), pp. 311–321. DOI: 10.1007/s00109-013-0993-5.

## 1.6. REFERENCES

---

- [138] Norihiro Nagai et al. "Angiotensin II Type 1 Receptor-Mediated Inflammation is Required for Choroidal Neovascularization". In: *Arteriosclerosis, Thrombosis, and Vascular Biology* 26.10 (2006), pp. 2252–2259. DOI: 10.1161/01.ATV.0000240050.15321.fe.
- [139] Gian M. Tosi, Maurizio Orlandini, and Federico Galvagni. "The Controversial Role of TGF- $\beta$  in Neovascular Age-Related Macular Degeneration Pathogenesis". In: *International Journal of Molecular Sciences* 19.11 (2018). DOI: 10.3390/ijms19113363.
- [140] Age-Related Eye Disease Study Research Group. "A randomized, Placebo-Controlled, Clinical Trial of High-Dose Supplementation with Vitamins C and E, Beta Carotene, and Zinc for Age-Related Macular Degeneration and Vision Loss: AREDS Report No. 8". In: *Archives of Ophthalmology* 119.10 (2001), pp. 1417–1436. DOI: 10.1001/archophth.119.10.1417.
- [141] Age-Related Eye Disease Study 2 (AREDS2) Research Group. "Lutein + Zeaxanthin and Omega-3 Fatty Acids for Age-Related Macular Degeneration: the Age-Related Eye Disease Study 2 (AREDS2) Randomized Clinical Trial". In: *Journal of the American Medical Association* 309.19 (2013), pp. 2005–2015. DOI: 10.1001/jama.2013.4997.
- [142] Age-Related Eye Disease Study 2 (AREDS2) Research Group. "Secondary Analyses of the Effects of Lutein/Zeaxanthin on Age-Related Macular Degeneration Progression: AREDS2 Report No. 3". In: *Journal of American Medical Association Ophthalmology* 132.2 (2014), pp. 142–149. DOI: 10.1001/jamaophth.132.2.142.
- [143] Yanhui Deng et al. "Age-Related Macular Degeneration: Epidemiology, Genetics, Pathophysiology, Diagnosis, and Targeted Therapy". In: *Genes & Diseases* 9.1 (2021), pp. 62–79. DOI: 10.1016/j.gendis.2021.02.009.
- [144] Katarina D. Kovacevic, James C. Gilbert, and Bernd Jilma. "Pharmacokinetics, Pharmacodynamics and Safety of Aptamers". In: *Advanced Drug Delivery Reviews* 134 (2018), pp. 36–50. DOI: 10.1016/j.addr.2018.10.008.
- [145] D. W. Drolet et al. "Pharmacokinetics and Safety of an Anti-Vascular Endothelial Growth Factor Aptamer (NX1838) Following Injection into the Vitreous Humor of Rhesus Monkeys". In: *Pharmaceutical Research* 17.12 (2000), pp. 1503–1510. DOI: 10.1023/a:1007657109012.
- [146] Julie A. Chapman and Cherylyn Beckey. "Pegaptanib: A Novel Approach to Ocular Neovascularization". In: *The Annals of Pharmacotherapy* 40.7-8 (2006), pp. 1322–1326. DOI: 10.1345/aph.1G604.
- [147] Eugene W. M. Ng et al. "Pegaptanib, a Targeted Anti-VEGF Aptamer for Ocular Vascular Disease". In: *Nature Reviews Drug Discovery* 5.2 (2006), pp. 123–132. DOI: 10.1038/nrd1955.
- [148] Laura García-Quintanilla et al. "Pharmacokinetics of Intravitreal Anti-VEGF Drugs in Age-Related Macular Degeneration". In: *Pharmaceutics* 11.8 (2019). DOI: 10.3390/pharmaceutics11080365.

## 1.6. REFERENCES

---

- [149] Jacques Gaudreault et al. "Pharmacokinetics and Retinal Distribution of Ranibizumab, a Humanized Antibody Fragment Directed Against VEGF-A, Following Intravitreal Administration in Rabbits". In: *Retina* 27.9 (2007), pp. 1260–1266. DOI: 10.1097/IAE.0b013e318134eecd.
- [150] Ryian Mohamed, David C. Saunders, and John P. Mathews. "Consulting the Consultants: Avastin in the Treatment of Wet AMD". In: *Eye* 33.4 (2019), pp. 529–531. DOI: 10.1038/s41433-018-0260-7.
- [151] Chandrakumar Balaratnasingam et al. "Aflibercept: A Review of its Use in the Treatment of Choroidal Neovascularization due to Age-Related Macular Degeneration". In: *Clinical Ophthalmology* 9 (2015), pp. 2355–2371. DOI: 10.2147/OPTH.S80040.
- [152] Nancy M. Holekamp. "Review of Neovascular Age-Related Macular Degeneration Treatment Options". In: *American Journal of Managed Care* 25.10 (2019), S172–S181.
- [153] Justus G. Garweg et al. "The Fate of Eyes with Wet AMD Beyond Four Years of Anti-VEGF Therapy". In: *Graefes Archive for Clinical and Experimental Ophthalmology* 256.4 (2018), pp. 823–831. DOI: 10.1007/s00417-018-3907-y.
- [154] Francine Behar-Cohen. "Recent Advances in Slow and Sustained Drug Release for Retina Drug Delivery". In: *Expert Opinion on Drug Delivery* 16.7 (2019), pp. 679–686. DOI: 10.1080/17425247.2019.1618829.
- [155] Omer Trivizki et al. "Noninfectious Inflammatory Response Following Intravitreal Bevacizumab Injections: Description of a Cluster of Cases in Two Centers and a Review of the Literature". In: *Ophthalmologica* 240.3 (2018), pp. 163–166. DOI: 10.1159/000492681.
- [156] Marc Schargus and Andreas Frings. "Issues with Intravitreal Administration of Anti-VEGF Drugs". In: *Clinical Ophthalmology* 14 (2020), pp. 897–904. DOI: 10.2147/OPTH.S207978.
- [157] Kunyong Xu et al. "Endophthalmitis after Intravitreal Injection of Vascular Endothelial Growth Factor Inhibitors: Management and Visual Outcomes". In: *Ophthalmology* 125.8 (2018), pp. 1279–1286. DOI: 10.1016/j.ophtha.2018.01.022.
- [158] Philip P. Storey and Sunir Garg. "Endophthalmitis Following Intravitreal Injection". In: *Current Ophthalmology Reports* 6.2 (2018), pp. 145–151. DOI: 10.1007/s40135-018-0176-1.
- [159] Anne-Sofie Petri et al. "Intravitreal Injections with Vascular Endothelial Growth Factor Inhibitors: A Practical Approach". In: *Ophthalmology and Therapy* 9.1 (2020), pp. 191–203. DOI: 10.1007/s40123-020-00230-4.
- [160] Anu Joseph. "Intravitreal Injections: A Brief Note". In: *Kerala Journal of Ophthalmology* 30.1 (2018), pp. 63–66. DOI: 10.4103/kjo.kjo-34-18.
- [161] Gustavo Barreto Melo et al. "Critical Analysis of Techniques and Materials Used in Devices, Syringes, and Needles Used for Intravitreal Injections". In: *Progress in Retinal and Eye Research* 80 (2021). DOI: 10.1016/j.preteyeres.2020.100862.

## 1.6. REFERENCES

---

- [162] Jea H. Yu et al. "Silicone Oil Droplets Following Intravitreal Bevacizumab Injections". In: *American Journal of Ophthalmology Case Reports* 10 (2018), pp. 142–144. DOI: 10.1016/j.ajoc.2017.07.009.
- [163] Joshua H. Uhr and Jason Hsu. "Endophthalmitis Following Intravitreal Injections Performed in the Office Versus Operating Room Setting". In: *Current Ophthalmology Reports* 7.2 (2019), pp. 128–135. DOI: 10.1007/s40135-019-00208-x.
- [164] Claudio Furino et al. "Intravitreal Injections in Arc Sterile Setting: Safety Profile after More Than 10,000 Treatments". In: *Journal of Ophthalmology* 2020 (2020), pp. 1–5. DOI: 10.1155/2020/3680406.
- [165] Christopher A. Reid et al. "Development of an Inducible Anti-VEGF rAAV Gene Therapy Strategy for the Treatment of Wet AMD". In: *Scientific Reports* 8 (2018). DOI: 10.1038/s41598-018-29726-7.
- [166] Kun Ding et al. "Proteosomal Degradation Impairs Transcytosis of AAV Vectors from Suprachoroidal Space to Retina". In: *Gene Therapy* 28.12 (2021), pp. 740–747. DOI: 10.1038/s41434-021-00233-1.
- [167] Michiko Mandai et al. "Autologous Induced Stem-Cell-Derived Retinal Cells for Macular Degeneration". In: *The New England Journal of Medicine* 376.11 (2017), pp. 1038–1046. DOI: 10.1056/NEJMoa1608368.
- [168] Sunao Sugita et al. "Immunological Aspects of RPE Cell Transplantation". In: *Progress in Retinal and Eye Research* 84 (2021). DOI: 10.1016/j.preteyeres.2021.100950.
- [169] Suvi Karuranga et al., eds. *IDF Diabetes Atlas - Nineth Edition*. Brussels, 2019.
- [170] Ryan Lee, Tien Y. Wong, and Charumathi Sabanayagam. "Epidemiology of Diabetic Retinopathy, Diabetic Macular Edema and Related Vision Loss". In: *Eye and Vision* 2.17 (2015). DOI: 10.1186/s40662-015-0026-2.
- [171] Ronald Klein et al. "The Wisconsin Epidemiologic Study of Diabetic Retinopathy XXII: The Twenty-Five-Year Progression of Retinopathy in Persons with Type 1 Diabetes". In: *Ophthalmology* 115.11 (2008), pp. 1859–1868. DOI: 10.1016/j.opthta.2008.08.023.
- [172] Charumathi Sabanayagam et al. "Incidence and Progression of Diabetic Retinopathy: A Systematic Review". In: *The Lancet Diabetes & Endocrinology* 7.2 (2019), pp. 140–149. DOI: 10.1016/S2213-8587(18)30128-1.
- [173] Michael Brownlee. "Biochemistry and Molecular Cell Biology of Diabetic Complications". In: *Nature* 414.6865 (2001), pp. 813–820. DOI: 10.1038/414813a.
- [174] Meng-Yu Wu et al. "The Oxidative Stress and Mitochondrial Dysfunction During the Pathogenesis of Diabetic Retinopathy". In: *Oxidative Medicine and Cellular Longevity* 2018 (2018), p. 3420187. DOI: 10.1155/2018/3420187.

## 1.6. REFERENCES

---

- [175] Osasenaga Macdonald Ighodaro. "Molecular Pathways Associated with Oxidative Stress in Diabetes Mellitus". In: *Biomedicine & Pharmacotherapy* 108 (2018), pp. 656–662. DOI: 10.1016/j.biopha.2018.09.058.
- [176] Thangal Yumnamcha et al. "Metabolic Dysregulation and Neurovascular Dysfunction in Diabetic Retinopathy". In: *Antioxidants* 9.12 (2020). DOI: 10.3390/antiox9121244.
- [177] Solani D. Mathebula. "Polyol Pathway: A Possible Mechanism of Diabetes Complications in the Eye". In: *African Vision and Eye Health* 74.1 (2015). DOI: 10.4102/aveh.v74i1.13.
- [178] Thomas Tien et al. "High Glucose Induces Mitochondrial Dysfunction in Retinal Müller Cells: Implications for Diabetic Retinopathy". In: *Investigative Ophthalmology & Visual Science* 58.7 (2017), pp. 2915–2921. DOI: 10.1167/iovs.16-21355.
- [179] P. J. Thornalley. "The Glyoxalase System: New Developments Towards Functional Characterization of a Metabolic Pathway Fundamental to Biological Life". In: *Biochemical Journal* 269.1 (1990), pp. 1–11. DOI: 10.1042/bj2690001.
- [180] Kevin J. Wells-Knecht et al. "Identification of Glyoxal and Arabinose as Intermediates in the Autoxidative Modification of Proteins by Glucose". In: *Biochemistry* 34.11 (1995), pp. 3702–3709. DOI: 10.1021/bi00011a027.
- [181] T. P. Degenhardt, S. R. Thorpe, and J. W. Baynes. "Chemical Modification of Proteins by Methylglyoxal". In: *Cellular and Molecular Biology* 44.7 (1998), pp. 1139–1145.
- [182] K. Suzuki et al. "Overexpression of Aldehyde Reductase Protects PC12 Cells from the Cytotoxicity of Methylglyoxal or 3-Deoxyglucosone". In: *Journal of Biochemistry* 123.2 (1998), pp. 353–357. DOI: 10.1093/oxfordjournals.jbchem.a021944.
- [183] Alan W. Stitt. "AGEs and Diabetic Retinopathy". In: *Investigative Ophthalmology & Visual Science* 51.10 (2010), pp. 4867–4874. DOI: 10.1167/iovs.10-5881.
- [184] Hongliang Zong, Micheal Ward, and Alan W. Stitt. "AGEs, RAGE, and Diabetic Retinopathy". In: *Current Diabetes Reports* 11.4 (2011), pp. 244–252. DOI: 10.1007/s11892-011-0198-7.
- [185] Jing Xu et al. "Involvement of Advanced Glycation End Products in the Pathogenesis of Diabetic Retinopathy". In: *Cellular Physiology and Biochemistry* 48.2 (2018), pp. 705–717. DOI: 10.1159/000491897.
- [186] Mohammad Amin Zaman, Suzanne Oparil, and David A. Calhoun. "Drugs Targeting the Renin–Angiotensin–Aldosterone System". In: *Nature Reviews Drug Discovery* 1.8 (2002), pp. 621–636. DOI: 10.1038/nrd873.
- [187] Seema Patel et al. "Renin-Angiotensin-Aldosterone (RAAS): The Ubiquitous System for Homeostasis and Pathologies". In: *Biomedicine & Pharmacotherapy* 94 (2017), pp. 317–325. DOI: 10.1016/j.biopha.2017.07.091.

## 1.6. REFERENCES

---

- [188] Mervi Holappa, Heikki Vapaatalo, and Anu Vaajanen. "Local Ocular Renin-Angiotensin-Aldosterone System: Any Connection with Intraocular Pressure? A Comprehensive Review". In: *Annals of Medicine* 52.5 (2020), pp. 191–206. DOI: 10.1080/07853890.2020.1758341.
- [189] Zohreh Rahimi, Mahmoudreza Moradi, and Hamid Nasri. "A Systematic Review of the Role of Renin Angiotensin Aldosterone System Genes in Diabetes Mellitus, Diabetic Retinopathy and Diabetic Neuropathy". In: *Journal of Research in Medical Sciences* 19.11 (2014), pp. 1090–1098.
- [190] Rajesh Choudhary et al. "Therapeutic Targets of Renin-Angiotensin System in Ocular Disorders". In: *Journal of Current Ophthalmology* 29.1 (2017), pp. 7–16. DOI: 10.1016/j.joco.2016.09.009.
- [191] A. H. Danser et al. "Angiotensin Levels in the Eye". In: *Investigative Ophthalmology & Visual Science* 35.3 (1994), pp. 1008–1018.
- [192] J. Wagner et al. "Demonstration of Renin mRNA, Angiotensinogen mRNA, and Angiotensin Converting Enzyme mRNA Expression in the Human Eye: Evidence for an Intraocular Renin-Angiotensin System". In: *British Journal of Ophthalmology* 80.2 (1996), pp. 159–163. DOI: 10.1136/bjo.80.2.159.
- [193] E. Savaskan et al. "Immunohistochemical Localization of Angiotensin-Converting Enzyme, Angiotensin II and AT1 Receptor in Human Ocular Tissues". In: *Ophthalmic Research* 36.6 (2004), pp. 312–320. DOI: 10.1159/000081633.
- [194] Sadie K. Dierschke and Michael D. Dennis. "Retinal Protein O-GlcNAcylation and the Ocular Renin Angiotensin System: Signaling Cross-Roads in Diabetic Retinopathy". In: *Current Diabetes Reviews* 1.1 (2021), pp. 1–15. DOI: 10.2174/1573399817999210111205933.
- [195] Xiaorui Li et al. "Müller Cells in Pathological Retinal Angiogenesis". In: *Translational Research* 207 (2019), pp. 96–106. DOI: 10.1016/j.trsl.2018.12.006.
- [196] Robert Hennig and Achim Goepferich. "Nanoparticles for the Treatment of Ocular Neovascularizations". In: *European Journal of Pharmaceutics and Biopharmaceutics* 95 (2015), pp. 294–306. DOI: 10.1016/j.ejpb.2015.02.027.
- [197] Sophie Cai and Neil M. Bressler. "Aflibercept, Bevacizumab or Ranibizumab for Diabetic Macular Oedema: Recent Clinically Relevant Findings from DRCR.net Protocol T". In: *Current Opinion in Ophthalmology* 28.6 (2017), pp. 636–643. DOI: 10.1097/ICU.0000000000000424.
- [198] Quan Dong Nguyen et al. "Placental Growth Factor and its Potential Role in Diabetic Retinopathy and Other Ocular Neovascular Diseases". In: *Acta Ophthalmologica* 96.1 (2018), e1–e9. DOI: 10.1111/aos.13325.
- [199] Kang Xiao et al. "Efficacy of Conversion to Aflibercept for Diabetic Macular Edema Previously Refractory to Bevacizumab or Ranibizumab: A Meta-Analysis of High-Quality Nonrandomized Studies". In: *The Annals of Pharmacotherapy* 54.8 (2020), pp. 750–756. DOI: 10.1177/1060028020904358.



## 1.6. REFERENCES

---

- [200] Adam R. Glassman et al. "Five-Year Outcomes after Initial Aflibercept, Bevacizumab, or Ranibizumab Treatment for Diabetic Macular Edema (Protocol T Extension Study)". In: *Ophthalmology* 127.9 (2020), pp. 1201–1210. DOI: 10.1016/j.ophtha.2020.03.021.
- [201] Yue Zhao and Rishi P. Singh. "The Role of Anti-Vascular Endothelial Growth Factor (Anti-VEGF) in the Management of Proliferative Diabetic Retinopathy". In: *Drugs in Context* 7 (2018). DOI: 10.7573/dic.212532.
- [202] Xintong Li, Marco A. Zarbin, and Neelakshi Bhagat. "Anti-Vascular Endothelial Growth Factor Injections: The New Standard of Care in Proliferative Diabetic Retinopathy?" In: *Developments in Ophthalmology* 60 (2017), pp. 131–142. DOI: 10.1159/000459699.
- [203] Shuang Gao, Zhongjing Lin, and Xi Shen. "Anti-Vascular Endothelial Growth Factor Therapy as an Alternative or Adjunct to Pan-Retinal Photocoagulation in Treating Proliferative Diabetic Retinopathy: Meta-Analysis of Randomized Trials". In: *Frontiers in Pharmacology* 11 (2020). DOI: 10.3389/fphar.2020.00849.
- [204] Jong Young Lee et al. "Effect of Alternate Treatment with Intravitreal Anti-Vascular Endothelial Growth Factor and Steroid for Treatment-Naive Diabetic Macular Edema in a Real-Life Setting". In: *Journal of Ocular Pharmacology and Therapeutics* 36.7 (2020), pp. 555–562. DOI: 10.1089/jop.2020.0012.
- [205] Thanitsara Rittiphairoj et al. "Intravitreal Steroids for Macular Edema in Diabetes". In: *The Cochrane Database of Systematic Reviews* 11.11 (2020). DOI: 10.1002/14651858.CD005656.pub3.
- [206] Tobias P. H. Nissen, Henrik Vorum, and Kristian Aasbjerg. "Biologic Therapy and Treatment Options in Diabetic Retinopathy with Diabetic Macular Edema". In: *Current Drug Safety* 16.1 (2021), pp. 17–31. DOI: 10.2174/1574886315666200902154322.
- [207] Elio Striglia et al. "Emerging Drugs for the Treatment of Diabetic Retinopathy". In: *Expert Opinion on Emerging Drugs* 25.3 (2020), pp. 261–271. DOI: 10.1080/14728214.2020.1801631.
- [208] Martin Friedlander. "Fibrosis and Diseases of The Eye". In: *The Journal of Clinical Investigation* 117.3 (2007), pp. 576–586. DOI: 10.1172/JCI31030.
- [209] Krysten M. Farjo and Jian-Xing Ma. "The Potential of Nanomedicine Therapies to Treat Neovascular Disease in the Retina". In: *Journal of Angiogenesis Research* 2 (2010). DOI: 10.1186/2040-2384-2-21.



## **Chapter 2**

# **Goals of the Thesis**

## 2.1 Concept

### 2.1.1 Considerations about a Nanoparticulate Platform

The major objective of this work was the establishment of a highly flexible nanoparticulate platform technology with the potential to become a therapeutic alternative for the treatment of wet age-related macular degeneration (AMD), proliferative diabetic retinopathy (PDR) and even other ocular diseases. Such a technology must fulfill the following criteria:

- (1) Biocompatibility and biodegradability
- (2) Adjustability of physicochemical properties (size, surface charge, etc.)
- (3) Active drug targeting
- (4) Carrier for a therapeutic drug
- (5) Long-term stability
- (6) GCP and GMP-compliant manufacturing techniques

An available nanoparticulate system, that is highly promising to fulfill all of these criteria, was established by Abstiens et. al. [1, 2]. Their core-shell-nanoparticles (NPs) consisted of polyethylene glycol (PEG)/ polylactic acid (PLA) block-co-polymers and poly(lactic-co-glycolic) acid (PLGA). These substances have already been approved and are available in market-authorized formulations. PLA as well as PLGA are among the synthetic biodegradable polymers with a long-administration history [3–5]. Both are FDA-approved for an *in vivo* application [6]. The coating of drugs and drug delivery systems with hydrophilic polymers like PEG is a common technique to enhance the circulation period after systemic application [7–9]. Although the postulated non-immunogenic properties are getting challenged [10–13], PEGylation is widely accepted as gold standard to provide long-term circulation of drug conjugates and drug delivery systems. Currently a couple of market products take advantage of the PEGylation technique [11] and the safety profile was assessed by the United States Food and Drug Administration (FDA) [14]. **(Criterion 1)**

Abstiens et. al. already demonstrated the tailoring of the NP properties [1]. The block-co-polymer synthesis strategy enabled the independent regulation of PEG as well as PLA length. Therefore the physicochemical properties like size or PEG surface configuration can be tuned precisely. Furthermore, different functional endgroups can be introduced, so that diverse NP surface charges can be easily achieved. **(Criterion 2)**

Beyond the introduction of different charges versatile endgroups offer the possibility to decorate these NPs with various ligands in order to address different targets. **(Criterion 3)**

Furthermore, it is possible to attach different surface bound ligands. This means that not only targeting ligands, but also therapeutic ligands can be attached. Besides the NPs can be loaded with therapeutic drugs. For instance Maslanka et. al. prepared pirfenidone-loaded core-shell-NPs [15]. **(Criterion 4)**

The long-term stability has not been not investigated so far. Since PLA and PLGA degrade via hydrolysis, a limited shelf-life is expected. The removal of water is a plausible approach to dramatically enhance the long-term stability, because it is the reaction partner for the degradation. Therefore, freeze-drying

seems to be an eligible method. **(Criterion 5)**

Moreover, the manufacturing procedure on a laboratory scale is truly trivial (nanoprecipitation technique) and there is the possibility for a scale-up using a microfluidic system [16]. A microfluidic manufacturing process also has the potential to become a GCP and GMP-compliant process. Although this was not part of this work. **(Criterion 6)**

### 2.1.2 Pre-Clinical Testing

Beyond the mentioned criteria, the core-shell NPs were highly suitable for experiments on the laboratory scale. They can be labeled with fluorescent dyes [1], ultra-small gold NPs [2] or radioactive indium ions (refer to chapter 8). This offers excellent tracing opportunities and provides access to a multitude of analytical methods.

### 2.1.3 EXP3174 - A Promising Pharmacon

Hennig et. al. reported that losartan carboxylic acid (EXP3174)-decorated NPs targeted the retinal and the choroidal vasculature [17]. They used inorganic quantum dots, that were not suitable for a therapeutic administration in humans. Therefore it was the focus of this thesis to transfer their achievements to a therapeutic nanoparticulate system for the treatment of ocular diseases. Core-shell NPs were identified as promising candidates, when they are decorated with losartan carboxylic acid (EXP3174). EXP3174 is the active metabolite of losartan [18], carrying a carboxylic group that was used for the covalent linkage to PEG-PLA-block-co-polymers (refer to chapter 3). Losartan was developed as an anti-hypertensive drug and received the market authorization already in 1995 (FDA) [19]. Approximately 10 % of orally administered losartan is metabolized to EXP3174, that is a potent non-peptide angiotensin II receptor type 1 (AT1R) antagonist with a 10-fold higher affinity than losartan itself [20]. EXP3174 ranks among the so-called insurmountable AT1R-antagonists, because its binding domain is deeper in the AT1R. Its carbonyl group facilitates a conformational change in the binding pocket, that hinders its dissociation tremendously [20].

Another aspect that encourages the use of EXP3174 is the involvement of the Renin-Angiotensin-Aldosterone System (RAAS) in the ocular neovascularization as it is extensively outlined in section 1.4.2. Therefore the inhibition of the AT1R was expected to prevent the secretion of vascular endothelial growth factor (VEGF) on an earlier stage, block other relevant pathogenetical pathways and furthermore follow a systemic application route. This means that an intravitreal administration will no longer be needed. All these aspects account for the use of EXP3174.

## 2.2 Goals of the Thesis

This work combines the outlined physicochemical properties of core-shell-NPs with the pharmacological potential of the AT1R-antagonist EXP3174. As it is already known, the covalent linkage of EXP3174 to a single PEG chain reduces its affinity to the AT1R tremendously [21]. However, NPs carry a multitude of EXP3174 ligands, so that an individual NP is able to block more than one AT1R. Such a multivalent binding overcomes the individual affinity loss upon PEGylation [21]. Therefore the aggregate of all individual ligand affinities is termed the NP's *avidity*. The hypothesis is that multivalent NPs occupy membrane cavities like clathrin-coated pits enabling several ligands to reach AT1Rs, despite the extreme surface curvature of a NP. The anticipated binding behavior is illustrated in figure 2.1 .

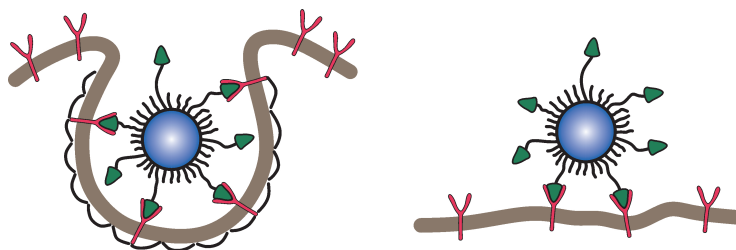


Figure 2.1: Two different binding states of a ligand carrying NP. Ligand (green) - receptor (pink) - complexes retain the NP at the target cell's membrane (brown). Left: NP is situated in a clathrin-coated pit. Right: The same NP is attached to a plane, uncurved cell membrane element.

In the following chapters all aspects from the polymer synthesis to the *in vivo* fate of the designed core-shell NPs are outlined:

**Chapter 3** introduces the synthesis and analytics of the customized polymers. The block-co-polymers were built up from a commercially available PEG macroinitiator that was synthetically modified via ring-opening polymerization to yield tailored PEG-PLA block-co-polymers. Furthermore, EXP3174 was synthesized, analyzed and covalently attached to an amino-terminated PEG-PLA-block-co-polymer. It was especially focused on the absence of free EXP3174 in the manufactured NP dispersions, since this would distort the subsequent binding assays. Apart from that, a commercially available PLGA was coupled to a fluorescent dye or ultra-small gold NPs in order to label the NPs for different experiments.

**Chapter 4** describes the manufacturing of core-shell NPs on the laboratory scale. It was focused on an extensive characterization of the NP properties. Since the determination of the particle number concentration (PNC) was crucial for further investigations, a PNC calculation method was established and validated against a direct PNC measurement technique. Additionally, the conformation of the PEG shell was predicted and the ligand density was determined.

**Chapter 5** deals with the long-term stability of the prepared core-shell-NPs in an aqueous dispersion. It was demonstrated that an adequate formulation technique is indispensable. Therefore, a lyophilization method was developed and the recovery of unaffected, EXP3174 decorated core-shell NPs was proven.

**Chapter 6** illustrates the outstanding binding properties of the designed core-shell-NPs to AT1R carrying cells. It was found that the designed NPs even overcome the affinity of naive EXP3174 molecules. A key element was the introduction of prolonged EXP3174 carrying polymers, that enhanced the NP avidity by orders of magnitude. Besides the binding pattern was visualized with the support of suitable imaging techniques. Furthermore, the avidity to model cells with an increased AT1R-density was investigated. This was intended to imitate a upregulated receptor density under pathological circumstances.

**Chapter 7** dealt with the issue of how many EXP3174 ligands per NP ultimately bind to the target cells. It was unveiled that only a couple of ligands actually bind. The findings were squared with the attachment of viruses as highly specialized, natural NPs targeting their host cells.

**Chapter 8** follows the fate of the designed core-shell NPs *in vivo*. Therefore, the NP stability was additionally evaluated in human plasma. Then, the NP dispersions were systemically administered to healthy mice in order to investigate the pharmacokinetics and the biodistribution.

## 2.3 References

- [1] Kathrin Abstiens, Manuel Gregoritz, and Achim Michael Goepferich. "Ligand Density and Linker Length are Critical Factors for Multivalent Nanoparticle-Receptor Interactions". In: *ACS Applied Materials & Interfaces* 11.1 (2019), pp. 1311–1320. DOI: 10.1021/acsami.8b18843.
- [2] Kathrin Abstiens et al. "Gold-Tagged Polymeric Nanoparticles with Spatially Controlled Composition for Enhanced Detectability in Biological Environments". In: *ACS Applied Nano Materials* 2.2 (2019), pp. 917–926. DOI: 10.1021/acsanm.8b02165.
- [3] Shiv Kumar Prajapati et al. "Biodegradable Polymers and Constructs: A Novel Approach in Drug Delivery". In: *European Polymer Journal* 120 (2019), p. 109191. DOI: 10.1016/j.eurpolymj.2019.08.018.
- [4] Maria Mir, Naveed Ahmed, and Asim ur Rehman. "Recent Applications of PLGA Based Nanostructures in Drug Delivery". In: *Colloids and Surfaces B: Biointerfaces* 159 (2017), pp. 217–231. DOI: 10.1016/j.colsurfb.2017.07.038.
- [5] Shi Su and Peter M. Kang. "Systemic Review of Biodegradable Nanomaterials in Nanomedicine". In: *Nanomaterials* 10.4 (2020). DOI: 10.3390/nano10040656.

### 2.3. REFERENCES

---

- [6] Enas M. Elmowafy, Mattia Tiboni, and Mahmoud E. Soliman. "Biocompatibility, Biodegradation and Biomedical Applications of Poly(lactic acid)/poly(lactic-co-glycolic acid) Micro and Nanoparticles". In: *Journal of Pharmaceutical Investigation* 49.4 (2019), pp. 347–380. DOI: 10.1007/s40005-019-00439-x.
- [7] Zohreh Amoozgar and Yoon Yeo. "Recent Advances in Stealth Coating of Nanoparticle Drug Delivery Systems". In: *Wiley Interdisciplinary Reviews Nanomedicine and Nanobiotechnology* 4.2 (2012), pp. 219–233. DOI: 10.1002/wnan.1157.
- [8] Deepa Yadav and Hitesh Kumar Dewangan. "PEGYLATION: An Important Approach for Novel Drug Delivery System". In: *Journal of Biomaterials Science, Polymer Edition* 32.2 (2021), pp. 266–280. DOI: 10.1080/09205063.2020.1825304.
- [9] Mehak Rastogi et al. "Role of Stealth Lipids in Nanomedicine-Based Drug Carriers". In: *Chemistry and Physics of Lipids* 235 (2021). DOI: 10.1016/j.chemphyslip.2020.105036.
- [10] Neville J. Butcher, Gysell M. Mortimer, and Rodney F. Minchin. "Drug Delivery: Unravelling the Stealth Effect". In: *Nature Nanotechnology* 11.4 (2016), pp. 310–311. DOI: 10.1038/nnano.2016.6.
- [11] Gergely Tibor Kozma et al. "Anti-PEG Antibodies: Properties, Formation, Testing and Role in Adverse Immune Reactions to PEGylated Nano-Biopharmaceuticals". In: *Advanced Drug Delivery Reviews* 154-155 (2020), pp. 163–175. DOI: 10.1016/j.addr.2020.07.024.
- [12] Lu Hong et al. "Antibodies Against Polyethylene Glycol in Human Blood: A Literature Review". In: *Journal of Pharmacological and Toxicological Methods* 102 (2020). DOI: 10.1016/j.vascn.2020.106678.
- [13] Nicola d'Avanzo et al. "Immunogenicity of Polyethylene Glycol Based Nanomedicines: Mechanisms, Clinical Implications and Systematic Approach". In: *Advanced Therapeutics* 3.3 (2020). DOI: 10.1002/adtp.201900170.
- [14] Zhengyi Zhu et al. "PEGylated Versus Non-PEGylated Drugs: A Cross-sectional Analysis of Adverse Events in the FDA Adverse Event Reporting System (FAERS) Database". In: *International Journal of Clinical Pharmacology and Therapeutics* 58.6 (2020), pp. 332–342. DOI: 10.5414/CP203735.
- [15] Sara Maslanka Figueroa et al. "Thermodynamic, Spatial and Methodological Considerations for the Manufacturing of Therapeutic Polymer Nanoparticles". In: *Pharmaceutical Research* 37.3 (2020). DOI: 10.1007/s11095-020-2783-4.
- [16] Kathrin Abstiens and Achim M. Goepferich. "Microfluidic Manufacturing Improves Polydispersity of Multicomponent Polymeric Nanoparticles". In: *Journal of Drug Delivery Science and Technology* 49 (2019), pp. 433–439. DOI: 10.1016/j.jddst.2018.12.009.
- [17] Robert Hennig et al. "Multivalent Nanoparticles Bind the Retinal and Choroidal Vasculature". In: *Journal of Controlled Release* 220.A (2015), pp. 265–274. DOI: 10.1016/j.jconrel.2015.10.033.



### 2.3. REFERENCES

---

- [18] M. McIntyre et al. "Losartan, an Orally Active Angiotensin (AT1) Receptor Antagonist: A Review of its Efficacy and Safety in Essential Hypertension". In: *Pharmacology & Therapeutics* 74.2 (1997), pp. 181–194. DOI: 10.1016/S0163-7258(97)82002-5.
- [19] Elizabeth Ripley and Ari Hirsch. "Fifteen Years of Losartan: What Have We Learned about Losartan that Can Benefit Chronic Kidney Disease Patients?" In: *International Journal of Nephrology and Renovascular Disease* 3 (2010), pp. 93–98. DOI: 10.2147/ijnr.d.s7038.
- [20] M. de Gasparo et al. "International Union of Pharmacology. XXIII. The Angiotensin II Receptors". In: *Pharmacological Reviews* 52.3 (2000), pp. 415–472.
- [21] Robert Hennig et al. "Nanoparticle Multivalency Counterbalances the Ligand Affinity Loss upon PEGylation". In: *Journal of Controlled Release* 194 (2014), pp. 20–27. DOI: 10.1016/j.jconrel.2014.07.062.



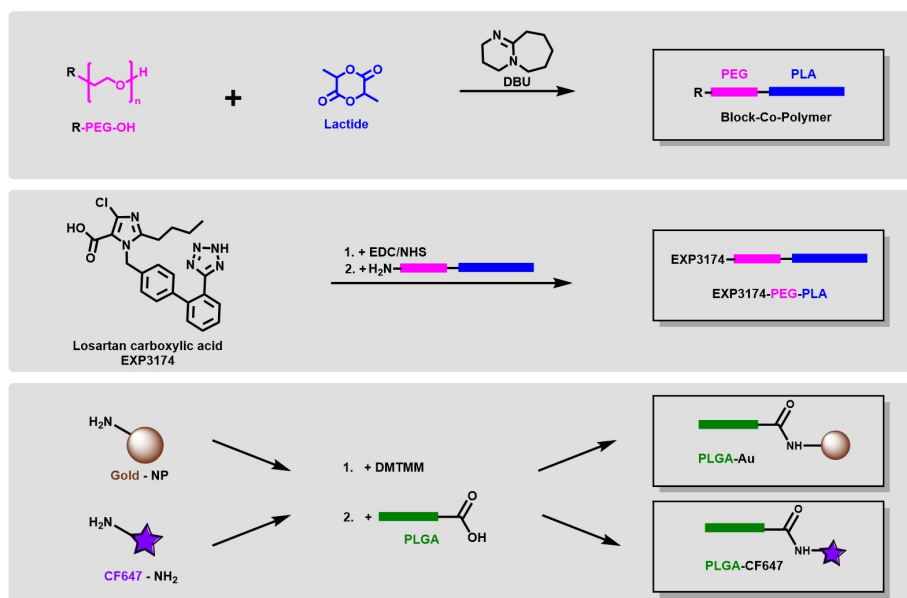
## Chapter 3

# The Building Blocks for the Nanoparticle Manufacturing\*

---

\* GPC measurements were performed by Manuel Roesener and Dr. Joerg Tesmar (University Hospital of Wuerzburg/ Germany)

## Graphical Abstract



## Abstract

Commercially available polyethylene glycol (PEG) macroinitiators were modified via ring-opening polymerization to yield PEG-poly(lactic acid) (PLA) block-co-polymers. This synthesis strategy offers several advantages: (1) controlling of PLA blocks' molecular weight (MW), (2) providing polymers with an outstanding narrow polydispersity index (PDI) and (3) introducing several functional endgroups. Furthermore, commercially available poly(lactic-co-glycolic) acid (PLGA) was tagged with ultra-small gold particles or a fluorescent dye. These components were needed to manufacture core-shell nanoparticles (NPs) that can be traced via a multitude of analysis technologies. Losartan carboxylic acid (EXP3174) was chosen to target and silence angiotensin II receptor type 1 (AT1R). Therefore EXP3174-PEG-PLA was synthesized to receive targeted core-shell NPs.

## 3.1 Introduction

The core-shell NPs were composed of: (1) a mixture of customized PEG-PLA block-co-polymers and (2) a commercial PLGA. This means that PEG, PLA and PLGA were the basic building blocks from a chemist's perspective. These substances are already used as excipients in numerous United States Food and Drug Administration (FDA)-approved pharmaceuticals including parenteral formulations [1]. Consequently, they own a positive risk and safety profile and

can be considered for the development of a therapeutic system.

PEG has already been applied as drug or excipient in versatile pharmaceuticals [2]. Since the 1950s PEG has been part of pharmaceutical formulations like suppositories, parenterals, tablets and pills [2]. Already in 1977, Abuchowski et. al. introduced a technique to hide proteins from the immune response. Therefore they conjugated PEG with albumine and provided evidence for an enhanced circulation time [3]. Nowadays, this phenomenon is better known as *stealth effect*. Especially nanomaterials and proteins are conjugated to PEG (commonly named PEGylation). PEG mediates a steric shielding and prevents the adsorption of plasma proteins (opsonins) that tag xenobiotics for the immune system [4–7]. On the contrary, there is a growing evidence for an immune response against PEG units after multiple administration [8–11]. Hence, there is a need for further investigation. Nevertheless, PEG is the gold standard for the enhancement of blood circulation time and active drug targeting so far. Therefore, it was also used for the manufacturing of these core-shell NPs.

Mono-functionalized PEG macroinitiators were purchased from a commercial producer with an outstanding narrow PDI (refer to figure 3.2). The PLA block was covalently attached to the macroinitiator via ring-opening polymerization. Therefore the PEG macroinitiator was reacted with 3,6-dimethyl-1,4-dioxane-2,5-dione (lactide) under the catalysis of 1,8-diazabicyclo[5.4.0]undec-7-ene (DBU). This synthesis strategy was already described in the literature [12]. Additionally, there is a deeper understanding of the reaction mechanism and the controlling parameters, so that a monomodal MW distribution with a narrow PDI and a minimum of side products can be obtained [13]. The MW of the attached PLA can be regulated via the initial PEG-to-lactide ratio. Finally, PEG-PLA block-co-polymers with different functionalities were prepared: (1) methoxy, (2) carboxy or (3) amino endgroup. The methoxy-terminated block-co-polymer provided an inert and uncharged endgroup, while carboxy- and amino-terminated block-co-polymers were intended to introduce negative or positive surface charges. Furthermore, the amino-terminated block-co-polymer was utilized to attach EXP3174 covalently. EXP3174 is an antagonist for the AT1R. It served as the targeting ligand and mediated the pharmacological effect. The carboxylic group of EXP3174 was activated via standard N-(3-dimethylaminopropyl)-N'-ethylcarbodiimide (EDC)/ N-hydroxysuccinimide (NHS) chemistry and covalently coupled to NH<sub>2</sub>-PEG-PLA. In particular, it was focussed on the absence of free EXP3174 in the manufactured NP dispersion, since this substance would distort the binding studies.

PLGA was purchased from a commercial producer as well. It is a lipophilic polymer, that is used to stabilize the NP's core. Beyond this stabilizing function, PLGA possesses a pivotal role during the early development stage. So PLGA was used to immobilize either fluorescent dyes or ultra-small gold particles in the NP's core. This enabled the detectability via various analysis techniques without changing the core-shell NP's properties fundamentally.

## 3.2 Material and Methods

### 3.2.1 Material

All chemicals were purchased from Sigma-Aldrich (Taufkirchen/ Germany), if not stated otherwise. For synthesis purpose at least synthetical-grade was used. For analytical purpose analytical-grade or better were used. All solvents used for high-performance liquid chromatography (HPLC) had HPLC-grade, while solvents used for mass spectrometry (MS) measurements had LC-MS grade.

Ultrapure water was freshly prepared using a Milli-Q water purification system (Millipore/ Schwabach/ Germany). It is subsequently termed *water*.

### 3.2.2 Synthesis of Block-co-Polymers

To synthesize the differently functionalized block-co-polymers, ring-opening polymerisation was adapted from the literature [12, 14]. PEG macroinitiators tBoc-NH-PEG-OH and HOOC-CH<sub>2</sub>-PEG-OH were purchased from JenKem (Allen/ TX/ USA). MeO-PEG-OH macroinitiators were purchased from Sigma-Aldrich (Taufkirchen/ Germany).

The particular PEG-macroinitiator was reacted with lactide under the catalysis of DBU (DCM, RT). The molar ratio of macroinitiator to lactide was calculated in order to yield the proposed PLA block length. In case of tert-butyloxycarbonyl (tBoc)-protected macroinitiators, the protecting group was removed by the addition of trifluoroacetic acid (TFA). All synthesized PEG-PLA block-co-polymers were stored in the freezer protected from light and moisture.

### 3.2.3 Analytics of Block-co-polymers

#### Nuclear Magnetic Resonance Spectroscopy

10 mg product were dissolved in 0.8 mL deuterated chloroform (CDCl<sub>3</sub>). <sup>1</sup>H-nuclear magnetic resonance (NMR) spectra were recorded on a Bruker Avance 300 operating at 300 MHz or on a Bruker Avance III HD 400 operating at 400 MHz.

#### Gel Permeation Chromatography

Purity and polydispersity of synthesized PEG-PLA block-co-polymers were checked with an OmniSEC Resolve and Reveal System (Malvern Panalytical/ United Kingdom) equipped with two LC4000L (300x8 mm) columns, (Malvern Panalytical/ Malvern/ United Kingdom) in line. The mobile phase was chloroform (CHCl<sub>3</sub>) and the flow rate was adjusted to 1.0 ml min<sup>-1</sup>. The samples were dissolved in CHCl<sub>3</sub> to a final concentration between 5.0 mg ml<sup>-1</sup> to 10.0 mg ml<sup>-1</sup>. The injection volume accounted 100 µl. All components and the solvent were equilibrated at 35 °C.

The system enables the detection of the refractive index, viscosity and scattered light simultaneously (triple detection), providing the intrinsic viscosity of the

sample. So the MW was determined by the universal calibration as it was described by the group of Benoit in 1967 [15]. Calibration was carried out with a PMMA 50 kDa standard (Malvern Panalytical/ United Kingdom).

#### 3.2.4 Synthesis of Losartan Carboxylic Acid

An icecold, aqueous solution (0.2 M) of potassium permanganate (EMSURE®/ Merck/ Darmstadt/ Germany) was added dropwise to an icecold alkaline solution of losartan potassium (Santa Cruz/ Heidelberg/ Germany) and reacted for 4 h. Finally there was a 2-fold molar excess of permanganate to losartan. Afterwards the reaction product was precipitated using 1 M hydrochloric acid (HCl). The precipitate was washed with water twice (10 000 xg, 4 °C, 15 min). Subsequently, the precipitate was dissolved by careful addition of 1 M sodium hydroxide (NaOH) to adjust moderate alkaline conditions. The remaining sediment (manganese dioxide) was removed by centrifugation (10 000 xg, 4 °C, 15 min). Supernatant was acidified again using 1 M HCl to precipitate the product. The pH must not fall below three. The precipitate was extracted with ethyl acetate, evaporated and once again dissolved in ethanol. Finally the product was precipitated in an excess of water and freeze-dried to obtain a dry powder. Identity and purity of EXP3174 was checked by means of <sup>1</sup>H-NMR, MS and reversed-phase (RP) HPLC.

#### 3.2.5 Analytics of Losartan Carboxylic Acid

##### Nuclear Magnetic Resonance Spectroscopy

<sup>1</sup>H-NMR spectra were recorded on a Bruker Avance III HD 400 operating at 400 MHz. 10 mg product were dissolved in 0.8 mL deuterated dimethyl sulphoxide (DMSO-d<sub>4</sub>). Frequency axis was calibrated using an internal tetramethylsilane (TMS) standard.

##### Mass Spectrometry

MW of synthesized EXP3174 was determined via MS. Therefore the ultra high performance liquid chromatography (UHPLC) system 1290 Infinity II (Agilent Technologies/ Waldbronn/ Germany) coupled with the Agilent 6540 Ultra High Definition Accurate-Mass quadrupole time-of-flight mass spectrometer (Q-TOF) detector (Agilent Technologies/ Waldbronn/ Germany) was utilized. The synthesis product was dissolved in methanol and injected onto a Luna Omega C18 (1.6 µm, 100 Å, 50x2.1 mm) column (Phenomenex/ Aschaffenburg/ Germany). Injection volume accounted 0.20 µl. The system was operated in gradient mode. Solvent A was ultrapure water acidified with formic acid (0.1%) and solvent B was acetonitrile (ACN) acidified with formic acid (0.1%). At the beginning of the analysis the mobile phase consisted of A: 98% and B: 2% for 4 min. Then B was raised continuously to 98% in 1 min. The flow rate was kept at 0.600 ml min<sup>-1</sup> during the complete run.

#### Liquid Chromatography

Additionally, identity and purity of synthesized EXP3174 was checked with RP-HPLC. The analytics was performed on an Agilent 1260 Infinity II system (Agilent/ Waldbronn/ Germany), that consisted of the binary pump G7112B, the autosampler G7129A, the column oven G7130A, the diode-array detector (DAD) G7115A and the fluorescence detector (FLD) G7121B. The system was equipped with a Poroshell EC-C18 (2.7  $\mu\text{m}$ , 120  $\text{\AA}$ , 50x3.0 mm) column (Agilent). Analysis method was adapted from monograph 2232 *losartan potassium* of the European Pharmacopoeia [16, pp. 4319–4322]. The solvents were water acidified with phosphoric acid (0.085 %) (A) and ACN 95 % (B). Elution was performed in gradient mode at 40 °C and at a constant flow rate of 1.0 ml min<sup>-1</sup>. Mobile phase comprised 75 % A for 3 min. Then A was reduced to 10 % in a period of 17 min. These conditions were kept for additional 6 min. Absorbance was detected at 220 nm with DAD. For fluorescence detection, analyts were excited at 250 nm and emitted light was detected at 370 nm.

Synthesis product was dissolved in methanol and diluted to a final concentration of 3.0 mg ml<sup>-1</sup> and 30 mg ml<sup>-1</sup>. Reference solutions were prepared from losartan potassium (Santa Cruz/ Heidelberg/ Germany) and losartan carboxylic acid (Santa Cruz/ Heidelberg/ Germany). They were diluted to a final concentration of 3.0 mg ml<sup>-1</sup> and 30 mg ml<sup>-1</sup>. Injection volume accounted 5  $\mu\text{l}$ .

#### 3.2.6 Coupling of EXP3174 to Block-Co-Polymer

EXP3174 and the coupling reagents DCC/ NHS were dissolved in dimethylformamide (DMF) and moderately stirred at room temperature (RT) for 2 h. The successful activation of EXP3174's carboxylic group was indicated by the precipitation of DCU. The precipitate was removed by centrifugation (10 000 xg, 4 °C, 5 min) and the subsequent filtration through a PTFE filter (I). Separately, amino-PEG<sub>5k</sub>-PLA<sub>20k</sub> (200 mg ml<sup>-1</sup>) was dissolved in DMF and alkalized with DIPEA (II). Afterwards II was added dropwise to moderately stirred I. The reactants were allowed to react for 20 h at RT. EXP3174 and the coupling reagents were in a molar excess of 3.5x and 3.3x relative to the NH<sub>2</sub>-PEG<sub>5k</sub>-PLA<sub>20k</sub> amount.

Subsequently, an icecold mixture of methanol and ether 1/15 % (v/v) was poured into a DMF solution to precipitate the reaction product. The reaction vessel was placed on ice for 10 min. The supernatant was removed by centrifugation (5000 xg, 4 °C). The remaining precipitate was dissolved in dichloromethane (DCM) and the remaining contaminants, especially uncoupled EXP3174, were extracted from the DCM layer using borate buffer (50 mM, pH 8.5) at least three times. To accelerate the phase separation a Brine solution was utilized. Next, the DCM layer was shaken out against a HCl dilution (0.1 M) to prevent the formation of poorly soluble block-co-polymer salts. Finally, the DCM layer was dried using anhydrous sodium sulfate, filtered with a glass frit and DCM was carefully evaporated. In order to obtain a nice powder, the reaction product was dissolved in a low volume of ACN, precipitated in pure water and freeze-dried.



### 3.2.7 Analytics of EXP3174-PEG-PLA

To analyse the coupling efficiency polymer micelles were prepared. Following the general NP manufacturing method 4.2.2, EXP3174-PEG<sub>5k</sub>-PLA<sub>20k</sub> was dissolved in ACN to obtain an organic phase with a final polymer concentration of 10 mg ml<sup>-1</sup>. The organic phase was dropped into vigorously stirred water (aqueous phase). ACN was evaporated for at least 3 h at atmospheric pressure (atm). The centrifugation step was skipped to prevent distortion of the analysis. This resulted in the formation of EXP3174-micelles, allowing analysis methods in an aqueous environment. Apart from EXP3174-micelles, methoxy-micelles and amino-micelles were prepared by the equal procedure.

#### Iodine Assay

The PEG amount was determined via an iodine assay according to Childs [17]. This is a complexation assay, where PEG forms a coloured complex with barium and iodine, that can be detected at 535 nm. MeO-PEG<sub>5k</sub>-OH (Sigma Aldrich/ Taufkirchen/ Germany) was diluted in water (3, 6, 9, 12, 15, 18 and 21 µg ml<sup>-1</sup>) and served as calibration standard. The detection reagent was freshly prepared by mixing 5 % (w/v) barium chloride in 1 M HCl solution (2/3) and 0.05 M iodine/ potassium iodide dilution (AVS Titrimorm/ VWR/ Ismaning/ Germany) (1/3). NP dilutions and calibration standards were rendered in 96-well-plate (140 µl). Then the detection reagent was added (60 µl). After 1 min incubation at RT, absorbance at 535 nm was measured with a FluoStar Omega fluorescence microplate reader (BMG Labtech/ Ortenberg/ Germany).

#### Quantification of Losartan Carboxylic Acid

EXP3174 was quantified utilizing a fluorescence assay as it is described in section 4.2.7. In derogation from that method, EXP3174-micelles (sample) as well as Methoxy-micelles and amino-micelles (both negative controls) were diluted at least 1:20 in 0.2 M acetic acid. Equally a series of acidified EXP3174-dilutions served as calibration standard. Measurements were executed in triplicates.

#### Floram Assay

With the help of an Floram Assay, it is possible to detect primary amino groups. Therefore 160 µl borate buffer (500 mM, pH 8.5) was rendered in a white F-bottom polystyrene (PS) 96-well plate (Greiner Bio One/ Frickenhausen/ Germany). All sample dispersions in the same experiment sequence were adjusted to an equal PEG concentration. The PEG concentration was determined with the iodine assay. Then 20 µL of the sample dilution were added to the rendered borate buffer and carefully mixed. Finally 20 µl of a freshly prepared, acetic 4-phenylspiro-[furan-2(3H),1-phthalan]-3,3'-dione, fluoresceamine (floram) dilution (0.3 mg ml<sup>-1</sup>) were added. Samples were excited at 390 nm and checked for fluorescence at 475 nm using a Synergy Neo2 (BioTek) plate reader. Measurements were executed in triplicates.

#### 3.2.8 Purity of Nanoparticle Dispersions

In order to ensure the absence of any contamination with free EXP3174 core-shell NPs were manufactured via nanoprecipitation. The manufacturing technique is described in section 4.2.2 (refer to EXP3174 decorated NP90 (EXP-NP90)).

#### Liquid Chromatography of Core-Shell Nanoparticles

Chromatographic separation was performed on an Agilent 1260 Infinity II system (Agilent/ Waldbronn/ Germany) that consisted of the binary pump G7112B, the autosampler G7129A, the column oven G7130A and the FLD G7121B. It was equipped with a PLRP-S (8  $\mu\text{m}$ , 4000  $\text{\AA}$ , 150x4.6 mm) column (Agilent). Analysis method was adapted from monograph 2232 *losartan potassium* of the European Pharmacopoeia [16, pp. 4319–4322]. The solvents were water acidified with TFA (0.1 %) (**A**) and ACN 95 % acidified with TFA (0.1 %) (**B**). Elution was performed in gradient mode at 60 °C and a constant flow rate of 1.2 ml min<sup>-1</sup>. The mobile phase consisted of 75 % **A** for 5 min. Then **A** was reduced to 10 % in 25 min and these conditions were kept for additional 5 min. 50  $\mu\text{l}$  of a EXP-NP90 dispersion (1.0 mg ml<sup>-1</sup>) was analyzed. Dilutions of EXP3174 and EXP3174-PEG<sub>5k</sub> served as references.

#### 3.2.9 Labeling of PLGA

##### Fluorochromes

Fluorescence labeling of PLGA was adapted from Abstiens et. al [14]. Acid terminated PLGA (Resomer®RG502H) was dissolved in anhydrous DMF and moderately stirred at RT. 4-(4,6-dimethoxy-1,3,5-triazin-2-yl)-4-methylmorpholinium chloride (DMTMM) was dissolved in anhydrous DMF separately and dropwise added to the PLGA solution. The mixture was stirred moderately at RT for 2 h(**A**). Successful activation was indicated by the precipitation of 4-methylmorpholinium chloride.

Meanwhile fluorescent dye suitable for labeling of carboxylic groups like CF<sup>TM</sup>647 amine was dissolved in anhydrous DMF (**B**) and was added dropwise to dispersion **A**. The mixture was reacted overnight at RT, protected from light and moisture. Afterwards, the dispersion was precipitated into water and dialyzed with a Spectra/Por®3 RC membrane (SpectrumLabs/ Rancho Dominguez/ CA/ United States) against water. Then the dispersion was freeze-dried. Remaining powder was additionally dried in an evacuated desiccator over silica gel drying bed and stored under inert gas in the freezer.

##### Gold Tag

Gold labeling procedure was done according to Abstiens et. al. [18]. In brief, monoamino gold NPs with an average size of 2.2 nm were received from Nanopartz (Loveland/ CO/ USA) and covalently coupled to acid terminated PLGA (Resomer®RG502H) using EDC/ NHS chemistry. Dispersion was precipitated in water, purified via centrifugation and freeze-dried. The brown powder was stored protected from light and moisture.

### 3.3 Results and Discussion

#### 3.3.1 Block-co-Polymers

Block-co-polymers were the key elements for the manufacturing of the core-shell-NPs. Like a huge toolbox, they built the basis to tailor the NP properties. The block-co-polymers consisted of two blocks: the hydrophilic PEG block and the lipophilic PLA block. They were covalently linked via an ester bond. Ring-opening polymerisation offered the opportunity to tune the MW of each block almost independently. Furthermore, different end groups were utilized at the PEG block. In general, the block-co-polymers were terminated by methoxy endgroups. They were inert and uncharged. Amino-terminated block-co-polymers were used to couple the targeting ligand EXP3174 covalently to the NP. Additionally, it can be used to introduce a positive surface charge. Carboxy-terminated block-co-polymers were used to introduce negative surface charges.

Here 2 kDa or 5 kDa PEG macroinitiators were chosen. Afterwards lactide equivalents were added to receive a 20 kDa PLA block. The synthesized block-co-polymer and there calculated MWs are listed in table 3.1.

Table 3.1: List of synthesized block-co-polymers (MW targets).

block-co-polymer	MW	protecting group (macro-initiator)	end group	PEG length	PLA length
MeO-PEG <sub>5k</sub> -PLA <sub>20k</sub>	25 kDa	-	MeO	5 kDa	20 kDa
MeO-PEG <sub>2k</sub> -PLA <sub>20k</sub>	22 kDa	-	MeO	2 kDa	20 kDa
HOOC-PEG <sub>2k</sub> -PLA <sub>20k</sub>	22 kDa	-	COOH	2 kDa	20 kDa
NH <sub>2</sub> -PEG <sub>5k</sub> -PLA <sub>20k</sub>	25 kDa	tBoc	NH <sub>2</sub>	5 kDa	20 kDa

#### Yield

MeO-PEG-PLA and HOOC-PEG-PLA were synthesized with an overall yield above 90 %. NH<sub>2</sub>-PEG-PLA block-co-polymers were synthesized with an overall yield above 55 %.

#### Molecular Weight

<sup>1</sup>H-NMR spectra revealed three main peaks, as depicted in figure 3.1. The <sup>1</sup>H-NMR spectrum of MeO-PEG<sub>2k</sub>-PLA<sub>20k</sub> is depicted as an representative example. The singlet at  $\delta$  3.6 corresponds to the methylene protons of the PEG block. The overlapping quartets at  $\delta$  5.2 and the overlapping doublets at  $\delta$  1.6 correspond to the methine and the methyl protons of the PLA block [19]. All signals were identified for the synthesized PEG-PLA-block-co-polymers, confirming the successful polymerisation reaction.

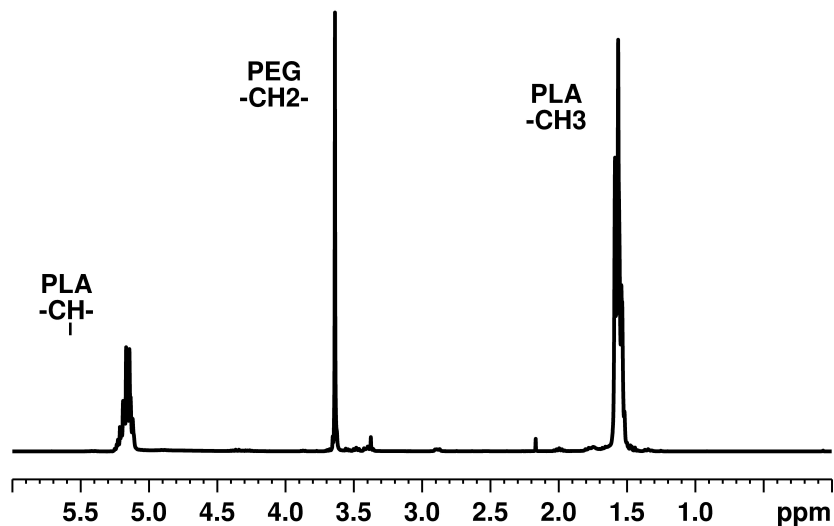


Figure 3.1: <sup>1</sup>H -NMR spectrum of MeO-PEG<sub>2k</sub>-PLA<sub>20k</sub> in CDCl<sub>3</sub> at RT.

The MW was calculated from the integrals of PLA protons in relation to the integral of the PEG protons [12]. The MWs of the PEG blocks were taken from the manufacturers Certificate of Analysis (CoA). The data is listed in table 3.1. The calculated MWs (refer to table 3.2 *Total*) were in excellent accordance to the aimed MWs listed in table 3.2.

Additionally, synthesized block-co-polymers were checked using gel permeation chromatography (GPC). Since block-co-polymers show another coiling behavior than homopolymers like the poly(methyl methacrylat) (PMMA) calibration standard, it is challenging to determine the exact MW of PEG-PLA block-co-polymers. However, simultaneous detection with refractive index (RI), viscometer and light scattering detector (triple detector) is the most precise way to determine its MW with this method. Absolute values (refer to table 3.2 *GPC*) largely confirm the NMR data. But it indicates an outstanding narrow PDI, as it was already reported by Quian et. al. [12].

The GPC chromatograms of each block-co-polymer are individually plotted in figure 3.2. Each chromatogram is complemented with the signal of the corresponding macroinitiator. It can be recognized, that the MW was raised during polymerisation, while the PDI increased only slightly. The elution profile for the MW of the PEG-PLA-block-co-polymer is shown on the secondary axis (solid red line). Furthermore, the weight fraction distribution is added to each chromatogram (shaded insert). The number-average MW and the weight-average MW are highlighted (blue vertical line). It confirmed a successful and homogenous polymerisation reaction.

### 3.3. RESULTS AND DISCUSSION

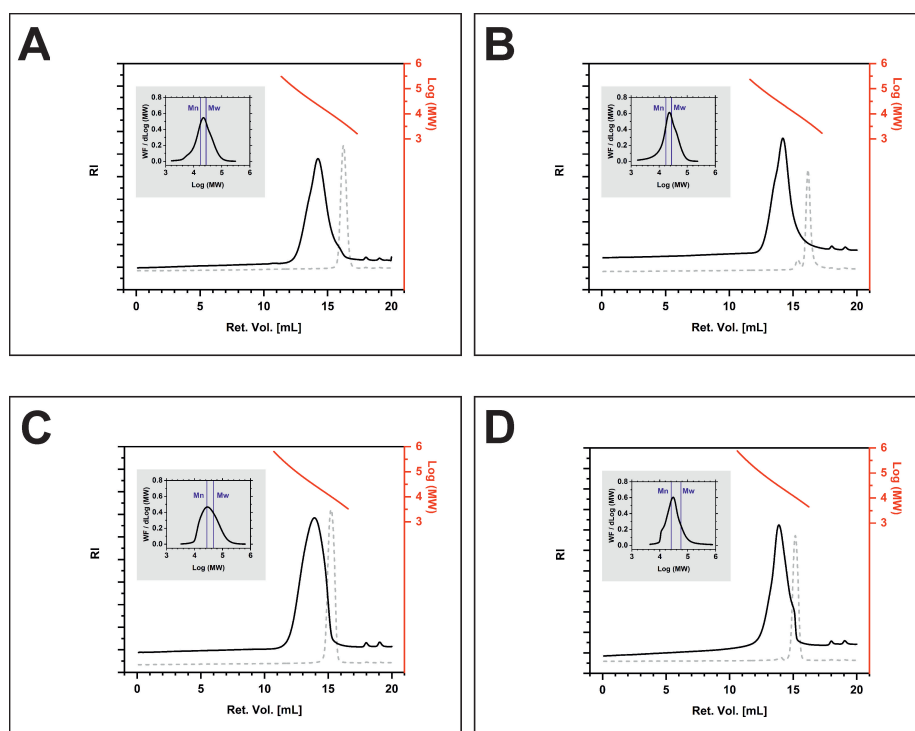


Figure 3.2: GPC chromatograms of synthesized block-co-polymers. Primary axis: RI detector response of block-co-polymer (solid black line) and PEG macroinitiator (dashed grey line). Secondary axis: MW elution profile (solid red line). Insert: weight fraction distribution with highlighted number-average MW and weight-average MW (blue vertical lines). **A:** MeO-PEG<sub>2k</sub>-PLA<sub>20k</sub>, **B:** HOOC-PEG<sub>2k</sub>-PLA<sub>20k</sub>, **C:** MeO-PEG<sub>5k</sub>-PLA<sub>20k</sub> and **D:** NH<sub>2</sub>-PEG<sub>5k</sub>-PLA<sub>20k</sub>.

### 3.3. RESULTS AND DISCUSSION

Table 3.2: List of MWs of synthesized block-co-polymer.

block-co-polymer	MW (number-average)				PDI <sup>(5)</sup>
	PEG <sup>(1)</sup> [kDa]	PLA <sup>(2)</sup> [kDa]	Total <sup>(3)</sup> [kDa]	GPC <sup>(4)</sup> [kDa]	
MeO-PEG <sub>2k</sub> -PLA <sub>20k</sub>	2.0	19.2	21.2	17.2	1.61
MeO-PEG <sub>5k</sub> -PLA <sub>20k</sub>	4.8	17.2	22.0	27.3	1.60
HOOC-CH <sub>2</sub> -PEG <sub>2k</sub> -PLA <sub>20k</sub>	2.1	19.6	21.7	17.2	1.61
NH <sub>2</sub> -PEG <sub>5k</sub> -PLA <sub>20k</sub>	5.0	19.1	24.1	25.6	2.28

<sup>(1)</sup> macroinitiator MW taken from manufacturers analysis certificate <sup>(2)</sup> <sup>1</sup>H-NMR data

<sup>(3)</sup> MW(PEG) + MW(PLA) <sup>(4)</sup> universal calibration <sup>(5)</sup> GPC data

#### 3.3.2 Losartan Carboxylic Acid

Losartan potassium was one of the first substances in a series of drugs introduced for the treatment of hypertension [20]. It is a potent, nonpeptide AT1R antagonist. The half maximal inhibitory concentration (IC<sub>50</sub>) value is in a low nano-molar range [21]. But losartan lacks a suitable functional group for the coupling to the amino-terminated block-co-polymers (refer to figure 3.3A). However, its active metabolite losartan carboxylic acid (EXP3174) carries a carboxylic group, that is highly suitable for that purpose (refer to figure 3.3B). The oxidation of losartan to EXP3174 in the human liver is catalyzed by cytochrome enzymes CYP3A4 and CYP2C9 [22].

Here potassium permanganate was used as an oxidizing agent. The procedure is described in section 3.2.4. The overall yield accounted 65%. The identity of EXP3174 was confirmed by <sup>1</sup>H-NMR and MS. <sup>1</sup>H-NMR analytics revealed the following signals:  $\delta$  7.7 to 6.9 (m, 8H, Ar-H),  $\delta$  5.59 (s, 2H),  $\delta$  2.57 (t, 2H,  $J=7.6$  Hz),  $\delta$  1.50 (quint, 2H,  $J=7.6$  Hz),  $\delta$  1.25 (sext, 2H,  $J=7.4$  Hz) and  $\delta$  0.81 (t, 3H,  $J=7.6$  Hz), that could be matched with EXP3174 [23].

LC-MS measurements found an exact mass of 437 (MH<sup>+</sup>) which corresponds exactly to EXP3174 [24].

The purity of EXP3174 was checked via RP-HPLC. The chromatograms are depicted in figure 3.4. The synthesis educt losartan (blue line) was completely converted, which was confirmed by the absence of losartan in the chromatogram of the synthesis product (black line). Since the retention time of the synthesis product and the reference substance coincide, the synthesis product was identified as EXP3174. Figure 3.4A shows the DAD response at 220 nm. The purity of the synthesis product was over 90%, that's why further purification was waived. Additionally, the FLD signal was recorded. Analyts were excited at 250 nm and emitted light was collected at 370 nm. The chromatograms are depicted in figure 3.4B. They confirm the previous results. The detected fluorescence is typical for this group of substances. The obtained retention times are listed in table 3.3.

### 3.3. RESULTS AND DISCUSSION

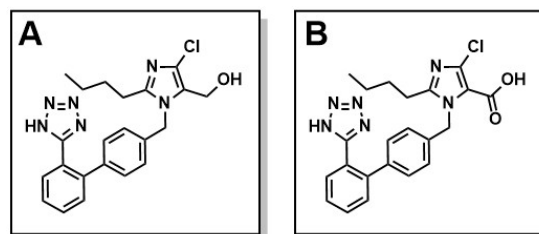


Figure 3.3: Chemical structure of losartan (A) and its active metabolite losartan carboxylic acid (EXP3174) (B)

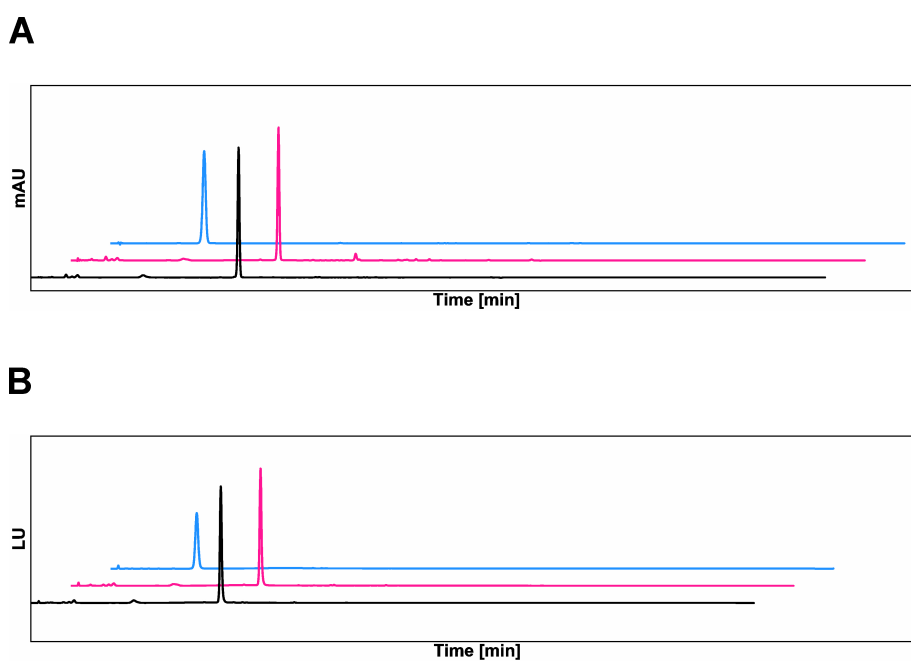


Figure 3.4: HPLC chromatograms for the synthesis product (EXP3174) (black line), the reference substance (EXP3174) (pink line) and the synthesis educt (losartan) (blue line). **A**: DAD response (absorbance at 220 nm). **B**: FLD response (Ex=250 nm; Em=370 nm).

### 3.3. RESULTS AND DISCUSSION

Table 3.3: HPLC analysis of synthesized EXP3174. List of retention times  $t_r$ .

Analyt	Detector signal		Substance
	DAD $t_r$ [min]	FLD $t_r$ [min]	
Synthesis educt	$3.308 \pm 0.001$	$3.340 \pm 0.005$	Losartan
Synthesis product	$7.321 \pm 0.003$	$7.351 \pm 0.001$	EXP3174
Reference substance	$7.327 \pm 0.001$	$7.357 \pm 0.008$	EXP3174

#### 3.3.3 EXP3174-PEG-PLA Block-co-Polymer

EXP3174 was chosen as targeting ligand of the core-shell-NPs. As an AT1R antagonist, EXP3174 also facilitates a pharmacological effect. There are two different coupling strategies: (1) EXP3174 is linked to the manufactured NP or (2) EXP3174 was covalently linked to the block-co-polymer prior NP manufacturing. Strategy (2) was favored, since it is easier to adjust the EXP3174-density. Furthermore, the polymer quality can be assessed prior to the NP manufacturing and the manufactured NPs can be used without additional laborious purification steps. The absence of free EXP3174 is absolutely needed, because it would challenge any binding study with the targeted core-shell NPs. The synthesis strategy encompassed the activation of the carboxylic group of EXP3174 that was carefully added to an alkalized  $\text{NH}_2$ -PEG-PLA dilution. The reaction was handled in a water-free environment to prevent polymer hydrolysis. EXP3174 was added in an 3.3-fold molar excess, so that naive EXP3174 must be removed via solvent extraction (refer to section 3.2.6). The absence of primary amino groups and the EXP3174-to-PEG-ratio were checked. Ideally, there are no remaining primary amino groups, since they vanish by a quantitative coupling reaction.

The performed analysis methods started from an aqueous sample. That's why pure micelles of EXP3174-PEG<sub>5k</sub>-PLA<sub>20k</sub> (sample),  $\text{NH}_2$ -PEG<sub>5k</sub>-PLA<sub>20k</sub> (positive control) and MeO-PEG<sub>5k</sub>-PLA<sub>20k</sub> (negative control) were prepared according to section 3.2.7. The results are plotted in figure 3.5, indicating a successful coupling reaction (coupling efficiency: 61.1%). These results were directly compared to PLA 10 kDa block-co-polymer micelles (data not shown), where the coupling efficiency accounted 91.1%. The coiling behavior of polymers with a longer PLA block potentially reduce the availability of the amino endgroups, so that the coupling efficiency decreases. Nevertheless, this coupling efficiency is acceptable at this development stage.

Furthermore, the EXP3174-to-PEG-ratio was determined as another quality attribute. An quantitative coupling of EXP3174 to the block-co-polymers was expected, since an excess of EXP3174 was added during the synthesis. The EXP3174 content and the PEG content were determined separately via two different methods. The PEG content was measured with an iodine assay, while the EXP3174 concentration was measured via a fluorescence assay. The EXP3174-to-PEG-ratio accounted 1.8. This result argues for the presence of free uncoupled EXP3174. But it must be considered that the calculation is based on the number-averaged MW, so that this is just an approximation.



### 3.3. RESULTS AND DISCUSSION

---

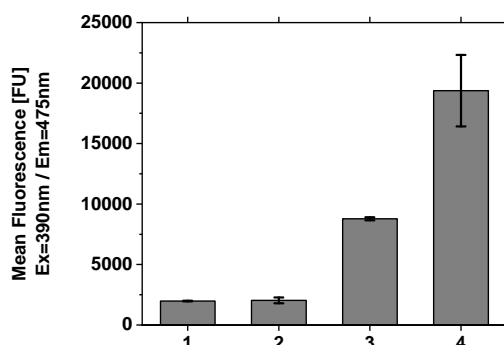


Figure 3.5: Fluram assay for the determination of primary amino groups. **1:** pure dispersant (double blank); **2:** methoxy-micelles (negative control), **3:** EXP3174-micelles (sample) and **4:** amino-micelles (positive control).

Moreover, the NP manufacturing technique includes a further purification step (ultra-centrifugation) in comparison to the preparation of polymer micelles. Therefore impurities with a MW clearly below 100 kDa are removed effectively. However, a dispersion with EXP3174-decorated core-shell NP was manufactured and checked for impurities via HPLC. The manufacturing procedure included the mentioned purification step (ultra-centrifugation molecular weight cut off (MWCO): 100 kDa). It is not trivial to separate small molecules from high-MW analyts like polymer micelles and intact NPs. Therefore, a PLRP-S column with a huge pore size (4000 Å) was chosen to retain the intact NPs. The PLRP-S column is built by pure unmodified polystyrene particles that were additionally able to retain lipophilic substances like EXP3174. The chromatograms are depicted in figure 3.6. Free EXP3174 and PEGylated EXP3174 served as references. The identified substances are highlighted by an arrow-head. The retention times are listed in table 3.4. It could be concluded that manufactured core-shell-NPs were not contaminated with free EXP3174. However, another impurity was still detected. It corresponds roughly to EXP3174-PEG<sub>5k</sub>. It was assumed that this impurity is a hydrolysis product of a EXP3174-PEG-PLA. Since the substance was detected with the FLD, it probably contains EXP3174. Contrasting the degradation of PEG and PLA in an aqueous environment, an ester hydrolysis is much more plausible. Therefore it is expected that this impurity was an EXP3174-PEG<sub>5k</sub>-PLA derivative. But this aspect was not further investigated, since PEGylated EXP3174 suffers from a tremendous affinity loss for the AT1R [25].

### 3.3. RESULTS AND DISCUSSION

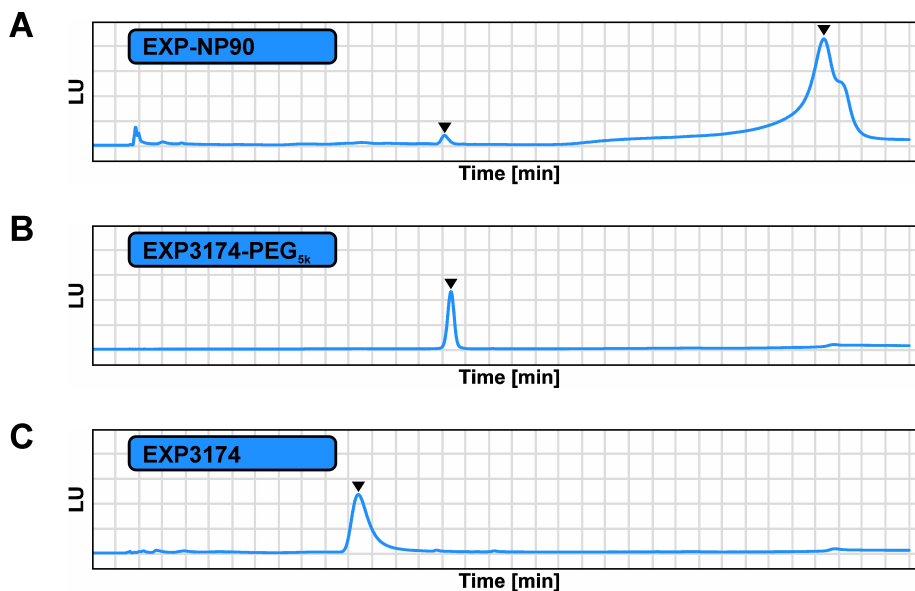


Figure 3.6: HPLC chromatograms of a core-shell NP dispersion (EXP-NP90) (A), the reference substance EXP3174-PEG<sub>5k</sub> (B) and naive EXP3174 (C). Identified peaks are indicated by an arrowhead. The retention times are listed in table 3.4.

Table 3.4: HPLC analysis of core-shell NPs (EXP-NP90). List of retention times  $t_r$ .

Analyt	Detector signal FLD $t_r$ [min]	Substance
NP dispersion	15.087	unknown
	31.340	EXP-NP90
Reference	15.365	EXP3174-PEG <sub>5k</sub>
Reference	11.380	EXP3174

#### 3.3.4 PLGA

PLGA is another essential component for the manufacturing of the core-shell NPs. As a water-insoluble polymer, it is preferentially located in the core of core-shell NPs. For an upcoming therapeutic formulation it would be possible to use ester-terminated or hydroxy-terminated PLGA, whereas the ester-terminated polymer is more lipophilic. PLGA can be tagged with different fluorescent dyes or even ultra-small gold particles, so that the core-shell-NPs can be analyzed in its almost naive configuration via a multitude of analytical techniques.

Here carboxy-terminated PLGA was covalently linked to CF<sup>TM</sup>647 amine using the DMTMM crosslinker. CF<sup>TM</sup>647 labeled NPs could be excited via a red laser ( $\lambda=635$  nm). This labeling procedure is adaptable for a wide range of fluorescent dyes with similar reactivities.

Besides, PLGA was linked to ultra-small monoamino gold NPs using EDC/NHS chemistry. This labeling technique offered the opportunity to prepare gold-tagged NPs, that could be detected via inductively coupled plasma (ICP)-MS. ICP-MS is a ultra-sensitive analysis method enabling the tracing of ultra-low gold amounts.

These labeling techniques give access to a plethora of analysis technique that can be used during the investigational phase.

### 3.4 Conclusion

Finally, four different block-co-polymers with a target MW of 22 kDa and 25 kDa were synthesized via ring-opening polymerization. They carried the endgroup functionalities methoxy, carboxy or amino, so that the surface charge of subsequently manufactured core-shell NPs can be tailored. Carboxy-terminated polymers introduced negative charges, while amino-terminated polymers introduced positive charges. The synthesized block-co-polymer were analyzed via <sup>1</sup>H-NMR and GPC in order to check the MW, the PDI and the purity. The block-co-polymers have an outstanding narrow PDI. The length of the PLA block can be tuned via the applied quantity of lactide (moles lactide per mol macroinitiator). Therefore, further customized PEG-PLA-block-co-polymers are easily accessible. The synthesized products were stored in a freezer, protected from light, oxygen (inert gas) and moisture in order to ensure their stability.

Beyond the possibility to introduce a positive surface charges, NH<sub>2</sub>-PEG-PLA was used to obtain a EXP3174 decorated block-co-polymer. EXP3174 was covalently coupled to NH<sub>2</sub>-PEG-PLA via EDC/ NHS chemistry. Therefore, losartan was purchased from a commercial supplier and oxidized with potassium permanganate to yield EXP3174. The identity of the synthesis product was verified via <sup>1</sup>H-NMR, MS and HPLC, whereas the HPLC chromatograms also indicated a purity of more than 90 %. Special attention was paid to the purity of EXP3174-PEG-PLA block-co-polymer, since the coupling reaction was facilitated with an molar excess of activated EXP3174. The coupling efficiency was 61.1 %. It was calculated from a fluorimetry assay, that is a fluorescence based analysis method detecting primary amino groups. It was discussed, if

the 20 kDa-PLA block reduces the availability of the primary amino groups during the coupling reaction. Controversially, the EXP3174-to-PEG ratio accounted 1.8, arguing for the presence of free EXP3174. However, it must be considered that the calculation is based on the number-averaged MW obtained from the  $^1\text{H}$ -NMR. In addition, it is possible that not the whole PEG amount could be detected via the iodine assay, since it is not completely available on the polymer-micelles surface. This hypothesis is also encouraged by the determined coupling efficiency and the reduced availability of the amino groups for the coupling reaction. All in all, these data gave evidence for a successful coupling reaction, although the coupling efficiency can be further improved. Nevertheless, it is absolutely suitable for the current development stage. It was focussed on the absence of free EXP3174 in the manufactured NP dispersion. That's why a HPLC method for the tracing of free EXP3174 in a core-shell NP dispersion was established. The absence of free EXP3174 was proven.

Last but not least, a commercially available PLGA was tagged with a fluorescent dye or ultra-small gold particles. These reactions were the basis for the subsequent detectability of the manufactured core-shell-NPs via various analysis techniques. Beyond that, the labeling procedure is also adaptable for a wide range of fluorescent dyes with similar reactivities and solubility properties. The gold tag gives access to further imaging techniques like transmission electron microscopy (TEM) or highly sensitive analysis methods like ICP-MS.

### 3.5 References

- [1] U.S. Food and Drug Administration. *Inactive Ingredient Database*. 22.07.2021.
- [2] Anisha A. D'souza and Ranjita Shegokar. "Polyethylene Glycol (PEG): A Versatile Polymer for Pharmaceutical Applications". In: *Expert Opinion on Drug Delivery* 13.9 (2016), pp. 1257–1275. DOI: 10.1080/17425247.2016.1182485.
- [3] A. Abuchowski et al. "Alteration of Immunological Properties of Bovine Serum Albumin by Covalent Attachment of Polyethylene Glycol". In: *Journal of Biological Chemistry* 252.11 (1977), pp. 3578–3581. DOI: 10.1016/S0021-9258(17)40291-2.
- [4] Zohreh Amoozgar and Yoon Yeo. "Recent Advances in Stealth Coating of Nanoparticle Drug Delivery Systems". In: *Wiley Interdisciplinary Reviews Nanomedicine and Nanobiotechnology* 4.2 (2012), pp. 219–233. DOI: 10.1002/wnan.1157.
- [5] Susanne Schoettler et al. "Protein Adsorption is Required for Stealth Effect of Poly(ethylene glycol)- and Poly(phosphoester)-Coated Nanocarriers". In: *Nature Nanotechnology* 11 (2016), pp. 372–377. DOI: 10.1038/NNANO.2015.330.
- [6] Susanne Schoettler, Katharina Landfester, and Volker Mailänder. "Controlling the Stealth Effect of Nanocarriers through Understanding the Protein Corona". In: *Angewandte Chemie Internationale Edition* 55.31 (2016), pp. 8806–8815. DOI: 10.1002/anie.201602233.

### 3.5. REFERENCES

---

- [7] Neville J. Butcher, Gysell M. Mortimer, and Rodney F. Minchin. "Drug Delivery: Unravelling the Stealth Effect". In: *Nature Nanotechnology* 11.4 (2016), pp. 310–311. DOI: 10.1038/nnano.2016.6.
- [8] Marwa Mohamed et al. "PEGylated Liposomes: Immunological Responses". In: *Science and Technology of Advanced Materials* 20.1 (2019), pp. 710–724. DOI: 10.1080/14686996.2019.1627174.
- [9] Nicola d'Avanzo et al. "Immunogenicity of Polyethylene Glycol Based Nanomedicines: Mechanisms, Clinical Implications and Systematic Approach". In: *Advanced Therapeutics* 3.3 (2020). DOI: 10.1002/adtp.201900170.
- [10] Lu Hong et al. "Antibodies Against Polyethylene Glycol in Human Blood: A Literature Review". In: *Journal of Pharmacological and Toxicological Methods* 102 (2020). DOI: 10.1016/j.vascn.2020.106678.
- [11] Gergely Tibor Kozma et al. "Anti-PEG Antibodies: Properties, Formation, Testing and Role in Adverse Immune Reactions to PEGylated Nano-Biopharmaceuticals". In: *Advanced Drug Delivery Reviews* 154-155 (2020), pp. 163–175. DOI: 10.1016/j.addr.2020.07.024.
- [12] Haitao Qian et al. "A Strategy for Control of "Random" Copolymerization of Lactide and Glycolide: Application to Synthesis of PEG-b-PLGA Block Polymers Having Narrow Dispersity". In: *Macromolecules* 44.18 (2011), pp. 7132–7140. DOI: 10.1021/ma201169z.
- [13] Nicholas J. Sherck, Hyun Chang Kim, and You-Yeon Won. "Elucidating a Unified Mechanistic Scheme for the DBU-Catalyzed Ring-Opening Polymerization of Lactide to Poly(lactic acid)". In: *Macromolecules* 49.13 (2016), pp. 4699–4713. DOI: 10.1021/acs.macromol.6b00621.
- [14] Kathrin Abstiens, Manuel Gregoritz, and Achim Michael Goepferich. "Ligand Density and Linker Length are Critical Factors for Multivalent Nanoparticle-Receptor Interactions". In: *ACS Applied Materials & Interfaces* 11.1 (2019), pp. 1311–1320. DOI: 10.1021/acsami.8b18843.
- [15] Z. Grubisic, P. Rempp, and H. Benoit. "A Universal Calibration for Gel Permeation Chromatography". In: *Journal of Polymer Science Part B: Polymer Letters* 5.9 (1967), pp. 753–759. DOI: 10.1002/pol.1967.110050903.
- [16] *Europäisches Arzneibuch 9.0 - 9.8: Amtliche deutsche Ausgabe*. 9.8. Stuttgart: Deutscher Apotheker Verlag, 2019.
- [17] C. E. Childs. "The Determination of Polyethylene Glycol in Gamma Globulin Solutions". In: *Microchemical Journal* 20.2 (1975), pp. 190–192. DOI: 10.1016/0026-265X(75)90038-7.
- [18] Kathrin Abstiens et al. "Gold-Tagged Polymeric Nanoparticles with Spatially Controlled Composition for Enhanced Detectability in Biological Environments". In: *ACS Applied Nano Materials* 2.2 (2019), pp. 917–926. DOI: 10.1021/acsanm.8b02165.
- [19] K. J. Zhu, Lin Xiangzhou, and Yang Shilin. "Preparation, Characterization, and Properties of Polylactide (PLA)–Poly(Ethylene Glycol) (PEG) Copolymers: A Potential Drug Carrier". In: *Journal of Applied Polymer Science* 39.1 (1990), pp. 1–9. DOI: 10.1002/app.1990.070390101.

### 3.5. REFERENCES

---

- [20] M. de Gasparo et al. "International Union of Pharmacology. XXIII. The Angiotensin II Receptors". In: *Pharmacological Reviews* 52.3 (2000), pp. 415–472.
- [21] K. L. Goa and A. J. Wagstaff. "Losartan Potassium: A Review of its Pharmacology, Clinical Efficacy and Tolerability in the Management of Hypertension". In: *Drugs* 51.5 (1996), pp. 820–845. DOI: 10.2165/00003495-199651050-00008.
- [22] R. A. Stearns et al. "Biotransformation of Losartan to its Active Carboxylic Acid Metabolite in Human Liver Microsomes. Role of Cytochrome P4502C and 3A Subfamily Members". In: *Drug Metabolism and Disposition* 23.2 (1995), pp. 207–215.
- [23] Vincenzo Santagada et al. "A Convenient Synthesis by Microwave Irradiation of an Active Metabolite (EXP-3174) of Losartan". In: *Tetrahedron Letters* 44.6 (2003), pp. 1149–1152. DOI: 10.1016/S0040-4039(02)02835-6.
- [24] National Center for Biotechnology Information. *PubChem Compound Summary for CID 108185, Losartan Carboxylic Acid*. 8.10.2019.
- [25] Robert Hennig et al. "Nanoparticle Multivalency Counterbalances the Ligand Affinity Loss upon PEGylation". In: *Journal of Controlled Release* 194 (2014), pp. 20–27. DOI: 10.1016/j.jconrel.2014.07.062.

## **Chapter 4**

# **Nanoparticle Manufacturing and Analytical Methods with special Focus on the Particle Number Concentration**

## Abstract

Core-shell nanoparticles (NPs) were identified as a highly flexible platform technology to design a novel therapeutic agent for the treatment of proliferative ocular diseases. Two promising candidates with different sizes and an outstanding narrow polydispersity index (PDI) were manufactured via nanoprecipitation: (1) larger, methoxy-terminated EXP-NP90 ( $105 \pm 13$  nm, PDI  $0.10 \pm 0.01$ ) and (2) smaller, carboxy-terminated EXP-NP60<sup>-</sup> ( $68 \pm 6$  nm, PDI  $0.09 \pm 0.02$ ). This work established a simple strategy to determine the particle number concentration (PNC) from the total polymer content (TPC) and the hydrodynamic diameter ( $d_h$ ). The polyethylene glycol (PEG) shell took an intermediate brush-like conformation. Both candidates were decorated with the angiotensin II receptor type 1 (AT1R) antagonist losartan carboxylic acid (EXP3174). The EXP3174 density was  $10.4 \pm 4.5$  molecules per  $100\text{nm}^2$  (EXP-NP90) and  $7.0 \pm 3.0$  molecules per  $100\text{nm}^2$  (EXP-NP60). Viruses served as the blueprint for the NP design, since they carry 0.01 (human immunodeficiency virus (HIV)) to 1.73 spikes per  $100\text{nm}^2$ .

## 4.1 Introduction

Hennig et. al. demonstrated the targeting of retinal and choroidal vasculature using multivalent NPs [1]. Therefore they used quantum dots that were composed of a nanocrystal core (cadmium selenid) surrounded by a hydrophilic shell (PEG coating) [2]. Hennig et. al. decorated those quantum dots with EXP3174 molecules as targeting ligands. Due to the intense fluorescent properties and the heavy metal content they were able to image and quantify the targeted Quantum Dots *in vivo* [1]. On the contrary, the heavy metal content is the reason why a therapeutic application of such NPs is not possible. Abstiens et. al. introduced a highly promising nanoparticulate system, allowing for the manufacturing of tailored NPs [3, 4]. The physicochemical as well as the targeting properties can be precisely tailored. These so-called *core-shell* NPs comprise only biocompatible and biodegradable building blocks. Consequently they can be considered for therapeutic applications. Beyond that, this work suggest different labeling techniques, providing access to a plethora of analysis techniques. This means that, they can be used for pre-clinical investigation and also for therapeutic applications.

Core-shell NPs can be manufactured via nanoprecipitation. Already in 1986, Fessi et. al. patented a NP preparation technique [5]. Just a few years later they refined their method and described the preparation of indomethacin loaded nanocapsules [6]. This was the foundation of an outstanding NP manufacturing technique which has not lost its importance up to the present day. They solved polylactic acid (PLA) and phospholipids in acetone (**organic phase**) and poured it into a moderately stirred aqueous poloxamer dilution (**aqueous phase**). Immediately, the dispersion showed a distinct opalescence, indicating the formation of nanocapsules, that were confirmed by transmission electron microscopy (TEM) images. Later this phenomenon became known as *Ouzo effect* [7, 8]. It was transferred to various at least ternary systems (solute/ solvent/ water) and today it is better known as *nanoprecipitation*. Nanoprecipita-



#### 4.1. INTRODUCTION

---

tion is a common strategy to manufacture polymer-based NPs. There are just a few prerequisites:

- Proportion of solute/ solvent/ water must be in the *Ouzo-region*[9]
- Solvent must be totally miscible with water
- Solute is insoluble in water

Lepeltier et. al. were dealing with the manufacturing of biodegradable, polymer-based NPs as drug delivery devices and described the formation steps in detail [9]. As it is depicted in their schematic ternary phase diagram, there is only a tiny *Quzo-region* where nanoprecipitation occurs. Dropping of the solute/solvent mixture (organic phase) into the stirred water phase (aqueous phase) leads to solvent droplets first. Rapidly water diffuses into the solvent droplets and reduces the solubilisation capacity of the solvent. The saturation concentration decreases with the increasing water content and generates a supersaturation of the solute in the equilibrium solvent/ water mixture. This is a highly instable thermodynamical situation and favors the formation of nuclei. The nucleation stops when the saturation concentration is reached. Afterwards, the primary nuclei can grow via Ostwald ripening as well as aggregation. In order to get NPs for an *in vitro* and *in vivo* testing, the solvent residues must be removed by evaporation. The samples can be purified and concentrated using ultra-centrifugation. Nowadays, researchers are focused on the encapsulation of potent drugs that can be precisely delivered to their target using NPs as carriers [10–12].

In this work block-co-polymers and poly(lactic-co-glycolic) acid (PLGA) were diluted in acetonitrile (ACN) to receive the organic phase. Afterwards the organic phase was carefully dropped into the vigorously stirred aqueous phase. Both phases immediately blended into a homogenous opalescent dispersion. Since the polymers of the organic phase are not soluble in the ACN-water-mixture they precipitate and built NPs. This technique was adapted from Abstiens et. al. [3]. The structure of the manufactured NPs is illustrated in figure 4.1.

The PLA blocks anchor the hydrophilic PEG-chains in the NP core. The core is stabilized with PLGA that can be tagged with a fluorescent dye or ultra-small gold particles. Therefore this NPs can be detected by a plethora of analysis techniques.

Beyond the manufacturing technique the NP properties were investigated in deep. This work introduces a straightforward strategy to determine the PNC from the TPC and the hydrodynamic diameter. This calculation method was confirmed by nanoparticle tracking analysis (NTA) measurements. In addition, it was focussed on the configuration of the PEG-shell. A dense PEG shell is very important for the NP stability *in vivo* [13, 14]. PEG can take a mushroom or a brush conformation [15]. Another really important parameter for the targeting effect is the ligand density. Here the AT1R antagonist EXP3174 served as targeting ligand, but also mediated a pharmacological effect. The number of surface presented ligands is crucial for the NP's target avidity. Therefore the ligand density was adjusted with respect to the spike density of viruses. Viruses use spike proteins to identify and to attach their host cells [16–19].

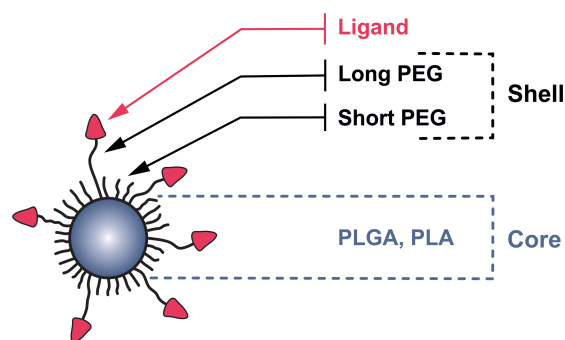


Figure 4.1: Schematic drawing of a manufactured core-shell NP. The PLA tail of the block-co-polymers anchors the hydrophilic PEG block in the NP core. The core is stabilized with PLGA. The PEG chains cover the lipophilic core and build the shell. The PEG shell was composed of longer and shorter PEG-chains. EXP3174 molecules (ligands) were linked to the longer PEG-chains.

## 4.2 Material and Methods

### 4.2.1 Material

The synthesis and analysis of PEG-PLA-block-co-polymers is described in chapter 3. PLGA<sub>13.4k</sub> (Resomer®RG 502 H) was purchased from Sigma Aldrich (Taufkirchen/ Germany) All other chemicals were purchased from Sigma-Aldrich (Taufkirchen/ Germany), if not stated otherwise. A Milli-Q purification system (Millipore/ Schwalbach/ Germany) was used to prepare fresh ultrapure water. It is hereinafter termed water.

### 4.2.2 Manufacturing of Nanoparticles

Initially, the particular block-co-polymer or PLGA was dissolved in HPLC-grade ACN (Merck/ Darmstadt/ Germany) to a concentration of 40 mg ml<sup>-1</sup> (stock dilution). Every stock dilution was individually and freshly prepared for each polymer.

Subsequently stock dilutions were mixed in the desired proportions so that an organic dilution with 10 mg ml<sup>-1</sup> was received (**organic phase**). The organic phase always consists of 70% and 30% PLGA. The 70:30 ratio turned out to provide the best particle size characteristics and manufacturing robustness [3, 20]. The organic phase was carefully dropped into vigorously stirred diluted Dulbecco's Phosphate Buffered Saline (x0.1) (DPBSx0.1) (**aqueous phase**), so that the equilibrium solvent content never exceeded 10% ACN. The dispersion was evaporated for at least 3 h at room temperature (RT) and atmospheric pressure. Afterwards, dispersions were transferred into 100 k MWCO spin filters (Pall corporation). The NP dispersions were purified and upconcentrated via centrifugation and washed with DPBSx0.1 at 1200 xg.

An NP batch consisted of 500 µl organic phase, which was dropped into 5 ml aqueous phase. The NP formulations are listed in table 4.1.

## 4.2. MATERIAL AND METHODS

Table 4.1: Basic formula for the manufacturing of a NP batch.

		NP90	EXP-NP90	NP60 <sup>*</sup>	EXP-NP60 <sup>*</sup>
Organic phase	Stock dil.				
	of	[ $\mu$ l]	[ $\mu$ l]	[ $\mu$ l]	[ $\mu$ l]
	EXP3174-PEG <sub>5k</sub> -PLA <sub>20k</sub>	-	18	-	18
	MeO-PEG <sub>5k</sub> -PLA <sub>20k</sub>	18	-	18	-
	MeO-PEG <sub>2k</sub> -PLA <sub>20k</sub>	62	62	-	-
	HOOC-PEG <sub>2k</sub> -PLA <sub>20k</sub>	-	-	62	62
PLGA <sub>13.4k</sub>	37	37	37	37	
ACN	383	383	383	383	
		[ml]	[ml]	[ml]	[ml]
Aqueous phase	DPBSx0.1	5.0	5.0	5.0	5.0

### 4.2.3 Dynamic Light Scattering

The hydrodynamic diameter of NPs was determined using a Zetasizer nano ZS (Malvern Instruments/ Herrenberg/ Germany). The concentrated NP dispersion was diluted 1:50 with 0.22  $\mu$ m-filtrated DPBSx0.1 and transferred into a single-use cuvette UV Micro ( $z = 8.5$  mm) (Carl Roth/ Karlsruhe/ Germany). The sample was illuminated with a He-Ne-laser (633 nm). Additionally the device was equipped with a narrow band filter in front of the detector. This prevented the detection of emitted light from fluorescently labeled NPs. The samples were equilibrated at 25 °C. Overall, three measurements were executed in the automatic mode. Finally the  $d_h$  and the PDI were reported.

Furthermore, the same Zetasizer nano ZS was used to determine the NP's zeta-potential. As recommended by the manufacturer, a disposable folded capillary cell (Malvern Instruments/ Herrenberg/ Germany) was filled according to the diffusion barrier technique [21]. Therefore 0.22  $\mu$ m filtered DPBSx0.1 was loaded first and the sample (5 mg ml<sup>-1</sup>) was just added to the bottom of the capillary cell. This avoids the contact of the sample with the electrodes, ensuring a reliable and reproducible measurement. Due to the moderate conductivity of the dispersant the voltage was restricted to 100 V. The sample was equilibrated at 25 °C. Overall, six measurements with twenty runs each were executed to realize changes of the samples. Finally the mean zeta-potential ( $\zeta$ -potential) was reported.

Raw data were analyzed and processed using the Zetasizer software version 7.12 (Malvern Instruments/ UK).

### 4.2.4 Nano Tracking Analysis

To measure the PNC directly a NanoSight NS300 (Malvern Instruments/ UK) was used. The samples were illuminated by a red laser (642 nm) and the scattered light was detected by a sCMOS camera. Three batches of EXP-NP90 as well as one batch of methoxy-terminated nanoparticle (NP90) with the identical TPC were manufactured. Samples were diluted 1:1000 with 0.22  $\mu\text{m}$  filtered double distilled water. This resulted in a PNC of approximately 60 particles/frame, as it is recommended for a high quality measurement. Here the *frame* describes the field of view, that is recorded by the sCMOS camera. It corresponds to an exactly defined unit (100  $\mu\text{m}$  x 80  $\mu\text{m}$  x 10  $\mu\text{m}$ ) in the sample chamber. To achieve a precise result every batch was individually diluted three times. Overall five segments of each dilution were measured after an equilibration at 25 °C for 30 s.

Raw records were analyzed by the NTA 3.1 software.

### 4.2.5 Determination of Total Polymer Content

Apart from NTA, the NP concentration was determined as the total polymer content. Therefore the PEG concentration was spectroscopically measured and converted to the total polymer content as it is described by Abstiens et. al. [3]. In brief, always three batches of NP90 and carboxy-terminated nanoparticle (NP60<sup>-</sup>) were manufactured according to 4.2.2 with one exception. Pure water was applied as the aqueous phase instead of DPBSx0.1. This was necessary to weigh out total polymer mass after freeze-drying. Purification and concentration procedure remained unchanged.

Three parts of each NP dispersion were splitted onto plastic tubes and freeze-dried, to remove water completely and weigh out the remaining polymer mass exactly. Therefore NP dispersions were frozen overnight at -40 °C in a single chamber benchtop freeze dryer Alpha 2-4 LSCplus, manufactured by the company Martin Christ (Osterode a. Harz/ Germany). Afterwards the chamber was evacuated (0.1 mbar) and the shelf temperature was raised to -30 °C for 24 h. Subsequently the shelf temperature was raised stepwise to 20 °C, while the pressure was reduced to 0.01 mbar. The whole process was finished after 90 h. Finally samples were situated in an evacuated desiccator at RT until the weight remained constant.

Concurrently the fourth part of each NP dispersion was used to perform an iodine assay according to Childs [22]. It is a complexation assay, where PEG forms a coloured complex with barium and iodine, that can be detected at 535 nm. MeO-PEG<sub>2k</sub>-OH was diluted in water (3, 6, 9, 12, 15, 18 and 21  $\mu\text{g ml}^{-1}$ ) and served as the calibration standard. The detection reagent was freshly prepared by mixing 5% (w/v) barium chloride in 1 M HCl solution ( $\frac{2}{3}$ ) and 0.05 M iodine/ potassium iodide dilution (AVS Titrimorm/ VWR/ Ismaning/ Germany) ( $\frac{1}{3}$ ). NP dilutions and calibration standards were rendered in 96-well-plate (140  $\mu\text{l}$ ). Then the detection reagent was added (60  $\mu\text{l}$ ). After 1 min incubation at RT, absorbance at 535 nm was measured with a FluoStar Omega fluorescence microplate reader (BMG Labtech/ Ortenberg/ Germany).

Finally the gravimetrically determined total polymer mass was correlated with the PEG amount, measured by the iodine assay. Under the assumption that all further NP batches provide identical NPs, the TPC can be calculated afterwards, based on an iodine assay and the obtained correlation curves.

#### 4.2.6 TEM Images and Size Analysis

NPs were manufactured according to 4.2.2 and diluted to 300 pM. Several microlitres were applied to a carbon-coat copper grid (Plano®Formavar, mesh 400) for 5 min. Afterwards dilution was removed carefully and the copper-grid was exposed for 20 s to an aqueous dilution of uranyl acetate (1 %). Several images at different positions were captured using a LIBRA®120 TEM (Carl Zeiss/Jena/ Germany). The acceleration voltage was adjusted to 90 kV.

The size of at least hundred NPs was analyzed using the ImageJ software version 1.52p. The results were plotted in a histogram and completed a distribution curve and a cumulative histogram (refer figure 4.5). Arithmetic mean and standard deviation (SD) are specified.

#### 4.2.7 Quantification of EXP3174

To quantify EXP3174 a fluorescence assay based on the procedure described by Hennig et. al. [23] was established. Samples were diluted at least 1:20 in 0.2 M acetic acid. EXP3174 (Santa Cruz/ Heidelberg/ Germany) was also diluted in 0.2 M acetic acid and served as the calibration standard (1, 3, 6, 9, 12, 15, 18 and 21 µM). Samples and standards were transferred into a white F-bottom polystyrene (PS) 96-well-plate (Greiner Bio One/ Frickenhausen/ Germany) and measured using the microplate reader Synergy Neo2 (BioTek). EXP3174 was excited at 250 nm and emitted light was detected at 370 nm. As already shown, linking of EXP3174 to PEG-chains did not change fluorescence properties [23].

### 4.3 Results and Discussion

Overall, two NP formulations turned out to be the most promising candidates. The basic composition is illustrated in figure 4.1. It should be emphasized that the targeting ligands were linked to the longer PEG chains. The NPs are intended to selectively silence AT1Rs in the ocular vasculature and inhibit pathological neovascularization. Therefore both candidates were decorated with the AT1R antagonist losartan carboxylic acid (EXP3174). EXP3174 is the NPs targeting ligand and concurrently mediates the pharmacological effect. This means that it was not necessary to encapsulate an additional drug - the NP was the pharmacon itself. The two candidates were (1) methoxy-terminated EXP-NP90 and (2) carboxy-terminated EXP-NP60. They only differed in the functional endgroup of the shorter PEG block-co-polymer (MeO-PEG<sub>2k</sub>-PLA<sub>20k</sub> vs. HOOC-PEG<sub>2k</sub>-PLA<sub>20k</sub>). The complete formulations are listed in table 4.1. The most characteristic difference between both candidates is the NP size (105 ± 13 nm vs. 68 ± 6 nm).

#### 4.3.1 Nanoparticle Analysis

Apart from the targeted EXP3174-decorated candidates, also naive non-targeted NP90 and NP60<sup>-</sup> were manufactured. The formulations were equivalent, but EXP3174-PEG<sub>5k</sub>-PLA<sub>20k</sub> was supplemented with MeO-PEG<sub>5k</sub>-PLA<sub>20k</sub>. The complete formulations are listed in table 4.1. Finally, the following core-shell NP compositions were manufactured:

- 1 NP90
- 2 EXP3174 decorated NP90 (EXP-NP90)
- 3 NP60<sup>-</sup>
- 4 EXP3174 decorated NP60<sup>-</sup> (EXP-NP60<sup>-</sup>)

The corresponding structures are depicted in figure 4.2A. The central blue sphere illustrates the NP core that is surrounded by the PEG shell. The short PEG-chains had a molecular weight (MW) of 2 kDa, while the longer PEG-chains had a MW of 5 kDa. PEG-chains depicted in black were methoxy-terminated, while light blue PEG-chains were carboxy-terminated and introduced negative charges into the inner shell. The pink triangles stand for the targeting ligand EXP3174.

The graphs of figure 4.2B show the NP size as hydrodynamic diameter, the polydispersity (PDI) and the surface charge ( $\zeta$ -potential). NP90 were  $97 \pm 11$  nm in size (N=20) with a narrow PDI of  $0.09 \pm 0.02$  and a  $\zeta$ -potential of  $-5.8 \pm 0.3$  mV. Their EXP3174-decorated equivalents (EXP-NP90) were  $105 \pm 13$  nm in size (N=20) with a narrow PDI of  $0.10 \pm 0.01$  and a  $\zeta$ -potential of  $-9.2 \pm 0.2$  mV. So EXP-NP90s were slightly larger than NP90s. The  $\zeta$ -potential is moderately negative. The reason therefore could be the use of acid-terminated PLGA. While the main PLGA chain is situated in the core, potentially the negatively charged carboxylic group orientates to the shell/dispersant interface. Apart from that, the reason for the moderately negative  $\zeta$ -potential could be found in the degradation process of the NPs. During the manufacturing process the NPs were getting in touch with the aqueous dispersant. This could already start the degradation process. Cleavage of the ester-bonds generates negatively charged carboxylic groups. Both hypotheses are plausible explanations.

NP60<sup>-</sup> were  $69 \pm 8$  nm in size (N=16) with a narrow PDI of  $0.08 \pm 0.04$  and a  $\zeta$ -potential of  $-13.2 \pm 0.6$  mV. Their EXP3174-decorated equivalents (EXP-NP60<sup>-</sup>) were  $68 \pm 6$  nm in size (N=16) with a narrow PDI of  $0.09 \pm 0.02$  and a  $\zeta$ -potential of  $-12.6 \pm 0.6$  mV. Consequently, it was possible to decrease the NP size clearly, by the exchange of uncharged MeO-PEG<sub>2k</sub>-PLA<sub>20k</sub> with negatively charged HOOC-PEG<sub>2k</sub>-PLA<sub>20k</sub>. Obviously the hydrophilicity of the polymers dictated the NP size. Besides, the introduction of the negatively charged surface groups lowered the  $\zeta$ -potential further.

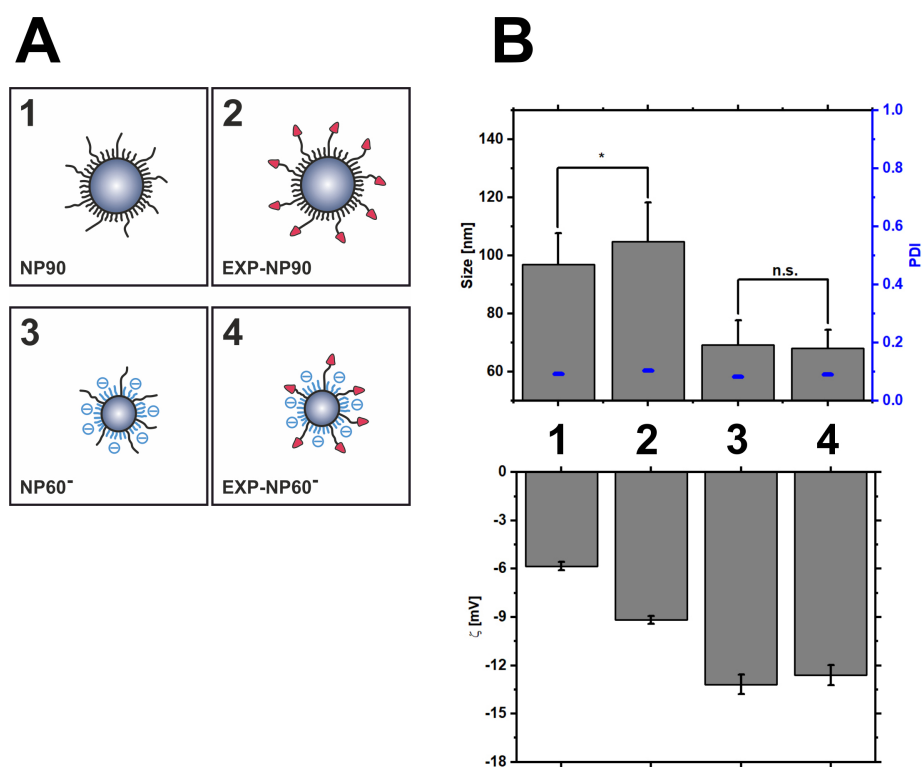


Figure 4.2: **A**: Schematic drawing of designed EXP3174-decorated methoxy-terminated - (2) and carboxy-terminated core-shell-NPs (4) as well as their non-ligand-carrying equivalents (1 and 3). **B**: Size (presented as hydrodynamic diameter  $d_h$ ), PDI (blue dashes) and  $\zeta$ -potential of the NPs. Statistical significance was tested using a two-sided t-test. (\*)  $p=0.05$ ; n.s. not significant

### 4.3.2 Nanoparticle Concentration

#### Total Polymer Content

It is quite challenging to determine the particle number concentration (PNC) exactly. That's why it is a popular method to report the NP concentration as total polymer content (TPC). Therefore the dispersant must be removed quantitatively, so that the TPC could be simply weight out. Usually NPs were prepared in pure water, freeze-dried and the remaining polymer mass was weighed out. However, this is a very time consuming process, so that this procedure was linked with a colorimetric quantification method, that is termed *iodine assay*. It allows the quantification of the PEG content and correlates with the number of NPs in the dispersion (PNC).

Initially, three individual batches of NP90 and NP60<sup>-</sup> were produced according to 4.2.2. However, pure water was used as the aqueous phase, since buffer salts would have been remained during freeze-drying. Therefore the effect of the aqueous phases DPBSx0.1 and pure water was proven. No significant changes in the NP size or the polydispersity were recognized (refer to figure 4.3A). Consequently it was possible to transfer the calibration.

The absorbance and the PEG concentration correlated over a wide concentration range (refer figure 4.3B). PEG builds a complex with barium ions and iodine that can be detected at 535 nm [22]. The correlation is linear ( $R^2 = 0.9990$ ). The determined PEG concentration was related to the weighed TPC to obtain calibration curves for both candidates (refer figures 4.3C and 4.3D). A linear relation was recognized ( $R^2 = 0.9986$  and  $R^2 = 0.9989$ ).

This means that the TPC could be calculated from the following functions:

Calibration curve for **NP90**:

$$TPC = 16.526 \times [PEG] + 0.085 \quad (4.1)$$

Calibration curve for **NP60<sup>-</sup>**:

$$TPC = 17.800 \times [PEG] - 6.262 \quad (4.2)$$

Here  $[PEG]$  is the PEG concentration in  $\mu\text{g ml}^{-1}$  obtained from an iodine assay according to 4.2.5. So TPC in  $\mu\text{g ml}^{-1}$  was calculated for NP90 and EXP-NP90 using equation 4.1 as well as for NP60<sup>-</sup> and EXP-NP60<sup>-</sup> using equation 4.2.

#### Particle Number Concentration

The gravimetric determination of the TPC is widely accepted. It offers a fundamental quantification method for polymeric NPs and the standardization of experiments. Nevertheless, it cannot report the absolute number of NPs (PNC). The comparability of experiments with NPs of different sizes was not possible.



### 4.3. RESULTS AND DISCUSSION

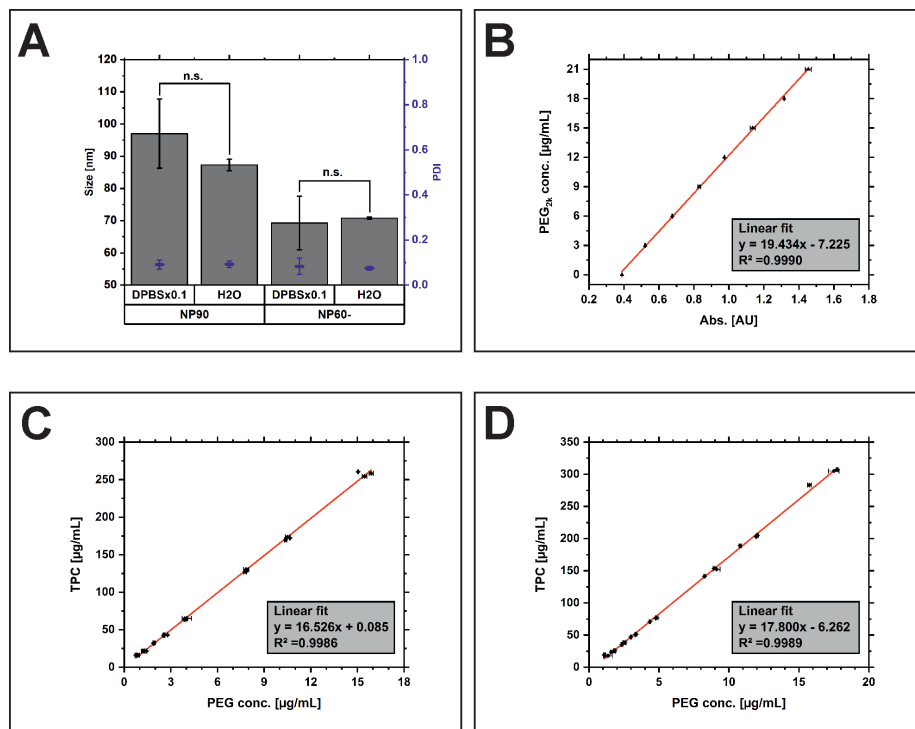


Figure 4.3: **A**: Effect of different aqueous phases (DPBSx0.1 vs. pure water) on the NP size and polydispersity (refer NP nanoprecipitation method 4.2.2. (n.s. not significant) **B**: Absorbance of PEG standards (iodine assay 4.2.5). **C**: Correlation of PEG content and NP90 TPC. **D**: Correlation of PEG content and NP60- TPC.

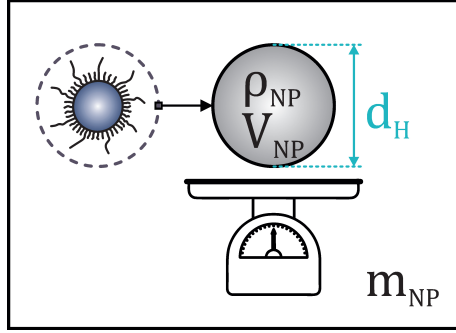


Figure 4.4: For the calculation of the PNC, NPs can be considered as an ideal sphere (grey). The mass of a single NP ( $m_{NP}$ ) can be calculated from its density ( $\rho_{NP}$ ) and its volume ( $V_{NP}$ ). To calculate  $V_{NP}$  the general formula for the volume of a sphere can be used. Therefore just the size is needed. Here the size is taken from the hydrodynamic diameter ( $d_h$ ).

This is also true for the candidates EXP-NP90 and EXP-NP60<sup>-</sup>. Hence, there was a major need for the determination of the PNC.

This issue is well-known and there are already existing basic considerations [24]. The PNC is a function of the TPC and the mass of a single NP ( $m_{NP}$ ):

$$PNC = \frac{m_{total}}{m_{NP} \times V_{Dis}} = \frac{TPC}{m_{NP}} \quad (4.3)$$

Here  $m_{total}$  is the remaining polymer mass after freeze-drying of the NP dispersion. The absence of any other additives like buffer salts is essential. That's why NPs must be manufactured in pure water, as it is already outlined above.  $V_{Dis}$  is the initial volume of the NP dispersion before freeze-drying.  $m_{NP}$  can be calculated from the NP density  $\rho_{NP}$  and its volume  $V_{NP}$ .

$$m_{NP} = \rho_{NP} \times V_{NP} \quad (4.4)$$

Considering the polymer NPs as an ideal sphere,  $V_{NP}$  can be calculated using the general formula for the volume of a sphere. The volume of a sphere is equal to  $\frac{4}{3} \pi (d/2)^3$ . The diameter of the sphere ( $d$ ) was taken from the measured hydrodynamic diameter ( $d_h$ ). For a better understanding all values are illustrated in figure 4.4.

$$m_{NP} = \rho_{NP} \times \frac{4}{3} \pi \left( \frac{d_H}{2} \right)^3 \quad (4.5)$$

### 4.3. RESULTS AND DISCUSSION

---

Combining equation 4.5 and equation 4.3 results in the following function that can be further simplified:

$$PNC = \frac{TPC}{\rho_{NP} \times \frac{4}{3}\pi \left(\frac{d_H}{2}\right)^3} = \frac{TPC}{\rho_{NP} \times \frac{1}{6}\pi (d_H)^3} \quad (4.6)$$

The unit of the resulting PNC is the number of particles per volume. The result can be converted with the Avogadro constant ( $N_A$ ) to report molar values as it is common for the avidity of NPs:

$$PNC = \frac{TPC}{\rho_{NP} \times \frac{1}{6}\pi (d_H)^3 \times N_A} \quad (4.7)$$

Equation 4.7 enables the calculation of the molar PNC. It is necessary to determine the TPC via an iodine assay the hydrodynamic diameter via dynamic light scattering (DLS).  $\rho_{NP}$  was taken from the literature. Rabanel et. al. published a  $\rho_{NP}$  of  $1.25 \text{ g cm}^{-3}$  for PEG-PLA NPs [25].

#### Error Propagation

The PNC calculation function had an immense importance for this work. But it was also necessary to be aware of their confidence range. This is the reason why the Gaussian error propagation was utilized. To this end, equation 4.7 was reduced to the error containing variables first:

$$PNC = K \times \frac{TPC}{(d_H)^3} \quad \text{by} \quad K = \frac{6}{\rho_{NP} \times \pi \times N_A} \quad (4.8)$$

According to the Gaussian error propagation the error  $s$  of  $PNC$  is given by the following function:

$$SD_{PNC} = \sqrt{\left(\frac{\partial PNC}{\partial TPC} \times SD_{TPC}\right)^2 + \left(\frac{\partial PNC}{\partial d_H} \times SD_{d_H}\right)^2} \quad (4.9)$$

A partial derivation of both parameters resulted in:

$$SD_{PNC} = \sqrt{\left(\frac{K}{(d_H)^3}\right)^2 \times (SD_{TPC})^2 + \left(\frac{-3 \times K \times TPC}{(d_H)^4}\right)^2 \times (SD_{d_H})^2} \quad (4.10)$$

Finally, equation 4.10 was further simplified and converted to receive the relative standard deviation (RSD) of each parameter:

$$\frac{SD_{PNC}}{PNC} = \sqrt{\left(\frac{SD_{TPC}}{TPC}\right)^2 + 9 \times \left(\frac{SD_{d_H}}{d_H}\right)^2}$$

$$\boxed{RSD_{PNC} = \sqrt{(RSD_{TPC})^2 + 9 \times (RSD_{d_H})^2}} \quad (4.11)$$

This means that, the error of the PNC calculation function 4.7 can be estimated with equation 4.11. It is obvious that the impact on the hydrodynamic diameter on the calculation accuracy is tremendous.

#### Error Quantification

The hydrodynamic diameter was determined via DLS and the TPC was determined according to 4.2.5. Both methods influence the accuracy of the PNC calculation method directly, while the hydrodynamic diameter was the critical parameter (refer to equation 4.11).

The hydrodynamic diameter ( $d_h$ ) is the diameter of an ideal sphere having the same diffusion coefficient according to the Stokes-Einstein equation like the observed NP itself. Thus, it includes its hydrate shell resulting in an overestimation of NP size. For a better estimation of the true NP size and the quantification of the calculation error of equation 4.7, the NP size was additionally determined from TEM images. Therefore samples were prepared and analyzed according to 4.2.6. Such microscopically size analysis techniques observe the 2D projection of single NPs. The maximum Feret diameter of all recognizable NPs was measured and the arithmetic mean specified as  $d_{TEM}$ . Additionally, the results were illustrated in figure 4.5. Particle size distributions were evaluated by means of a histogram, a distribution curve and a cumulative histogram. The size of NP90 was  $84 \pm 24$  nm (figure 4.5A) and  $84 \pm 28$  nm for the EXP3174-decorated equivalent EXP-NP90 (figure 4.5B). The distribution curve and the SD indicates a narrower particle size distribution for the non-ligand carrying NP90. The size of NP60<sup>-</sup> was  $59 \pm 19$  nm (figure 4.5C) and  $46 \pm 18$  nm for the EXP3174-decorated equivalent EXP-NP60<sup>-</sup> (figure 4.5D).

The inserts in figure 4.5 show single core-shell NPs. Uranyl acetate is known for its affinity to negative charges of nucleic acids or carboxylic groups.[26] These core-shell NPs possessed negative surface charges (refer to figure 4.2B) that originated from ester-terminated PLGA and HOOC-PEG-PLA. The contrasting agent uranyl acetate did not migrate into the inner NP, so that the core appeared clearly brighter.

### 4.3. RESULTS AND DISCUSSION

---

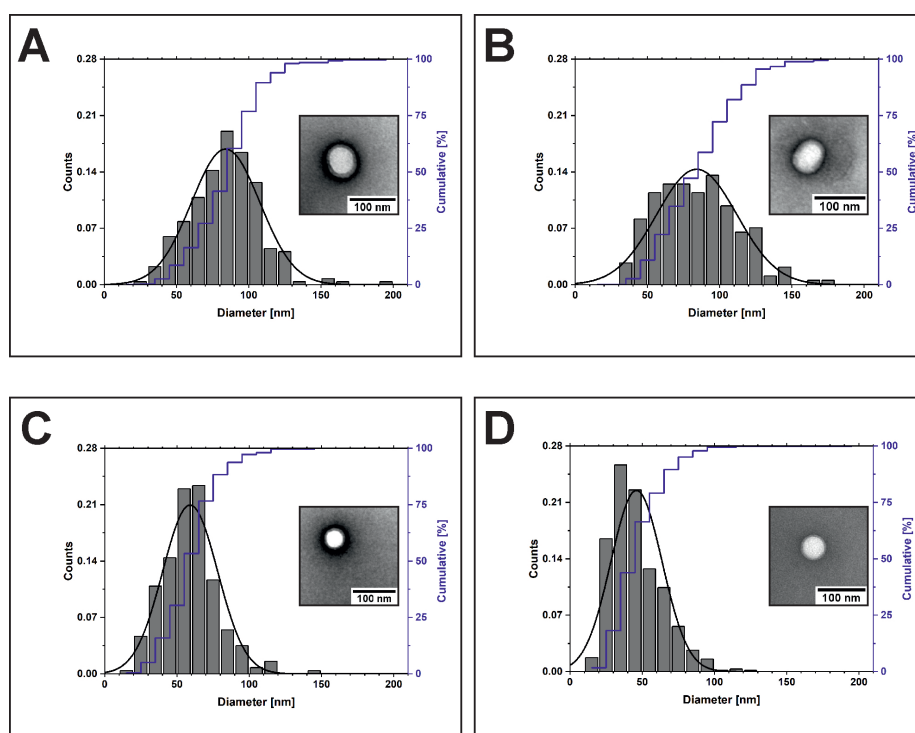


Figure 4.5: Particle size distribution and a typical TEM image (insert) of NP90 (A), EXP-NP90 (B), NP60 (C) and EXP-NP60 (D).

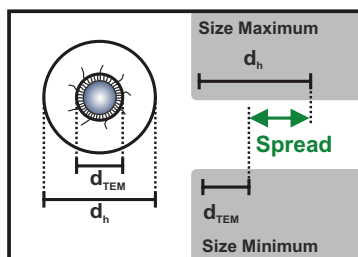


Figure 4.6: Thoughts for the derivation of the maximum size deviation (*Max. Error*, green) for the PNC calculation according to equation 4.7. The approach is referred to the  $d_h$ , because it is used for the mentioned PNC calculation. *Max. Error* is limited by  $d_{TEM}$  minus SD. The absolute values are listed in table 4.2.

In fact, the evaluation of the TEM images indicated smaller NP sizes than the DLS measurements. The values are listed in table 4.2. However, both techniques had their limitations. For one thing, DLS measurements overestimated the NP size due to the considered hydrate shell. On the other hand, PEG is a neutral polymer that cannot be stained by uranyl acetate and remains invisible in TEM images [27]. This means that the TEM-based NP size was underestimated. Consequently, the true NP size lies between the hydrodynamic diameter and the diameter based on transmission electron microscopy images ( $d_{TEM}$ ). These aspects are visualized in figure 4.6. The difference between both size values is termed *spread*. It is the maximum deviation of the NP size.

Table 4.2 lists the spread for each type of core-shell NP. In order to assess equation 4.11, the values were transformed into the RSD. Therefore the spread was normalized to  $d_h$  and listed as RSD in the last column of table 4.2. These values illustrate the maximum error in an worst-case approach. It can be assumed that the actual RSD is truly smaller.

Table 4.2: List of hydrodynamic diameter ( $d_h$ ) and TEM-based NP diameter  $d_{TEM}$ .

	$d_{TEM}$ nm	$d_h$ nm	Spread <sup>(1)</sup> nm	RSD <sup>(2)</sup> %
<b>NP90</b>	$84 \pm 24$	$109 \pm 1$	25	23
<b>EXP-NP90</b>	$84 \pm 28$	$118 \pm 1$	34	29
<b>NP60<sup>-</sup></b>	$59 \pm 19$	$90 \pm 1$	31	34
<b>EXP-NP60<sup>-</sup></b>	$46 \pm 18$	$71 \pm 1$	25	35

<sup>(1)</sup> difference between  $d_h$  and  $d_{TEM}$     <sup>(2)</sup> spread normalized to  $d_h$

In order to determine the confidence range of the TPC quantification method 4.3.2, their standard deviation  $SD_{xO}$  was estimated according to DIN 32645 [28].

$$SD_{xO} = \frac{SD_{y,x}}{b} \quad (4.12)$$

Here  $SD_{y,x}$  is the residual standard deviation for the calibration function and  $b$  is the slope of the linear correlation function. To determine  $SD_{y,x}$  equation 4.13 was used.

$$SD_{y,x} = \sqrt{\frac{\sum_{i=1}^n (\hat{y}_i - y_i)^2}{n - 2}} \quad \text{by} \quad \hat{y}_i = a + bx_i \quad (4.13)$$

Here  $\hat{y}$  is the estimated value for  $y_i$ ,  $a$  is the  $y$ -intercept of the linear correlation function,  $n$  is the number of calibration samples and  $i$  is the running number of each calibration sample. Thus the sum of squared deviations from the estimated  $y_i$ -values are the basis for the calculation of the standard deviation for the procedure  $SD_{xO}$ . It owns the same unit like the  $y$ -values. It is therefore an absolute SD. For the determination of the PNC calculation error according to equation 4.11 the RSD for TPC was needed. That's why the coefficient of variation of the procedure  $v_{xO}$  is finally calculated according to equation 4.14.

$$v_{xO} = \frac{SD_{xO}}{\bar{x}} \quad (4.14)$$

Here  $SD_{xO}$  is normalized to the mean of the  $x$ -values ( $\bar{x}$ ). The coefficient of variation was 3.5 % for the methoxy-terminated NPs NP90 and EXP-NP90 as well as 2.8 % for the carboxy-terminated NPs NP60<sup>-</sup> and EXP-NP60<sup>-</sup>.

Based on these considerations, it was possible to specify the accuracy of the PNC calculation method (equation 4.7). The values are listed in table 4.3. The accuracy of the PNC calculation was estimated in a worst-case scenario. The NP size is the critical parameter. Since the TEM imaging does not consider the PEG-shell a clearly higher accuracy can be expected.

#### Calculation Verification

The PNC can be calculated using equation 4.7. Apart from that there is another strategy to measure the PNC directly. For this purpose nanoparticle tracking analysis (NTA) is a suitable technique. Here strongly diluted dispersions were illuminated by a laser and the scattered light was visualized with a special microscope. Individual NPs appeared as fast moving spheres. The observed particle movements are caused by the Brownian motion. Tracking each motion path automatically provided a motion speed that was retraced to a hydrodynamic diameter ( $d_H$ ) via the Stokes-Einstein equation. This means that NTA

### 4.3. RESULTS AND DISCUSSION

Table 4.3: Accuracy of PNC calculation method for the core-shell NPs.

NP type	$\left(\frac{SD_{TPC}}{TPC}\right)$ (1) %	$\left(\frac{SD_{d_H}}{d_H}\right)$ (2) %	$\left(\frac{SD_{PNC}}{PNC}\right)$ (3) %
NP90	3.5	23	69
EXP-NP90	3.5	29	87
NP60 <sup>-</sup>	2.8	34	102
EXP-NP60 <sup>-</sup>	2.8	35	105

(1) RSD of TPC determination obtained from equation 4.14

(2) RSD of hydrodynamic diameter taken from table 4.2

(3) Accuracy of PNC calculation based on equation 4.11

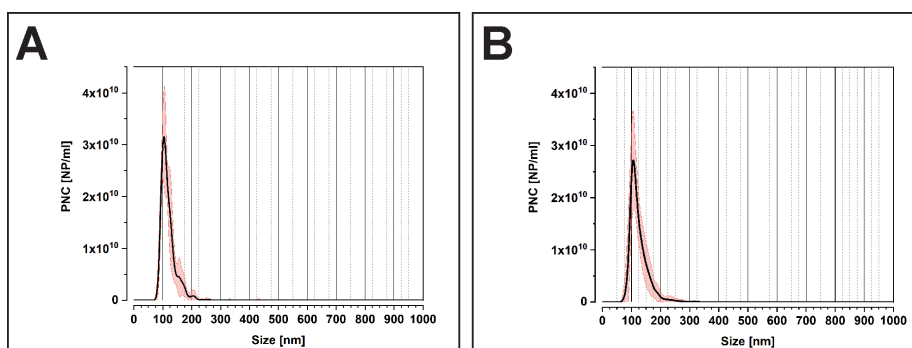


Figure 4.7: Number-weighted NP size distribution of NP90 (A) and EXP-NP90 (B) obtained from NTA measurements. Errors are indicated in red.

and DLS both rely on the light scattering properties of NPs. But DLS measurements do not resolve individual particles. The technique relies on intensity fluctuation of scattered light originating from **all** NPs passing the laser beam. Thus it is more difficult to resolve minor particle populations. The NTA based particle size distributions are plotted in figure 4.7. The hydrodynamic diameter obtained from DLS and NTA measurements are compared in table 4.4. There the discrepancy between intensity-weighted  $d_h$  and number-weighted  $d_h$  is recognizable. It is remarkable that the mode of NTA measured NP size fits very well the  $d_h$  of DLS measurements. This emphasizes the underestimation of small particle size populations in DLS measurements and explains the small difference between the two determination methods.

However, the recorded frames corresponded to an accurately defined optical unit. Therefore the number of NPs could have been related to the volume of the sample chamber and directly provided the PNC. Here the size and the PNC were determined for NP90 and EXP-NP90 using NTA to finally verify the aforementioned PNC calculation method (equation 4.7). Since the NTA software tracked single NPs it was necessary to strongly dilute the NP dispersions. High quality measurements required approximately 60 nanoparticles per frame, meaning that the NP dispersions must be diluted



### 4.3. RESULTS AND DISCUSSION

extremely. Every stock dispersion was diluted in triplicates. Then each sample dispersion was measured in quintuplicates. The procedure was extremely time-consuming, which limits its usability as a routinely quality control method.

The PNC for selected NP batches was determined with both strategies. The results are listed in table 4.4. For one thing, the PNC was calculated according to equation 4.7 that relied on DLS measurements (**Strategy A**). On the contrary, PNC was directly measured using NTA measurements (**Strategy B**). Both methods provided PNCs in the same order of magnitude. This means that the outlined calculation method (equation 4.7) was suitable to determine the PNC of core-shell NPs with a sufficient accuracy.

Table 4.4: List of calculated PNC according to equation 4.7 (**Strategy A**) and directly measured PNC (**Strategy B**).

	<b>Strategy A</b> -calculated-		<b>Strategy B</b> -measured-		
	$d_h$ nm	PNC <sup>(1)</sup> nM	mode nm	$d_h$ nm	PNC nM
<b>NP90</b>	100 ± 1	8.90 ± 6.14	104	119 ± 3	2.18 ± 0.15
<b>EXP-NP90</b>	108 ± 4	7.46 ± 6.49	106	126 ± 8	2.08 ± 0.37

<sup>(1)</sup> PNC was calculated by equation 4.7. SD originates from the RSD for NP90 and EXP-NP90 listed in table 4.3

#### 4.3.3 Further Consideration to the PEG Shell

The candidates EXP-NP90 and EXP-NP60<sup>+</sup> were designed for a therapeutic application. There is a plethora of requirements reported, that an NP formulation must fulfil, to have already the chance for a successful *in vivo* administration. Apart from NP size and  $\zeta$ -potential, the structure of the PEG shell as well as the ligand availability are often focused. Hence, this section gives further understanding for the composition of the investigated NPs.

PEG is a synthetic polymer, grafted from ethylene glycol units  $-(CH_2-CH_2-O)-$ . Each unit has a MW of  $44 \text{ g mol}^{-1}$  [29]. PEG polymers are soluble in water up to high MWs. Its hydrophilic character is exploited from a huge number of different NP types. The PEG chains cover the lipophilic NP core. They prevent agglomeration due to sterical shielding and ensure the stability of the NP dispersions. Furthermore, PEG is biocompatible and enhances blood circulation via the well-known stealth effect. In general the PEG-chains can arrange in a bulky, compact (*mushroom*) or in a stretched out conformation (*brush*) (refer to figure 4.9). There are many different parameters for the characterization of a NP's PEG shell:[30]

- weight coverage-density ( $\Gamma$ , [ $\text{g cm}^{-2}$ ]) PEG mass per surface unit
- surface chain coverage density ( $\sigma$ , [PEG/ $\text{nm}^2$ ]) number of PEG-chains per surface unit

### 4.3. RESULTS AND DISCUSSION

---

- surface coverage/ coating efficiency ([%]) percentage of surface covered by PEG
- PEG coating efficiency ([%]) percentage of surface bound PEG normalized to the total PEG amount per NP
- PEG footprint ( $S_n$ , [nm<sup>2</sup>]) projected area that is occupied by a single PEG chain
- chain distance ( $D$ , [nm]) average distance between two PEG chains
- thickness ( $t$ , [nm]) thickness of the PEG layer, surrounding the NP core

Especially,  $D$  and  $t$  in relation to the Flory radius ( $R_F$ ) of a naive PEG chain with an equal MW.  $R_F$  is illustrated in figure 4.8 and can be calculated from equation 4.15 [15, 29, 31, 32].

$$R_F = \alpha N^{3/5} \quad (4.15)$$

Here  $\alpha$  is the length of an ethylene glycol unit ( $\alpha = 3.5 \text{ \AA}$  [29]) and  $N$  is the number of ethylene glycol units per PEG polymer chain. For a 2 kDa PEG the  $R_F$  is 3.44 nm. For a 5 kDa PEG the  $R_F$  is calculated to be 5.98 nm.

If  $D$  is larger than  $R_F$  the PEG shell takes a mushroom conformation, while a  $D$  smaller than  $R_F$  would favor a brush conformation.

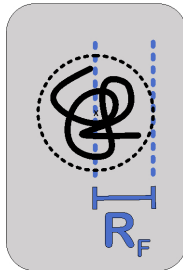


Figure 4.8: Illustration of the Flory radius  $R_F$  from a random coiled PEG chain.

Damodaran et. al. refined that allocation by adding the thickness  $t$  as another criterion. Moreover, they defined an intermediate state:[15]

**A: Mushroom**  $D > R_F$  and  $t \leq R_F$

**B: Intermediate**  $R_F < t < 2R_F$

**C: Brush**  $D < R_F$  and  $t > 2R_F$

#### PEG Footprint

Gref et. al. reported the following procedure for the determination of the PEG footprint ( $S_n$ ) [33]. They reduced each NP to an ideal sphere with the surface

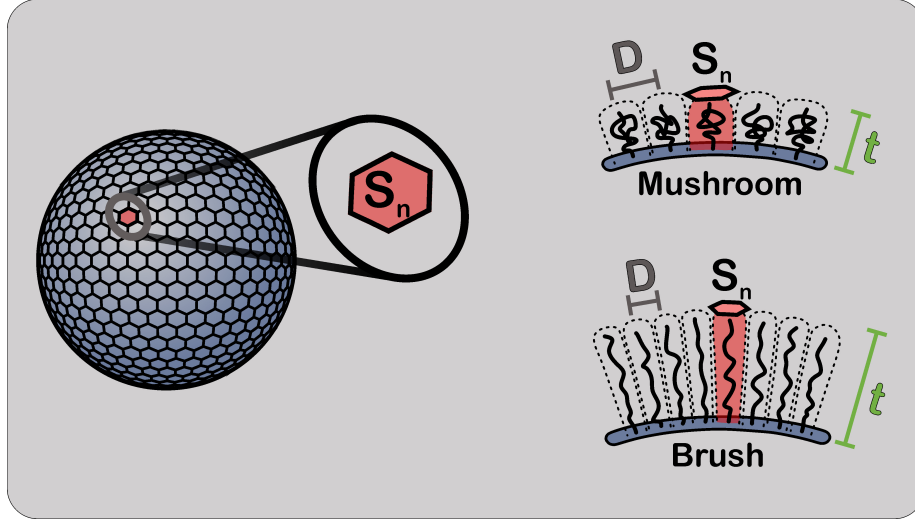


Figure 4.9: Detailed considerations about the PEG-shell of the introduced block-co-polymers NPs. **Left:** Single NP depicted as an ideal sphere. The surface of the sphere  $S$  is segmented into  $n$  identical area elements. **Right:** Conformational arrangement of PEG chains on the NP.  $D$  is the average distance between two PEG chains. The hexagon at the PEG-chains surface is a single surface area element  $S_n$ .  $t$  is the thickness of the PEG shell.

$S$ .  $S$  can be easily accessed by  $\pi (d)^2$ . Here the diameter is given by  $d_h$ , so  $S$  can be calculated from equation 4.16.

$$S = \pi (d_h)^2 \quad (4.16)$$

Then surface  $S$  was segmented into  $n$  identical area elements. This approach is visualized in figure 4.9. Each area element  $S_n$  is represented by a hexagon. The area beneath each hexagon is occupied by a single PEG-chain (red areas, figure 4.9).  $n$  is the number of hexagons per NP and concurrently the number of PEG-chains covering every NP.  $S_n$  is given by equation 4.17 [30, 31, 33]:

$$S_n = \frac{\pi (d_h)^2}{n} \quad (4.17)$$

whereas  $n$  was estimated by 4.18 [33]:

$$n = \frac{m_{NP} \times f \times N_A}{MW_{PEG}} \quad (4.18)$$

Here  $m_{NP}$  is the mass of a single NP.  $m_{NP}$  was calculated by equation 4.5, whereas  $\rho_{NP}$  was again taken from the literature ( $1.25 \text{ g cm}^{-3}$  [25]).  $f$  is the mass fraction of surface-presented PEG or rather the ratio of  $[PEG]$  and  $TPC$ . Both values were determined from an iodine assay (refer to section 4.3.2).  $N_A$

### 4.3. RESULTS AND DISCUSSION

is the Avogadro constant. Since the NPs were composed of a hybrid PEG shell a notional value of 2609 Da was estimated for  $MW_{PEG}$ . Therefore it was assumed that the molar ratio of 25 kDa to 22 kDa PEG-PLA polymers in the organic phase prior manufacturing (refer to table 4.1) and in the finished core-shell-NP were identical.

Combining equations 4.17 and 4.18 lead to the following function:

$$S_n = \frac{6 \times MW_{PEG} \times TPC}{d_h \times N_A \times [PEG] \times \rho_{NP}} \quad (4.19)$$

Equation 4.19 was eventually used to calculate the characteristic surface parameter  $S_n$  for NP90, EXP-NP90, NP60<sup>-</sup> and EXP-NP60<sup>-</sup>. The results are listed in table 4.5.

#### PEG Chain Distance

The average distance between two PEG chains  $D$  can be calculated by equation 4.20, published by Rabane et. al. [30]. The equation is valid for a circular PEG footprint area that is equal to the surface area of a hexagon  $S_n$ .

$$D = 2\sqrt{\frac{S_n}{\pi}} \quad (4.20)$$

#### Thickness of PEG

The tickness of the PEG shell  $t$  as it is illustrated in figure 4.9 was calculated using equation 4.21. This equation is commonly used for the estimation of  $t$  [30, 34].

$$t = \alpha \times N \left( \frac{\alpha}{D} \right)^{2/3} \quad (4.21)$$

#### Conformation of the PEG shell

The results of the aforementioned considerations are listed in table 4.5. As already described elsewhere, a notional value of 2609 Da was entered into equation 4.19 as  $MW_{PEG}$  since the NPs are composed of a hybrid PEG shell. The  $R_F$  of a 2609 Da PEG is 4.04 nm.

Table 4.5: Parameters for characterization of the PEG shell.

	NP90	EXP-NP90	NP60 <sup>-</sup>	EXP-NP60 <sup>-</sup>
$S_n$ <sup>(1)</sup> [nm <sup>2</sup> ]	3.58 ± 0.37	3.33 ± 0.45	5.25 ± 0.55	5.33 ± 0.43
$D$ <sup>(2)</sup> [nm]	2.13 ± 0.11	2.06 ± 0.14	2.58 ± 0.14	2.60 ± 0.11
$t$ <sup>(3)</sup> [nm]	6.19 ± 0.22	6.35 ± 0.27	5.45 ± 0.21	5.41 ± 0.16

<sup>(1)</sup> equation 4.19    <sup>(2)</sup> equation 4.20    <sup>(3)</sup> equation 4.21

### 4.3. RESULTS AND DISCUSSION

---

For the larger methoxy-terminated NP90 and EXP-NP90  $D$  was clearly smaller than  $R_F$  indicating a *brush* conformation. But  $t$  is between  $R_F$  and  $2R_F$ . This means that the PEG shell of NP90 and EXP-NP90 probably took an *intermediate* conformation.

The same conformation of the PEG shell was indicated for the smaller carboxy-terminated NP60<sup>-</sup> and EXP-NP60<sup>-</sup>. They probably appeared with an *intermediate* PEG conformation as well. Hence, both NP types do not have a true *brush*-like PEG shell, that would be beneficial regarding an *in vivo* application. It is striking that  $S_n$  of NP60<sup>-</sup> and EXP-NP60<sup>-</sup> is larger than  $S_n$  of NP90 and EXP-NP90. So the PEG chains of NP60<sup>-</sup> and EXP-NP60<sup>-</sup> need to occupy a larger area. Consequently the average distance between two PEG chains  $D$  is higher and the thickness of the PEG shell  $t$  is smaller. The difference in the composition of both NP types is just the functional end group of 2 kDa PEG. Potentially, the differences originate from the negative charge and the surrounding bulky hydrate shell.

Gref et.al. investigated adsorption of plasma proteins onto PEG-PLA NPs. They found a maximum protein reduction for blends with  $S_n = 2.1 \text{ nm}^2$  and  $D = 1.4 \text{ nm}$  [33]. Both types of NPs are characterized by a greater  $S_n$  and  $D$  than these limits. Jeon and Andrade developed a mathematical model for the interaction of globular proteins and a PEG-coated surface. They predicted an upper  $D$  limit of 1 nm for the adsorption of small proteins (40 Å in diameter) and an upper  $D$  limit of 1.5 nm for the adsorption of large proteins (120 Å to 160 Å in diameter) [35]. The calculated  $D$  values for NP90, EXP-NP90, NP60<sup>-</sup> and EXP-NP60<sup>-</sup> all exceed these limits as well.

Summing up, the PEG shell of the manufactured NPs tends to a *brush*-like conformation. But it was probably not a dense brush. According to Damodaran et. al., it can be categorized into the intermediate state, since the PEG shell thickness  $t$  does not exceed  $2R_F$  [15]. Furthermore the  $S_n$  as well as  $D$  exceed the upper limits that were known to prevent the adsorption of plasma proteins.

#### 4.3.4 Ligand Density

EXP-NP90 and EXP-NP60<sup>-</sup> were decorated with EXP3174 molecules as targeting ligands and concurrently mediating the pharmacological response. To quantify the ligand density and to estimate the average distance between EXP3174 ligands, it was relied on a fluorescence assay described in section 4.2.7. EXP3174 was covalently coupled to the PEG-PLA block-co-polymers. The absence of free EXP3174 was proven using high-performance liquid chromatography (HPLC) (refer to chapter 3). Moreover, manufactured NPs were purified via ultra-centrifugation with a very high molecular weight cut off (MWCO) of 100 kDa. This purification step was another level of security to ensure the absence of naive EXP3174 (< 1 kDa) and guarantee the validity of the fluorescence assay.

Following the approach for the estimation of the conformation of the NP's PEG shell (refer subsection 4.3.3) the average distance between EXP3174 ligands was calculated. Equally to equation 4.17 the NP surface was divided into  $l$  segments.  $l$  was the number of ligands (EXP3174 molecules) on the surface of

### 4.3. RESULTS AND DISCUSSION

a single NP.

$$S_l = \frac{\pi (d_h)^2}{l} \quad (4.22)$$

$$\text{with } l = \frac{c_{EXP}}{PNC} \quad (4.23)$$

Here  $S_l$  is the surface area available for a single EXP3174 molecule.  $l$  is the number of EXP3174 molecules per NP.  $c_{EXP}$  is the molar concentration of EXP3174. PNC as calculated from equation 4.7. The average distance between EXP3174 ligands  $D_L$  was calculated with equation 4.20:

$$D_L = 2\sqrt{\frac{S_l}{\pi}} \quad (4.24)$$

To facilitate comparability to the number of ligands (spikes) per virus,  $l$  was additionally related to the NP's surface  $S$ :

$$\Psi = \frac{l}{S} \quad (4.25)$$

Here  $\Psi$  is the number of ligands (EXP3174 molecules) per surface area. The calculated values are listed in table 4.6.

Table 4.6: Ligand density of EXP-NP90 and EXP-NP60<sup>-</sup>. (# EXP3174 molecules)

		EXP-NP90		EXP-NP60 <sup>-</sup>	
		Mean ± SD	CI 95 %	Mean ± SD	CI 95 %
$l$ <sup>(1)</sup>	[#/NP]	3500 ± 1499	[4213 ; 2788]	1017 ± 382	[1211 ; 824]
$D_L$ <sup>(2)</sup>	[nm]	3.75 ± 0.84		4.54 ± 0.98	
$\Psi$ <sup>(3)</sup>	[#/100nm <sup>2</sup> ]	10.37 ± 4.52		7.03 ± 2.97	

<sup>(1)</sup> equation 4.23    <sup>(2)</sup> equation 4.24    <sup>(3)</sup> equation 4.25

The average distance between PEG chains  $D$  was approximately half of the average distance between ligands  $D_L$ . This means that the ligand density is high. The EXP3174 ligands were intended for the targeting of AT1Rs. Maslanka et. al. estimated the diameter of the AT1R with approximately 4.6 nm [36]. Therefore they used Erickson's calculation method and reduced the AT1R to a protein with globular shape and an average specific volume of 0.73 g cm<sup>-3</sup> [37]. Despite these simplifications, it can be recognized that the distance between the ligands was in the range of the targeting receptors size.

Additionally the results can be compared to viruses, that are a kind of natural NPs. For viruses the surface located targeting sites are called spikes instead of ligands. For example, the HIV, the Influenza A virus and the hepatitis C virus (HCV) represent the full spectrum of spike density for viruses. With 0.01, 1 and 1.73 spikes /100nm<sup>2</sup> they are ranked from low to high spike density [38–40]. So the ligand density of EXP-NP90 and EXP-NP60<sup>-</sup> is clearly higher than

the spike density of viruses, that are a kind of natural blueprint for NPs. Alkilnay et. al. also recognized that many of the synthesized NPs are composed that way [41]. Currently it is not known, if a higher ligand density is beneficial. But it is known that the infectivity of HIV is quite low, due to the low spike density [41]. So the higher ligand density can be an advantage, but the spatial considerations suggest that the ligand density was rather close to a maximum value.

## 4.4 Conclusion

This chapter introduces two distinct NP formulations that were promising candidates for an *in vivo* administration. It was the aim to design a biocompatible NP formulation with the ability to target retinal and choroidal vessels as it was shown for the model NPs of Henni et. al. [1]. For this purpose it was relied on a manufacturing technique that was reported by Abstiens et. al. [3, 4]. It led to core-shell NPs that can be precisely tailored. Chapter 3 already introduced the chemistry behind the implemented block-co-polymers. In analogy to Hennig's model NPs, EXP-NP90 and EXP-NP60<sup>-</sup> possessed a PEG shell, that was decorated with EXP3174 molecules. However, the mix of longer, ligand-decorated and shorter naive PEG chains as it is illustrated in figure 4.1 was crucial for the NP design. Already the exchange of the shorter PEG's methoxy endgroup with a carboxylic endgroup reduced the absolute size from  $105 \pm 13$  nm (EXP-NP90) to  $68 \pm 6$  nm (EXP-NP60<sup>-</sup>). This means that, increasing the hydrophilicity of the block-co-polymers, decreases the size of resulting NPs tremendously. Thus, a larger and a smaller NP formulation were available for the *in vitro* and the *in vivo* testings.

Both NP species owned a negative  $\zeta$ -potential, whereas a higher absolute value was measured for EXP-NP60<sup>-</sup>. This can be easily explained by the introduced negative carboxylic endgroups. A negative surface charge is certainly beneficial, since there is a broad consensus, that positively charged particles in the sub-micrometer range bind more unspecifically to non-target cells [42–49]. The explanation therefore was thought to be found in the negatively charged cell membrane, favoring electrostatic interactions between the particle and the cell. However, there is newer literature available, pointing out the importance of the protein corona that changes the surface properties *in vivo* [50–52]. For that reason the NPs were designed with a brush-like PEG shell. But the determined parameters *PEG footprint*, *thickness* and the *chain distance* (refer to table 4.5) unveil the possibility for further improvement. There are several publications endorsing an even denser PEG brush to effectively impede the absorption of plasma proteins [33, 35]. This would be easily accessible via the reduction of the PLA block to a MW of 10 kDa.

Moreover, this chapter introduced a plethora of methods to analyze and characterize the NP formulations EXP-NP90 and EXP-NP60<sup>-</sup>. However, the outlined analysis strategies are elementarily adaptable for further NP formulations following the blueprint of these core-shell NPs. Especially to be emphasised is the development of a straightforward strategy to determine the PNC just from the TPC and the NP size. Since this relationship is an outstanding

## 4.5. REFERENCES

---

fundamental of this work, equation 4.7 is subsequently repeated:

$$PNC = \frac{TPC}{\rho_{NP} \times \frac{1}{6}\pi (d_h)^3 \times N_A}$$

Their validity was verified with a direct NP counting technique (NTA), so that this relationship is available to rapidly estimate the exact PNC. The procedure enables the comparability especially of binding experiments between the larger EXP-NP90 and the smaller EXP-NP60<sup>-</sup>.

Lastly, the ligand density was analyzed in order to optimize the targeting properties. It is possible to tailor the ligand density via the amount of EXP3174-PEG<sub>5k</sub>-PLA<sub>20k</sub> in the organic phase prior the nanoprecipitation. The considerations in section 4.3.4 gave evidence for the dense decoration of the NP surface with targeting molecules. In relation to viruses as a kind of natural NPs, maybe the ligand density could be further reduced without losing the targeting effect.

Beyond this work, it must be emphasized that it is possible to situate more than one ligand on the surface. So Fleischmann et. al. used this nanoparticulate platform and augment the EXP3174-decorated NP with an oligopeptide to enable sequential binding [53]. In addition, Maslanka et. al. performed first experiments for the encapsulation of a therapeutic drug [54]. These examples substantiate the potential of this nanoparticulate platform technology becoming a real therapeutic option. Here fundamental methods were provided to proof the quality of the NP formulations that is absolutely needed for any further pre-clinical testings.

## 4.5 References

- [1] Robert Hennig et al. "Multivalent Nanoparticles Bind the Retinal and Choroidal Vasculature". In: *Journal of Controlled Release* 220.A (2015), pp. 265–274. DOI: 10.1016/j.jconrel.2015.10.033.
- [2] W. A. Hild, M. Breunig, and A. Goepferich. "Quantum dots – Nano-sized probes for the exploration of cellular and intracellular targeting". In: *European Journal of Pharmaceutics and Biopharmaceutics* 68.2 (2008), pp. 153–168. DOI: 10.1016/j.ejpb.2007.06.009.
- [3] Kathrin Abstiens, Manuel Gregoritz, and Achim Michael Goepferich. "Ligand Density and Linker Length are Critical Factors for Multivalent Nanoparticle-Receptor Interactions". In: *ACS Applied Materials & Interfaces* 11.1 (2019), pp. 1311–1320. DOI: 10.1021/acsami.8b18843.
- [4] Kathrin Abstiens et al. "Gold-Tagged Polymeric Nanoparticles with Spatially Controlled Composition for Enhanced Detectability in Biological Environments". In: *ACS Applied Nano Materials* 2.2 (2019), pp. 917–926. DOI: 10.1021/acsanm.8b02165.



#### 4.5. REFERENCES

---

- [5] Hatem Fessi et al. "Process for the Preparation of Dispersible Colloidal Systems of a Substance, in the Form of Nanoparticles". FR2608988A1.
- [6] Hatem Fessi et al. "Nanocapsule Formation by Interfacial Polymer Deposition Following Solvent Displacement". In: *International Journal of Pharmaceutics* 55.1 (1989), R1–R4. DOI: 10.1016/0378-5173(89)90281-0.
- [7] Steven A. Vitale and Joseph L. Katz. "Liquid Droplet Dispersions Formed by Homogeneous Liquid–Liquid Nucleation: "The Ouzo Effect"". In: *Langmuir* 19.10 (2003), pp. 4105–4110. DOI: 10.1021/1a026842o.
- [8] Ganachaud François and Joseph L. Katz. "Nanoparticles and Nanocapsules Created Using the Ouzo Effect: Spontaneous Emulsification as an Alternative to Ultrasonic and High-Shear Devices". In: *ChemPhysChem* 6.2 (2005), pp. 209–216. DOI: 10.1002/cphc.200400527.
- [9] Elise Lepeltier, Claudie Bourgaux, and Patrick Couvreur. "Nanoprecipitation and the "Ouzo effect": Application to Drug Delivery Devices". In: *Advanced Drug Delivery Reviews* 71 (2014), pp. 86–97. DOI: 10.1016/j.addr.2013.12.009.
- [10] Claudia Janeth Martínez Rivas et al. "Nanoprecipitation Process: From Encapsulation to Drug Delivery". In: *International Journal of Pharmaceutics* 532.1 (2017), pp. 66–81. DOI: 10.1016/j.ijpharm.2017.08.064.
- [11] Jihye Yoo et al. "Active Targeting Strategies Using Biological Ligands for Nanoparticle Drug Delivery Systems". In: *Cancers* 11.5 (2019), p. 640. DOI: 10.3390/cancers11050640.
- [12] Niloufar Maghsoudnia et al. "Application of Nano-based Systems for Drug Delivery and Targeting: A Review". In: *Journal of Nanoparticle Research* 22.8 (2020), p. 245. DOI: 10.1007/s11051-020-04959-8.
- [13] Susanne Schoettler et al. "Protein Adsorption is Required for Stealth Effect of Poly(ethylene glycol)- and Poly(phosphoester)-Coated Nanocarriers". In: *Nature Nanotechnology* 11 (2016), pp. 372–377. DOI: 10.1038/NNANO.2015.330.
- [14] Susanne Schoettler, Katharina Landfester, and Volker Mailänder. "Controlling the Stealth Effect of Nanocarriers through Understanding the Protein Corona". In: *Angewandte Chemie Internationale Edition* 55.31 (2016), pp. 8806–8815. DOI: 10.1002/anie.201602233.
- [15] Vinod Babu Damodaran et al. "Conformational Studies of Covalently Grafted Poly(ethylene glycol) on Modified Solid Matrices Using X-Ray Photoelectron Spectroscopy". In: *Langmuir* 26.10 (2010), pp. 7299–7306. DOI: 10.1021/1a9041502.
- [16] Lauren Byrd-Leotis, Richard D. Cummings, and David A. Steinhauer. "The Interplay Between the Host Receptor and Influenza Virus Hemagglutinin and Neuraminidase". In: *International Journal of Molecular Sciences* 18.7 (2017). DOI: 10.3390/ijms18071541.
- [17] Bing Chen. "Molecular Mechanism of HIV-1 Entry". In: *Trends in Microbiology* 27.10 (2019), pp. 878–891. DOI: 10.1016/j.tim.2019.06.002.

#### 4.5. REFERENCES

---

- [18] Krishnaraju Madavaraju et al. "Herpes Simplex Virus Cell Entry Mechanisms: An Update". In: *Frontiers in Cellular and Infection Microbiology* 10 (2020), p. 617578. DOI: 10.3389/fcimb.2020.617578.
- [19] Lalitha Guruprasad. "Human Coronavirus Spike Protein-Host Receptor Recognition". In: *Progress in Biophysics and Molecular Biology* 161 (2021), pp. 39–53. DOI: 10.1016/j.pbiomolbio.2020.10.006.
- [20] Sara Maslanka Figueroa et al. "Influenza A Virus Mimetic Nanoparticles Trigger Selective Cell Uptake". In: *Proceedings of the National Academy of Sciences* 116.20 (2019). DOI: 10.1073/pnas.1902563116.
- [21] Malvern Instruments Limited. *The Diffusion Barrier Technique for Accurate and Reproducible Protein Mobility Measurement: Practical Aspects of the Diffusion Barrier Technique and How to Interpret Data (Application Note 120906)*. 2012.
- [22] C. E. Childs. "The Determination of Polyethylene Glycol in Gamma Globulin Solutions". In: *Microchemical Journal* 20.2 (1975), pp. 190–192. DOI: 10.1016/0026-265X(75)90038-7.
- [23] Robert Hennig et al. "Nanoparticle Multivalency Counterbalances the Ligand Affinity Loss upon PEGylation". In: *Journal of Controlled Release* 194 (2014), pp. 20–27. DOI: 10.1016/j.jconrel.2014.07.062.
- [24] Cong-Ying Wen et al. "Determination of the Absolute Number Concentration of Nanoparticles and the Active Affinity Sites on their Surfaces". In: *Analytical Chemistry* 88.20 (2016), pp. 10134–10142. DOI: 10.1021/acs.analchem.6b02613.
- [25] Jean-Michel Rabanel et al. "Effect of the Polymer Architecture on the Structural and Biophysical Properties of PEG–PLA Nanoparticles". In: *ACS Applied Materials & Interfaces* 7.19 (2015), pp. 10374–10385. DOI: 10.1021/acsami.5b01423.
- [26] Alberto Tiraferri and Menachem Elimelech. "Direct Quantification of Negatively Charged Functional Groups on Membrane Surfaces". In: *Journal of Membrane Science* 389 (2012), pp. 499–508. DOI: 10.1016/j.memsci.2011.11.018.
- [27] Benjamin J. Rackstraw et al. "Microscopic Investigations into PEG Cationic Polymer-Induced DNA Condensation". In: *Langmuir* 17.11 (2001), pp. 3185–3193. DOI: 10.1021/1a001456x.
- [28] Deutsches Institut für Normung e.V. *Chemische Analytik – Nachweis-, Erfassungs- und Bestimmungsgrenze unter Wiederholbedingungen – Begriffe, Verfahren, Auswertung*. DIN 32645:2008-11.
- [29] Charmainne Cruje and Devika B. Chithrani. "Polyethylene Glycol Functionalized Nanoparticles for Improved Cancer Treatment". In: *Reviews in Nanoscience and Nanotechnology* 3.1 (2014), pp. 20–30. DOI: 10.1166/rnn.2014.1042.
- [30] Jean-Michel Rabanel, Patrice Hildgen, and Xavier Banquy. "Assessment of PEG on Polymeric Particles Surface, a Key Step in Drug Carrier Translation". In: *Journal of Controlled Release* 185 (2014), pp. 71–87. DOI: 10.1016/j.jconrel.2014.04.017.

#### 4.5. REFERENCES

---

- [31] Jesse V. Jokerst et al. "Nanoparticle PEGylation for Imaging and Therapy". In: *Nanomedicine* 6.4 (2011), pp. 715–728. DOI: 10.2217/nmm.11.19.
- [32] Jillian L. Perry et al. "PEGylated PRINT Nanoparticles: The Impact of PEG Density on Protein Binding, Macrophage Association, Biodistribution, and Pharmacokinetics". In: *Nano Letters* 12.10 (2012), pp. 5304–5310. DOI: 10.1021/nl302638g.
- [33] R. Gref et al. "'Stealth' Corona-Core Nanoparticles Surface Modified by Polyethylene Glycol (PEG): Influences of the Corona (PEG Chain Length and Surface Density) and of the Core Composition on Phagocytic Uptake and Plasma Protein Adsorption". In: *Colloids and Surfaces B: Biointerfaces* 18.3-4 (2000), pp. 301–313. DOI: 10.1016/S0927-7765(99)00156-3.
- [34] Luise Tomasetti et al. "Influence of PEGylation on Nanoparticle Mobility in Different Models of the Extracellular Matrix". In: *European Journal of Pharmaceutics and Biopharmaceutics* 108 (2016), pp. 145–155. DOI: 10.1016/j.ejpb.2016.08.007.
- [35] S.I Jeon and J.D Andrade. "Protein-Surface Interactions in the Presence of Polyethylene Oxide". In: *Journal of Colloid and Interface Science* 142.1 (1991), pp. 159–166. DOI: 10.1016/0021-9797(91)90044-9.
- [36] Sara Maslanka Figueroa et al. "The Effect of Ligand Mobility on the Cellular Interaction of Multivalent Nanoparticles". In: *Macromolecular Bioscience* 20.4 (2020). DOI: 10.1002/mabi.201900427.
- [37] Harold P. Erickson. "Size and Shape of Protein Molecules at the Nanometer Level Determined by Sedimentation, Gel Filtration, and Electron Microscopy". In: *Biological Procedures Online* 11.1 (2009), pp. 32–51. DOI: 10.1007/s12575-009-9008-x.
- [38] Joshua S. Klein and Pamela J. Bjorkman. "Few and Far Between: How HIV may be Evading Antibody Avidity". In: *Public Library of Science Pathogens* 6.5 (2010). DOI: 10.1371/journal.ppat.1000908.
- [39] Masashi Yamaguchi et al. "Zernike Phase Contrast Electron Microscopy of Ice-Embedded Influenza A Virus". In: *Journal of Structural Biology* 162.2 (2008), pp. 271–276. DOI: 10.1016/j.jsb.2008.01.009.
- [40] Andreas Merz et al. "Biochemical and Morphological Properties of Hepatitis C Virus Particles and Determination of their Lipidome". In: *Journal of Biological Chemistry* 286.4 (2011), pp. 3018–3032. DOI: 10.1074/jbc.M110.175018.
- [41] Alaaldin M. Alkilany et al. "Ligand Density on Nanoparticles: A Parameter with Critical Impact on Nanomedicine". In: *Advanced Drug Delivery Reviews* 143 (2019), pp. 22–36. DOI: 10.1016/j.addr.2019.05.010.
- [42] Chunbai He et al. "Effects of Particle Size and Surface Charge on Cellular Uptake and Biodistribution of Polymeric Nanoparticles". In: *Biomaterials* 31.13 (2010), pp. 3657–3666. DOI: 10.1016/j.biomaterials.2010.01.065.
- [43] Feng Zhao et al. "Cellular Uptake, Intracellular Trafficking, and Cytotoxicity of Nanomaterials". In: *Small* 7.10 (2011), pp. 1322–1337. DOI: 10.1002/smll.201100001.

#### 4.5. REFERENCES

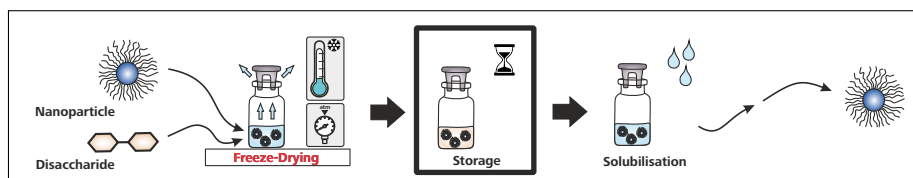
---

- [44] Ayush Verma and Francesco Stellacci. "Effect of Surface Properties on Nanoparticle-Cell Interactions". In: *Small* 6.1 (2010), pp. 12–21. DOI: 10.1002/smll.200901158.
- [45] Slavko Kralj et al. "Effect of Surface Charge on the Cellular Uptake of Fluorescent Magnetic Nanoparticles". In: *Journal of Nanoparticle Research* 14.10 (2012). DOI: 10.1007/s11051-012-1151-7.
- [46] Christoph Schweiger et al. "Quantification of the Internalization Patterns of Superparamagnetic Iron Oxide Nanoparticles with Opposite Charge". In: *Journal of Nanobiotechnology* 10 (2012). DOI: 10.1186/1477-3155-10-28.
- [47] Galya Orr et al. "Syndecan-1 Mediates the Coupling of Positively Charged Submicrometer Amorphous Silica Particles with Actin Filaments Across the Alveolar Epithelial Cell Membrane". In: *Toxicology and Applied Pharmacology* 236.2 (2009), pp. 210–220. DOI: 10.1016/j.taap.2009.01.022.
- [48] Seung-Hyun Yang et al. "Role of Surface Charge in Cytotoxicity of Charged Manganese Ferrite Nanoparticles Towards Macrophages". In: *Nanotechnology* 23.50 (2012). DOI: 10.1088/0957-4484/23/50/505702.
- [49] Zhan-Guo Yue et al. "Surface Charge Affects Cellular Uptake and Intracellular Trafficking of Chitosan-Based Nanoparticles". In: *Biomacromolecules* 12.7 (2011), pp. 2440–2446. DOI: 10.1021/bm101482r.
- [50] Valérie Forest and Jérémie Pourchez. "Preferential Binding of Positive Nanoparticles on Cell Membranes is due to Electrostatic Interactions: A too Simplistic Explanation that does not take into account the Nanoparticle Protein Corona". In: *Materials Science and Engineering: C* 70 (2017), pp. 889–896. DOI: 10.1016/j.msec.2016.09.016.
- [51] Valérie Forest, Michèle Cottier, and Jérémie Pourchez. "Electrostatic Interactions Favor the Binding of Positive Nanoparticles on Cells: A Reductive Theory". In: *Nano Today* 10.6 (2015), pp. 677–680. DOI: 10.1016/j.nantod.2015.07.002.
- [52] Moritz Nazarenus et al. "In Vitro Interaction of Colloidal Nanoparticles with Mammalian Cells: What have we Learned thus far?" In: *Beilstein Journal of Nanotechnology* 5 (2014), pp. 1477–1490. DOI: 10.3762/bjnano.5.161.
- [53] Daniel Fleischmann et al. "Adenovirus-Mimetic Nanoparticles: Sequential Ligand-Receptor Interplay as a Universal Tool for Enhanced In Vitro/In Vivo Cell Identification". In: *ACS Applied Materials & Interfaces* 12.31 (2020), pp. 34689–34702. DOI: 10.1021/acscami.0c10057.
- [54] Sara Maslanka Figueroa et al. "Thermodynamic, Spatial and Methodological Considerations for the Manufacturing of Therapeutic Polymer Nanoparticles". In: *Pharmaceutical Research* 37.3 (2020). DOI: 10.1007/s11095-020-2783-4.

## **Chapter 5**

# **Nanoparticle Stability and Freeze Drying**

## Graphical Abstract



## Abstract

Core-shell nanoparticles (NPs) are composed of biodegradable polyethylene glycol (PEG)-polylactic acid (PLA) block-co-polymers and poly(lactic-co-glycolic) acid (PLGA). These polymers are sensitive for hydrolysis, so that the degradation already starts during the manufacturing process. For non-targeted core-shell NPs a half-life of  $180 \pm 18$  days (NP90; hydrodynamic diameter  $97 \pm 11$  nm) and  $153 \pm 29$  days (carboxy-terminated nanoparticles (NP60<sup>s</sup>); hydrodynamic diameter  $69 \pm 8$  nm) was determined. Therefore a freeze-drying process to receive a stable pharmaceutical formulation was developed. It turned out that core-shell-NPs must be prepared in a buffer-free dispersion and supplemented with Sucrose (D(+)-Saccharose) (Suc) as cryoprotector. The freeze-drying protocol also enabled the formulation of targeted core-shell NPs. They retained their particle size distribution and furthermore their sub-nanomolar target avidity. This was an outstanding result, since an avidity loss (potency loss) upon freeze-drying is commonly known for various pharmaceutical market formulations.

## 5.1 Introduction

The core-shell NPs were composed of two types of polymers: (a) PEG-PLA-block-co-polymers and (b) PLGA. The monomers of the PLA block as well as PLGA are linked via ester bonds (refer to Chapter 3 for further details). Ester bonds are sensitive to water (hydrolysis), so that even the dried polymer substance must be stored in the freezer under inert gas. The degradation kinetics depends on factors like polymer architecture (PEG/PLA proportion), molecular weight (MW), crystallinity, surface-to-volume-ratio and pH-value of the surrounding dispersant [1, 2]. NPs are characterized by an especially high surface-to-volume-ratio, causing a massive vulnerability for hydrolytic degradation [3]. The interconnection of hydrophilic building blocks like PEG further increases this vulnerability [1]. Based on these considerations the NP stability has been monitored for a period of three months.

Concurrently to the ongoing stability study it was searched for a suitable stabilizing method. Since water is the reaction partner for the degradation mechanism, the quantitative removal of water was pursued. In addition, hydrolysis is a temperature sensitive reaction [4–6] facilitating a decreasing pH

(acidic reaction products) that further speeds up the degradation rate [5, 7]. Freeze-drying is a very gentle dehydration method at low temperatures. It is a common technique in the pharmaceutical field to formulate therapeutical proteins (for example vaccins, antibodies, fusion proteins or other *Biologics*) [8–11]. Freeze-drying processes include three sequential phases: (1) Freezing, (2) Primary Drying and (3) Secondary Drying [12]. The freezing phase involves a lowering of the shelf temperature (at atmospheric pressure). Water molecules crystallize below the dispersion's freezing temperature, so that the concentration of the remaining components raise continuously. The upconcentrations trigger a lot of stressors for the NPs including raise of osmotic pressure [13, 14], shift of pH [15–17] and mechanical stress (ice crystals) [18, 19]. Hence, freezing is the most critical step that was investigated via freeze-thaw experiments first. The results raised the need for the addition of a cryoprotector. Therefore especially the disaccharids Suc and D(+)-Trehalose (Tre) were identified as prominent candidates to stabilize the core-shell NP formulation [20–23].

The preliminary studies were performed using non-targeted model nanoparticles (mNPs) to design a basic freeze-drying process. Macroscopic appearance and the particle size distribution were investigated since they represented the critical quality attributes. Finally targeted core-shell NPs were freeze-dried according to the designed protocol. Radioligand binding assays were additionally performed to investigate the target avidity of freeze-dried core-shell NPs.

## 5.2 Material and Methods

### 5.2.1 Material

Sucrose (D(+)-Saccharose) (Suc) was purchased in molecular biology grade from VWR Chemicals (Electran®/ VWR International/ Ismaning/ Germany). D(+)-Trehalose (Tre) was purchased in biochemical grade from Carl Roth (Karlsruhe/ Germany). All other chemicals were purchased from Sigma-Aldrich (Taufkirchen/ Germany), if not stated otherwise. A Milli-Q purification system (Millipore/ Schwalbach/ Germany) was used to prepare fresh ultrapure water. It is hereinafter just named water.

### 5.2.2 Manufacturing and Quality of Nanoparticle Dispersions

The core-shell NPs were manufactured via nanoprecipitation as it is described in section 4.2.2. The pre-studies were performed using model nanoparticles (mNPs) that were manufactured from a modified organic phase:

- 88  $\mu\text{l}$  MeO-PEG<sub>5k</sub>-PLA<sub>20k</sub> (40 mg ml<sup>-1</sup>)
- 37  $\mu\text{l}$  PLGA<sub>13.4k</sub> (40 mg ml<sup>-1</sup>)
- 375  $\mu\text{l}$  acetonitrile (ACN).

This organic phase was injected into 5 ml of diluted Dulbecco's Phosphate Buffered Saline (x0.1) (DPBSx0.1) (mNP<sub>DPBSx0.1</sub>) or water (mNP<sub>H<sub>2</sub>O</sub>). This means that the mNPs were exclusively composed of block-co-polymers with 5 kDa PEG. The overall molar ratio of block-co-polymer to PLGA was kept.

## 5.2. MATERIAL AND METHODS

---

The PEG content was determined via an iodine assay and correlated to the total polymer content (TPC) as it is described in section 4.2.5. MeO-PEG<sub>5k</sub>-OH served as reference standard.

The manufacturing procedure of targeted core-shell NPs (EXP3174 decorated NP90 (EXP-NP90) and EXP3174 decorated NP60<sup>-</sup> (EXP-NP60<sup>-</sup>)) as well as their non-targeted equivalents (methoxy-terminated nanoparticle (NP90) and NP60<sup>-</sup>) is described in section 4.2.2. However pure water was used as aqueous phase. This means that the NP dispersions were manufactured in a buffer-free dispersant. The quality attributes were determined according to the methods 4.2.3, 4.2.5 and 4.2.7 prior to the addition of the cryoprotectors.

### 5.2.3 Nanoparticle Size Characterization

NP size was determined via dynamic light scattering (DLS). The method is outlined in section 4.2.3. The actual hydrodynamic diameter was normalized to the initial  $d_h$ . This means that an increasing ratio indicated particle growth. In addition, the polydispersity index (PDI) and the derived count rate (DCR) were examined. The DCR correlates with the NP concentration.

A constant particle size distribution served as stability indicator. Viscosity correction has been waived, since the normalized parameters (ratios) were specified. The sublimated water was precisely supplemented after freeze-drying to ensure the comparability.

### 5.2.4 Freeze-Thaw

Lyophilization vials were filled with 2.0 mL NP-dispersion each. The final polymer concentration was 1.0 mg mL<sup>-1</sup>. Dispersions were supplemented without any additives (buffer-free) but the cryoprotector (10 %, 15 % and 20 % Tre or 2 %, 5 % and 10 % of Suc). Afterwards the samples were freeze-dried according to different protocols listed in table 5.1.

Table 5.1: List of the freezing protocols

Protocol	Temperature		Duration
G1	-20 °C	freezer	overnight
G2	-40 °C	pre-cooled shelves	overnight
G3	-80 °C	ultra-freezer	overnight
G4	-196 °C	liquid nitrogen	6.0 min

Subsequently, NP-dispersions were thawed at room temperature (RT) and visually checked. Eventually, the stability of the NP dispersions was proven as described above (refer to section 5.2.3).



### 5.2.5 Lyophilization Process

For the freeze-drying experiments the single-chamber bench-top freeze dryer Alpha 2-4 LSCplus, manufactured by the company Martin Christ (Osterode am Harz, Germany) was used. The freeze-drying protocol is listed in table 5.2.

Table 5.2: Freeze-drying protocol for core-shell NPs.  $T$  is the shelf temperature and  $P$  is the chamber pressure.

		Freezing	Primary Drying			Secondary Drying	
Total	hh:mm	10:45	11:45	13:15	61:15	63:15	81:15
Segment	hh:mm	10:45	01:00	01:30	48:00	02:00	18:00
$T$	°C	-40	-40	-	-25	-	20
$\Delta T$	$\frac{^{\circ}\text{C}}{\text{min}}$	-	-	$\frac{1}{6}$	-	$\frac{3}{8}$	-
$P$	mbar	atm	-	0.05	0.05	0.05	0.05
$\Delta P$	$\frac{\text{mbar}}{\text{min}}$	-	16.67	-	-	-	-

### 5.2.6 Radioligand Binding Studies

The avidity of targeted core-shell NPs was investigated via radioligand binding studies. Therefore, core-shell NPs (EXP-NP90 and EXP-NP60<sup>-</sup>) were decorated with the angiotensin II receptor type 1 (AT1R) antagonist losartan carboxylic acid (EXP3174) and tested at AT1R-positive rat mesangial cells (rMCs). The competition binding experiments were performed as it is described in section 6.2.7. Cryoprotectors of the freeze-dried NP dispersions were quantitatively removed via ultra-centrifugation. This means that the radioligand binding studies were performed with aqueous NP dispersions without any additives like cryoprotectors or buffer salts. The particle number concentration (PNC) was calculated with equation 4.7 in accordance with section 4.3.2.

## 5.3 Results and Discussion

### 5.3.1 Nanoparticle Stability

The core-shell NPs consisted of biodegradable building blocks. Their ester bonds could be cleaved in an aqueous environment autocatalytically or enzymatically [24]. For one thing, the biodegradability prohibits NP accumulation after multiple administration. But the degradation already started in *status nascendi* and limited the shelf life essentially. To illustrate the long-term stability NPs size, PDI and DCR have been monitored over 100 days.

The results are plotted in figure 5.1. The hydrodynamic diameter (figure 5.1A) and the PDI (figure 5.1B) increased only slightly during the incubation period. Additionally, a second population in the particle size distribution was growing and indicated particle agglomeration. Storage at 4 °C favours agglomeration, due to the reduced NP mobility at lower temperatures. Moreover, the particle size distribution (PDI) was broadening even after 30 days of incubation.

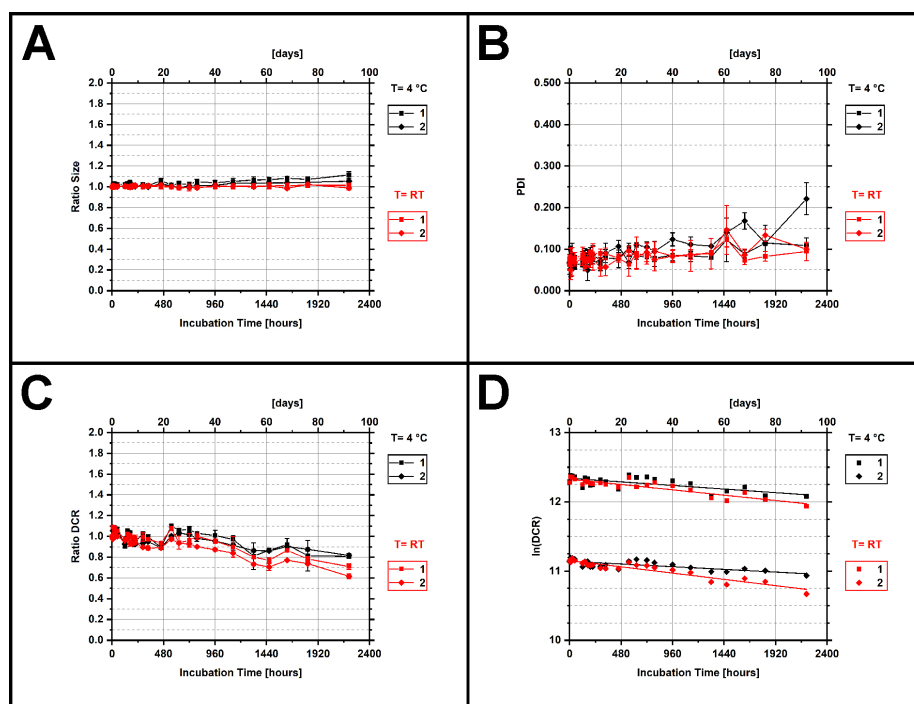


Figure 5.1: Long-term stability of NP90 at 4°C (1, black) and RT (1, red) as well as NP60 at 4°C (2, black) and RT (2, red). A: Ratio of the hydrodynamic diameter ( $d_h$ ) at time point  $t$  and initial  $d_h$ . B: PDI of NP dispersion. C: Ratio of the DCR at time point  $t$  and the initial DCR. D: Semi-logarithmic of DCR- $t$ -plot.

### 5.3. RESULTS AND DISCUSSION

DLS detects photons, that particles scatter after illumination with a laser. The number of detected photons is given by the count rate (kilo counts per second/ kcps), that correlates linearly with the PNC in a certain range [24, 25]. To obtain valid measurement results the software automatically adjusts the count rate using light filters attenuating the emitted laser light. Each light filter has an attenuation factor that enables the calculation of the DCR. The DCR is the count rate that would be obtained at 100 % laser power. The DCR ratios ( $\text{DCR}_t/\text{DCR}_0$ ) are depicted in in figure 5.1C. The decline correlated with the degradation of the NPs. Two substrates, the biodegradable polymer and water are involved in the cleaving reaction. Water is the main compound of the dispersant and present in a huge excess. Consequently, the PNC is decisive for the degradation speed. Therefore the degradation process could be described by first order kinetics (pseudo-first order kinetics):

$$-\frac{dC}{dt} = k \cdot C \quad (5.1)$$

$$C_t = C_0 \cdot e^{-k \cdot t} \quad (5.2)$$

$$\ln(C_t) = \ln(C_0) - k \cdot t \quad (5.3)$$

$$T_{1/2} = \frac{\ln(2)}{k} \quad (5.4)$$

Equation 5.1 is the rate law for a first order kinetics, where  $\frac{dC}{dt}$  is the concentration change of the substrate per time,  $k$  is the rate constant and  $C$  is the concentration of the substrate. Integration of the rate law between 0 and  $t$  leads to the rate equation 5.2 that can be linearized using the natural logarithm (equation 5.3). To determine  $k$ , a semi-logarithmic DCR- $t$ -plot was provided (refer to figure 5.1D). The half-life was calculated using equation 5.4. Table 5.3 lists the determined half-life of NP90 and NP60<sup>-</sup> at 4 °C and RT.

Table 5.3: Half-life  $t_{1/2}$  of non-targeted core-shell NPs.

NP type	Incubation Temperature	$k[\text{h}^{-1}]$	$t_{1/2}[\text{d}]$
NP90	4 °C	$-1.08 \cdot 10^{-4}$	$267 \pm 58$
NP90	RT	$-1.60 \cdot 10^{-4}$	$180 \pm 18$
NP60 <sup>-</sup>	4 °C	$-0.81 \cdot 10^{-4}$	$355 \pm 70$
NP60 <sup>-</sup>	RT	$-1.89 \cdot 10^{-4}$	$153 \pm 29$

The degradation of the NPs slowed down, if NP dispersions were stored at 4 °C. That's why an intermediate storage in the fridge was recommended. However, NP s reveal a very short shelf life. Even after 6 months at RT or 1 year at 4 °C more than 50 % were degraded.

However, the absolute values are of limited reliability, because the DCR is a

strongly fluctuating parameter. It is influenced by the NP's size and surface morphology [26]. Both parameters are influenced during the degradation process. Zolnik and Burgess investigated the degradation of PLGA microspheres at neutral and acidic conditions [27]. At neutral pH water diffuses into the PLGA core - the particles are swelling and change their size. Due to the presence of water, ester bonds are progressively cleaved to lactic and glycolic acid. The cleavage products lower the pH in the PLGA core, accelerating the degradation process until the integrity of the particle is lost [26]. This degradation mechanism was already reported for MeO-PEG-PLGA NPs. Avgoustakis et. al. incubated MeO-PEG-PLGA NPs in phosphate buffered saline (pH=7.4). They were able to detect degradation products like lactic acid after a few days already [28].

Since NP90 and NP60 were composed of PEG-PLA block-co-polymers and PLGA, it was expected that the degradation process was quite similar. However, surface bound PEG was fixed via ester bonds and could be cleaved as well. This means that the targeted core-shell NPs lost both, the sterical stabilization and the surface bound ligands, resulting in agglomeration and the loss of the targeting effect. This was another instability that could not be detected via DLS. Consequently, an even shorter shelf life must be hypothesized.

The results clearly indicated the need of developing a gentle method to remove the entire water from the NP dispersion and extend the shelf life. Freeze-drying is an excellent method for that purpose. Additionally, there is a plethora of literature concerning freeze-drying of polymer-based NPs offering excellent starting points for the development of a freeze-drying formulation [20, 22].

#### 5.3.2 Freeze-Thaw

##### Pure Nanoparticle Dispersions

The freezing step is pivotal to ensure NP integrity during freeze-drying [29, 30]. It affects NPs stability rather more than the following drying steps [31]. That's why NP dispersions were frozen according to different freezing protocols **G1** - **G4** (refer to table 5.1). Higher freezing temperatures result in a moderate freezing rate, slight supercooling and less crystallisation nuclei. Ostwald ripening builds up larger crystals, leaving larger pores after sublimation so that the lyophilization process is much faster. However, the described processes went along with a tremendous upconcentration of the components in the unfrozen phase [8, 12]. This concerns both buffer salts as well as NPs itself and favors agglomeration. Quench-freezing in liquid nitrogen (**G4**) can limit this upconcentration and is known to be beneficial for freeze-drying of polymer-based NPs in certain cases [30, 32].

Taking these considerations into account, mNPs were manufactured in pure water (mNP<sub>H<sub>2</sub>O</sub>) and DPBSx0.1 (mNP<sub>DPBSx0.1</sub>). Both mNP species were characterized by a monomodal super narrow particle size distribution, as shown in figure 5.2. The hydrodynamic diameter of mNP<sub>H<sub>2</sub>O</sub> was  $63 \pm 1$  nm and the PDI was  $0.086 \pm 0.034$ . For mNP<sub>DPBSx0.1</sub> hydrodynamic diameter ( $d_h$ ) was  $62 \pm 1$  nm and the PDI was  $0.103 \pm 0.022$ . This means that the chosen aqueous phase did not alter the particle size properties of mNP.

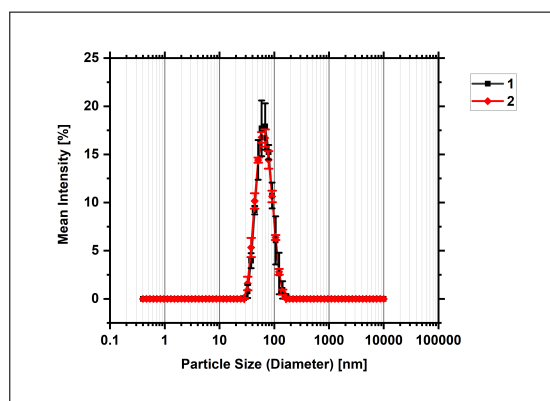


Figure 5.2: Intensity-weighted particle size distributions of  $mNP_{H_2O}$  (1, black) and  $mNP_{DPBS \times 0.1}$  (2, red).

Then,  $mNP_{H_2O}$  and  $mNP_{DPBS \times 0.1}$  were frozen according to the different freezing protocols (**G1** - **G4**) (refer to table 5.1) and afterwards thawed at RT. In figure 5.3 the intensity-weighted particle size distributions for the  $mNP_{H_2O}$  (**A**) and the  $mNP_{DPBS \times 0.1}$  (**B**) are depicted. The change in  $mNP$ 's size after freezing and thawing is clearly visible by the stacked lines (red: **G1**, blue: **G2**, green: **G3** and purple: **G4**) in reference to the corresponding  $mNP$  dispersion before freezing (black). The maxima shifted to larger values, the particle size distribution showed broadening or a second population.

This means that the mechanism of particle enlargement was different. For buffer-free dispersions ( $mNP_{H_2O}$ ) a second population was growing with decreasing freezing temperature (refer to figure 5.3A). After freezing in liquid nitrogen (**10G4**) the initial population was completely vanished. The observed trend indicated an agglomeration of  $mNPs$ . The macroscopic evaluation confirmed the DLS measurements. Prior freezing the  $mNP$  dispersion was clear up to slightly opalescent. After thawing all dispersions went turbid. Additionally, large flakes occurred at lower freezing temperatures.

The buffer containing dispersions ( $mNP_{DPBS \times 0.1}$ ) showed a broadening of particle size distribution from **20G1** to **20G4** (refer to in figure 5.3B). **20G1** showed a monomodal particle size distribution as well. However, the hydrodynamic diameter and the PDI were raising from  $63 \pm 1$  nm (**20**) to  $69 \pm 1$  nm and from  $0.078 \pm 0.012$  to  $0.135 \pm 0.021$ . The broadening suggests that particles coalesce instead of agglomerate. Besides these dispersions went turbid after thawing as well.

During the freezing process pure ice crystals occur initially. Hence, the concentration of the components in the remaining liquid phase raised continuously. This favored the agglomeration or coalescence of  $NPs$ . Stronger freezing rates caused deeper supercooling and a higher amount of ice nuclei [18, 19]. These ice crystals exerted mechanical stress to the  $NPs$  and may be one reason for the rise in size at lower freezing temperatures. Besides, the upconcentration of buffer salts caused a tremendous raise of the osmotic pressure. For example, the concentration of isotonic saline solutions undergo an up to 20-fold in-

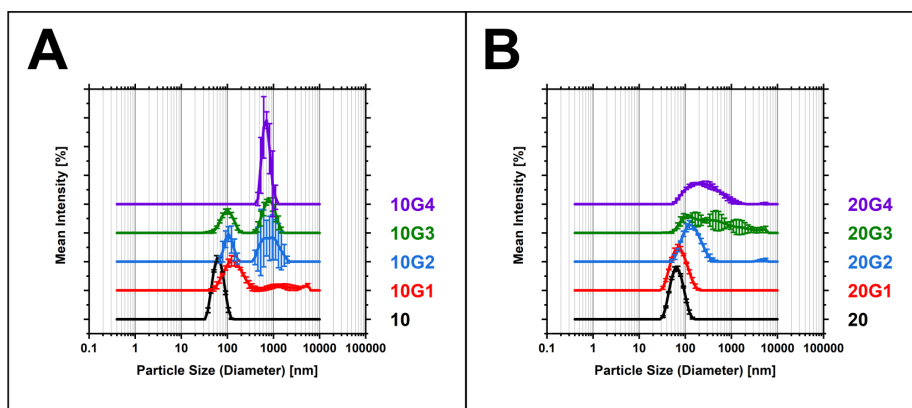


Figure 5.3: Intensity-weighted particle size distributions of mNP<sub>H2O</sub> (A) and mNP<sub>DPBSx0.1</sub> (B): Before freezing as a reference (black) and after freezing according to G1 (red), G2 (blue), G3 (green) and G4 (purple).

crease during freezing [13]. Rabanel et. al. determined the critical coagulation concentration of PEG-PLA NPs [14]. Their results illustrate the sensitivity to osmotic pressure. Apart from that, buffer salts can precipitate separately, due to unequal solubility. Depending on the particular buffer salt, this results in a considerable pH shift. A prominent example is phosphate buffer. Their pH of a neutral solution dropped under 4 while freezing [15–17]. Since mNP as well NP90 and NP60<sup>-</sup> consist of ester-based polymers, they are sensitive to pH shifts. Summing up, there existed several plausible explanations for the instability of mNP<sub>H2O</sub> and mNP<sub>DPBSx0.1</sub>. It was not the aim of this work to understand the instability mechanism in detail. In fact, this study showed the need of cryoprotectors to ensure NP's integrity.

#### Disaccharides as Cryoprotectors

To avoid instabilities a cryoprotector must be added to mNP<sub>H2O</sub> and mNP<sub>DPBSx0.1</sub> dispersions. A plethora of suitable cryoprotectors are described in literature. For NPs with a PEG shell, disaccharides like Suc and Tre are most popular [20]. Hence, mNP<sub>H2O</sub> and mNP<sub>DPBSx0.1</sub> were supplemented with Suc or Tre in common concentrations.

The results are plotted in figure 5.4. In general, neither Suc nor Tre were able to conserve the size of mNP<sub>DPBSx0.1</sub> during freezing. At a maximum the mean NP's size increased 18-fold. The size properties were substantially better for the Suc supplemented mNP<sub>DPBSx0.1</sub> dispersions. But they were also unstable, except for the two samples frozen at  $-80^{\circ}\text{C}$  (2S5G3 and 2S10G3).

However, the buffer-free mNP<sub>H2O</sub> dispersions were stable, apart from samples supplemented with only 2% Suc and some samples with high sugar concentration, frozen at only  $-20^{\circ}\text{C}$  (1S10G1, 1T15G1 and 1T20G1).

Summing up, mNPs must be prepared buffer-free, supplemented with 5% to 10% Suc or 10% to 20% Tre to survive freezing at not more than  $-40^{\circ}\text{C}$ .

5.3. RESULTS AND DISCUSSION

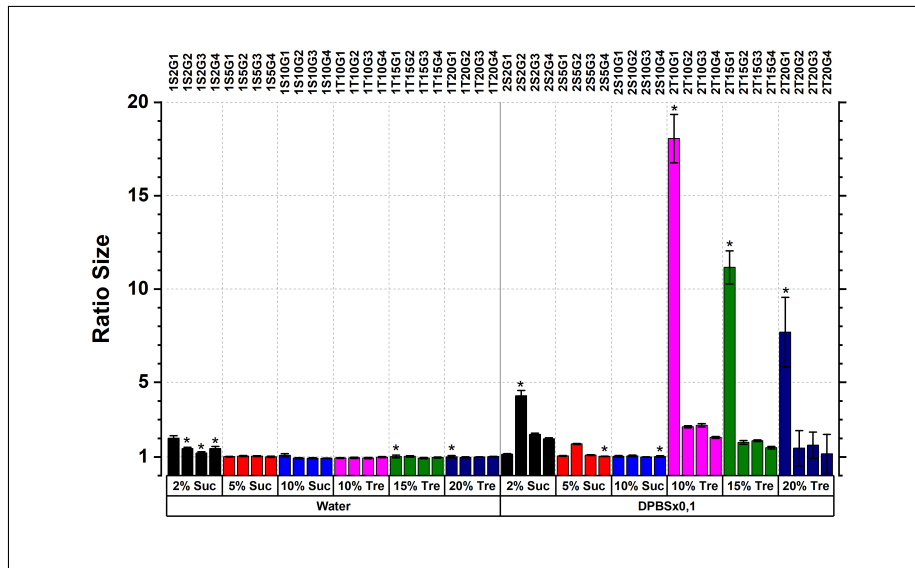


Figure 5.4: Ratios of hydrodynamic diameter ( $d_h(t)/d_h(0)$ ). A size ratio of 1.00 indicated no size changes. The results for  $mNP_{H_2O}$  are plotted on the left side ('water') and for the  $mNP_{DPBSx0.1}$  on the right side ('DPBSx0.1'). Both mNPs were supplemented with Suc (2%, 5% and 10%) or Tre (10%, 15% and 20%). The same bar colour highlights the same excipient in the same concentration. Each testing group was separately treated according to the freezing protocols **G1-G4** (refer to table 5.1). Asterix (\*) indicates a second population in the particle size distribution.

A deeper understanding of these results is given by binary Suc-water and Tre-water mixtures. The addition of disaccharids decreases the freezing temperature ( $T_f$ ) and raises the glass transition temperature ( $T_g$ ) compared to pure water [33]. During freezing of unsaturated Suc- and Tre-dilutions, pure water crystals appear first. The remaining liquid phase concentrates until it reaches the concentration of the maximal freeze-concentrated dispersion ( $w'$ ). Further freezing leads to the complete solidification of the dispersion that is characterized by the glass transition temperature of the maximal freeze-concentrated dispersion ( $T'_g$ ). For binary Suc-water mixtures  $w'$  is  $-85\%$ (w/w) and  $T'_g$  is  $-32\text{ }^\circ\text{C}$  [12]. It is absolutely necessary to keep the product temperature below  $T'_g$  for the whole primary drying of a lyophilization process to keep the dispersion in a glassy state. In the context of these freeze-thaw experiments it explains why a  $T_f$  of  $-20\text{ }^\circ\text{C}$  (**G1**) usually led to instabilities. Besides it means that these dispersions were not completely frozen. So some samples could appear to be stable in this experiments without being completely frozen so far. Consequently, freezing the mNP dispersions on the pre-cooled shelves at  $-40\text{ }^\circ\text{C}$  is the most recommended way for the following lyophilization process.

#### 5.3.3 Freeze-Drying of Model Nanoparticles

Combining literature values [34] and the results of section 5.3.2 a lyophilization protocol was designed. The mNP dispersions were frozen on the pre-cooled shelves of the freeze dryer at  $-40\text{ }^\circ\text{C}$ . Additional lavish preconditioning like freezing in an external freezer or in liquid nitrogen was not necessary. For further formulation development, it was focused on buffer-free mNP<sub>H2O</sub> dispersions that were supplemented with Suc (5 % or 10 %) or Tre (10 %, 15 % or 20 %).

However, in this study the effect of different NP concentrations was investigated. Each experimental group contained  $0.1\text{ mg ml}^{-1}$ ,  $0.5\text{ mg ml}^{-1}$ ,  $1.0\text{ mg ml}^{-1}$ ,  $2.5\text{ mg ml}^{-1}$  or  $5.0\text{ mg ml}^{-1}$  of mNPs. In the top box of figure 5.5 photographs of the whole 10 % Suc sample series are depicted. They are arranged in five columns, representing the increasing mNP concentration. Assessing the mNP dispersions immediately before the freezing step (first row - *Initial*), the increasing turbidity was obvious. The higher the NP concentration the more intense is scattered light. After freeze-drying the remaining cake of all samples showed shrinkage (second row - *Lyophilized*). Finally, the sublimated water was exactly supplemented (third row - *Redispersed*) and the cake vanished completely. The degree of turbidity for each sample was similar to the initial dispersion. But after redispersing bubbles up to a clear foam was left and its volume raised by increasing mNP concentration. The core-shell NPs were surface-active and occupied the interface like a surfactant.

This effect was only moderately visible for the 10 % Suc test dispersions, but more intense for the Tre samples (refer to the bottom box of figure 5.5). Additionally, the turbidity of the dispersions with  $\geq 1.0\text{ mg ml}^{-1}$  increased dramatically. The raise of turbidity indicated a clear instability that was observed for most of the Tre samples.

Apart from the macroscopic appearance the particle size distributions were checked via DLS. The results are plotted in figure 5.6. Changes of the hydro-



### 5.3. RESULTS AND DISCUSSION

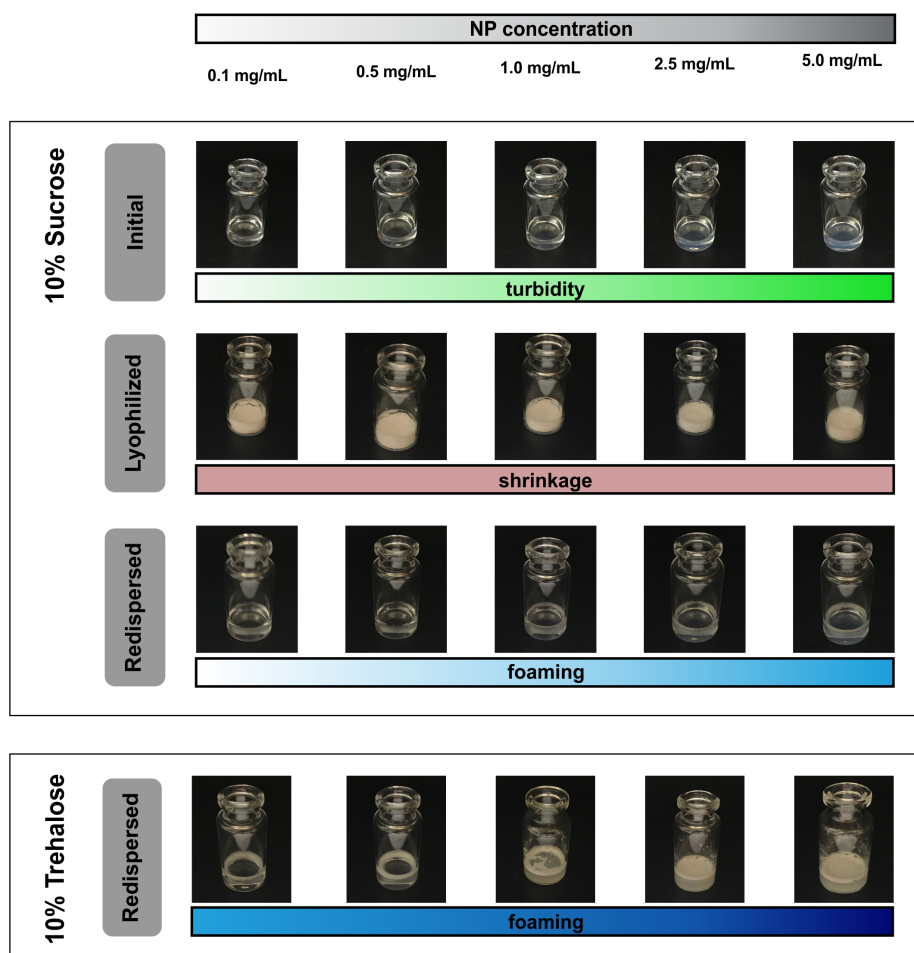


Figure 5.5: Photographs of the mNP dispersions in different process stages. The photographs are sorted in increasing NP concentration. In the **top box** the full set of 10 % Suc samples are depicted: mNP dispersions prior freeze-drying (**'Initial'**), remaining cakes after freeze-drying (**'Lyophilized'**) and redispersed samples (**'Redispersed'**). The Tre samples showed a much more intense foaming. In the **bottom box** the redispersed 10 % Tre samples are depicted.

dynamic diameter (**A**) and the PDI (**B**) are indicated by a ratio divergent from 1.0. If the ratio exceeded 1.0, mNPs raised in size or PDI. Bars, highlighted by an asterix (\*), indicate a second population in the particle-size distribution that was larger than the initial mNPs population. Tre was not suitable to stabilize the mNPs during freeze-drying. As already mentioned above, Tre samples underwent macroscopic changes. This observation was confirmed by the DLS measurements. An increasing size ratio, a second larger NP population and/or an increasing PDI ratio were observed for all tested dispersions. Consequently, pure Tre was not suitable as cryoprotector.

However, Suc turned out to be a much better candidate for cryoprotection. Even though mNP dispersions supplemented with 5 % Suc still showed a weak second population and a raise in the PDI ratio for the lower mNP concentrations (**1S5-01**, **1S5-05** and **1S5-10**), it has already been able to conserve the size properties of concentrated mNP dispersions **1D5-25** and **1S-50**. Nevertheless 10% Suc provided the best results. All examined parameters remained unchanged during the freeze-drying process across the investigated NP concentration range (**1S10-01** up to **1S10-50**). That's why 10% Suc were chosen for the further freeze-drying studies. Photographs of this entire sample series are plotted in the top box of figure 5.5.

#### 5.3.4 Freeze-Drying of Targeted Core-Shell Nanoparticles

The freeze-drying process was transferred to the targeted EXP3174-decorated EXP-NP90 and EXP-NP60<sup>-</sup>. There is a plethora of literature available, dealing with freeze-drying of various types of NPs, including polymer [22, 35, 36], lipid [37, 38] or inorganic [39, 40] NPs. But the majority is just focused on the NPs size characteristics. It is popular to encapsulate an active pharmaceutical ingredient (e.g. small molecules and biologicals) and monitor its biological activity. Here EXP3174 was the surface-presented targeting ligand. Therefore, the particle-size distribution and the avidity to AT1R-positive rMCs prior and after freeze-drying was investigated. In a worst-case scenario the targeting molecules could vanish irreversibly in the PEG shell or the inner NP. In this case the targeted core-shell NPs may lose their targeting effect upon freeze-drying. Consequently, the targeting effect was proven via radioligand binding studies in addition to the conventional particle size analytics.

The results are summarized in figure 5.7. Besides the targeted EXP-NP90 (**2**) and EXP-NP60<sup>-</sup> (**4**) as well as their non-targeted equivalents NP90 (**1**) and NP60<sup>-</sup> (**3**) were studied. The top box shows photographs of the targeted NP dispersions (refer to figure 5.7A). The first photograph per triplicate is the initial dispersion supplemented with 10 % Suc, prior the freeze-drying process (**2a** and **4a**). As already recognized in figure 5.5 these dispersions were slightly turbid, due to the light scattering effect of the NPs. In the centric photographs the remaining cake after freeze-drying is depicted. Here again a weak shrinkage was recognizable. However, the further results demonstrated that this was just a cosmetic issue without any impact on the NP stability. The last photographs of each triplet showed the redispersed NP samples (**2b** and **4b**). They were again characterized by a slight turbidity, similar to the initial dispersions. Here again a slight foaming was visible on the dispersions surface. The particle size

### 5.3. RESULTS AND DISCUSSION

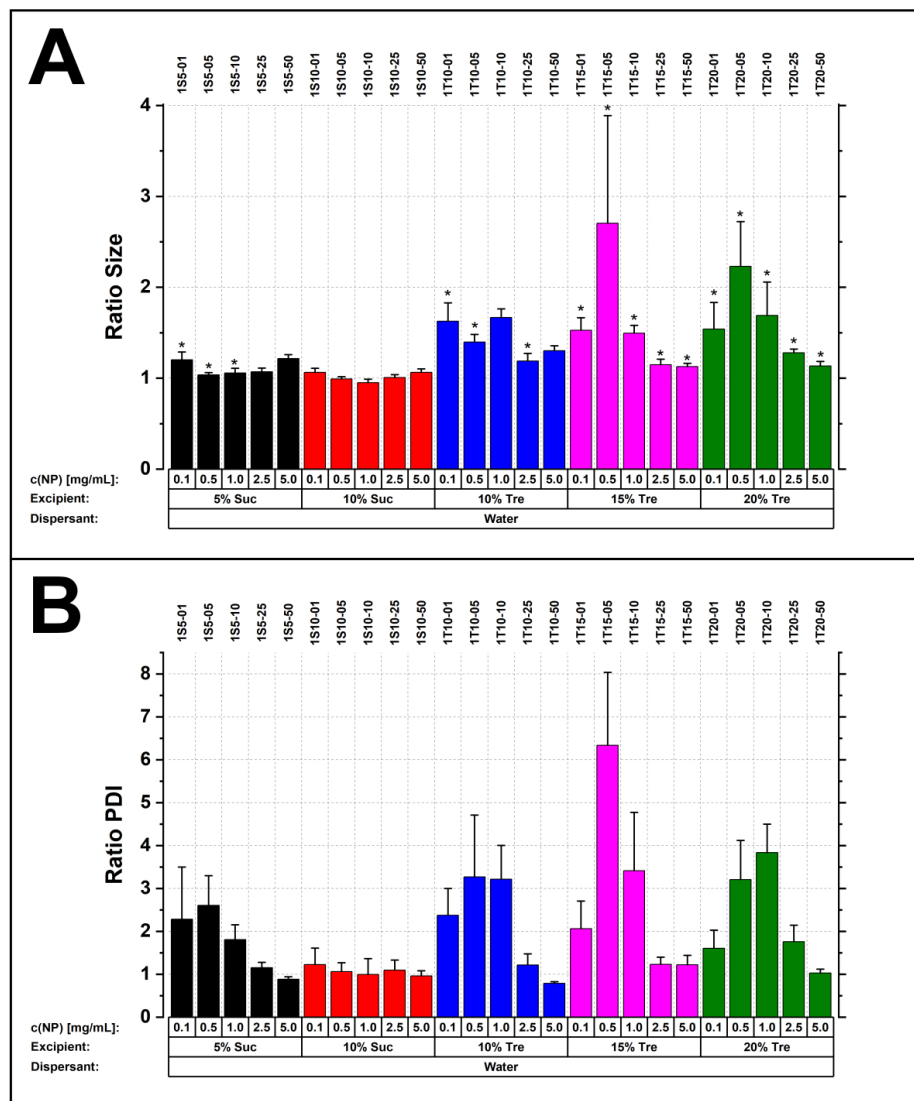


Figure 5.6: Changes of mNPs size parameters after freeze-drying (5.2.5): hydrodynamic diameter ratios (A) and PDI ratios (B). The actual value after freeze-drying was normalized to the initial value. Hence, a ratio of 1.0 indicated unaltered size parameters, while a ratio >1.0 indicated an increase. MNPs were supplemented with Suc (5 % and 10 %) or Tre (10 %, 15 % and 20 %). Similar bar colours highlight the identical excipient concentration. Asterisk (\*) highlights a second population in the particle-size distributions.

## 5.4. CONCLUSION

properties are plotted in figure 5.7B. There are three graphs displaying NPs size ratios, the polydispersity (PDI) and the DCR ratios. Each ratio was calculated by normalizing the value after freeze-drying to the initial value. Consequently a ratio of 1.0 indicates stable size parameters. All quality attributes remained completely unchanged. Thus, Suc as the exclusive excipient was able to stabilize EXP3174-decorated NPs. Competitive radioligand binding assays are plotted in figure 5.7 C. The assays were performed for targeted (EXP-NP90 and EXP-NP60<sup>-</sup>) and non-targeted core-shell NPs (NP90 and NP60<sup>-</sup>) prior and after freeze-drying. Non-targeted core-shell NPs were not able to replace the radioligand. They served as a negative controls and were not shown in figure 5.7. The graphs display the dose response curves of EXP-NP90 and EXP-NP60<sup>-</sup> each before (2a, 4a) and after freeze-drying (2b, 4b). The dose response curves were congruent and there was no avidity loss detectable. The determined half maximal inhibitory concentration (IC<sub>50</sub>) and negative decimal logarithm of IC<sub>50</sub> (pIC<sub>50</sub>) values are listed in table 5.4.

Table 5.4: IC<sub>50</sub> values of polymer NPs before and after freeze-drying. (n.q. - not quantifiable)

NP type	N=	Before lyophilization		After lyophilization	
		IC <sub>50</sub> [pM]	pIC <sub>50</sub>	IC <sub>50</sub> [pM]	pIC <sub>50</sub>
NP90	3	n.q.	n.q.	n.q.	n.q.
EXP-NP90	3	47 ± 8	10.33 ± 0.07	51 ± 7	10.30 ± 0.06
NP60 <sup>-</sup>	3	n.q.	n.q.	n.q.	n.q.
EXP-NP60 <sup>-</sup>	3	84 ± 24	10.09 ± 0.13	135 ± 10	9.87 ± 0.03

Both EXP-NP90 and EXP-NP60<sup>-</sup> retained their full avidity during freeze-drying. Apart from an unchanged size characteristics, this is critical for a successful formulation development. In comparison to other freeze-dried market formulation, these findings were outstanding. For example, there are vaccines containing attenuated or inactivated viruses. Mostly they are on the market as a liquid formulation, but there are freeze-dried formulations as well [41]. The biological activity (for vaccines usually named potency) is equally a critical quality attribute for the long-term stability of vaccines. It is generally accepted that freeze-drying lead to a potency loss of several vaccines [42, 43]. In case of the measles virus this could account three decades [41]. It is assumed, that agglomeration of individual virus particles are responsible for the tremendous potency loss [43]. In this light the obtained results were outstanding and highly promising for further development.

## 5.4 Conclusion

The degradation kinetics of core-shell NPs was studied using DLS. The half-life of non-targeted NP90 and NP60<sup>-</sup> was 180 ± 18 days and 153 ± 29 days. Storing in a fridge slowed down the degradation process clearly. Nevertheless, the shelf life of an aqueous core-shell NP dispersion was too short for a market formulation. Furthermore, they must be prepared freshly for any experiment.

## 5.4. CONCLUSION

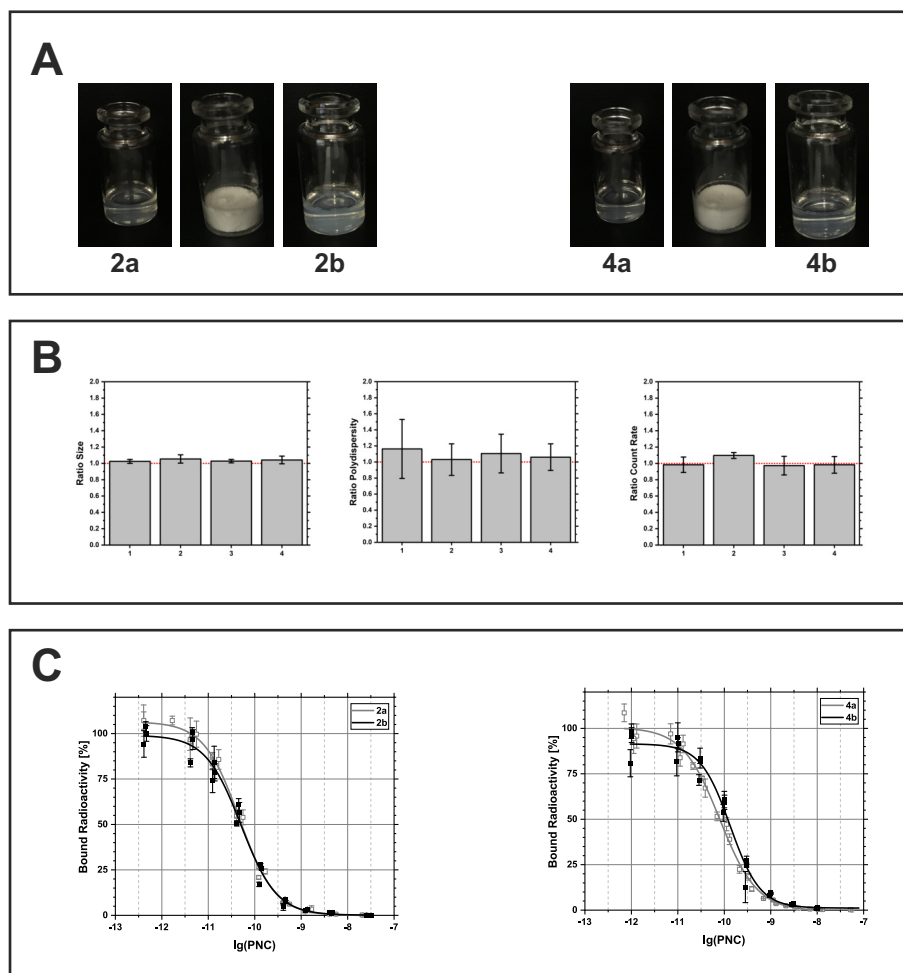


Figure 5.7: Summary of critical quality attributes of freeze-dried core-shell-NPs: macroscopic appearance (**A**), particle size characteristics (**B**) and target avidity (**C**). EXP3174-decorated EXP-NP90 (**2**) and EXP-NP60<sup>-</sup> (**4**) as well as their non-targeted controls NP90 (**1**) and NP60<sup>-</sup> (**3**) were investigated. Selected photographs of the NP dispersions prior freeze-drying (**2a**, **4a**), the remaining cake after freeze-drying and the redispersed samples (**2b**, **4b**) are depicted. In the centric box the ratios of the size (hydrodynamic diameter), the polydispersity (PDI) and the NP number (DCR) are plotted in bar diagrams. A ratio of 1.0 indicates stable NPs without any changes of the size properties. Graphs of the competitive radioligand binding assays are displayed in the bottom box. IC<sub>50</sub> values are listed in table 5.4.

#### 5.4. CONCLUSION

---

These results emphasized the need for a conservation method. Here it was relied on freeze-drying as a technique that carefully removes water completely from the NP dispersion. This is beneficial since water was the reaction partner during the degradation (hydrolysis).

Initially, freeze-thaw experiments were utilized to study the freezing behavior and identify suitable cryoprotectors. On this basis, promising excipients and the formulation range were investigated. Targeted core-shell NPs EXP-NP90 and EXP-NP60<sup>-</sup> were freeze-dried according to the developed process. To ensure the quality after redispersion the critical quality attributes macroscopic appearance, particle size distribution and target avidity were assessed. Thus, the development of a pre-clinical formulation was successfully completed. The subsequent process parameters turned out to be critical for the freeze-drying protocol:

- 1 Formulation must be free of buffer salts
- 2 Broad formulation range (0.1 mg ml<sup>-1</sup> to 5.0 mg ml<sup>-1</sup>)
- 3 Addition of a cryoprotector is obligatory (recommended: 10 % (w/v) Suc)
- 4 Freezing at -40 °C

The developed formulation process is a powerful method to extend the shelf life of the core-shell NPs substantially. They conserve their size properties as well as their targeting effect. At this stage of development the formulation is suitable for further pre-clinical experiments.

However, for a market formulation the (a) foaming after redispersion and the (b) cake appearance can be optimized. As anti-foaming agent Layre et. al. recommended the addition of tensides [44]. They can occupy the interfaces and reduce their interaction with the NPs consequently. But it must be considered that PEG containing tensides are not eligible, since they would interfere with the iodine assay, which is the basis for the NP quantification.

As depicted in figure 5.5 and 5.7, cake shrinkage and rarely peripheral cracks were apparent issues. But these issues do not limit the NP stability, they were only of cosmetic concern. Currently the impact of the cake appearance on the product quality and patient safety is intensively discussed [45, 46]. Patel et. al. were dealing with the cake appearance to solve the question 'What is Acceptable?' [47]. They systematically listed and illustrated the common irregularities of lyophilization cakes, described their origin (if known) as well as the implications for product quality and patient safety. Additionally they concluded that cake shrinkage and cracked cakes do not mitigate the product quality. Furthermore, they conducted interviews of lyophilization professionals from the pharmaceutical industries. The acceptability of different irregular cakes must be examined by means of photographs of lyophilized market products. All respondents consider shrinkage and cracking as completely acceptable. The reason for that clear statements can be found in the origin of shrinkage and cracking. These irregularities are typical for disaccharides like Tre and Suc. During freezing pure ice crystals grow first. The remaining liquid phase concentrates until  $w^f$  is reached. Further freezing lead to the complete solidification of the dispersion. In the case of amorphous excipients like Suc and Tre it is a vitrification. So-called 'unfrozen' water is embedded in the highly viscous

glas. Unfrozen water molecules are interacting with the glas components very strongly and can be removed only by the secondary drying [12]. The removal of unfrozen water leads to tensions in the cake structure that could be relaxed by shrinkage or cracking. The higher  $w'$  the more apparently shrinkage or cracking occurs [48].  $w'$  accounts 35.9% for Suc and only 16.7% for Tre [49]. Consequently, shrinkage of Suc cakes are particularly clear and account 17% of the initial cake volume regardless of the drying conditions [50]. So shrinkage and cracking are both impacts of tension relaxation in the cake during secondary drying. They are in an inverse relationship [48]. Ullrich et. al. found out that low Tre concentrations favor shrinkage, while higher Tre concentrations favor cracking [48]. These facts challenge the need of further investigations with the goal to optimize the cake appearance.

## 5.5 References

- [1] Yihan Xu et al. "Polymer Degradation and Drug Delivery in PLGA-Based Drug-Polymer Applications: A Review of Experiments and Theories". In: *Journal of Biomedical Materials Research Part B: Applied Biomaterials* 105.6 (2017), pp. 1692–1716. DOI: 10.1002/jbm.b.33648.
- [2] Frank Alexis. "Factors Affecting the Degradation and Drug-Release Mechanism of Poly(lactic acid) and Poly[(lactic acid)-co-(glycolic acid)]". In: *Polymer International* 54.1 (2005), pp. 36–46. DOI: 10.1002/pi.1697.
- [3] Sue Anne Chew, Marco A. Arriaga, and Victor A. Hinojosa. "Effects of Surface Area to Volume Ratio of PLGA Scaffolds with Different Architectures on Scaffold Degradation Characteristics and Drug Release Kinetics". In: *Journal of Biomedical Materials Research. Part A* 104.5 (2016), pp. 1202–1211. DOI: 10.1002/jbm.a.35657.
- [4] S. H. Hilal et al. "Estimation of Carboxylic Acid Ester Hydrolysis Rate Constants". In: *QSAR & Combinatorial Science* 22.9-10 (2003), pp. 917–925. DOI: 10.1002/qsar.200330836.
- [5] Chhaya Engineer, Jigisha Parikh, and Ankur Raval. "Review on Hydrolytic Degradation Behavior of Biodegradable Polymers from Controlled Drug Delivery System". In: *Trends in Biomaterials and Artificial Organs* 25.2 (2011), pp. 79–85.
- [6] V. Piemonte and F. Gironi. "Kinetics of Hydrolytic Degradation of PLA". In: *Journal of Polymers and the Environment* 21.2 (2013), pp. 313–318. DOI: 10.1007/s10924-012-0547-x.
- [7] Georgette L. Siparsky. "Degradation Kinetics of Poly(hydroxy) Acids: PLA and PCL". In: *Polymers from Renewable Resources*. Ed. by Carmen Scholz. Vol. 764. ACS Symposium Series. Washington, D.C.: American Chemical Society, 2000, pp. 230–251. DOI: 10.1021/bk-2000-0764.ch016.
- [8] Geoffrey Lee. "Stabilisierung von Peptidarzneistoffen durch Gefriertrocknung". In: *PZ Prisma* 3.2 (1996), pp. 105–116.

## 5.5. REFERENCES

---

- [9] Ken-ichi Izutsu. "Applications of Freezing and Freeze-Drying in Pharmaceutical Formulations". In: *Survival Strategies in Extreme Cold and Desiccation: Adaptation Mechanisms and Their Applications*. Ed. by Mari Iwaya-Inoue, Minoru Sakurai, and Matsuo Uemura. Singapore: Springer Singapore, 2018, pp. 371–383. DOI: 10.1007/978-981-13-1244-1<sub>20</sub>.
- [10] Kevin R. Ward and Paul Matejtschuk, eds. *Lyophilization of Pharmaceuticals and Biologicals: New Technologies and Approaches*. Methods in Pharmacology and Toxicology. New York: Humana Press and Springer, 2019. DOI: 10.1007/978-1-4939-8928-7.
- [11] Bakul Bhatnagar and Serguei Tchessalov. "Advances in Freeze Drying of Biologics and Future Challenges and Opportunities". In: *Drying Technologies for Biotechnology and Pharmaceutical Applications*. Ed. by Satoshi Ohtake, Ken-ichi Izutsu, and David Lechuga-Ballesteros. Wiley, 2020, pp. 137–177. DOI: 10.1002/9783527802104.ch6.
- [12] Heiko Schiffter-Weinle. "Immer Schön Trocken Bleiben: Gefriertrocknung zur Stabilisierung Empfindlicher Proteine". In: *Deutsche Apotheker Zeitung* 156.44 (2016), pp. 4404–4412.
- [13] Felix Franks. "Freeze-Drying of Bioproducts: Putting Principles into Practice". In: *European Journal of Pharmaceutics and Biopharmaceutics* 45.3 (1998), pp. 221–229. DOI: 10.1016/S0939-6411(98)00004-6.
- [14] Jean-Michel Rabanel et al. "Effect of the Polymer Architecture on the Structural and Biophysical Properties of PEG–PLA Nanoparticles". In: *ACS Applied Materials & Interfaces* 7.19 (2015), pp. 10374–10385. DOI: 10.1021/acsami.5b01423.
- [15] L. van den Berg. "The effect of Addition of Sodium and Potassium Chloride to the Reciprocal System:  $\text{KH}_2\text{PO}_4\text{-Na}_2\text{HPO}_4\text{-H}_2\text{O}$  on pH and Composition During Freezing". In: *Archives of Biochemistry and Biophysics* 84.2 (1959), pp. 305–315. DOI: 10.1016/0003-9861(59)90595-8.
- [16] G. Gómez, M. J. Pikal, and N. Rodríguez-Hornedo. "Effect of Initial Buffer Composition on pH Changes During Far-From-Equilibrium Freezing of Sodium Phosphate Buffer Solutions". In: *Pharmaceutical Research* 18.1 (2001), pp. 90–97. DOI: 10.1023/A:1011082911917.
- [17] D. L. Williams-Smith et al. "Changes in Apparent pH on Freezing Aqueous Buffer Solutions and Their Relevance to Biochemical Electron-Paramagnetic-Resonance Spectroscopy". In: *Biochemical Journal* 167.3 (1977), pp. 593–600. DOI: 10.1042/bj1670593.
- [18] Eva Meister and Henning Gieseler. "Freeze-Dry Microscopy of Protein/Sugar Mixtures: Drying Behavior, Interpretation of Collapse Temperatures and a Comparison to Corresponding Glass Transition Data". In: *Journal of Pharmaceutical Sciences* 98.9 (2009), pp. 3072–3087. DOI: 10.1002/jps.21586.
- [19] James A. Searles, John F. Carpenter, and Theodore W. Randolph. "The Ice Nucleation Temperature Determines the Primary Drying Rate of Lyophilization for Samples Frozen on a Temperature-Controlled Shelf". In: *Journal of Pharmaceutical Sciences* 90.7 (2001), pp. 860–871. DOI: 10.1002/jps.1039.



## 5.5. REFERENCES

---

- [20] Wassim Abdelwahed et al. "Freeze-Drying of Nanoparticles: Formulation, Process and Storage Considerations". In: *Advanced Drug Delivery Reviews* 58.15 (2006), pp. 1688–1713. DOI: 10.1016/j.addr.2006.09.017.
- [21] Melisande Holzer et al. "Physico-Chemical Characterisation of PLGA Nanoparticles After Freeze-Drying and Storage". In: *European Journal of Pharmaceutics and Biopharmaceutics* 72.2 (2009), pp. 428–437. DOI: 10.1016/j.ejpb.2009.02.002.
- [22] Pedro Fonte, Salette Reis, and Bruno Sarmiento. "Facts and Evidences on the Lyophilization of Polymeric Nanoparticles for Drug Delivery". In: *Journal of Controlled Release* 225 (2016), pp. 75–86. DOI: 10.1016/j.jconrel.2016.01.034.
- [23] Maarten A. Mensink et al. "How Sugars Protect Proteins in the Solid State and During Drying (Review): Mechanisms of Stabilization in Relation to Stress Conditions". In: *European Journal of Pharmaceutics and Biopharmaceutics* 114 (2017), pp. 288–295. DOI: 10.1016/j.ejpb.2017.01.024.
- [24] A. I. Bulavchenko and P. S. Popovetskiy. "Determining the Hydrodynamic Radii of AOT Micelles with Silver Nanoparticles by Means of Photon Correlation Spectroscopy". In: *Russian Journal of Physical Chemistry A* 86.6 (2012), pp. 999–1003. DOI: 10.1134/S0036024412050068.
- [25] Jing Shang and Xiaohu Gao. "Nanoparticle Counting: Towards Accurate Determination of the Molar Concentration". In: *Chemical Society Reviews* 43.21 (2014), pp. 7267–7278. DOI: 10.1039/c4cs00128a.
- [26] Changhui Li, George W. Kattawar, and Ping Yang. "Effects of Surface Roughness on Light Scattering by Small Particles". In: *Journal of Quantitative Spectroscopy & Radiative Transfer* 89.1-4 (2004), pp. 123–131. DOI: 10.1016/j.jqsrt.2004.05.016.
- [27] Banu S. Zolnik and Diane J. Burgess. "Effect of Acidic pH on PLGA Microsphere Degradation and Release". In: *Journal of Controlled Release* 122.3 (2007), pp. 338–344. DOI: 10.1016/j.jconrel.2007.05.034.
- [28] K. Avgoustakis et al. "PLGA–mPEG Nanoparticles of Cisplatin: In Vitro Nanoparticle Degradation, In Vitro Drug Release and In Vivo Drug Residence in Blood Properties". In: *Journal of Controlled Release* 79.1-3 (2002), pp. 123–135. DOI: 10.1016/S0168-3659(01)00530-2.
- [29] Pedro Fonte et al. "Effect of the Freezing Step in the Stability and Bioactivity of Protein-Loaded PLGA Nanoparticles Upon Lyophilization". In: *Pharmaceutical Research* 33.11 (2016), pp. 2777–2793. DOI: 10.1007/s11095-016-2004-3.
- [30] Jonghwi Lee and Yu Cheng. "Critical Freezing Rate in Freeze Drying Nanocrystal Dispersions". In: *Journal of Controlled Release* 111.1-2 (2006), pp. 185–192. DOI: 10.1016/j.jconrel.2005.12.003.
- [31] Nae-Oh Chung, Min Kyung Lee, and Jonghwi Lee. "Mechanism of Freeze-Drying Drug Nanosuspensions". In: *International Journal of Pharmaceutics* 437.1-2 (2012), pp. 42–50. DOI: 10.1016/j.ijpharm.2012.07.068.

## 5.5. REFERENCES

---

- [32] Jakob Beirowski et al. "Freeze-Drying of Nanosuspensions, 1: Freezing Rate Versus Formulation Design as Critical Factors to Preserve the Original Particle Size Distribution". In: *Journal of Pharmaceutical Sciences* 100.5 (2011), pp. 1958–1968. DOI: 10.1002/jps.22425.
- [33] K. D. Roe and T. P. Labuza. "Glass Transition and Crystallization of Amorphous Trehalose-Sucrose Mixtures". In: *International Journal of Food Properties* 8.3 (2005), pp. 559–574. DOI: 10.1080/10942910500269824.
- [34] Alexander Grebner. "Organic and Hybrid Nanoparticles for Controlled Instigation of Inertial Cavitation Using Therapeutic Ultrasound". Dissertation. Friedrich-Alexander University Erlangen-Nuremberg, 2017.
- [35] Abdulaziz Almalik et al. "Effect of Cryoprotection on Particle Size Stability and Preservation of Chitosan Nanoparticles with and without Hyaluronate or Alginate Coating". In: *Saudi Pharmaceutical Journal* 25.6 (2017), pp. 861–867. DOI: 10.1016/j.jsps.2016.12.008.
- [36] Flávia Sousa et al. "A New Paradigm for Antiangiogenic Therapy Through Controlled Release of Bevacizumab from PLGA Nanoparticles". In: *Scientific Reports* 7.1 (2017). DOI: 10.1038/s41598-017-03959-4.
- [37] A. del Pozo-Rodríguez et al. "Short- and Long-Term Stability Study of Lyophilized Solid Lipid Nanoparticles for Gene Therapy". In: *European Journal of Pharmaceutics and Biopharmaceutics* 71.2 (2009), pp. 181–189. DOI: 10.1016/j.ejpb.2008.09.015.
- [38] Rebecca L. Ball, Palak Bajaj, and Kathryn A. Whitehead. "Achieving Long-Term Stability of Lipid Nanoparticles: Examining the Effect of pH, Temperature, and Lyophilization". In: *International Journal of Nanomedicine* 12 (2017), pp. 305–315. DOI: 10.2147/IJN.S123062.
- [39] Worapol Ngamcherdtrakul et al. "Lyophilization and Stability of Antibody-Conjugated Mesoporous Silica Nanoparticle with Cationic Polymer and PEG for siRNA Delivery". In: *International Journal of Nanomedicine* 13 (2018), pp. 4015–4027. DOI: 10.2147/IJN.S164393.
- [40] Kun Liu et al. "Stable Gadolinium Based Nanoscale Lyophilized Injection for Enhanced MR Angiography with Efficient Renal Clearance". In: *Biomaterials* 158 (2018), pp. 74–85. DOI: 10.1016/j.biomaterials.2017.12.023.
- [41] Ozan S. Kumru et al. "Vaccine Instability in the Cold Chain: Mechanisms, Analysis and Formulation Strategies". In: *Biologicals* 42.5 (2014), pp. 237–259. DOI: 10.1016/j.biologicals.2014.05.007.
- [42] O'Neil Wiggan et al. "Novel Formulations Enhance the Thermal Stability of Live-Attenuated Flavivirus Vaccines". In: *Vaccine* 29.43 (2011), pp. 7456–7462. DOI: 10.1016/j.vaccine.2011.07.054.
- [43] Wei Qi et al. "Urea Improves Stability of Inactivated Polio Vaccine Serotype 3 During Lyophilization and Storage in Dried Formulations". In: *Journal of Pharmaceutical Sciences* 107.8 (2018), pp. 2070–2078. DOI: 10.1016/j.xphs.2018.04.019.

## 5.5. REFERENCES

---

- [44] A.-M. Layre et al. "Freeze-Drying of Composite Core-Shell Nanoparticles". In: *Drug Development and Industrial Pharmacy* 32.7 (2006), pp. 839–846. DOI: 10.1080/03639040600685134.
- [45] Christina Haeuser et al. "Imaging Techniques to Characterize Cake Appearance of Freeze-Dried Products". In: *Journal of Pharmaceutical Sciences* 107.11 (2018), pp. 2810–2822. DOI: 10.1016/j.xphs.2018.06.025.
- [46] Laura Milner et al. "Physical, Textural and Sensory Characteristics of Reduced Sucrose Cakes, Incorporated with Clean-Label Sugar-Replacing Alternative Ingredients". In: *Innovative Food Science & Emerging Technologies* 59 (2020). DOI: 10.1016/j.ifset.2019.102235.
- [47] Sajal Manubhai Patel et al. "Lyophilized Drug Product Cake Appearance: What Is Acceptable?" In: *Journal of Pharmaceutical Sciences* 106.7 (2017), pp. 1706–1721. DOI: 10.1016/j.xphs.2017.03.014.
- [48] Sabine Ullrich, Stefan Seyferth, and Geoffrey Lee. "Measurement of Shrinkage and Cracking in Lyophilized Amorphous Cakes. Part I: Final-Product Assessment". In: *Journal of Pharmaceutical Sciences* 104.1 (2015), pp. 155–164. DOI: 10.1002/jps.24284.
- [49] R. H. M. Hatley and F. Franks. "Applications of DSC in the Development of Improved Freeze-Drying Processes for Labile Biologicals". In: *Journal of Thermal Analysis* 37.8 (1991), pp. 1905–1914. DOI: 10.1007/BF01912221.
- [50] S. Rambhatla et al. "Cake Shrinkage During Freeze Drying: A Combined Experimental and Theoretical Study". In: *Pharmaceutical Development and Technology* 10.1 (2005), pp. 33–40. DOI: 10.1081/PDT-35871.



## **Chapter 6**

# **Design of Antagonistic Nanoparticles with Sub-Nanomolar Avidity**

## Abstract

Two promising candidates of biocompatible core-shell nanoparticles (NPs) were investigated for their avidity to angiotensin II receptor type 1 (AT1R)-positive rat mesangial cells (rMCs): (a) larger, methoxy-terminated EXP-NP90 ( $105 \pm 13$  nm) and (b) smaller, carboxy-terminated EXP-NP60<sup>-</sup> ( $68 \pm 6$  nm). Both candidates were decorated with losartan carboxylic acid (EXP3174), that is an antagonist for AT1Rs. EXP3174 molecules were attached as targeting ligands to longer polyethylene glycol (PEG)-chains, so that they stand out of the PEG-shell like spikes of a virus. This architecture was crucial to receive core-shell NP with a sub-nanomolar avidity to target cells. Larger EXP-NP90 had an  $\text{pIC}_{50}$  of  $9.60 \pm 0.11$  (calcium mobilization assay (CaA)) respectively  $10.04 \pm 0.23$  (radioligand binding experiment (RL-A)). Whereas smaller EXP-NP60<sup>-</sup> only reached  $9.27 \pm 0.11$  (CaA) respectively  $9.34 \pm 0.07$  (RL-A). Both candidates remained on the surface of target cells, since antagonistic EXP3174 decorated NPs do not induce endocytosis as it was observed for the agonistic NPs of Maslanka et. al. [1]. Additionally, the avidity of EXP-NP90 and EXP-NP60<sup>-</sup> was tested to rMCs with an increased AT1R density (HRD-rMC) to mimic pathological circumstances [2, 3]. But an avidity gain could not be seen in this experiments.

## 6.1 Introduction

Hennig et. al. demonstrated that ligand-decorated model nanoparticle (mNP) targeted the retinal and choroidal vasculature [4]. They decorated PEG-coated Quantum Dots with the AT1R antagonist EXP3174. However, their Quantum Dots were composed of a cadmium selenid core and consequently not suitable for a therapeutic administration. This work is focussed on the development of a NP formulation with similar targeting properties but suitable for a clinical application. In this context the core-shell NPs, that were established by Abstiens et. al. [5], offered a tremendous tool box to design therapeutic NPs with tailored properties. Two NP formulations turned out as promising candidates for this purpose: (a) EXP-NP90 and (b) EXP-NP60<sup>-</sup>. Both candidates were decorated with the targeting ligand EXP3174. EXP-NP90 carried a shell with methoxy terminated PEG chains, while EXP-NP60<sup>-</sup> had negatively charged, carboxy terminated PEG chains. Even just this small endgroup modification generated a giant size difference. The EXP-NP90 had a diameter of  $105 \pm 13$  nm, while the smaller EXP-NP60<sup>-</sup> had a diameter of only  $68 \pm 6$  nm. Furthermore, the non-ligand carrying equivalents NP90 and NP60<sup>-</sup> were manufactured as controls for various experiments. The manufacturing procedure (nanoprecipitation) and the characterization methods are described in chapter 4.

The design of the PEG shell was absolutely crucial. The EXP3174 molecules were attached to PEG chains with a molecular weight (MW) of 5 kDa, while all other PEG chains had a MW of only 2 kDa. Therefore, the EXP3174 molecule received the flexibility to reach their target receptors (AT1R). This NP architecture was adopted from viruses that are a kind of natural targeting NPs [6, 7]. Viruses use surface presented spike proteins to target their host cells. These

targeting proteins stick out like spines, so that they are called *spike proteins*. In addition to the targeting effect, EXP3174 molecules are also able to silence AT1Rs and consequently mediate a pharmacological effect. The targeting and the silencing effect of EXP3174-decorated core-shell NPs was quantified *in vitro* using an AT1Rs-positive cell line (rMCs) [1].

The candidates are intended to be applied against proliferative ocular diseases like proliferative diabetic retinopathy (PDR) and wet age-related macular degeneration (AMD). Silencing of ocular AT1Rs is expected to downregulate ocular neovascularization (refer to chapter 1). During pathological circumstances the density of ocular AT1Rs increases [2, 3]. It is known that the avidity of multivalent NPs increases for target cells with an upregulated target receptor density [8]. That's why it was expected that EXP3174 decorated core-shell NPs show an increased avidity to cell lines with an upregulated AT1R density. This hypothesis was proven at a high-AT1R-density cell line (HRD-rMC), so that pathophysiological circumstances could be simulated .

Here the terms *affinity* and *avidity* are used coexistently. For one thing, the ligand-related *affinities* were specified to compare different types of NPs like the EXP3174-decorated methoxy terminated nanoparticles with a 5 kDa PEG shell (EXP-NP<sub>5k</sub>) with the candidates EXP-NP90 and EXP-NP60<sup>-</sup>. Basically, it was quite easier to access the ligand concentration directly using a fluorescence assay. The calculation of the NP's *avidity* required the laborious determination of the particle number concentration (PNC) as it is described in chapter 4. This time-consuming procedure was waived during the pre-studies. Afterwards the *avidity* was consistently specified for both candidates (EXP-NP90 and EXP-NP60<sup>-</sup>).

## 6.2 Material and Methods

### 6.2.1 Material

The synthesis and analysis of EXP3174 is described in chapter 3. All other chemicals were purchased from Sigma-Aldrich (Taufkirchen/ Germany) in analytical or cell culture grade , if not stated otherwise. A Milli-Q purification system (Millipore/ Schwalbach/ Germany) was used to prepare fresh ultra-pure water. It is hereinafter just named water.

### 6.2.2 Manufacturing and Characterization of Nanoparticles

The manufacturing procedure of non-ligand carrying methoxy-terminated nanoparticle (NP90) and carboxy-terminated nanoparticle (NP60<sup>-</sup>) as well as their targeted equivalents EXP3174 decorated NP90 (EXP-NP90) and EXP3174 decorated NP60<sup>-</sup> (EXP-NP60<sup>-</sup>) is described in section 4.2.2. In order to perform flow cytometry and confocal laser scanning microscopy (CLSM) experiments a fluorescence label was attached. Therefore acid terminated poly(lactic-co-glycolic) acid (PLGA) was supplemented with fluorescent PLGA-CF<sup>TM</sup>647.

The coupling protocol is described in section 3.2.9.

The NP size (refer to section 4.2.3), the total polymer content (TPC) (refer to section 4.2.5) and the EXP3174 content (refer to section 4.2.7) were determined for every NP batch. The PNC was calculated from equation 4.7, which is repeated below:

$$PNC = \frac{TPC}{\rho_{NP} \times \frac{1}{6}\pi (d_h)^3 \times N_A}$$

This function is the basis for the determination of the NP avidity. The mathematical derivation is explained in section 4.3.2.

### 6.2.3 Cell Culture

The cell lines were cultured in TC-treated flasks 75 cm<sup>2</sup> or 175 cm<sup>2</sup> (Eppendorf/ Hamburg/ Germany) in a water-saturated carbon dioxide enriched (5% CO<sub>2</sub>) atmosphere at 37 °C. Therefore a CellXpert® 170 (Eppendorf/ Hamburg/ Germany) was used.

Rat mesangial cells (rMCs) were a kind gift from Prof. Armin Kurtz (Institute of Physiology/ University of Regensburg/ Germany). The cells were cultured in RPMI 1640 medium supplemented with 10% fetal bovine serum (FBS) (Biowest/ Nuaillé/ France), insulin-transferrin-selenium (ITS) (Invitrogen™) and 100 nM hydrocortisone. RMCs were chosen due to their stable AT1R expression over numerous passages. AT1R expression was previously shown by Maslanka et. al. [1].

The culture medium for the transfected high-receptor density rat mesangial cells (HRD-rMCs) was additionally supplemented with 600 µg ml<sup>-1</sup> geneticin.

### 6.2.4 Transfection of Rat Mesangial Cells

RMCs were transfected with the pCXN2-HA-AT1R-YFP plasmid encoding for a fluorescently tagged AT1R. The rMCs were treated by Maslanka et. al. [9]. For the transfection they used lipofectamine 2000 according to the manufacturer's instructions. Transfected rMCs are subsequently named HRD-rMC.

The plasmid pCXN2-HA-AT1R-YFP was a gift from Yusuke Ohba (Addgene plasmid #101659; <http://n2t.net/addgene:101659>; RRID:Addgene\_101659) [10].

### 6.2.5 Flow Cytometry

RMCs were seeded into TC-treated 24-well plates (Eppendorf/ Hamburg/ Germany) at a density of 40 000 cells /well and cultivated for 2 days. At the day of the experiment rMCs reached a confluency of at least 90%.

After removing the culture medium, living rMCs were washed with 500 µl Dulbecco's Phosphate Buffered Saline (DPBS) (Gibco™/Life Technologies/ Paisly/ UK), twice. Afterwards rMCs were covered with 200 µl incubation



## 6.2. MATERIAL AND METHODS

---

buffer. The incubation buffer was composed of Leibovitz L-15 medium without phenol red (Gibco™/ Life Technologies/ Grand Island/ USA) and bovine serum albumin (BSA) (0.1 %).

At the beginning of the experiment (designated 0 h) always 25 µl of the EXP3174 stock dilution (5 µM) or incubation buffer were added. The plates were gently shaken on a tumbling device for 30 min at room temperature (RT). Afterwards 25 µl NP stock dilution (5.0 mg ml<sup>-1</sup>) were added. Plates were gently shaken for additional 45 min at RT. So the final working volume accounted 250 µl. During the experiment the TPC of NPs was 0.5 mg ml<sup>-1</sup>, while the EXP3174 concentration was 500 nM. After the incubation period NP containing supernatant was removed by suction and the cells were washed with 500 µl DPBS twice. For the cell detachment 300 µl pre-warmed trypsin-EDTA 0.25 % (Gibco™/ Life Technologies/ Paisley/ UK) were used. Trypsin was stopped with 500 µl FBS-containing cell culture medium, centrifuged (200xg, 5 min, 4 °C) and resuspended in 400 µl DPBS. Samples were placed on ice and kept in the dark until the measurement was performed.

RMCs were measured on a FACS Calibur flow cytometer (Becton Dickinson/ Franklin Lakes/ NJ/ USA). CF™647-tagged NPs were excited from the red laser (633 nm). The fluorescent cells were detected at 661 nm (bandpass filter 16 nm).

The geometric mean of the fluorescence intensity was reported. Raw data were normalized to the mean fluorescence of EXP-NP90 respectively EXP-NP60. Significance level was estimated based on one-sided student t-test (N=9).

### 6.2.6 Calcium Mobilization Assay

CaAs were utilized to investigate the avidity of EXP3174-decorated NPs. The radiometric procedure was established by Gryniewicz et. al. [11]. It relies on a fluorescent calcium chelator, indicating calcium influx into the cytosol. The protocol was adapted from Hennig et. al. [12]. In brief, suspension of rMCs was centrifuged (200xg, 5 min) and the supernatant was removed. Then, the cells were resuspended in loading buffer, composed of Leibovitz L-15 medium (without phenol red) (Gibco™/ Life Technologies/ Grand Island/ USA) supplemented with the cell permeant calcium-sensitive dye Fura-2 AM (Invitrogen™/ Life Technologies/ Carlsbad/ CA/ USA) (5.0 µM), Pluronic F-127 (0.05 %) and Probenecid (2.5 mM). After 1 h of light-protected incubation at RT, the loading buffer was removed and the cells were washed with incubation buffer twice. The incubation buffer was composed of Leibovitz L-15 medium (without phenol red) supplemented with Probenecid (2.5 mM). The cell suspension was adjusted to  $2.0 \times 10^6$  cells /ml.

For the experiment a dilution series of naive EXP3174, PEGylated EXP3174 or the NPs dispersion was prepared (sample dilution). 10 µl of each sample dilution was rendered in a white polystyrene (PS) half-area 96-well-plate (Greiner Bio One/ Frickenhausen/ Germany). Then 45 µl of the cell suspension were added, carefully homogenized and incubated for 30 min at RT. Immediately before the measurement 45 µl stimulation buffer was injected automatically using a FluoStar Omega fluorescence microplate reader (BMG Labtech/ Ortenberg/ Germany) equipped with two built-in reagent injectors. The stimulation

## 6.2. MATERIAL AND METHODS

---

buffer was composed of Leibovitz L-15 medium (without phenol red) supplemented with angiotensin II (Ang II) (Bachem/ Bubendorf/ Switzerland).

During the measurement  $9 \times 10^5$  rMCs were stimulated with the AT1R-agonist Ang II (final concentration 135 nM = EC<sub>80</sub>). The EC<sub>80</sub> was determined for Fura-2 loaded rMCs in a separate experiment (refer to figure S1). Immediately after the injection of the stimulation buffer the samples were alternately excited at 340/20 nm and 380/20 nm. Emitted light was recorded at 510/20 nm for 30 s. To determine the maximum calcium signal, Fura-2 loaded rMCs were dissolved with 0.1 % Triton™-X 100 to release the complete cellular calcium stock (R<sub>max</sub>). To determine the background noise the Fura-2 loaded rMCs were dissolved in the presence of EGTA (R<sub>min</sub>). EGTA is a strong calcium chelating agent, stronger than Fura-2 itself.

Subsequently, the intracellular calcium concentration was calculated from the maximum fluorescence ratios using the equation published by Grynkiewicz et. al. [11]. K<sub>d</sub> for the Fura-2-calcium-complex was taken from the literature (225 nM) [11]. The data were plotted semi-logarithmic and analyzed using the Origin 2020 SR1 software (OriginLab/ Northampton/ MA/ USA). Dose-response curves were fitted with the sigmoidal fitting function:

$$y = A1 + \frac{A2 - A1}{1 + 10^{(\lg IC_{50} - x)p}} \quad (6.1)$$

Here A2 is the top plateau and A1 is the bottom plateau.  $\lg IC_{50}$  is the centre of the dose-response curve and  $p$  is the slope. The intracellular calcium concentration was normalized to A2 and specified as calcium response in percent. EC<sub>50</sub>, EC<sub>80</sub> and IC<sub>50</sub> values are indicated as *mean ± SEM*.

### 6.2.7 Radioligand Binding Experiment

The tritium labeled angiotensin II derivative radioligand ([<sup>3</sup>H]UR-MK292) [13] was kindly provided by Dr. Max Keller (Pharmaceutical Chemistry/ University of Regensburg/ Regensburg/ Germany). UR-MK292 had a specific activity of 1.407 TBq mmol<sup>-1</sup>. It was used for both, the saturation binding and the competitive binding experiments.

Furthermore, the binding buffer and the lysis buffer were freshly prepared for the RL-As. The binding buffer was composed of Leibovitz L-15 medium (without phenol red) (Gibco™/ Life Technologies/ Grand Island/ USA), BSA (0.1 %) and bacitracin (100 µg ml<sup>-1</sup>). The lysis buffer was composed of urea (Merck/ Darmstadt/ Germany) (8M), Triton™X-100 (1 %) and glacial acetic acid (Merck/ Darmstadt/ Germany) (3M).

EXP3174 was soluted in cell-culture grade dimethyl sulphoxide (DMSO) (50 mM) and further diluted with binding buffer to receive the EXP3174 concentrates.

Since the AT1R-density of HRD-rMC was significantly higher than the AT1R-density of rMC (refer table 6.2), the experimental setup was different:

RMC were seeded into TC-treated PS 24-well-plates (Eppendorf/ Hamburg/ Germany) at a seeding density of  $4 \times 10^4$  cells /well. During the experiment

the working volume was 250  $\mu\text{l}$ . After completion of the experiment, cell lysates were transferred into scintillation vials pre-filled with 2.5 ml liquid scintillator (Rotiszint eco plus/ Carl Roth/ Karlsruhe/ Germany). The samples were homogenized, kept in the dark for 30 min and counted by the liquid scintillation counter LS 6500 (Beckmann-Coulter/ Munich/ Germany) for 5.0 min each.

**HRD-rMC** were seeded into flat clear-bottom white TC-treated PS 96-well-plates (Corning<sup>®</sup> Incorporated Life Sciences/ Tewksbury/ MA/ USA) at a seeding density of  $1 \times 10^4$  cells /well. During the experiment the working volume was 200  $\mu\text{l}$ . After completion of the experiment, cell lysates remained in the 96-well-plates and liquid scintillator (Optiphase Supermix/ PerkinElmer) was added. The plates were sealed with a transparent sealing tape and the liquids were carefully mixed by inversion for several times. The plates were kept in the dark for at least 30 min and radioactivity was measured with a Micro-Beta2 plate counter (PerkinElmer).

### Saturation Binding

Prior to the experiment, seeded cells were cultured for 2 d. On the day of the experiment confluency was at least 90 %. After removing the culture medium, living cells were washed with DPBS (Gibco<sup>™</sup>/ Life Technologies/ Paisly/ UK) twice. Afterwards, the cells were covered with binding buffer (80 % of the working volume).

At the beginning of the experiment (designated 0 min), EXP3174 concentrates and radioligand stock dilutions (*unspecific binding*) or binding buffer and radioligand stock dilutions (*total binding*) were added. Therewith, the working volume was achieved and the incubation interval started immediately.

During the saturation binding experiments the cells were exposed to a series of radioligand concentrations (total binding). Apart from that, EXP3174 was added in a 500-fold excess to block AT1Rs (unspecific binding). The plates were gently shaken at RT for 120 min. Afterwards, supernatants were removed by suction, cells were washed with ice-cold DPBS twice and the *lysis buffer* was added for additional 30 min. Depending on the cell type (rMC or HRD-rMC), the lysates were prepared as mentioned above and their radioactivity was detected.

The data were analyzed using the Origin 2020 SR1 software (OriginLab/ Northampton/ MA/ USA). Radioligand concentration  $c_{RL}$  (x-axis) and bound radioactivity (y-axis) were plotted. Unspecific binding was subtracted from total binding to obtain the *specific binding*. Specific binding was fitted with the Michaelis-Menten function:

$$y = \frac{B_{\max} x}{K_d + x} \quad (6.2)$$

Here  $B_{\max}$  is the maximal number of binding sites and  $K_d$  is the equilibrium dissociation constant of the ligand-receptor complex. Unspecific binding was fitted with linear regression. The receptor density was calculated from  $B_{\max}$ .

### Competition Binding

Prior to the experiment, seeded cells were cultured for two days. On the day of the experiment the confluency was at least 90 %. After removing the culture medium, living cells were washed with DPBS (Gibco™/ Life Technologies/ Paisly/ UK), twice. Afterwards the cells were covered with binding buffer (80 % of the working volume).

At the beginning of the experiment (designated 0 min), EXP3174 concentrate (unspecific binding), binding buffer (total binding) or the sample dilutions were added. The applied volume accounted 10 % of the working volume. The cells were gently shaken on a tumbling device and pre-incubated at RT for 30 min. The samples were naive EXP3174, PEGylated EXP3174 and the manufactured NP dispersions (NP90, EXP-NP90, NP60<sup>-</sup> and EXP-NP60<sup>-</sup>). Then the radioligand stock dilution was added and the final working volume was achieved.

During the competition binding experiments the radioligand concentration was 1 nM, that met the equilibrium dissociation constant of the ligand-receptor complex ( $K_d$ ) of rMC and HRD-rMC (refer to the figures S2 and S3). To determine the unspecific binding EXP3174 was added in a 500-fold excess (500 nM) to block AT1Rs quantitatively. The plates were gently shaken at RT for further 90 min. Afterwards, supernatants were removed by suction, cells were washed with ice-cold DPBS twice and the lysis buffer was added for additional 30 min. Depending on the cell type (rMC or HRD-rMC), the lysates were handled as previously described.

The data were analyzed using the Origin 2020 SR1 software (OriginLab/ Northampton/ MA/ USA). Decadic logarithm of the sample concentration (x-axis) and bound radioactivity (y-axis) were plotted (dose-response curve). Unspecific binding was subtracted from the sample radioactivity to receive the bound radioactivity. Dose-response curves were fitted with the sigmoidal fitting function:

$$y = A1 + \frac{A2 - A1}{1 + 10^{(\lg IC_{50} - x)p}} \quad (6.3)$$

Here  $A2$  is the top plateau  $y$ -value and  $A1$  is the bottom plateau  $y$ -value.  $\lg IC_{50}$  is the centre of the dose-response curve and  $p$  is the slope.

The bound radioactivity was normalized to the total binding in order to receive the percentage of bound radioactivity.  $IC_{50}$  values are indicated as *mean*  $\pm$  *SEM*.

### 6.2.8 Confocal Laser Scanning Microscopy

To identify the cells during CLSM, their cytosol was stained with a fluorescent dye. Therefore, rMCs were captured in FBS-free culture medium supplemented with 25  $\mu$ M CellTracker™Green (Invitrogen™) and incubated at 37 °C for 30 min. Afterwards, medium was removed by centrifugation (200xg, RT, 5 min), cells were resuspended in culture medium and seeded into eight-well plastic bottom  $\mu$ -slides (Ibidi/ Graefelfing/ Germany) at a density of  $6 \times 10^3$  cells/well.

RMC were grown for two days. On the day of the experiment, medium was

removed and adherent cells were washed with DPBS (Gibco™/ Life Technologies/ Paisly/ UK) twice. Then the cells were covered with 225 µl association buffer, that was composed of Leibovitz L-15 medium (without phenol red) (Gibco™/ Life Technologies/ Grand Island/ USA) and BSA (0.1%). Subsequently, 25 µl of the CF™647-labeled NP dispersion (NP90, EXP-NP90, NP60<sup>-</sup> or EXP-NP60<sup>-</sup>) was added. After the incubation interval (30 min, 37 °C) the association buffer was removed, the cells were washed with ice-cold DPBS and fixed with 300 µl paraformaldehyde (PFA) 4% in DPBS for 15 min. Lastly PFA was removed, the cells were washed, covered with DPBS and analyzed with the laser-scanning microscope LSM 710 (Carl Zeiss/ Jena/ Germany) using the objective C-Apochromat 63x/1.20 W autocorr M27.

CellTracker™Green was excited at 488 nm and emitted light was detected with a 493 nm to 552 nm bandpass filter. The cell fluorescence is color-coded in green. The  $\gamma$  value was set to 0.45. CF™647-labeled NPs were excited at 633 nm and emitted light was detected with a 638 nm to 747 nm bandpass filter. NP fluorescence is color-coded on a red-to-white scale. The gamma value was set to 2.0.

## 6.3 Results and Discussion

Both EXP3174-decorated candidates EXP-NP90 and EXP-NP60<sup>-</sup> were investigated for their *in vitro* binding performance at AT1R-positive rMCs. The following aspects were investigated:

- Targeting of AT1Rs
- Silencing of AT1R signalling
- Localization during binding

Therefore, a series of experiments was performed. That included RL-As, functional CaAs, flow cytometry experiments and CLSM.

### 6.3.1 Milestone in Nanoparticle Development

EXP3174 is a very potent AT1R antagonist with an extremely low dissociation rate. Since EXP3174 induces a conformational change in the binding pocket of the AT1R, it is an insurmountable antagonist [14, 15]. So it is very difficult to replace binding EXP3174 from an AT1R. This is an excellent property to hold the NP close to the membrane and to enable multivalent binding of further EXP3174 ligands. However, covalent attachment of EXP3174 to a PEG-chain (PEGylation) causes a clear affinity loss [12]. The carboxyl group is engaged in a salt bridge with an arginine residue in the binding pocket of the AT1R [15]. Consequently, the IC<sub>50</sub> values were determined using a competitive CaA. Thereby, the calcium influx into the cytosol was induced through the injection of Ang II. The final concentration of Ang II was adjusted to the EC<sub>80</sub>. The maximum calcium influx was defined as 100% calcium response. By the administration of different doses of native EXP3174 or PEGylated EXP3174 the calcium influx was inhibited. The results are plotted in figure 6.1. For EXP3174 an IC<sub>50</sub> of  $0.5 \pm 0.1$  nM ( $pIC_{50}=9.3 \pm 0.1$ ) was determined. This was in good

### 6.3. RESULTS AND DISCUSSION

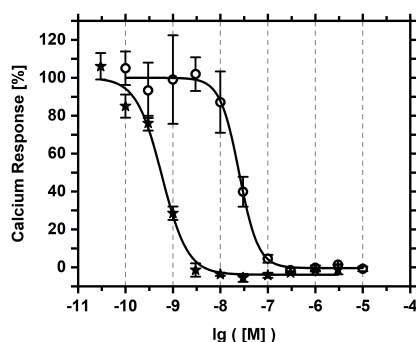


Figure 6.1: Competitive CaA for EXP3174 (stars) and PEGylated EXP3174 (circles).

agreement with the literature. Hennig et. al. found an  $IC_{50}$  of 1.1 nM for rMCs [12], while Sachinidis et. al. determined 5 nM for vascular smooth muscle cells [16].

For PEGylated EXP3174 an  $IC_{50}$  of  $22.9 \pm 2.1$  nM ( $pIC_{50}=7.6 \pm < 0.1$ ) was determined. This means that PEGylation caused an affinity loss due to steric hindrance in the binding pocket. But PEGylated EXP3174 was still potent enough to bind the AT1Rs. Subsequently both substances served as references to rank the NP's affinities.

During the NP development process one structural feature turned out to be crucial. For this purpose differently composed core-shell NPs were manufactured:

- 1 EXP-NP<sub>5k</sub>, depicted in figure 6.2 (red frame)
- 2 EXP-NP90, depicted in figure 6.2 (blue frame)

The difference between these core-shell NPs can be found in the structure of the PEG shell. For both samples the targeting ligand EXP3174 was connected to a **5 kDa PEG chain** (EXP3174-PEG<sub>5k</sub>-polylactic acid (PLA)). But not the entire PEG shell was built of EXP3174 carrying PEG-PLA block-co-polymers. The shell was filled by methoxy-terminated PEG-PLA block-co-polymers (filling PEG).

The filling PEG had a MW of **5 kDa** for the EXP-NP<sub>5k</sub> and was reduced to **2 kDa** for the EXP-NP90. Their  $IC_{50}$  values were determined using a competitive CaA. The  $IC_{50}$  of EXP-NP<sub>5k</sub> accounted 225  $\mu$ M ( $pIC_{50}=3.6$ ). The  $IC_{50}$  of EXP-NP90 accounted only 235 nM ( $pIC_{50}=6.6$ ). This means that reducing the length of the filling PEG resulted in a tremendous affinity gain of three orders of magnitude. The EXP3174 molecules must be able to reach out of the PEG-shell to bind AT1Rs. The spike proteins of viruses are arranged in the same way [17–19].

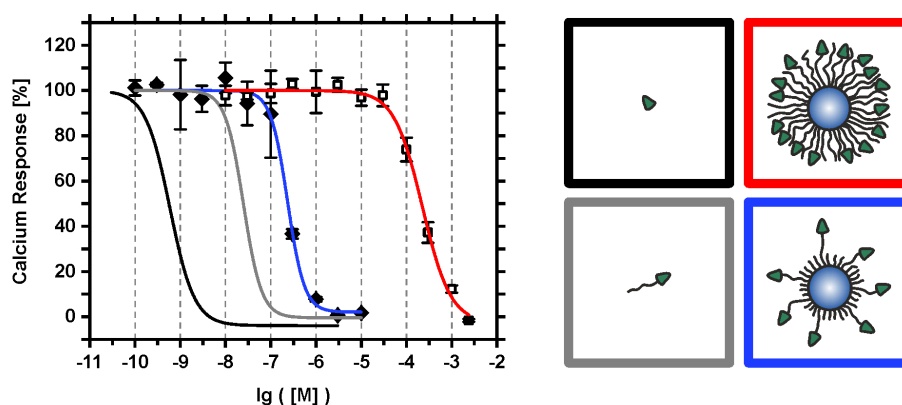


Figure 6.2: Competitive CaAs of EXP-NP90 (blue) and EXP3174-decorated NP with full 5k PEG shell (red). The fits of native EXP3174 (black) and PEGylated EXP3174 (grey) from figure 6.1 are plotted as a reference.

### 6.3.2 Ligand-Decorated Nanoparticles with a Sub-Nanomolar Avidity

The architecture of the PEG shell was essential for the affinity to target cells (refer to figure 6.2). However, 2 kDa MeO-PEG-PLA block-co-polymers increased the lipophilic proportion in the core-shell NPs. As a result the NP size was raised dramatically. So the hydrodynamic diameter of EXP-NP<sub>5k</sub> accounted  $41 \pm 1$  nm, while EXP-NP90 had a hydrodynamic diameter of  $105 \pm 13$  nm. This was a 2.5-fold increase. The polydispersity index (PDI) was identical ( $0.10 \pm 0.01$ ).

It was assumed that NPs must fit into clathrin-coated pits to enable multi-valent binding, as it is illustrated in figure 6.3. Clathrin is a protein coating the intracellular plasma membrane (PM). It builds a cage-like structure and induces cavities, namely clathrin-coated pits. Naive clathrin-coated pits have a size of 50 nm to 80 nm [20]. Different adapter proteins connect clathrin triskelions and the PM. Additionally, there are different cargo receptors discerning the proper cargo, for example NPs. Complexes of cargo and cargo receptors are mounted into the clathrin-coated pits via specific adapter proteins. The trapped cargo is subsequently totally wrapped by the clathrin-coated membrane until a clathrin-coated vesicles pinches off the PM (refer to figure 6.3) [21, 22].

Following this concept, EXP-NP90 were too large to fit into naive clathrin-coated pits. That's why MeO-PEG<sub>2k</sub>-PLA<sub>20k</sub> was completely substituted with HOOC-PEG<sub>2k</sub>-PLA<sub>20k</sub> to increase the hydrophilicity of the block-co-polymer. The substitution induced negative surface charges. The resulting EXP-NP60<sup>-</sup> had a hydrodynamic diameter of  $68 \pm 6$  nm (refer to figure 4.2) that was excellently fitting into clathrin-coated pits. But it must be admitted that clathrin-coated vesicles can grow up to 200 nm [20, 23] depending on the cargo properties. McMahon and Boucrot demonstrated the flexible pit size with electron micrographs for different organisms [23]. This means that, the larger EXP-

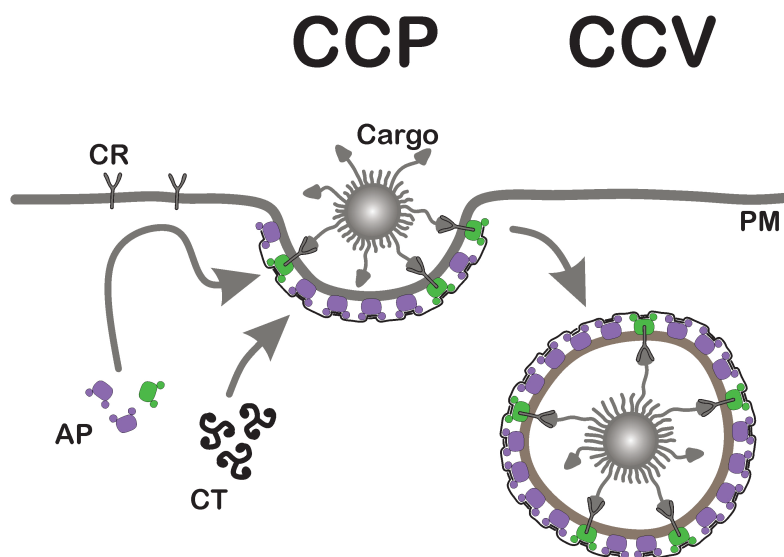


Figure 6.3: Formation of a clathrin-coated pit (CCP) and its maturation to a clathrin-coated vesicle (CCV). The size depends on the size of the trapped cargo [20, 23]. Specialized cargo receptors (CR) selectively bind their cargo and navigate them into clathrin-coated vesicles. In doing so, adapter proteins (AP) connect cargo receptors with the clathrin triskelions (CT) and induce a plasma membrane (PM) curvature until the cargo is fully wrapped [21, 22].

NP90 were still a promising candidate, since their larger surface area enables more targeting ligands to reach a target receptor.

Since the AT1R is a G-protein coupled receptor (GPCR) or rather a  $G_q$ -coupled GPCR, its activation leads to a calcium influx into the cytoplasm. Ang II is the physiological agonist for AT1Rs [14]. Its activation starts a signalling cascade, that mediates inter alia the secretion of vascular endothelial growth factor (VEGF). VEGF plays a key role in the pathogenesis of ocular diseases like AMD and diabetic retinopathy (DR) (refer to chapter 1). Consequently, promising pharmaceuticals have to interrupt the signalling cascade to prevent the secretion of VEGF. There are different tools to proof the specificity of EXP3174-decorated NPs for the AT1R-positive rMCs:

- 1 Displacement studies using flow cytometry
- 2 Indirect competition binding (CaA)
- 3 Competition binding (RL-A)

Non-targeted NP90 and NP served as controls for their EXP3174-decorated equivalents EXP-NP90 and NP60. Their architecture is illustrated in figure 6.4A.



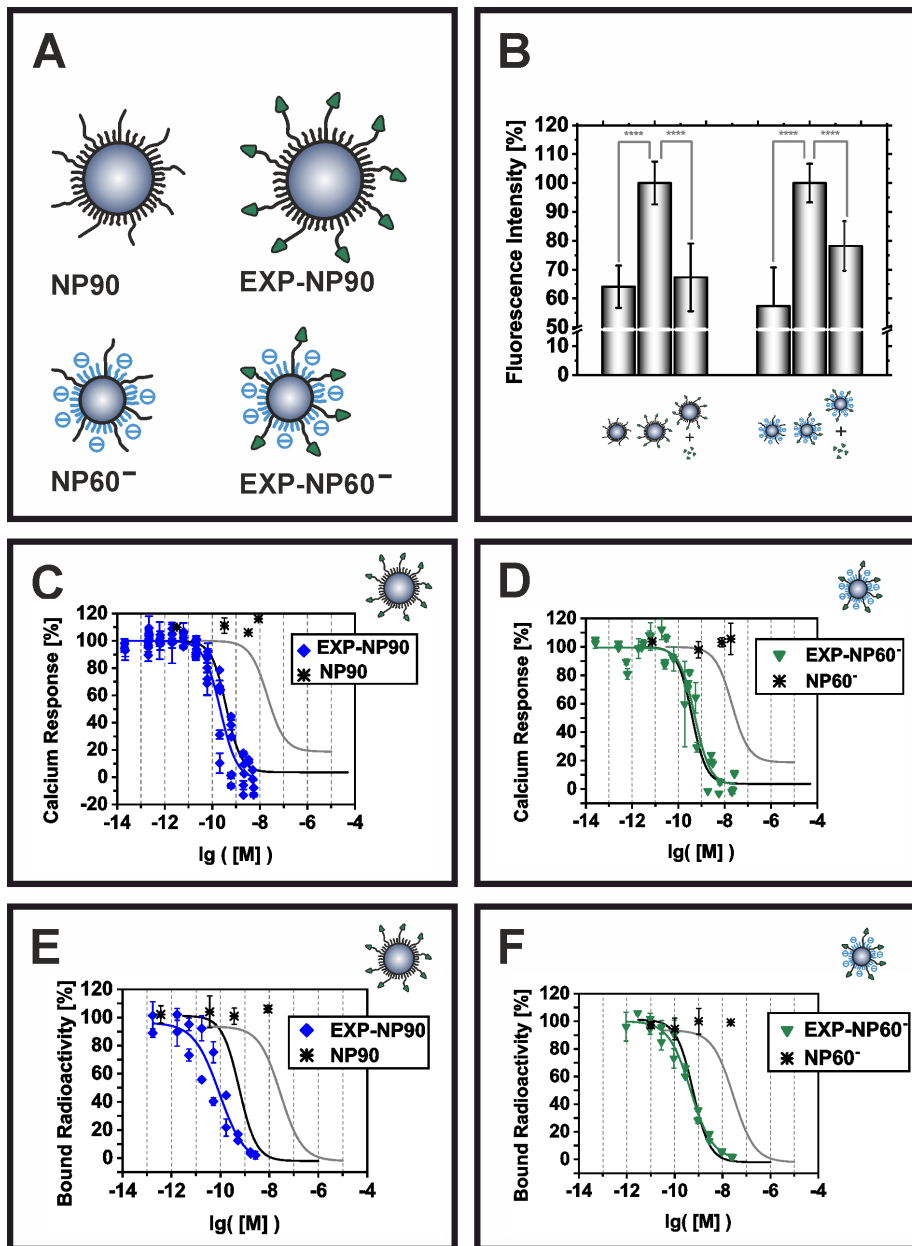


Figure 6.4: Overview of the binding experiments of EXP-NP90 and EXP-NP60<sup>-</sup>. (A): Architecture of investigated core-shell NPs. (B): Flow cytometry based displacement studies. (C-F): Competition binding assays ranked by the references naive EXP3174 (black line) and PEGylated EXP3174 (grey line).

In detail: CaA for EXP-NP90 (blue diamonds) and the non-targeted control NP90 (black asterisk) (C). CaA for EXP-NP60<sup>-</sup> (green triangles) and the non-targeted control NP60<sup>-</sup> (black asterisk) (D). RL-A for EXP-NP90 (blue diamonds) and the non-targeted control NP90 (black asterisk) (E). RL-A for EXP-NP60<sup>-</sup> (green triangles) and the non-targeted control NP60<sup>-</sup> (black asterisk) (F).

#### Displacement Studies

Flow cytometry is an analytical technique that enables the measurement of individual cells. The core-shell NPs were tagged with the fluorescent dye CF<sup>TM</sup>647. After the incubation and a thorough washing procedure rMCs were separated and analyzed. If the NPs were binding to the PM or taken up, emitted light in the deep red area could be detected. The results are plotted in figure 6.4B. The average fluorescence intensity of the incubated rMCs is illustrated in a bar chart.

NP90 obtained a fluorescence intensity of  $64.1 \pm 7.3\%$ , that was a significantly lower amount compared to the targeted EXP-NP90  $100.0 \pm 7.4\%$  ( $p = 0.0001$ ). This was expected because NP60<sup>-</sup> cannot specifically bind to the rMCs. Additionally the rMCs were pre-incubated with an excess of naive EXP3174 to block AT1Rs completely. Thus EXP-NP90 were no longer able to access the AT1Rs. The fluorescence intensity dropped down to  $67.3 \pm 11.7\%$ , that was the niveau of the control. This provides evidence for an AT1R-mediated binding of EXP-NP90 to rMCs.

The outlined experiments were performed for the EXP-NP60<sup>-</sup>s with the identical procedure. RMCs incubated with ligand-free NP60<sup>-</sup> obtained a mean fluorescence intensity of  $57.4 \pm 13.4\%$  normalized to the targeted EXP-NP60<sup>-</sup> with  $100.0 \pm 6.7\%$ . The fluorescence intensity of rMCs pre-incubated with an excess of naive EXP3174 again indicated a drop down. But a diminution to  $78.2 \pm 8.6\%$  was not the niveau of the corresponding control. Nevertheless, both differences were statistically significant ( $p = 0.001$ ). So the binding of EXP-NP60<sup>-</sup> was mediated by AT1Rs, too.

The results also reveal the high unspecific uptake of control NPs. The reason was not conclusively clarified. But the explanation could potentially found by the different routes of NPs into cells. There are many influencing parameters like physical properties (size, shape, rigidity), interaction with serum proteins (opsonization) and the NP architecture (polymeric, gold, silica, liposomes and much more) [24]. Since the difference between the targeted NPs and their corresponding controls is just the decoration with EXP3174 molecules, it must be assumed, that the targeted NPs follow other pathways into the cell than their controls.

In general, particles enter cells via energy-dependent processes, which could be subsumed under the term *endocytosis*, including:

- Pinocytosis
  - Macropinocytosis
  - Receptor-mediated endocytosis
    - \* Clathrin-mediated endocytosis
    - \* Caveolin-mediated endocytosis
    - \* Other specific receptors
- Phagocytosis

After activation of AT1Rs with its biological agonist Ang II, the GPCR undergoes a conformational change, starting the signalling cascade. Besides it

### 6.3. RESULTS AND DISCUSSION

---

enables the formation of a complex with adapter protein 2,  $\beta$ -arrestin and other proteins [25–27]. Adapter protein 2 owns a binding side for clathrin triskelion [25]. It guides the AT1R into clathrin-coated pits and initiates an internalization via clathrin-mediated endocytosis [28]. This pathway was confirmed by different groups, who inhibited clathrin mediated endocytosis with Sucrose (D(+)-Saccharose) (Suc) or pitstop-2 and found a profound decline in the uptake of radiolabeled Ang II [28, 29].

But EXP3174 is an AT1R-antagonist, it cannot induce the mentioned conformational change [14]. In good accordance, Conchon et. al. found a strong decline to less than 30 % for the uptake of non-peptidic AT1R antagonist losartan [29]. But this was still 1/3. Besides, this amount was further reduced to less than 15 % after inhibition of the clathrin mediated endocytosis pathway by incubating the cells with Suc [29]. Last but not least the peptidic antagonist [Sar1-Ile8]-Ang II induced an uptake of more than 75 %, that is practically identical to the peptidic agonist [Sar1]-Ang II [29].

Fierens et. al. investigated the internalization of candesartan, that is another insurmountable AT1R-antagonist [30]. They determined a very tight long-lasting binding to AT1Rs and found a high fraction of acid-resistant candesartan binding [30]. To remove surface bound molecules from the extracellular PM, cells were often incubated with moderate acidic solutions. Thus a high candesartan fraction after incubation at moderate acidic conditions pleads for a high uptake of candesartan. But the authors were sceptical, if surface bound candesartan could be removed under acidic conditions and propagated the residence of candesartan-AT1R complexes on the cell surface [30].

This data show the controversy of the topic. Insurmountable AT1R antagonists like EXP3174 or candesartan seem to remain on the PM without being endocytosed. This is due to the lack of interaction between the antagonist-receptor complex and the clathrin triskelion. Apart from that EXP3174-decorated NPs may behave differently. NP-related effects potentially change the uptake mechanism. But the strong attraction of EXP3174-decorated NPs and AT1Rs on the PM clearly plead for a receptor-mediated endocytosis pathway. From a thermodynamic perspective, multivalent NPs are able to address more receptors on a curved PM as it is the case in clathrin-coated pits than the same multivalent NP on the plane uncurved PM.

Summing up, EXP3174-decorated NPs most likely use a receptor mediated endocytosis pathway. It was expected that EXP3174-decorated NPs reside in clathrin-coated pits and remain on the cell surface. On the other hand side, the naive control NPs cannot take receptor-mediated endocytotic pathways, due to the lacking targeting ligands. They could potentially bind to the rMCs via macropinocytosis or if they were opsonized via phagocytosis. Maslanka et. al. manufactured similar core-shell NPs that were decorated with either angiotensin I (Ang I) [1] or Ang I plus EXP3174 [31]. The Ang I pro-ligands were enzymatically activated to Ang II, triggering the cellular uptake. Maslanka et. al. also used naive MeO-terminated NPs as a control in their flow cytometry studies [1]. The difference between the control and the targeted Ang I NPs was clearer. Their findings complement these results excellently. EXP-NP90 and EXP-NP60<sup>-</sup> lack of an endocytosis triggering ligand. That's why they remain

### 6.3. RESULTS AND DISCUSSION

---

on the cell surface, that is quickly saturated with NPs during the incubation interval. Without NP endocytosis there is no uptake and no enrichment of NPs in the cells, so that the measured fluorescence signal is less intensive. It can be concluded that EXP3174-decorated NPs reside on the extracellular PM and do not trigger an urged uptake.

#### Calcium Mobilisation Assays

The activation of  $G_q$ -coupled GPCRs initiates the influx of calcium ions into the cytoplasm. The average  $EC_{50}$  value was  $60.8 \pm 16.8$  nM ( $pEC_{50}=7.27 \pm 0.10$ ). This was in good accordance to the literature. Hennig et. al. determined an  $EC_{50}$  of  $70.1 \pm 1.8$  nM [12].

For the indirect competition assays rMCs were consistently stimulated with Ang II ( $EC_{80}$ ). Through the addition of different concentrations of naive EXP3174, PEGylated EXP3174 (EXP3174-PEG<sub>5k</sub>) or the different types of NPs their ability to suppress the calcium response was measured. The results are plotted in figure 6.4C-D. The references naive EXP3174 (black line) and EXP3174-PEG<sub>5k</sub> (grey line) are plotted. Figure 6.4C shows the results for NP90 (control) (black asterisk) and EXP-NP90 (blue diamonds). Whereas the results for NP60<sup>-</sup> (control) (black asterisk) and EXP-NP60<sup>-</sup> are depicted in figure 6.4D. Both controls (NP90 and NP60<sup>-</sup>) were not decorated with EXP3174 molecules and could not suppress the calcium response. However, the EXP3174-decorated NPs (EXP-NP90 and EXP-NP60<sup>-</sup>) inhibited the calcium response completely. This means that EXP3174-decorated core-shell NPs were able to target and silence the target receptor AT1R. Since the logarithmic PNC was plotted, the avidity for all NP types was obtained. While NP90 and NP60<sup>-</sup> had no avidity to the AT1Rs, EXP-NP90 had an  $IC_{50}$  value of  $293 \pm 65$  pM ( $pIC_{50}=9.60 \pm 0.11$ ) and EXP-NP60<sup>-</sup> had an  $IC_{50}$  value of  $591 \pm 145$  pM ( $pIC_{50}=9.27 \pm 0.11$ ).

Thus, both candidates had a sub-nanomolar avidity for AT1R-carrying rMCs. The larger EXP-NP90 even with a slightly higher avidity, since their larger surface area facilitated to reach more target receptors.

#### Radioligand Binding Assays

Keller et. al. kindly provided the tritium labeled angiotensin II derivative radioligand ( $[^3H]$ UR-MK292) [13]. RMCs were incubated with different concentrations of the radioligand  $[^3H]$ UR-MK292 (saturation binding) to determine the  $K_d$  and the average number of AT1Rs per cell. The  $K_d$  was  $1.2 \pm 0.1$  nM and the rMCs carried  $73\,258 \pm 18\,643$  AT1R per cell. These parameters were determined from independent saturation binding experiments. The binding curves are plotted in figure S2.

Furthermore, competitive RL-As were performed. RMCs were again pre-incubated with different concentrations of naive EXP3174, PEGylated EXP3174 or dilutions of the core-shell NP candidates.  $[^3H]$ UR-MK292 was added and the rMC-associated radioactivity was measured after the incubation time. The results are plotted in figure 6.4E-F. Naive EXP3174 (black line) and PEGylated EXP3174 (grey line) served as references. For naive EXP3174 an

### 6.3. RESULTS AND DISCUSSION

Table 6.1: Overview of the binding performance of the EXP3174-decorated core-shell NPs EXP-NP90 and EXP-NP60<sup>-</sup>. IC<sub>50</sub> and pIC<sub>50</sub> are specified as particle-related avidity. (\*) p=0.1; \* p=0.05

		EXP-NP90	EXP-NP60 <sup>-</sup>	Level of significance
Displacement <sup>(1)</sup>		Yes	Yes	
Competition <sup>(2)</sup>	IC <sub>50</sub> [pM]	293 ± 65	591 ± 145	(*)
	pIC <sub>50</sub>	9.60 ± 0.11	9.27 ± 0.11	
Competition <sup>(3)</sup>	IC <sub>50</sub> [pM]	98 ± 49	459 ± 49	*
	pIC <sub>50</sub>	10.04 ± 0.23	9.34 ± 0.07	

<sup>(1)</sup> flow cytometry experiments    <sup>(2)</sup> CaA    <sup>(3)</sup> RL-A using [<sup>3</sup>H]UR-MK292

IC<sub>50</sub> of 0.65 ± 0.09 nM (pIC<sub>50</sub>=9.19 ± 0.06) and for PEGylated EXP3174 an IC<sub>50</sub> of 30.5 ± 4.3 nM (pIC<sub>50</sub>=7.52 ± 0.04) was determined. Subfigure 6.4E shows the binding curve for EXP-NP90 (blue diamonds) and their non-targeted control NP90 (black asterisk). EXP3174-free NP90 were not able to inhibit the binding of [<sup>3</sup>H]UR-MK292. However, EXP-NP90 suppressed the binding of [<sup>3</sup>H]UR-MK292 completely and the IC<sub>50</sub> (NP-related avidity) was 98 ± 49 pM (pIC<sub>50</sub>=10.04 ± 0.23). The IC<sub>50</sub> can also be specified as ligand-related affinity, that was 517 ± 305 nM.

Subfigure 6.4F shows the binding curves for EXP-NP60<sup>-</sup> (green triangles) and their non-targeted control NP60<sup>-</sup> (black asterisk). EXP3174-free NP60<sup>-</sup> were not able to inhibit the binding of [<sup>3</sup>H]UR-MK292, whereas EXP-NP60<sup>-</sup> suppressed the binding completely with an IC<sub>50</sub> (NP-related avidity) of 459 ± 69 pM (pIC<sub>50</sub>=9.34 ± 0.07). The IC<sub>50</sub> can also be specified as ligand-related affinity, that was 488 ± 46 nM.

#### Comparison of the Binding Performance

Both EXP3174-decorated candidates (EXP-NP90 and EXP-NP60<sup>-</sup>) bound specifically to AT1Rs, which was confirmed by three independent techniques. The results are summarized in table 6.1 and checked for statistical significance. The competition binding assays (CaA and RL-A) coincidentally indicated a sub-nanomolar avidity. Furthermore, it was concluded that the larger EXP-NP90 had a statistically significant stronger avidity to the target cells (refer to table 6.1) than the smaller EXP-NP60<sup>-</sup>. The reason therefore was the higher surface area and the corresponding ability to reach more AT1Rs per NP.

#### 6.3.3 Localization of Binding Nanoparticles

The candidates EXP-NP90 and EXP-NP60<sup>-</sup> were decorated with EXP3174 molecules. EXP3174 is an insurmountable AT1R antagonist and cannot induce the conformational change [14] needed to expose the binding site for the clathrin mediated endocytosis pathway [25, 26, 28, 32]. That's why it was assumed that the targeted NPs reside on the surface of the rMCs. This

phenomenon was already described for naive candesartan, another insurmountable AT1R-antagonist [30].

To locate the NPs, adherent rMCs were incubated with CF<sup>TM</sup>647-labeled NPs and investigated with CLSM. The results are depicted in figure 6.5. RMCs are color-coded in green and the NPs on a red-to-white scale. Subfigures **A** show the binding of non-targeted NP90 (control) and the EXP3174-decorated EXP-NP90, whereas subfigure **B** illustrates the binding of non-targeted NP60<sup>-</sup> (control) and the EXP3174-decorated EXP-NP60<sup>-</sup>. Both subfigures indicated that EXP3174-decorated NPs remained cell associated after thorough washing steps. It can be recognized that these NPs are arranged in a sharp line bordering the cell's surface. The cell lumen was widely free of NP fluorescence. These pictures visualized the residence of EXP3174-decorated NPs on the cell surface. Maslanka et. al. designed Ang I-decorated core-NPs [33]. Ang I was enzymatically activated to Ang II, so that they can be described as agonist-decorated NPs. The authors also incubated adherent rMC with these agonistic NPs. Maslanka et. al. located agonistic core-shell NPs clearly in the cell lumen [33]. So the difference in the binding dynamics of agonistic- and antagonistic NPs became obvious.

Moreover, the NP distribution in a couple of planes was recorded through the z-axis. The corresponding z-stacks are depicted in figure 6.5C (EXP-NP90) and D (EXP-NP60<sup>-</sup>). Both candidates were located in the cell planes. This again confirmed the residence of the antagonistic EXP3174-decorated NPs on the cell surface.

#### 6.3.4 Nanoparticle Avidity to Cells with High Receptor Density

Inflammatory processes are able to trigger an upregulation of AT1Rs [2, 3]. That's why the NP avidity was additionally determined with a high-receptor density cell line. An increased avidity for high-receptor-density cells would suggest reduced off-target effects under pathological circumstances. Therefore, rMCs were transfected with a plasmid encoding for a human AT1R to receive HRD-rMC. Again saturation binding experiments with [<sup>3</sup>H]UR-MK292 were performed to determine the K<sub>d</sub> value and the AT1R density (refer to figure S3 for details). The K<sub>d</sub> of [<sup>3</sup>H]UR-MK292 for the transfected rMCs remained unchanged ( $1.0 \pm 0.2$  nM for HRD-rMC vs.  $1.2 \pm 0.1$  nM for untreated rMC). The receptor density increased 5-fold ( $356\,841 \pm 13\,877$  AT1R/HRD-rMC vs.  $73\,258 \pm 18\,643$  AT1R/rMC).

The competitive RL-As were repeated with the HRD-rMCs. Again naive EXP3174 and PEGylated EXP3174 served as references. The binding curves are plotted in figure 6.6C. The obtained half maximal inhibitory concentrations (IC<sub>50</sub>s) values for naive EXP3174 (black stars) and PEGylated EXP3174 (grey circles) accounted  $4.8 \pm 0.4$  nM (pIC<sub>50</sub>= $8.32 \pm 0.04$ ) and  $190.1 \pm 0.4$  nM (pIC<sub>50</sub>= $6.72 \pm < 0.01$ ).

In figure 6.6A the binding curves of EXP3174-decorated EXP-NP90 (blue diamonds) and the non-targeted control NPs NP90 (black asterisk) are plotted. EXP-NP90 had an IC<sub>50</sub> value of  $166.9 \pm 38.1$  pM (pIC<sub>50</sub>= $9.79 \pm 0.10$ ). Since they were lacking of EXP3174-ligands, the control NPs (NP90) were not able

6.3. RESULTS AND DISCUSSION

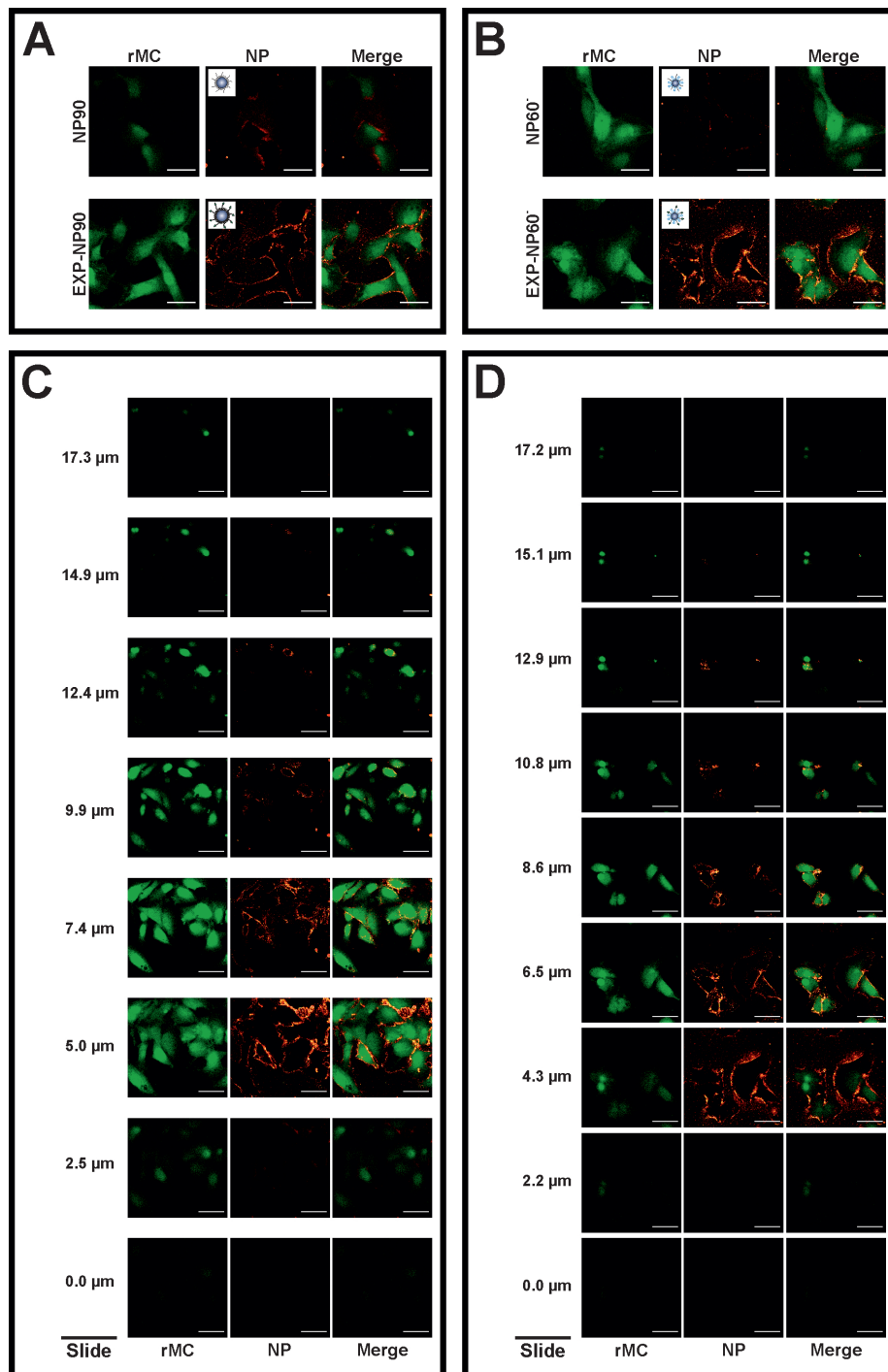


Figure 6.5: Images of CLSM experiments. The rMCs are color-coded in green and the CF<sup>TM</sup>647-labeled NPs in red-to-white. **A:** rMCs incubated with EXP-NP90 or NP90 (control). **B:** rMCs incubated with EXP-NP60<sup>-</sup> or NP60<sup>-</sup> (control). **C:** Z-stacks of EXP-NP90 sample. **D:** Z-stacks of EXP-NP60<sup>-</sup> sample. Scale bar corresponds to 50 μm.

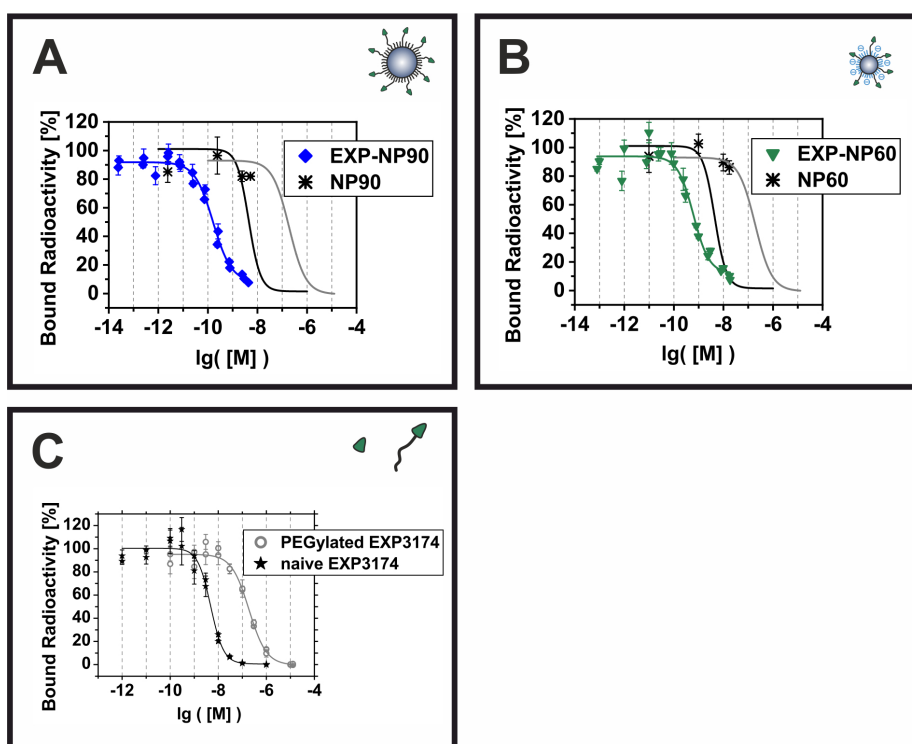


Figure 6.6: RL-A of EXP3174-decorated core-shell NPs using HRD-rMCs. **A:** EXP3174-decorated EXP-NP90 (blue diamonds) and the non-targeted control NP90 (black asterisk) in relation to naive EXP3174 (black fitting curve) and PEGylated EXP3174 (grey fitting curve). **B:** EXP3174-decorated EXP-NP60<sup>-</sup> (green triangles) and the non-targeted control NP60<sup>-</sup> (black asterisk) in relation to naive EXP3174 (black fitting curve) and PEGylated EXP3174 (grey fitting curve). **C:** Naive EXP3174 (black stars) and PEGylated EXP3174 (grey circles).



### 6.3. RESULTS AND DISCUSSION

to suppress the binding of the radioligand. Similarly, the binding curve of EXP3174-decorated EXP-NP60<sup>-</sup> (green triangles) and the non-targeted control NP60<sup>-</sup> (black asterisk) are plotted in figure 6.6B. EXP-NP60<sup>-</sup> had an IC<sub>50</sub> value of  $606.6 \pm 140.3$  pM ( $pIC_{50}=9.23 \pm 0.10$ ). NP60<sup>-</sup> were not able to suppress the binding of the radioligand, due to the lacking EXP3174-ligands. The binding parameters for rMC and HRD-rMC are summarized in table 6.2.

Table 6.2: Binding performance of naive EXP3174, PEGylated EXP3174 and EXP3174-decorated core-shell NPs to AT1R-carrying rMCs with different AT1R densities.

		rMC	HRD-rMC
Receptor Density	[AT1R/cell]	73 258 $\pm 18 643$	356 841 $\pm 13 877$
Naive EXP3174	IC <sub>50</sub> [nM] pIC <sub>50</sub>	$0.65 \pm 0.09$ $9.19 \pm 0.06$	$4.8 \pm 0.5$ $8.32 \pm 0.05$
PEGylated EXP3174	IC <sub>50</sub> [nM] pIC <sub>50</sub>	$30.5 \pm 4.3$ $7.52 \pm 0.04$	$190.1 \pm 0.5$ $6.72 \pm < 0.01$
EXP-NP90	IC <sub>50</sub> [pM] pIC <sub>50</sub>	$98 \pm 49$ $10.04 \pm 0.23$	$167 \pm 54$ $9.79 \pm 0.14$
EXP-NP60 <sup>-</sup>	IC <sub>50</sub> [pM] pIC <sub>50</sub>	$459 \pm 69$ $9.34 \pm 0.07$	$607 \pm 198$ $9.23 \pm 0.14$

The AT1R density of rMCs was raised 5-fold via transfection to receive HRD-rMCs. HRD-rMC served as a model cell line to mimic pathological circumstances. However, an avidity gain had not been found, but even a slight avidity loss. The reasons were not finally clarified in this work. Potentially, this was an effect that arose from the transfection process. HRD-rMCs carried murine and human AT1Rs that could explain that weak shift. However, these findings did not indicate a preference of EXP-NP90 or EXP-NP60<sup>-</sup> for HRD-rMCs. A plausible reason was found in the formation process of clathrin-coated pits. Since cargo receptors like AT1Rs guide their cargo (for instance NPs) into the pit (compare figure 6.3) and regulate their size [32], the morphology of the NPs, especially the number of available ligands, was pivotal for their avidity. Clathrin-coated pits are highly dynamic. Their initial sites pop up on the PM randomly. If there is cargo, stabilizing the PM curvature and recruiting more cargo receptors the assembly of the clathrin lattice is launched until the cargo was fully wrapped [34]. Consequently, an increased receptor density of the target cells would not alter the NP's avidity, since the cargo receptors are recruited to the assembling pits after initial NP attachment. However, these experiments were performed under static conditions. Fleischmann et. al. gave evidence that the binding behavior differs for static and dynamic conditions [35]. An injection of the NP dispersion into the bloodstream and the rapid distribution

through the circuit belongs to dynamic conditions. There is just a narrow time frame for the specific recognition of the target cells. That's why, an increased receptor density could still increase the likelihood for an initial binding and reduce off-target effects *in vivo*.

## 6.4 Conclusion

The avidity of EXP3174-decorated core-shell NPs EXP-NP90 and EXP-NP60<sup>-</sup> to an AT1R-positive model cell line was proven. Both candidates featured a sub-nanomolar avidity, that was proven by a functional CaA and a direct RL-A (refer to figure 6.4). These findings were outstanding, since it means that the NP's avidity overcome the affinity of the naive targeting molecule EXP3174 itself. Consequently, both candidates showed a stronger avidity than the EXP3174-decorated model NPs that were introduced by Hennig et. al. [12]. In addition, these experiments substantiated the NP's ability to target AT1Rs and concurrently to silence the receptor signalling. These properties are mandatory for a therapeutical application. Further experiments gave valuable information about the NP's binding behavior. So the displacement studies confirmed the receptor-mediated binding to target cells for another time. Besides the localization of the NPs during binding fortified the antagonistic nature of the designed NPs (refer to section 6.3.3).

Apart from that, an avidity gain for target cells with an increased target receptor density was not substantiated. However, these static *in vitro* testings could not mimic the dynamic conditions after an systemic application. During the circulation in the bloodstream, targeting of pathologically changed cells could still be favored due to the increased target receptor density. EXP-NP90 as well as EXP-NP60<sup>-</sup> core-shell NPs were promising candidates for an *in vivo* application. Based on these findings, both candidates should be tested in a mouse model.

## 6.5 References

- [1] Sara Maslanka Figueroa et al. "Influenza A Virus Mimetic Nanoparticles Trigger Selective Cell Uptake". In: *Proceedings of the National Academy of Sciences* 116.20 (2019). DOI: 10.1073/pnas.1902563116.
- [2] Georg Nickenig and David G. Harrison. "The AT1-Type Angiotensin Receptor in Oxidative Stress and Atherogenesis: Part II: AT1 Receptor Regulation". In: *Circulation* 105.4 (2002), pp. 530–536. DOI: 10.1161/hc0402.102619.
- [3] Toshihide Kurihara et al. "Neuroprotective Effects of Angiotensin II Type 1 Receptor (AT1R) Blocker, Telmisartan, via Modulating AT1R and AT2R Signaling in Retinal Inflammation". In: *Investigative Ophthalmology & Visual Science* 47.12 (2006), pp. 5545–5552.
- [4] Robert Hennig et al. "Multivalent Nanoparticles Bind the Retinal and Choroidal Vasculature". In: *Journal of Controlled Release* 220.A (2015), pp. 265–274. DOI: 10.1016/j.jconrel.2015.10.033.

## 6.5. REFERENCES

---

- [5] Kathrin Abstiens, Manuel Gregoritz, and Achim Michael Goepferich. "Ligand Density and Linker Length are Critical Factors for Multivalent Nanoparticle-Receptor Interactions". In: *ACS Applied Materials & Interfaces* 11.1 (2019), pp. 1311–1320. DOI: 10.1021/acsami.8b18843.
- [6] Mathai Mammen, Seok-Ki Choi, and George M. Whitesides. "Polyvalent Interactions in Biological Systems: Implications for Design and Use of Multivalent Ligands and Inhibitors". In: *Angewandte Chemie Internationale Edition* 37.20 (1998), pp. 2754–2794. DOI: 10.1002/(SICI)1521-3773(19981102)37:20<2754::AID-ANIE2754>3.0.CO;2-3.
- [7] Alaaldin M. Alkilany et al. "Ligand Density on Nanoparticles: A Parameter with Critical Impact on Nanomedicine". In: *Advanced Drug Delivery Reviews* 143 (2019), pp. 22–36. DOI: 10.1016/j.addr.2019.05.010.
- [8] Justin E. Silpe et al. "Avidity Modulation of Folate-Targeted Multivalent Dendrimers for Evaluating Biophysical Models of Cancer Targeting Nanoparticles". In: *ACS Chemical Biology* 8.9 (2013), pp. 2063–2071.
- [9] Sara Maslanka Figueroa et al. "Nanoparticles Mimicking Viral Cell Recognition Strategies are Superior Transporters into Mesangial Cells". In: *Advanced Science* 7.11 (2020). DOI: 10.1002/advs.201903204.
- [10] Takayuki Inuzuka et al. "Attenuation of Ligand-Induced Activation of Angiotensin II Type 1 Receptor Signaling by the Type 2 Receptor via Protein Kinase C". In: *Scientific Reports* 6 (2016). DOI: 10.1038/srep21613..
- [11] G. Grynkiewicz, M. Poenie, and R. Y. Tsien. "A New Generation of Ca<sup>2+</sup> Indicators with Greatly Improved Fluorescence Properties". In: *Journal of Biological Chemistry* 260.6 (1985), pp. 3440–3450. DOI: 10.1016/S0021-9258(19)83641-4.
- [12] Robert Hennig et al. "Nanoparticle Multivalency Counterbalances the Ligand Affinity Loss upon PEGylation". In: *Journal of Controlled Release* 194 (2014), pp. 20–27. DOI: 10.1016/j.jconrel.2014.07.062.
- [13] Max Keller et al. "Mimicking of Arginine by Functionalized N $\omega$ -Carbamoylated Arginine as a New Broadly Applicable Approach to Labeled Bioactive Peptides: High Affinity Angiotensin, Neuropeptide Y, Neuropeptide FF, and Neurotensin Receptor Ligands as Examples". In: *Journal of Medicinal Chemistry* 59.5 (2016), pp. 1925–1945. DOI: 10.1021/acs.jmedchem.5b01495.
- [14] M. de Gasparo et al. "International Union of Pharmacology. XXIII. The Angiotensin II Receptors". In: *Pharmacological Reviews* 52.3 (2000), pp. 415–472.
- [15] Haitao Zhang et al. "Structure of the Angiotensin Receptor Revealed by Serial Femtosecond Crystallography". In: *Cell* 161.4 (2015), pp. 833–844. DOI: 10.1016/j.cell.2015.04.011.
- [16] A. Sachinidis et al. "EXP3174, a Metabolite of Losartan (MK 954, DuP 753) is more Potent than Losartan in Blocking the Angiotensin II-Induced Responses in Vascular Smooth Muscle Cells". In: *Journal of Hypertension* 11.2 (1993), pp. 155–162. DOI: 10.1097/00004872-199302000-00007.

## 6.5. REFERENCES

---

- [17] Tomasz Wierzbicki et al. “Effect of Receptors on the Resonant and Transient Harmonic Vibrations of Coronavirus”. In: *Journal of the Mechanics and Physics of Solids* 150 (2021). DOI: 10.1016/j.jmps.2021.104369.
- [18] Wan Beom Park et al. “Virus Isolation from the First Patient with SARS-CoV-2 in Korea”. In: *Journal of Korean Medical Science* 35.7 (2020). DOI: 10.3346/jkms.2020.35.e84.
- [19] Ping Zhu et al. “Distribution and Three-Dimensional Structure of AIDS Virus Envelope Spikes”. In: *Nature* 441.7095 (2006), pp. 847–852. DOI: 10.1038/nature04817.
- [20] B. M. Pearse and R. A. Crowther. “Structure and Assembly of Coated Vesicles”. In: *Annual Review of Biophysics and Biophysical Chemistry* 16 (1987), pp. 49–68. DOI: 10.1146/annurev.bb.16.060187.000405.
- [21] F. M. Brodsky. “Clathrin and Clathrin-Dependent Endocytosis”. In: *Encyclopedia of Cell Biology*. Vol. 2, pp. 384–393. DOI: 10.1016/B978-0-12-394447-4.20038-2.
- [22] Marko Kaksonen and Aurélien Roux. “Mechanisms of Clathrin-Mediated Endocytosis”. In: *Nature Reviews Molecular Biology* 19.5 (2018), pp. 313–326. DOI: 10.1038/nrm.2017.132.
- [23] Harvey T. McMahon and Emmanuel Boucrot. “Molecular Mechanism and Physiological Functions of Clathrin-Mediated Endocytosis”. In: *Nature Reviews Molecular Biology* 12.8 (2011), pp. 517–533. DOI: 10.1038/nrm3151.
- [24] Darío Manzanares and Valentín Ceña. “Endocytosis: The Nanoparticle and Submicron Nanocompounds Gateway into the Cell”. In: *Pharmaceutics* 12.4 (2020). DOI: 10.3390/pharmaceutics12040371.
- [25] Delphine Fessart, May Simaan, and Stéphane A. Laporte. “C-Src Regulates Clathrin Adapter Protein 2 Interaction with Beta-Arrestin and the Angiotensin II Type 1 Receptor During Clathrin-Mediated Internalization”. In: *Molecular Endocrinology* 19.2 (2005), pp. 491–503. DOI: 10.1210/me.2004-0246.
- [26] Marie-Eve Poupart et al. “ARF6 Regulates Angiotensin II Type 1 Receptor Endocytosis by Controlling the Recruitment of AP-2 and Clathrin”. In: *Cellular Signalling* 19.11 (2007), pp. 2370–2378. DOI: 10.1016/j.cellsig.2007.07.015.
- [27] Robert J. Lefkowitz and Sudha K. Shenoy. “Transduction of Receptor Signals by  $\beta$ -Arrestins”. In: *Science* 308.5721 (2005), pp. 512–517. DOI: 10.1126/science.1109237.
- [28] Thomas A. Morinelli et al. “Clathrin-Dependent Internalization of the Angiotensin II AT1A Receptor Links Receptor Internalization to COX-2 Protein Expression in Rat Aortic Vascular Smooth Muscle Cells”. In: *European Journal of Pharmacology* 748 (2015), pp. 143–148. DOI: 10.1016/j.ejphar.2014.12.018.
- [29] Sophie Conchon et al. “Internalization of the Rat AT1a and AT1b Receptors: Pharmacological and Functional Requirements”. In: *FEBS Letters* 349.3 (1994), pp. 365–370. DOI: 10.1016/0014-5793(94)00703-9.

## 6.5. REFERENCES

---

- [30] Frederik L.P. Fierensa et al. "Tight Binding of the Angiotensin AT1 Receptor Antagonist [3H]Candesartan is Independent of Receptor Internalization". In: *Biochemical Pharmacology* 61.10 (2001), pp. 1227–1235. DOI: 10.1016/S0006-2952(01)00614-1.
- [31] Sara Maslanka Figueroa et al. "Thermodynamic, Spatial and Methodological Considerations for the Manufacturing of Therapeutic Polymer Nanoparticles". In: *Pharmaceutical Research* 37.3 (2020). DOI: 10.1007/s11095-020-2783-4.
- [32] Manojkumar A. Puthenveedu and Mark von Zastrow. "Cargo Regulates Clathrin-Coated Pit Dynamics". In: *Cell* 127.1 (2006), pp. 113–124. DOI: 10.1016/j.cell.2006.08.035.
- [33] Sara Maslanka Figueroa et al. "The Effect of Ligand Mobility on the Cellular Interaction of Multivalent Nanoparticles". In: *Macromolecular Bioscience* 20.4 (2020). DOI: 10.1002/mabi.201900427.
- [34] Emanuele Cocucci et al. "The First Five Seconds in the Life of a Clathrin-Coated Pit". In: *Cell* 150.3 (2012), pp. 495–507. DOI: 10.1016/j.cell.2012.05.047.
- [35] Daniel Fleischmann, Sara Maslanka Figueroa, and Achim Goepperich. "Steric Shielding of cRGD-Functionalized Nanoparticles from Premature Exposition to Off-Target Endothelial Cells under a Physiological Flow". In: *ACS Applied Bio Materials* 4.1 (2021), pp. 640–650. DOI: 10.1021/acsbm.0c01193.



## **Chapter 7**

# **Number of Binding Ligands**

## Abstract

Core-shell nanoparticles (NPs) decorated with the angiotensin II receptor type 1 (AT1R) antagonist losartan carboxylic acid (EXP3174) had a sub-nanomolar avidity for their target cells. The  $pIC_{50}$  of larger EXP-NP90 (size  $105 \pm 13$  nm) was  $10.04 \pm 0.23$  and  $9.34 \pm 0.07$  for the smaller EXP-NP60<sup>-</sup> (size  $68 \pm 6$  nm). The reason for this outstanding avidity was found in the multivalent binding. But how many EXP3174 molecules of a single core-shell NP were needed to develop such an outstanding avidity? The experiments revealed 9.2 EXP3174 molecules per EXP-NP90 particle and 7.7 per EXP-NP60<sup>-</sup> particle. This means that less than 1% of the available ligands had bound to the plasma membrane (PM)-presented target receptors. The investigated core-shell NPs were labeled with ultra-small gold particles, so that they were traceable via inductively coupled plasma (ICP)-mass spectrometry (MS). After the disintegration in *aqua regia* the number of PM-attached core-shell NPs could be determined.

## 7.1 Introduction

It is the intention of active drug targeting to navigate pharmaceuticals to their target site. As a result, side effects should be clearly reduced that is especially important for anti-cancer drugs [1]. In particular, active drug targeting is utilized in the field of nanomedicine [2–4]. Therefore different kinds of NPs are decorated with widely varying targeting molecules (ligands) [5, 6]. These molecules recognize receptors, so that the carrying NP binds to the corresponding cell. However, the collision between the receptor and the ligand is basically needed for the formation of any ligand-receptor complex [7, 8]. Multivalent NPs carry a multitude of ligand molecules, so that the chance for the formation of further ligand-receptor complexes rises dramatically after the initial binding. But this raises the question how many ligands are needed to design a NP with an outstanding avidity to its target cells?

For this purpose, two differently sized polymeric core-shell NPs were designed: (a) large methoxy-terminated EXP-NP90 ( $105 \pm 13$  nm) and (b) small carboxy-terminated EXP-NP60<sup>-</sup> ( $68 \pm 6$  nm). Both candidates were decorated with EXP3174 molecules. They possessed a sub-nanomolar avidity for AT1R-positive cells ( $pIC_{50}(\text{EXP-NP90})=10.04 \pm 0.23$  and  $pIC_{50}(\text{EXP-NP60}^-)=9.44 \pm 0.07$ , refer to chapter 6). The NP shell was composed of polyethylene glycol (PEG) with a molecular weight (MW) of 2 kDa. However, the EXP3174 ligands were attached via 5 kDa PEG chains. Thus the EXP3174 ligands were situated on the NP surface like spikes of a virus [9, 10]. Each NP was decorated with  $3500 \pm 1499$  (EXP-NP90) or  $1017 \pm 382$  (EXP-NP60<sup>-</sup>) EXP3174 molecules. Considering their different sizes, the average distance between two ligands was 3.75 nm and 4.54 nm (refer to chapter 4). The targeting receptor (AT1R) consists of 359 amino acids [11]. Maslanka et. al. calculated 4.6 nm for the diameter of a single AT1R [12]. Consequently, the average distance between two ligands was smaller than the AT1R itself. This means that those NPs carried more ligands than theoretically bind on mathematical terms. It is hypothesized that binding NPs were situated in membrane cavities like clathrin-coated pits. So they were able to reach more AT1Rs than they could



reach on a plane membrane element. These considerations are illustrated in figure 7.2.

Here the core-shell NP candidates EXP-NP90 and EXP-NP60<sup>-</sup> were tagged with ultra-small gold particles to determine the amount of cell associated NPs during binding. It is the goal to receive further information about the ideal design of core-shell NPs for active drug targeting.

## 7.2 Material and Methods

### 7.2.1 Material

EXP3174 was synthesized as previously described (refer to section 3.2.4). All other chemicals were purchased from Sigma-Aldrich (Taufkirchen/ Germany), if not stated otherwise. A Milli-Q purification system (Millipore/ Schwalbach/ Germany) was used to prepare fresh ultrapure water. It is hereinafter just named water.

### 7.2.2 Manufacturing Gold-Tagged Nanoparticles

Core-shell NPs were manufactured via nanoprecipitation as it is described in section 4.2.2. The manufacturing formula was adapted to receive the gold-tagged NPs **EXP3174 decorated NP90 (EXP-NP90)-Au** and **EXP3174 decorated NP60<sup>-</sup> (EXP-NP60<sup>-</sup>)-Au**. The poly(lactic-co-glycolic) acid (PLGA)-stock solution was partly replaced by a PLGA-Au solution. Monoamino gold NPs were purchased from Nanopartz (Loveland/ CO/ USA) and covalently bound to PLGA polymers. The coupling procedure is described in section 3.2.9. The monoamino gold NPs had a size of 2.2 nm. Due to solubility aspects PLGA-Au was soluted to a final concentration of 10 mg ml<sup>-1</sup>. The final formulation is listed in table 7.1.

### 7.2.3 Analytics of the Nanoparticle Dispersions

The NP size and the particle size distribution were measured via dynamic light scattering (DLS). To determine the particle number concentration (PNC) the following function was used:

$$PNC = \frac{TPC}{\rho_{NP} \times \frac{1}{6}\pi (d_H)^3 \times N_A} \quad (7.1)$$

*TPC* is the total polymer content,  $\rho_{NP}$  is the NP density,  $d_h$  is the hydrodynamic diameter and  $N_A$  is the Avogadro constant. The derivation is described in chapter 4. The EXP3174 content of the NP dispersions was quantified with a fluorescence assay. The absence of naive EXP3174 contamination has already been proven (refer to chapter 3).

#### Dynamic Light Scattering

The NP dispersions were analyzed with a Zetasizer nano ZS (Malvern Instruments/ Malvern/ UK). Here, hydrodynamic diameter ( $d_h$ ) and polydispersity index (PDI) were reported. The protocol is described in section 4.2.3.

## 7.2. MATERIAL AND METHODS

Table 7.1: Manufacturing formulation of a **gold-tagged** NP batch.

		EXP-NP90-Au	EXP-NP60-Au
Organic phase	Stock dil. of	[ $\mu$ l]	[ $\mu$ l]
	EXP3174-PEG <sub>5k</sub> -PLA <sub>20k</sub>	18	18
	MeO-PEG <sub>2k</sub> -PLA <sub>20k</sub>	62	-
	HOOC-PEG <sub>2k</sub> -PLA <sub>20k</sub>	-	62
	<b>PLGA</b> <sub>13.4k</sub>	<b>32</b>	<b>32</b>
	<b>PLGA-Au</b> <sup>(1)</sup>	<b>20</b>	<b>20</b>
<b>ACN</b>		<b>368</b>	<b>368</b>
		[ml]	[ml]
Aqueous phase	DPBSx0.1	5.0	5.0

<sup>(1)</sup> stock dilution with 10 mg ml<sup>-1</sup>

### Particle Number Concentration

The total polymer content (TPC) was measured with an iodine assay using the previously described calibration (refer to section 4.2.5). The hydrodynamic diameter was determined via DLS and  $\rho_{NP}$  was taken from the literature (1.25 g cm<sup>-3</sup> for PEG-poly(lactic acid) (PLA) NPs [13]).

### EXP3174 Content

The content of EXP3174 ligands was quantified via fluorescence measurements. The samples were excited at 250 nm and the emitted light was detected at 350 nm. The protocol is described in section 4.2.7.

### 7.2.4 Cell Culture

Rat mesangial cells (rMCs) were a kind gift of Prof. Armin Kurtz (Institute of Physiology/ University of Regensburg/ Germany). The cells were cultured in RPMI 1640 medium supplemented with 10% fetal bovine serum (FBS) (Biowest/ Nuaille/ France), insulin-transferrin-selenium (ITS) (Invitrogen) and 100 nM hydrocortisone. They were grown in a water-saturated carbon dioxide enriched atmosphere (5% CO<sub>2</sub>) at 37 °C. Therefore the incubator CellXpert®170 (Eppendorf/ Hamburg/ Germany) was used.

Rat mesangial cells (rMCs) were chosen due to their stable AT1R expression over numerous passages. AT1R expression was previously shown by Maslanka et. al. [14].

### 7.2.5 Ligand-Receptor Complexes per Nanoparticle

For the determination of the average number of ligand-receptor complexes that a single core-shell NP established, a complex experimental setup was designed. The total number of available AT1Rs during the experiment were measured with a saturation binding experiment using the tritium labeled angiotensin II derivative radioligand ( $[^3\text{H}]\text{UR-MK292}$ ) [15]. In order to measure the number of target cell attached NPs, the complete cell layer and the attached NPs were disintegrated in *aqua regia*. Since the core-shell NPs carried a gold-tag, it was possible to measure the gold concentration via ICP-MS and to calculate the number of cell-attached core-shell NPs. Moreover, the cell number during the experiment was counted with a Neubauer-improved counting chamber to calculate the AT1R expression level.

$3 \times 10^5$  rMCs per well were seeded into TC-treated cell culture 12-well plates (Eppendorf/ Hamburg/ Germany) from a homogeneous cell suspension. On the day of the experiment confluency of the rMCs was at least 90 %.

After removing the culture medium, living rMCs were washed with 500  $\mu\text{l}$  Dulbecco's Phosphate Buffered Saline (DPBS) (Gibco<sup>TM</sup>/Life Technologies/ Paisly/ UK) twice. Then the cell layers were covered with 600  $\mu\text{l}$  binding buffer. The binding buffer was composed of Leibovitz L-15 medium (without phenol red) (Gibco<sup>TM</sup>/ Life Technologies/ Grand Island/ USA) and bovine serum albumin (BSA) (0.1 %). For the saturation binding experiments the binding buffer was additionally supplemented with bacitracin (100  $\mu\text{g ml}^{-1}$ ).

#### Saturation Binding

At the beginning of the experiment (designated 0h) always 75  $\mu\text{l}$  of the EXP3174 and the radioligand concentrates (x10) (=unspecific binding) OR 75  $\mu\text{l}$  of the binding buffer and the radioligand concentrates (x10) (=total binding) were added. The final working volume accounted 750  $\mu\text{l}$ .  $[^3\text{H}]\text{UR-MK292}$  was kindly provided by Dr. Max Keller (Pharmaceutical Chemistry/ University of Regensburg/ Regensburg/ Germany) [15]. The specific activity was 1.407 TBq  $\text{mmol}^{-1}$ . EXP3174 was soluted in cell-culture grade dimethyl sulphoxide (DMSO) (50 mM) and further diluted with binding buffer.

During the experiment rMCs were exposed to a series of radioligand concentrations ranging from 0.08 nM to 10 nM (total binding). Separately, EXP3174 was additionally added in a 500-fold excess to block AT1Rs (unsecific binding). The plates were gently shaken during the incubation period of 2 h at room temperature (RT). Afterwards the supernatants were removed by suction, rMCs were washed with ice-cold DPBS twice and 800  $\mu\text{l}$  lysis buffer were added. The lysis buffer was composed of urea (Merck/ Darmstadt/ Germany) (8 M), Triton<sup>TM</sup>X-100 (1 %) and glacial acetic acid (Merck/ Darmstadt/ Germany) (3 M). After a further incubation period of 30 min the cell lysates were transferred into scintillation vials filled with 2.5 ml liquid scintillator (Rotiszint eco plus/ Carl Roth/ Karlsruhe/ Germany) and counted with the liquid scintillation counter LS6500 (Beckmann-Coulter).

The data were analyzed using the Origin 2020 SR1 software (OriginLab/ Northampton/ MA/ USA). Unspecific binding was substracted from total

binding to obtain the specific binding.

#### Cell Disintegration and ICP-MS Analytics

At the beginning of the experiment 75  $\mu\text{l}$  EXP3174 stock dilution ( $\times 10$ ) OR binding buffer were added carefully and pre-incubated for 30 min at RT. Then 75  $\mu\text{l}$  of the gold-tagged NP dispersions were added and incubated for 1.5 h at RT. Afterwards the incubation media were removed by suction and the cell layers were washed with ice-cold DPBS twice. Then the supernatants were removed and 1.5 ml freshly prepared *aqua regia* (one part of 65 % nitric acid (Fisher Scientific/ Loughborough/ UK) and three parts 37 % hydrochloric acid (VWR International/ Fontenay-sous-Bois/ France) were used to disintegrate the cells and the gold completely. The plates were situated in a water bath at 60 °C for at least 4 h. Afterwards the solution was transferred quantitatively into volumetric flasks (nominal volume 5 ml), spiked with 10  $\mu\text{l}$  scandium calibration solution (10  $\mu\text{g ml}^{-1}$ ) (Perkin Elmer/ Shelton/ CT/ USA) as internal standard and filled up with 1 M nitric acid.

Multi-element standard solution (PerkinElmer/ Shelton/ CT/ USA) containing 10  $\mu\text{g ml}^{-1}$  gold was used to prepare calibration standards from 0.1 pbb to 60 pbb. Each calibration standard was supplemented with 10  $\mu\text{l}$  of the mentioned scandium calibration solution.

The gold measurements were performed on an ICP-MS ELAN 9000 (Perkin Elmer). The device was operated with the Elan software version 3.0. The results were normalized to the internal scandium standard.

#### Cell Counting

At the beginning of the experiment 75  $\mu\text{l}$  binding buffer was added twice. The cell plates were incubated for 2 h at RT. Afterwards the incubation media were removed by suction and the cell layers were washed with ice-cold DPBS once. Then rMCs were quantitatively detached using trypsin-EDTA 0.25 % (Gibco™/Life Technologies/ Paisley/ UK), centrifuged (200 $\times$ g, 5 min, 4 °C) and resuspended in DPBS. The cells were counted using a Neubauer improved counting cell (Laboroptik/ Friedrichsdorf/ Germany) in duplicates. The average cell number per well was determined for a complete plate.

## 7.3 Results and Discussion

### 7.3.1 Theoretical Background

The following approach was established to unveil how many ligands of a single NP bind to a target cell. Basically, ligand-carrying NPs were incubated with a model cell line, while the average number of ligand-receptor complexes was quantified. Here the number of binding ligands ( $N_{bound}$ ) was equal to the number of EXP3174-occupied AT1Rs ( $N_{oc}$ ). Additionally, the absolute number of PM attached NPs ( $N_{LR}$ ) was needed to calculate  $N_{bound}$ . Consequently,  $N_{bound}$  was calculated by the following function:

### 7.3. RESULTS AND DISCUSSION

---

$$N_{bound} = \frac{N_{oc}}{N_{LR}} \quad (7.2)$$

These considerations supposed that NPs exclusively interacted via AT1Rs with the rMCs.  $N_{oc}$  and  $N_{LR}$  were determined in separate experimental parts. The protocols were almost identical, although the sample preparation and the final read out differed. The cell culture plates were seeded from a unique homogeneous cell suspension and incubated simultaneously to ensure a homogeneous testing environment.

$N_{oc}$  was investigated utilizing a **saturation binding experiment** with the tritium labeled angiotensin II derivative radioligand ( $[^3\text{H}]\text{UR-MK292}$ ) [15].  $N_{LR}$  was investigated using gold-tagged NPs that were quantified via ICP-MS analysis. Therefore, an *aqua regia* based **gold disintegration** procedure was developed.

#### Number of Occupied Receptors - $N_{oc}$

The number of ligand-receptor complexes  $N_{oc}$  was derived from the total number of available AT1R receptors ( $N_{AT1R}$ ). Two different approaches were conceivable:

- 1 NPs were applied in an **50-fold excess** with respect to their equilibrium dissociation constant ( $K_i$ ), so that practically all AT1Rs were occupied by ligands:

$$N_{oc} = N_{AT1R}$$

or

- 2 NPs were **equally** applied to their  $K_i$  value, so that half of the total number of available AT1Rs ( $N_{AT1R}$ ) were occupied by ligands:

$$N_{oc} = 0.5 \times N_{AT1R}$$

Approach 1 required the preparation of a vigorously up-concentrated NP stock dilution. This was not feasible due to stability aspects. Hence, the NPs were applied exactly at their  $K_i$  (approach 2). Combining approach 2 and equation 7.2 gave the following function:

$$N_{bound} = \frac{0.5 \times N_{AT1R}}{N_{LR}} \quad (7.3)$$

$N_{AT1R}$  was determined with the **saturation binding experiment**. Since the investigated NPs were not radioactively labeled itself,  $K_i$  must be calculated from their half maximal inhibitory concentration ( $\text{IC}_{50}$ ) value using the Cheng-Prusoff correction: [16]

$$K_i = \frac{\text{IC}_{50}}{\left(\frac{[\text{RL}^*]}{K_d} + 1\right)} \quad (7.4)$$

### 7.3. RESULTS AND DISCUSSION

Here  $[RL^*]$  is applied concentration of  $[^3H]UR-MK292$  during the competitive binding assay ( $[RL^*] = 1.0 \text{ nM}$ ). The equilibrium dissociation constant of the ligand-receptor complex ( $K_d$ ) value of  $[^3H]UR-MK292$  was  $1.2 \text{ nM}$  (refer to figure S2). The  $IC_{50}$  values (ligand-related affinity) were taken from chapter 6. The calculated  $K_i$  values are listed in table 7.2.

Table 7.2: Ligand-related  $K_i$  and  $IC_{50}$  values of EXP-NP90 and EXP-NP60<sup>-</sup>.

	EXP-NP90	EXP-NP60 <sup>-</sup>
$IC_{50} \text{ [nM]}$	517	488
$K_i \text{ [nM]}$	<b>282</b>	<b>266</b>

The concentration of core-shell NPs was adjusted to their individual  $K_i$  value. Therefore half of the available AT1Rs were occupied with EXP3174 ligands.

#### 7.3.2 Experimental

As already mentioned,  $N_{bound}$  can be calculated on the basis of equation 7.3.  $N_{AT1R}$  was determined with a straightforward **saturation binding experiment**, while the determination of  $N_{LR}$  was more complex. The cell layers and the gold-tagged core-shell NPs were disintegrated using *aqua regia* (**gold disintegration**) and quantified via ICP-MS. Both experiments are explained in the following two sections.

##### Saturation Binding Experiment

To measure  $N_{AT1R}$ , cells were incubated with different concentrations of the radioligand UR-MK292 (total binding). Unspecific binding was determined using a 500-fold excess of EXP3174 to block the AT1R. In figure 7.1 the specific binding (circles) and the unspecific binding (diamonds) are plotted. Specific binding was fitted with the non-linear function 7.5 (red line).

$$[RL^*R] = \frac{[RL^*] \times B_{max}}{[RL^*] + K_d} \quad (7.5)$$

Here  $[RL^*R]$  is the concentration of radioligand receptor complexes (specific binding). The maximal number of binding sites ( $B_{max}$ ) can be extracted from the fitting parameters, since it is the critical value of the fit. Unspecific binding was fitted with linear regression (black line).

Finally,  $B_{max}$  was transformed using equation 7.6 to receive  $N_{AT1R}$ . The specific activity ( $a$ ) of  $[^3H]UR-MK292$  was  $1.407 \text{ TBq mmol}^{-1}$ .

$$N_{AT1R} = \frac{B_{max}}{a} \times N_A \quad (7.6)$$

Based on the outlined saturation binding experiment  **$135 \pm 9 \times 10^9$  AT1Rs per well** were detected. Since  $870\,625 \pm 154\,881$  cells per well were counted, a single rMC carried  $154\,884 \pm 38\,053$  AT1Rs during the experiment.

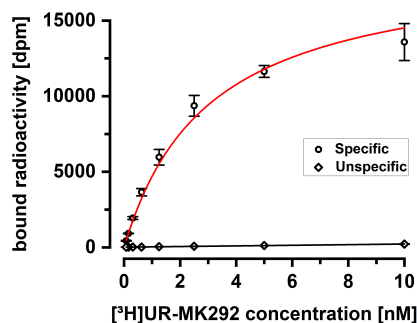


Figure 7.1: Saturation binding experiment. AT1R-positive rMCs were incubated with a range of concentrations of the radioligand UR-MK292.

### Gold Disintegration

In order to measure  $N_{LR}$ , NPs were tagged with ultra-small gold particles, enabling the detection via ICP-MS. RMCs were incubated with the gold-tagged EXP-NP90 or EXP-NP60<sup>-</sup> until equilibrium was reached. After removing the supernatant, cells were completely disintegrated together with the attached gold-tagged NPs using *aqua regia*. Subsequently the gold amount in the solutions was measured via ICP-MS and converted to  $N_{LR}$ . The analysis results are listed in table 7.3.

Table 7.3: Comparison between gold-tagged and untagged core-shell NPs ( $\#_{EXP3174}$  number of EXP3174 molecules per core-shell NP,  $X_{Au}$  gold amount per core-shell NP,  $m_{Au}$  gold mass per core-shell NP and  $\#_{Au}$  number of ultra-small gold particles per core-shell NP).

	EXP-NP90		EXP-NP60 <sup>-</sup>	
	Yes	No	Yes	No
N	1	20	1	16
$d_h$ [nm]	75	105 ± 13	62	68 ± 6
PDI	0.16	0.10 ± 0.01	0.09	0.09 ± 0.02
$\#_{EXP3174}$	4880	3500 ± 1499	2032	1017 ± 382
$X_{Au}$ [%]	0.13	-	0.13	-
$m_{Au}$ [ $10^{-18}$ g]	0.363	-	0.209	-
$\#_{Au}$	0.42	-	0.24	-

The size parameters of untagged core-shell NPs (refer to chapter 4) are listed in table 7.3 for comparison only. Gold-tagged NPs showed a smaller hydrodynamic diameter, but this result was not statistically verified. Again a narrow particle size distribution ( $PDI < 0.20$ ) was substantiated. The added amount of ultra-small gold particles was kept as low as possible. EXP-NP90-Au and EXP-NP60<sup>-</sup>-Au contained 0.13 % of solid gold. This was an essentially lower amount than Abstiens et. al. reported for their hybrid NPs (0.74 % to 0.76 %) and cRGD-decorated polymeric NPs (0.49 % to 0.51 %) [17]. The gold-tagged core-shell NPs EXP-NP90-Au and EXP-NP60<sup>-</sup>-Au carried 0.42 and 0.24 ultra-

## 7.4. CONCLUSION

---

small gold particles per NP. This means that less than every second NP was tagged. Hence, the effect of the gold-tag was reduced to a mandatory minimum.

### 7.3.3 Number of Binding Ligands

The saturation binding experiment provided the number of available AT1Rs ( $N_{AT1R}$ ), while the gold disintegration provided the actual number of PM-attached, gold-tagged NPs ( $N_{LR}$ ) during the experiment. Both values were needed to estimate  $N_{bound}$  on the basis of function 7.3. The calculation sequence is listed in table 7.4.

Table 7.4: Calculation of  $N_{bound}$  using function 7.3

	EXP-NP90-Au	EXP-NP60 <sup>-</sup> -Au
$N_{AT1R}$ [ $\times 10^9$ per well]	134.845 $\pm$ 9.141	
$N_{LR}$ [ $\times 10^9$ per well]	7.344 $\pm$ 1.590	8.776 $\pm$ 1.382
$N_{bound}$	9.2 $\pm$ 2.6	7.7 $\pm$ 1.7

## 7.4 Conclusion

This chapter provided a valuable approach to estimate how many ligands of a single NP actually bind to a target cell. It was assumed that the core-shell NPs must be situated in curved membrane cavities, because otherwise a single NP would not be able to reach an average of 9.2 or 7.7 receptors of a target cell. The membrane cavities may be clathrin-coated pits as it is illustrated in figure 7.2. It is remarkable that only a very few EXP3174 ligands mediate such a strong avidity gain that was evidenced in chapter 6. EXP-NP90 and EXP-NP60<sup>-</sup> showed an avidity in the sub-nanomolar range. This was stronger than the affinity of the naive ligand EXP3174 itself. Coincidentally, the results gave an explanation for the observation that the larger EXP-NP90 had a stronger avidity to rMCs than the smaller EXP-NP60<sup>-</sup> (refer to table 6.1). The EXP3174 ligands of larger core-shell NPs were able to reach a larger surface area of the PM and therefore a few ligands more had bound to a target receptor.

As already described, the gold amount was kept at a mandatory minimum. It was calculated that less than every second NP already carried a gold NP. Nevertheless, an influence of the gold-tag was recognized. Therefore it must be considered to repeat these experiments with an alternative tagging method. Such an alternative is provided by the radioactive tracer <sup>111</sup>indium (<sup>111</sup>In), that was successfully used for biodistribution studies (refer to chapter 8).

Nevertheless, this approach provided an approximation of how many ligands of a single core-shell NP bound to their target cell. It revealed that the number of surface bound EXP3174 molecules can be definitely reduced. Only 0.2% respectively 0.4% of the ligands were eventually needed. This is in accordance to the architecture of natural viruses. For example, the severe acute respiratory syndrome corona virus type 2 (SARS-CoV-2) carried 16 to 22 spikes per virion



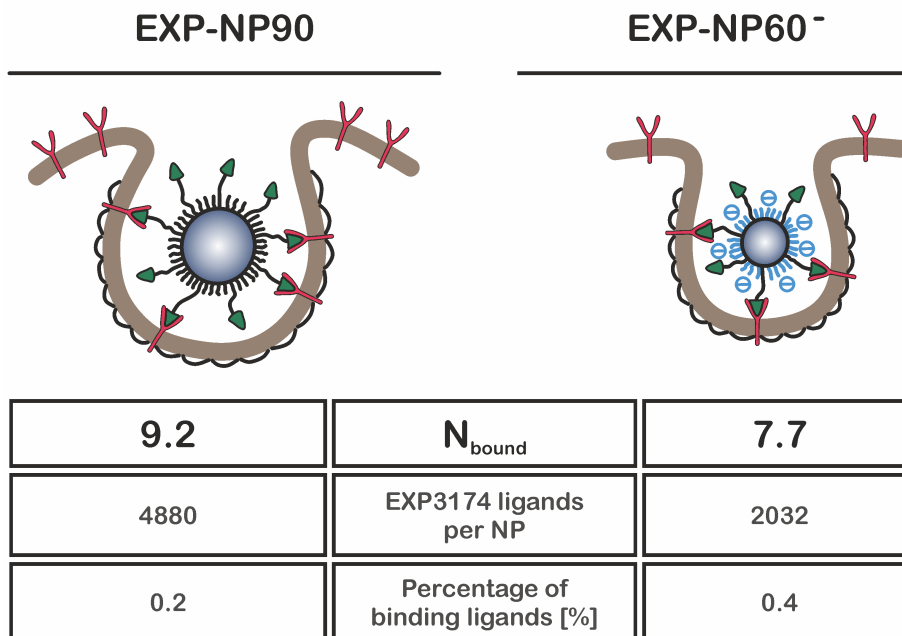


Figure 7.2: EXP-NP90 and EXP-NP60<sup>-</sup> trapped in clathrin-coated pits. Just a very few EXP3174-ligands (green) were binding to their target AT1R (pink). The estimated number of binding ligands  $N_{bound}$  is listed in below.

[18] (size of the virus: 70 nm to 80 nm [19]) and human immunodeficiency virus (HIV) 14 only [20]. Therefore the number of EXP3174 molecules per core-shell NP can be distinctly reduced without fearing a decline in the NP's avidity.

## 7.5 References

- [1] Md Habban Akhter et al. "Nanocarriers in Advanced Drug Targeting: Setting Novel Paradigm in Cancer Therapeutics". In: *Artificial Cells, Nanomedicine, and Biotechnology* 46.5 (2018), pp. 873–884. DOI: 10.1080/21691401.2017.1366333.
- [2] Chenyang Zhang et al. "Progress, Challenges, and Future of Nanomedicine". In: *Nano Today* 35 (2020). DOI: 10.1016/j.nantod.2020.101008.
- [3] Amanda K. Pearce and Rachel K. O'Reilly. "Insights into Active Targeting of Nanoparticles in Drug Delivery: Advances in Clinical Studies and Design Considerations for Cancer Nanomedicine". In: *Bioconjugate Chemistry* 30.9 (2019), pp. 2300–2311. DOI: 10.1021/acs.bioconjchem.9b00456.
- [4] Anna Salvati and Klaas Poelstra. "Drug Targeting and Nanomedicine: Lessons Learned from Liver Targeting and Opportunities for Drug Innovation". In: *Pharmaceutics* 14.1 (2022). DOI: 10.3390/pharmaceutics14010217.
- [5] Fatemeh Salahpour Anarjan. "Active Targeting Drug Delivery Nanocarriers: Ligands". In: *Nano-Structures & Nano-Objects* 19 (2019). DOI: 10.1016/j.nanoso.2019.100370.
- [6] Nadda Muhamad, Tullayakorn Plengsuriyakarn, and Kesara Nabangchang. "Application of Active Targeting Nanoparticle Delivery System for Chemotherapeutic Drugs and Traditional/Herbal Medicines in Cancer Therapy: A Systematic Review". In: *International Journal of Nanomedicine* 13 (2018), pp. 3921–3935. DOI: 10.2147/IJN.S165210.
- [7] Xing Du et al. "Insights into Protein-Ligand Interactions: Mechanisms, Models, and Methods". In: *International Journal of Molecular Sciences* 17.2 (2016). DOI: 10.3390/ijms17020144.
- [8] Gregory T. Tietjen et al. "Focus on Fundamentals: Achieving Effective Nanoparticle Targeting". In: *Trends in Molecular Medicine* 24.7 (2018), pp. 598–606. DOI: 10.1016/j.molmed.2018.05.003.
- [9] Chongyang Shen and Scott A. Bradford. "Why are Viruses Spiked?" In: *mSphere* 6.1 (2021). DOI: 10.1128/mSphere.01339-20..
- [10] Stephen Ornes. "Science and Culture: The Evolving Portrait of a Virus". In: *Proceedings of the National Academy of Sciences* 118.29 (2021). DOI: 10.1073/pnas.2111544118.
- [11] M. de Gasparo et al. "International Union of Pharmacology. XXIII. The Angiotensin II Receptors". In: *Pharmacological Reviews* 52.3 (2000), pp. 415–472.
- [12] Sara Maslanka Figueroa et al. "The Effect of Ligand Mobility on the Cellular Interaction of Multivalent Nanoparticles". In: *Macromolecular Bioscience* 20.4 (2020). DOI: 10.1002/mabi.201900427.

## 7.5. REFERENCES

---

- [13] Jean-Michel Rabanel et al. "Effect of the Polymer Architecture on the Structural and Biophysical Properties of PEG-PLA Nanoparticles". In: *ACS Applied Materials & Interfaces* 7.19 (2015), pp. 10374–10385. DOI: 10.1021/acsami.5b01423.
- [14] Sara Maslanka Figueroa et al. "Influenza A Virus Mimetic Nanoparticles Trigger Selective Cell Uptake". In: *Proceedings of the National Academy of Sciences* 116.20 (2019). DOI: 10.1073/pnas.1902563116.
- [15] Max Keller et al. "Mimicking of Arginine by Functionalized N $\omega$ -Carbamoylated Arginine as a New Broadly Applicable Approach to Labeled Bioactive Peptides: High Affinity Angiotensin, Neuropeptide Y, Neuropeptide FF, and Neurotensin Receptor Ligands as Examples". In: *Journal of Medicinal Chemistry* 59.5 (2016), pp. 1925–1945. DOI: 10.1021/acs.jmedchem.5b01495.
- [16] Yung-Chi Cheng and William H. Prusoff. "Relationship Between the Inhibition Constant (KI) and the Concentration of Inhibitor which Causes 50 Per Cent Inhibition (I50) of an Enzymatic Reaction". In: *Biochemical Pharmacology* 22.23 (1973), pp. 3099–3108. DOI: 10.1016/0006-2952(73)90196-2.
- [17] Kathrin Abstiens et al. "Gold-Tagged Polymeric Nanoparticles with Spatially Controlled Composition for Enhanced Detectability in Biological Environments". In: *ACS Applied Nano Materials* 2.2 (2019), pp. 917–926. DOI: 10.1021/acsanm.8b02165.
- [18] Tomasz Wierzbicki et al. "Effect of Receptors on the Resonant and Transient Harmonic Vibrations of Coronavirus". In: *Journal of the Mechanics and Physics of Solids* 150 (2021). DOI: 10.1016/j.jmps.2021.104369.
- [19] Wan Beom Park et al. "Virus Isolation from the First Patient with SARS-CoV-2 in Korea". In: *Journal of Korean Medical Science* 35.7 (2020). DOI: 10.3346/jkms.2020.35.e84.
- [20] Ping Zhu et al. "Distribution and Three-Dimensional Structure of AIDS Virus Envelope Spikes". In: *Nature* 441.7095 (2006), pp. 847–852. DOI: 10.1038/nature04817.



## Chapter 8

# Nanoparticles to Target Retinal Vessels\*

---

\* Radiolabeling of core-shell NPs and SPECT-CT based biodistribution study were performed by Alain Blanc and Dr. Martin Behe (Paul Scherrer Institut/ Villingen/ Switzerland)

## Abstract

In this chapter differently sized core-shell nanoparticles (NPs) (a) EXP-NP90 (size  $105 \pm 13$  nm) and (b) EXP-NP60<sup>-</sup> (size  $68 \pm 6$  nm) were investigated for their ability to target the ocular vasculature. Both candidates were decorated with losartan carboxylic acid (EXP3174) molecules to target and silence the angiotensin II receptor type 1 (AT1R) *in vivo*. The core-shell NPs were tagged with radioactive [<sup>111</sup>In]indium ions, so that they can be traced via single-photon emission computed tomography (SPECT)/ computed tomography (CT) imaging. Targeted EXP-NP60<sup>-</sup> resided for more than 48 h at the liver. An accumulation in the kidneys and the spleen were determined, indeed this was not the case for the ocular vasculature. In another *in vivo* experiment murine retinae were scanned for fluorescently labeled EXP-NP90 and EXP-NP60<sup>-</sup>, but the results confirmed the biodistribution study. The NP size, the polyethylene glycol (PEG) shell conformation and the NP stability were identified as plausible reasons. Both candidates were rapidly eliminated via renal excretion. The half-life of large EXP-NP90 was  $1.90 \pm 0.10$  h and  $2.16 \pm 0.14$  h for the smaller EXP-NP60<sup>-</sup>.

## 8.1 Introduction

It was the major goal of this work to develop a therapeutic nanoparticulate formulation that is able to target the ocular vasculature as it was reported by Henig et. al. for EXP3174-decorated anorganic NPs [1]. In this context EXP3174-decorated core-shell NPs with a sub-nanomolar avidity were designed. Here two promising candidates were investigated for their *in vivo* performance to reach the ocular vasculature: (a) large EXP-NP90 (size  $105 \pm 13$  nm) with an IC<sub>50</sub> of  $10.04 \pm 0.23$  and (b) smaller EXP-NP60<sup>-</sup> (size  $68 \pm 6$  nm) with an IC<sub>50</sub> of  $9.34 \pm 0.07$  (refer to chapter 6). The sub-nanomolar avidity was obtained from a multivalent binding of several targeting molecules: (a) 9.2 EXP3174 molecules per EXP-NP90 and (b) 7.7 per EXP3174 decorated NP60<sup>-</sup> (EXP-NP60<sup>-</sup>) (refer to chapter 7). Multivalent binding requires an intact NP. The core-shell NP were composed of the biodegradable poly(lactic-co-glycolic) acid (PLGA) and PEG-poly(lactic acid) (PLA) block-co-polymers. For one thing, the degradability prevents an accumulation. But a very rapid degradation would impair multivalent binding, so that the avidity would be lost. Therefore the non-targeted equivalents of both candidates (NP90 and NP60<sup>-</sup>) were incubated in human plasma to investigate their stability.

Beyond that, a SPECT-CT based biodistribution study with EXP-NP60<sup>-</sup> was performed. The NP dispersions were systemically administered into healthy mice. This experiment provided 3D images of the entire laboratory animals, so that the distribution and the elimination were followed. Therefore the core-shell NPs were tagged with radioactive [<sup>111</sup>In]indium ions. In addition, it was focussed on the targeting effect for ocular vessels. Both candidates (large EXP-NP90 and small EXP-NP60<sup>-</sup>) were systemically injected into healthy mice. Afterwards the retinae were scanned for the retention of EXP3174-decorated core-shell NPs. Both studies revealed important achievements, but also evoked the need of further investigation.

## 8.2 Material and Methods

### 8.2.1 Material

Human serum was obtained from an autologous blood donation. Therefore blood was collected using a couple of S-Monovettes<sup>®</sup> Serum with clot activator (Cat. no. 01.1601) (Sarstedt/ Nümbrecht/ Germany). The blood was allowed to clot at room temperature (RT). Clotted blood was centrifuged (3849xg; RT; 10 min). Afterwards the serum was collected, pooled, aliquoted and frozen until usage.

The mounting medium was composed of glycerol (Merck/ Darmstadt/ Germany), Mowiol 4-88 (Carl Roth/ Karlsruhe/ Germany), water, TRIS-buffer ( $pH = 8.5$ ) and DABCO (Carl Roth/ Karlsruhe/ Germany).

All other chemicals were purchased from Sigma Aldrich (Taufkirchen/ Germany) at least in analytical grade, if not stated otherwise.

Ultrapure water was freshly prepared using a Milli-Q water purification system (Millipore/ Schwabach/ Germany). It is subsequently termed *water*.

### 8.2.2 Nanoparticle Stability Study

The stability study was performed with non-targeted core-shell NPs. NP90 and NP60<sup>-</sup> were manufactured via nanoprecipitation as previously described (refer to section 4.2.2). NP size, polydispersity and total polymer content (TPC) were also determined as previously described (refer to sections 4.2.3 and 4.2.5). The particle number concentration (PNC) was calculated with the following function:

$$PNC = \frac{TPC}{\rho_{NP} \times \frac{1}{6}\pi (d_H)^3 \times N_A} \quad (8.1)$$

TPC is the total polymer content,  $\rho_{NP}$  is the NP density,  $d_h$  is the hydrodynamic diameter and  $N_A$  is the Avogadro constant (refer to chapter 4 for further details). The PNC was adjusted to 30 nM using diluted Dulbecco's Phosphate Buffered Saline (x0.1) (DPBSx0.1).

20  $\mu$ l of pre-warmed serum or DPBSx0.1 were rendered in reaction tubes (Eppendorf/ Hamburg/ Germany). Then 10  $\mu$ l NP dispersion was added. The mixture was carefully homogenized, sealed and incubated for 0.5 h, 1 h, 2 h, 4 h, 8 h, 24 h, 72 h and 168 h. During all the steps the reaction tubes were situated on tempered metal racks (37 °C) to ensure temperature compliance.

After the incubation period, 90  $\mu$ l of ice-cold, pharma-grade ethanol absolute (neoFROXX/ Einhausen/ Germany) was added to precipitate the serum proteins. The samples were centrifuged (4 °C; 2000xg; 15 min) to remove the serum proteins.

The pure supernatant was measured with a Zetasizer nano ZS (Malvern Instruments/ Herrenberg/ Germany) using a single-use cuvette UV Micro ( $z = 8.5$  mm) (Carl Roth/ Karlsruhe/ Germany). The samples were equilibrated at 25 °C and illuminated with a He-Ne-laser (633 nm) during the measurement. Overall, three measurements were executed in the automatic mode. Finally

the hydrodynamic diameter, the polydispersity index (PDI) and the derived count rate (DCR) were reported, while hydrodynamic diameter and DCR were normalized to the initial value ( $t = 0$  h) and plotted as ratio.

### 8.2.3 Biodistribution Study

This study was performed in collaboration with the Center for Radiopharmaceutical Science (Paul Scherrer Institute/ Villingen/ Switzerland). The experiments were approved by the Cantonal Committee of Animal Experimentation (License No. 75700) and met the standards of the Swiss Animal Protection Laws.

#### Nanoparticle Manufacturing

The NP dispersions were manufactured via nanoprecipitation as it is described in section 4.2.2, but the aqueous phase was pure water. The TPC was determined as it is described in section 4.2.5 and adjusted using DPBSx0.1.

#### Radiolabeling

The NPs dispersions ( $1.0 \text{ mg ml}^{-1}$ ) were incubated with radioactive [ $^{111}\text{In}$ ]InCl<sub>3</sub> and subsequently analyzed via high-performance liquid chromatography (HPLC).

50  $\mu\text{l}$  NP dispersion were spiked with 10  $\mu\text{l}$  radioactive [ $^{111}\text{In}$ ]InCl<sub>3</sub> solution (5–10 MBq) (Covidien Medtronic Deutschland/ Neustadt a. d. Donau/ Germany) and incubated for 1 h at 37 °C ( $^{111}\text{In-NP}$ ). Then  $^{111}\text{In-NP}$  were diluted 1:10 using water and splitted. One part was directly injected into the HPLC ( $^{111}\text{In-NP}_{1:10}$ ), the other part was supplemented with an aqueous DTPA pentasodium dilution (0.5 M) and again incubated for 15 min at 37 °C ( $^{111}\text{In-NP}_{1:10}+\text{DTPA}$ ). 5  $\mu\text{l}$  of  $^{111}\text{In-NP}_{1:10}$  and  $^{111}\text{In-NP}_{1:10}+\text{DTPA}$  were successively injected on a BioSEC-5 (2000 Å, 5  $\mu\text{m}$ ) HPLC column (Agilent Technologies). The column was installed in Merck Hitachi Elite HPLC system, equipped with a L-2130 pump, a L-2200 autosampler, the diode-array detector (DAD) L-2455 and the radiodetector Bioscan Flow counter A. Elution was done using an aqueous isopropanol mixture (10 %) at 30 °C. The flow rate was kept at  $0.350 \text{ ml min}^{-1}$ . The NPs were detected at 220 nm and the radioactivity was measured with the radiodetector.

A [ $^{111}\text{In}$ ]InCl<sub>3</sub> solution ([ $^{111}\text{In}$ ]In<sup>3+</sup>) and a solution of chelated [ $^{111}\text{In}$ ]indium ions ([ $^{111}\text{In}$ ][In(DTPA)]<sup>2-</sup>) served as references.

#### Experimental Procedure

Female, six to eight week-old 129 mice (129S2/SvPasCrl) were purchased from Charles River (Sulzfeld/ Gemany). 100  $\mu\text{l}$  of  $^{111}\text{In}$ -carboxy-terminated nanoparticle (NP60<sup>-</sup>) (**control group**) or  $^{111}\text{In}$ -EXP-NP60<sup>-</sup> (**experimental group**) ( $15 \text{ mg ml}^{-1}$  TPC, 4–6 MBq radioactivity) were injected into the lateral tail vein. The mice were incubated for 1 h, 4 h, 24 h and 48 h.



### SPECT/CT Imaging

After the incubation interval was completed, the isoflurane anesthetized mice were scanned. Therefore a 4-head multiplexing multi-pinhole camera (NanoSPECT/CTplus/ Bioscan/ Poway/ CA/ USA) was used. It provided a time-dependent 3D visualization of the  $^{111}\text{In}$ -NPs biodistribution. SPECT images were acquired in 45 min each. The frame duration was 60 s.

*Post mortem* the dissected head of one mouse (24 h) of the **control group** and the **experimental group** were scanned concurrently. Here the frame duration was raised to 600 s.

### 8.2.4 Nanoparticle Tracing in Retinal Vasculature

This study was performed in collaboration with the research groups of Prof. Tamm and Prof. Schweda (Institute of Physiology/ University of Regensburg). The experiments were approved by the local authorities (Regierung von Unterfranken, reference number 55.-2532-2-329) and met the national and international standards for animal research.

#### Nanoparticle Manufacturing

The NP dispersions were manufactured via nanoprecipitation as it is described in section 4.2.2. But PLGA was supplemented with fluorescent CF<sup>TM</sup>647-PLGA. The synthesis and analytics of CF<sup>TM</sup>647-PLGA are described in chapter 3. The TPC was determined according to section 4.2.5 and adjusted using DPBSx0.1.

#### Experimental Procedure

Female, six to eight week-old 129 mice (129S2/SvPasCrl) were purchased from Charles River (Sulzfeld/ Germany). The laboratory animals were anesthetized with inhaled isoflurane and buprenorphine (0.1 mg/kgKG). Then, 100  $\mu\text{l}$  of fluorescently labeled NP dispersions (15 mg  $\text{ml}^{-1}$ ) were injected into the vena jugularis. After 5 min, blood samples were collected via puncture of the facial vein ( $t = 0$ ), while mice were still anesthetized. From that moment the incubation intervals of 2 h, 4 h and 8 h started. All experiments were executed in triplicates ( $N = 3$ ). In order to reduce the number of laboratory animals, the 4 h and 8 h intervals were waived for the control group. After the incubation intervals mice were deeply anesthetized with a mixture of ketamine (85 mg/kgKG) and Xylazin (6 mg/kgKG). Subsequently, mice were perfused through the left ventricle. Therefore a 50 mg  $\text{ml}^{-1}$  solution of high molecular weight (MW) (2.000 kDa) FITC-dextran (TdB Consultancy/ Uppsala/ Sweden) and Dulbecco's Phosphate Buffered Saline (DPBS) (Gibco<sup>TM</sup>/ Life Technologies/ Paisly/ UK) was used.

#### Preparation of Retina Flatmounts

After the experiments the eyes of the perfused mice were carefully enucleated. Beginning from that moment, the eyes were strictly handled under light protection. They were fixed in a DPBS solution containing 4 % paraformaldehyde

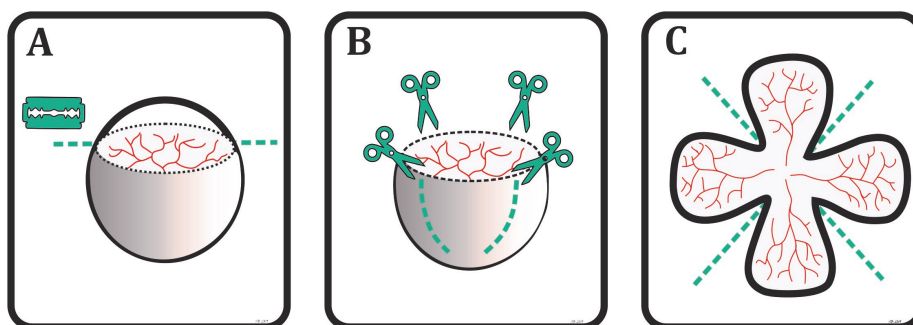


Figure 8.1: Preparation of retina flatmounts. **A:** Cornea clipping. **B:** Cutting of the retinal cup. **C:** Draped retina flatmount.

(PFA) for 1.5 h. If necessary they had an interim storage in 0.1 M phosphate buffer ( $pH = 7.4$ ) for a maximum of 1 h until further preparation. Then the cornea was clipped (refer to figure 8.1A) and the lens as well as the retinal cup were removed very cautiously. The cup-shaped retina was cut four to five times (refer to figure 8.1B) in order to open the retinal cup and receive retina flatmounts (refer to figure 8.1C). This sequence is illustrated in figure 8.1. Lastly, flatmounts were mounted with mounting medium and stored in the fridge overnight.

### Fluorescence Microscopy

The retinal flatmounts were investigated on an Axiomager Z1 fluorescence microscope (Carl Zeiss/ Göttingen/ Germany) using the Axiovision software version 4.8 (Carl Zeiss/ Germany). The system was equipped with an Apotome and an AxioCam 503 camera. Mounted retina flatmounts were scanned in dual-channel mode. In the first channel (**Ch1**) the flatmounts were illuminated at 653 nm to detect the fluorescent NPs (emission wavelength 668 nm). The second channel (**Ch2**) was illuminated at 488 nm to detect the retinal vasculature (emission wavelength 509 nm). An overview of the whole retina flatmount was recorded as a stitched tile image using a Plan-Apochromat objective with 20-fold magnification. Furthermore a z-stack of the ROI was recorded using an EC Plan-Neofluar objective with 40-fold magnification and immersion oil. Here it was focussed on the upper, intermediate and lower retinal plexus.

## 8.3 Results and Discussion

### 8.3.1 Nanoparticle Stability in Human Serum

The NP stability was checked in human serum at body temperature ( $37^{\circ}\text{C}$ ). As already outlined, the core-shell NPs were biodegradable. For one thing, this is a really useful feature, because it prevents the accumulation in the organism. On the other hand, NP integrity is absolutely needed for a multivalent binding to the target cells.

Dynamic light scattering (DLS) was chosen to follow up the NP size distribution during the incubation period. Human serum comprises an abundant

amount of serum albumin and other proteins. Due to their size of several nanometers, these colloids scatter light that is overlapping the NP signal. Consequently serum proteins must be removed prior to the DLS measurements. The addition of strong acids (e.g. TCA and perchloric acid) or organic solvents (e.g. ACN, acetone, ethanol or methanol) are most popular and initiate protein precipitation [2]. These reagents are still in use for sample preparation prior to several highly sensitive analysis techniques [3–5]. Nevertheless, most reagents were not suitable for this kind of polymer NPs. Strong acids force the hydrolysis of ester bonds, so that the NPs immediately disintegrate. Organic solvents like acetonitrile (ACN) and acetone directly dissolve the NPs. For example, ACN was the solvent for the organic phase of the nanoprecipitation procedure (refer to section 4.2.2). Finally, pure ethanol turned out to be the most suitable reagent for the deproteinization. According to Blanchard, a three-fold excess of ethanol must be applied to precipitate more than 99 % of the plasma proteins [2].

During this stability study, non-targeted large methoxy-terminated nanoparticles (NP90s) and non-targeted, small NP60<sup>s</sup> were investigated. The sample dispersions were dispersed in DPBSx0.1 (control) and human serum. Inhere a vigorous centrifugation step was implemented to remove the proteins after precipitation quantitatively. To survive this procedure the NPs needed an intact PEG shell. The results are summarized in figure 8.2. The parameters size (A and B), PDI (C and D) and DCR (E and F) were evaluated. The DCR provided semiquantitative information about the PNC. Subfigures 8.2A, C and E correspond to the larger NP90 (hollow squares), while B, D and F correspond to the NP60<sup>s</sup> (hollow circles). For both NP types the size and the PDI remained unchanged within 8 h. This was essential for the *in vivo* experiments. Longer incubation indicated an increasing NP size and a broadening of the size distribution (PDI). The size of serum incubated core-shell NPs increased earlier than the size of the DPBSx0.1-incubated core-shell NPs. This could be triggered by opsonization with plasma proteins and subsequent degradation reactions. It is striking that the size and the PDI of the control group increased later and less intense. Monitoring of the DCR indicated a clear diminution of the PNC that was beginning instantly at the incubation start. Even after 8 h the DCR dropped about approximately 50 % for the NP90 and approximately 75 % for the NP60<sup>s</sup>. So the disintegration of the smaller NP60<sup>s</sup> is clearly faster. Apart from that, the DCR of the control group remains stable over at least 24 h. Afterwards the DCR was even rising. This may be caused by NP swelling, agglomeration or changes in the surface roughness.

However, there is a striking difference between the incubation in human serum and buffer solution (DPBSx0.1). Human plasma comprises 90 % water, 8 % proteins (mainly albumin and globulin) and other components (electrolytes, glucose, vitamins, enzymes as well as urea, uric acid, creatinine and other metabolites) [6]. There is a plethora of literature available, investigating the degradation of biodegradable polymers like PLA and PLGA manufactured in different dosage forms (e.g. NPs, microspheres, implants or films) [7–10]. Overall a hydrolytic mechanism is favored. In brief, water diffuses into the polymer matrix and causes swelling. Then, ester bonds are cleaved, cutting the polymer chains into shorter oligomers. Resulting carboxylic groups mediate

### 8.3. RESULTS AND DISCUSSION

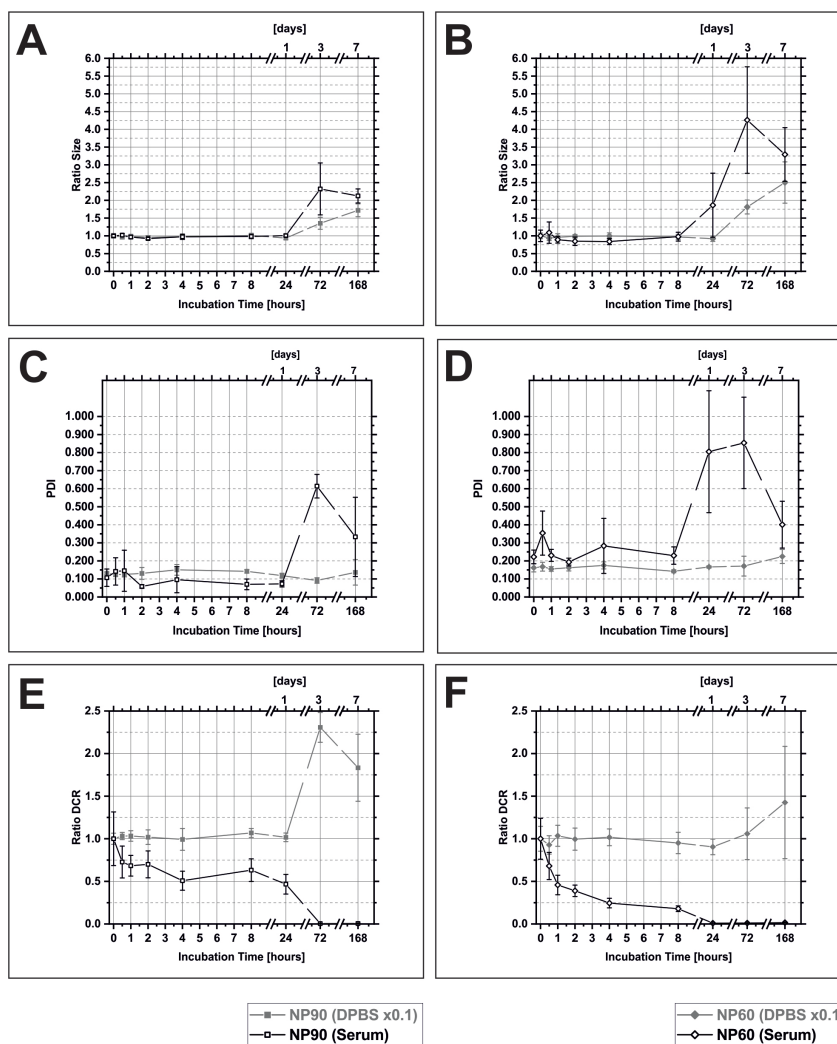


Figure 8.2: Short-term stability of polymer NPs in human serum. NP90 (hollow boxes in subfigures A, C and E) and NP60 (open diamonds in subfigures B, D and F) were investigated. The grey line indicates the NPs incubated in the regular storage medium DPBSx0.1 as a reference. A, B: Ratio of hydrodynamic diameter at time point  $t$  and initial hydrodynamic diameter. C, D: PDI of NP dispersion. E, F: Ratio of DCR at a time point  $t$  and the initial DCR.

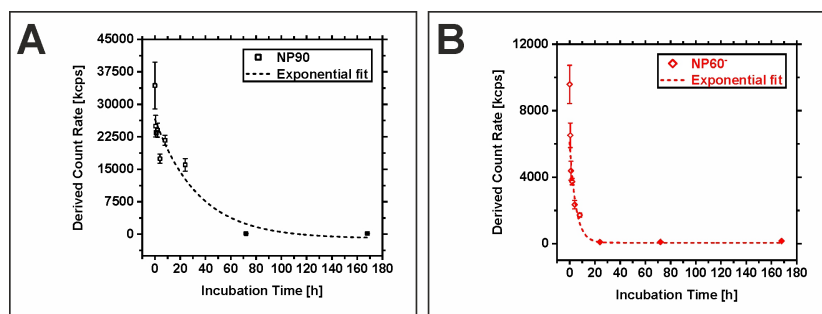


Figure 8.3: DCR- $t$ -profile for NP90 (A) and NP60<sup>-</sup> (B) incubated in human serum. Both profiles were fitted with an exponential function (dashed lines) and revealed good fitting parameters (A:  $R^2 = 0.881$  and B:  $R^2 = 0.940$ )

an acidification and speed up the autocatalytical ester hydrolysis. For larger polymer matrices, the diffusion path of cleaved oligomers to the outside is substantially longer. Consequently, the acidifying oligomers reside much longer inside the polymer matrix and speed up the degradation [7]. Furthermore, the degradation speed depends on a multitude of physical and chemical parameters [11]. The involvement of enzymes is also discussed occasionally [11–13]. However, the literature is usually focused on pure PLGA matrices, rarely on PEG-PLA or PEG-PLGA based particles. Here, enzymes potentially play a key role in the cleavage of the PEG-shell, that is essential for the sterical stabilization and the targeting effect of these polymer NPs. There are many enzymes possessing an esterase activity, that is essential for the metabolism of different drugs [14]. It is also remarkable, that albumin itself shows an esterase activity [15].

The Flory radius ( $R_F$ ) indicated an *intermediate* PEG-shell conformation (refer to section 4.3.3). Furthermore, the average distance between the PEG chains was greater than 1.4 nm (refer to section 4.3.3), which was found as critical value to reduce the adsorption of plasma proteins to the surface of PEG-PLA NPs [16]. This means that both candidates were vulnerable for opsonization and enzymatic degradation. After cleaving a first PEG-chain from a PLA-block there are numerous PEG chains in the direct neighbourhood, so that the degradation accelerates step by step.

The DCR- $t$ -profiles are depicted in figure 8.3. An exponential function revealed good fitting parameters and indicated a first-order kinetics. The semilogarithmic DCR- $t$ -plot (figure 8.4) provided the degradation constants  $k$  for both NP types. The values are listed in table 8.1.

Table 8.1: Half-life of Core-Shell NPs

NP type	Incubation Temperature	$k[h^{-1}]$	$T_{1/2}[h]$
NP90	37 °C	$-2.11 \times 10^{-2}$	$32.9 \pm 14.1$
NP60 <sup>-</sup>	37 °C	$-1.78 \times 10^{-1}$	$3.89 \pm 0.27$

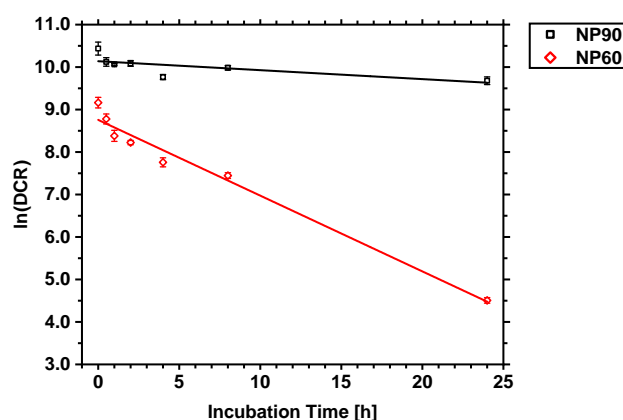


Figure 8.4: Semilogarithmic DCR- $t$ -plot for NP90 (black hollow boxes) and NP60<sup>-</sup> (red hollow rhombs) incubated in human serum. The determined degradation constants  $k$  and the NP half-lives are listed in table 8.1.

All in all, larger NP90 had a half-life of 32.9 h in human serum at body temperature. This was clearly higher than the half-life of the smaller NP60<sup>-</sup> (3.89 h). The degradation kinetics in subfigures 8.2E and F clearly indicated a different degradation mechanism. The contact to plasma proteins speeds up the degradation tremendously. Nevertheless, both NP types can survive in human serum for several hours. This was the essential prerequisite for an multivalent binding of targeted core-shell NPs and the subsequent *in vivo* studies.

### 8.3.2 Biodistribution of Core-Shell Nanoparticles

#### Radiolabel

Prior to the biodistribution study, the different NP dispersions were labeled with radioactive [<sup>111</sup>In]indium cations. Therefore, it is in common to attach a chelating agent like DTPA or DOTA covalently to the pharmacon, e.g. peptides [17, 18], proteins [19], nucleic acids [20], antibodies [21] or NPs [22–24]. Following this tagging strategy, a DTPA-PEG-PLA polymer was synthesized and added to the organic phase during the manufacturing process as it is described in section 4.2.2. Due to solubility issues it was not possible to manufacture core-shell NPs without further modifications. Consequently, the NP dispersions were directly incubated with a diluted [<sup>111</sup>In]InCl<sub>3</sub> solution. Any other chemical modifications were waived. Nevertheless, the radiolabel was stable enough for an *in vivo* application. This was proven via HPLC analysis. The results are depicted in figures S4 (NP90 and EXP-NP90), S5 (NP60<sup>-</sup> and EXP-NP60<sup>-</sup>) and S6 (references: pure [<sup>111</sup>In]In<sup>3+</sup> and [<sup>111</sup>In]In-DTPA<sup>2-</sup>). Radioactive [<sup>111</sup>In]indium cations were matched with the signal of the core-NPs (refer to subfigures S4a, S4c, S5a and S5c). In a separate analysis, a pentasodium DTPA dilution was added to the <sup>111</sup>In-NPs dispersions to detect free or loosely bound [<sup>111</sup>In]indium cations. It was not possible to trace [<sup>111</sup>In]In-DTPA<sup>2-</sup>. These results verified the stability of the radiolabel (refer to subfigures

S4b, S4d, S5b and S5d), although any chemical modifications were waived. Potentially, the [ $^{111}\text{In}$ ]indium cations were chelated by carboxylic groups and/or carbonyl groups. So the incorporated [ $^{111}\text{In}$ ]indium cations were not accessible for complexing agents like pentasodium DTPA. The real mechanism has remained unclear so far. Nevertheless, this radiolabeling method was suitable for *in vivo* imaging purpose.

#### **Biodistribution and SPECT/CT Imageing**

In this study, the *in vivo* fate of EXP3174-decorated, smaller EXP-NP60<sup>-</sup> and the non-targeted NP60<sup>-</sup> was investigated. The NP dispersions were injected into the lateral tail vein of healthy female 129 mice. Gamma-emitting [ $^{111}\text{In}$ ]indium cations were immobilized within the core-shell NPs, so that their time-dependent biodistribution was studied. A scintillation camera system rotated 360° around the scanned animal and provided 3D projections. Simultaneously, CTs were performed to record the animal anatomy. The 3D scans were acquired after 1 h, 4 h, 24 h and 48 h. In figure 8.5 coronal and sagittal images are depicted for each experimental group at different time points. The injection failed for the laboratory animal that received NP60<sup>-</sup> and was intended to scan after an incubation period of one hour.

The majority of the core-shell NPs was detected in the liver. It is commonly known that the main part of a systemical administered NP dose accumulate in the liver. Zhang et. al. reported a depostion of 30 % to 99 % of the administered dose [25]. The liver is crucial for the detoxification of the organism. Its anatomy and physiology is highly specialized for the processing of foreign substances and particulates.

Blood of the portal vein and the hepatic artery merge during flowing through the hepatic sinusoids and end up in the caval vein. The liver parenchym is mainly built by hepatocytes (60 % to 80 % [26]). In front of the hepatocytes there is the space of Dissé, that is lined by a porous monolayer of liver sinusoidal endothelial cells. The pores range from approximately 60 nm to 200 nm [27]. A basal membrane, which is typical for endothial cells, lacks. Hence, plasma components (e.g. fluids, proteins and substances with low MW) can diffuse almost freely into the space of Dissé and reach the hepatocytes for further processing. Additionally, Kupffer cells, biliary cells, stellate cells and intrahepatic lymphocytes are situated in the liver [26].

In general, NPs are eliminated from the blood flow by the hepatobiliary system and the mononuclear phagocyte system (MPS) [25, 28]. The MPS comprises both tissue-resident macrophages (e.g. Kupffer cells and liver sinusoidal endothelial cells) and blood circulating macrophages (monocytes, granulocytes and dendritic cells) [29]. Especially Kupffer cells are able to take up NPs in a broad size range [30, 31]. Furthermore, non-phagocytosed NPs can diffuse into to space of Dissé and interact with hepatocytes. The phagocytosing cells engulf and process NPs further. This is the reason why the majority of a sytemically administered NP dose is generally expected in the liver.

As expected, also the core-shell NPs accumulate mainly in the liver. This was clearly concluded from the SPECT/CTs. After 48 h almost the complete dose of non-targeted NP60<sup>-</sup> was eliminated. The right box within figure 8.5 shows

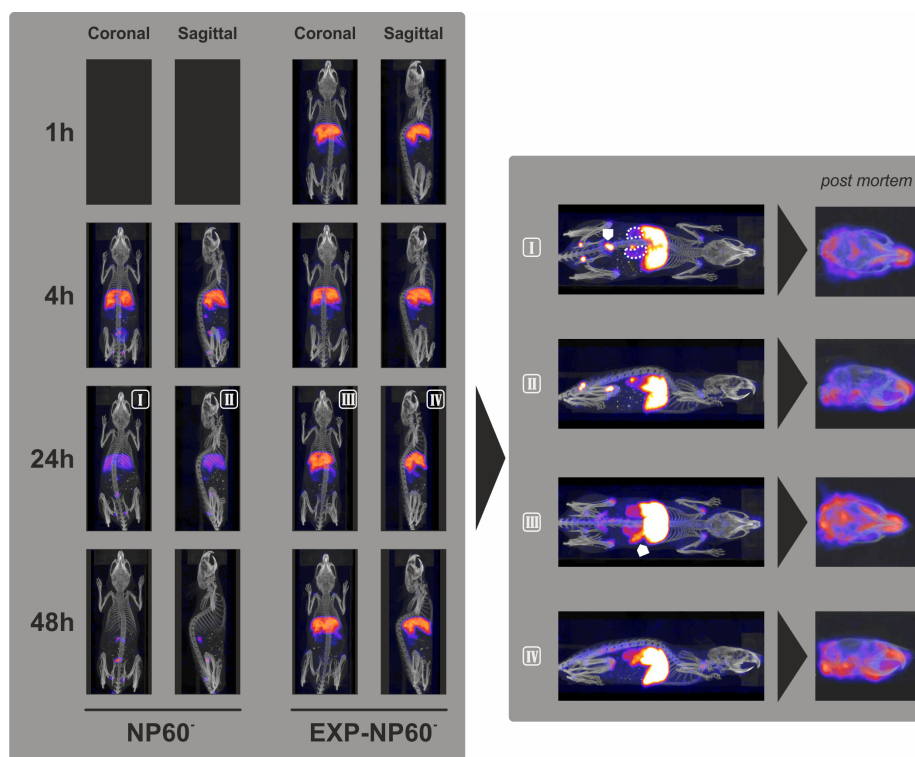


Figure 8.5: SPECT imaging of  $^{111}\text{In-NP60}^-$  and  $^{111}\text{In-EXP-NP60}^-$  in healthy female 129 mice after 1 h, 4 h, 24 h and 48 h. Small white arrows highlight NP accumulation apart from the liver. Additional *post mortem* SPECT images of the mice heads after 24 h.



### 8.3. RESULTS AND DISCUSSION

---

several images with an adapted intensity scale. The two dashed circles in image I highlight the kidneys. Radioactivity concentrated in the bladder (white arrow), before it was almost completely eliminated.

The renal molecular weight cut off (MWCO) is approximately 48 kDa [32]. This is much smaller than an intact core-shell NP, but larger than the initial MW of the used block-co-polymers itself. Obviously the NP60<sup>-</sup> were degraded into hydrophilic compounds (ester hydrolysis) and eliminated on a renal route. Beyond that, pure [<sup>111</sup>In]indium ions are known to be chelated by transferrin and transported into the bone marrow [33–36]. Transferrin is the physiological transporter of iron(III)ions that is essential for the haematopoiesis. It is conceivable that during the NP degradation [<sup>111</sup>In]indium cations were released or trans-chelated by transferrin and further distributed. In this context the two hot spots at the lower extremities and the blue areas at the knees and shoulders were interpreted as unspecific uptake.

However, the pharmacokinetics and the biodistribution of targeted <sup>111</sup>In-EXP-NP60<sup>-</sup> is widely different. As it is depicted in figure 8.5 the EXP-NP60<sup>-</sup>s accumulate in the liver in a similar way, but an excretion within 48 h was not observed. Additionally a radioactivity signal was also lacking in the bladder after 24 h (refer to **III** in the right box of figure 8.5). Combining the remaining signal in the liver and the lacking accumulation of degradation products in the bladder means that the degradation of EXP-NP60<sup>-</sup> is much slower. With respect to section 6.3.3, the targeted core-shell NPs were traced exclusively on the plasma membrane (PM). This phenomenon was linked to the antagonistic EXP3174 molecules that were inhibiting a cellular uptake and therefore subsequent cellular degradation processes. This finding is also confirmed by the fact, that Kupffer cells express AT1Rs [37].

AT1Rs were available especially in different tissues of the kidneys [38, 39]. Therefore it is plausible that the EXP-NP60<sup>-</sup>s bind to renal tissues as it is indicated by figure 8.5 (refer to **III** in the right box). The lack of a radioactive signal in the bladder as it was observed for the NP60<sup>-</sup> argues for a specific binding and not for an accumulation of degradation products. Furthermore, the targeting of mesangial cells within the kidney for EXP3174 and cycloRGD-decorated core-shell NPs [40]. Beyond the accumulation in hepatic and renal tissue, there was a clear radioactivity signal detected within the spleen (refer to the white arrow in image **III** of the right box in figure 8.5). A binding to splenic tissue was not observed for the non-targeted NP60<sup>-</sup>. Potentially the binding was attributed to the reservoir of undifferentiated monocytes in the spleen [41, 42]. The release of splenic monocytes is triggered by angiotensin II (Ang II), so that monocytes also carry AT1R and angiotensin II receptor type 2 (AT2R) [43–45]. But this was not the focus of this work.

However, this study was focused on the targeting effect of EXP-NP60<sup>-</sup>s to ocular tissue. That's why the heads of several mice were scanned *post mortem* with a substantially enhanced frame duration to enhance detection sensitivity. A clear radioactivity signal in the area of the eyes or the orbital cavities was not identified. This is especially recognizable in the sagittal images depicted in figure 8.5 (*post mortem* images on the right). Since ocular vasculature is very filigree, the sensitivity of the method was potentially not enough. In the follow up study outlined in section 8.3.3, mice of the same strain received these kind

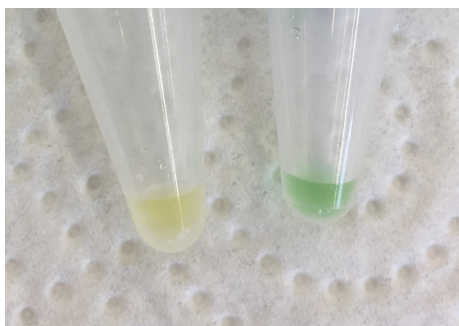


Figure 8.6: Collected urine of a laboratory animal prior (left plastic tube) and after (right plastic tube) the administration of CF<sup>TM</sup>647-labeled core-shell NPs.

of core-shell NPs again. The retinæ were removed and intensively scanned via microscopic methods. It was focussed on the ocular vasculature and the findings were re-evaluated taking these results into account.

#### 8.3.3 Nanoparticle Tracing in Ocular Vasculature

Hennig et. al. showed that EXP3174-decorated, PEG-coated model nanoparticles (mNPs) were able to target the choroidal and retinal vasculature [1]. They used in-house bred NMRI (nu/ nu) mice. In a first approach the NMRI (CrI:NMRI(Han)) mice were purchased from Charles River (Sulzfeld/ Germany) to investigate the targeting effect of the core-shell NPs EXP3174 decorated NP90 (EXP-NP90) and EXP-NP60<sup>-</sup> *in vivo*. After the experiment both eyes were enucleated and prepared for different analysis technologies. One eye was fixed, pre-treated with sucrose dilutions, embedded and sliced with a cryotome (the method is described elsewhere [46–48]) to analyze the choroidal vasculature. The other eye was used to obtain retinal flatmounts. The technique is illustrated in figure 8.1. The flatmounts enabled the scanning of the retinal vasculature. Both techniques aimed to identify fluorescent core-shell NPs in the ocular vasculature. However, it was not possible to substantiate a targeting effect in the choroidal or retinal vasculature (data not shown). However, several laboratory animals showed degenerated retinæ and must be excluded from the evaluation (data not shown). For that reason the mouse strain was changed and the experiments were repeated with 129 mice (129S2/SvPasCrI). 129 mice were also used for the biodistribution studies (refer to section 8.3.2).

In the second approach it was solely focussed on the retinal vasculature, due to the retinal degeneration of some NMRI mice. After the injection of the test dispersions into the blood circulation blood was collected ( $t_0$ ) and analyzed. Blood was additionally collected at the end of the incubation interval (2 h, 4 h and 8 h). The plasmaprofiles are depicted in figure 8.7. The core-shell NPs were rapidly eliminated from the blood circulation. Solely  $5.5 \pm 1.3\%$  of the EXP-NP90-dose and  $6.2 \pm 2.4\%$  of the EXP-NP60<sup>-</sup>-dose were determined after the 2 h incubation interval. With respect to figure 8.5, the core-shell NPs accu-

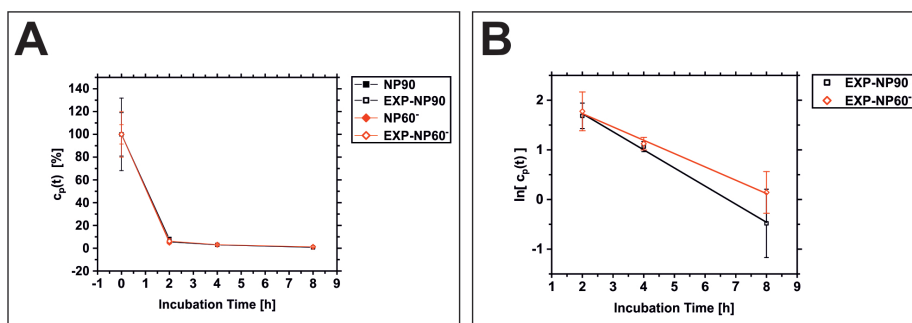


Figure 8.7: Plasmaprofile of core-shell NPs NP90, EXP-NP90, NP60<sup>-</sup> and EXP-NP60<sup>-</sup> in 129 mice (A). Semilogarithmic plot of the plasmaprofile for targeted EXP-NP90 and EXP-NP60<sup>-</sup> (B).

multate in the liver. Furthermore, the coloration of the urine changed after the administration of fluorescently labeled NP dispersions (refer to figure 8.6). The urine appeared in a green coloration that was the overlapping of physiological yellow coloration and the fluorescent dye CF<sup>TM</sup>647. CF<sup>TM</sup>647 was covalently coupled to PLGA (refer to section 3.2.9). This observation again confirmed the renal elimination pathway for the core-shell NPs as it was concluded from the biodistribution studies (refer to 8.3.2). But it was not finally investigated if the green coloration originated from degraded CF<sup>TM</sup>647 or PLGA-CF<sup>TM</sup>647. Nevertheless, both cases were the result of core-shell NP degradation.

However, it can be concluded that the core-shell NPs circulated only for a very short time interval. Especially a long circulation time is needed to reach the target site effectively. In order to deduce the elimination constant  $\beta$ , the last plasma concentrations were illustrated in a semilogarithmic plot (refer to figure 8.7). The slope of the linear fit provided the elimination constants.

The determined elimination constant  $\beta$  and the calculated plasma half-life are listed in table 8.2.

Table 8.2: Plasma half-life of EXP-NP90 and EXP-NP60<sup>-</sup> determined in 129 mice.

NP type	$\beta$ [h <sup>-1</sup> ]	$T_{1/2}$ [h]	$R^2$
EXP-NP90	$-3.65 \cdot 10^{-1}$	$1.90 \pm 0.10$	0.997
EXP-NP60 <sup>-</sup>	$-2.68 \cdot 10^{-1}$	$2.16 \pm 0.14$	0.995

The plasma half-lives of the core-shell NPs were widely similar.

After the completed incubation interval, mice were deeply anesthetized and perfused with a fluorescent dextrane to visualize the vasculature. Again retina flatmounts were prepared as it is depicted in figure 8.1. Retina flatmounts were scanned with a fluorescence microscope. A full scale tile image of the retinae was recorded, first. Channel 1 (Ch1) was the NP channel and channel 2 (Ch2) illustrates the vasculature. Several retinal ROIs were scanned as a z-stack for focussing the upper, intermediate and lower plexus. As representative examples the scans of a single retina flatmount are depicted in figure 8.8

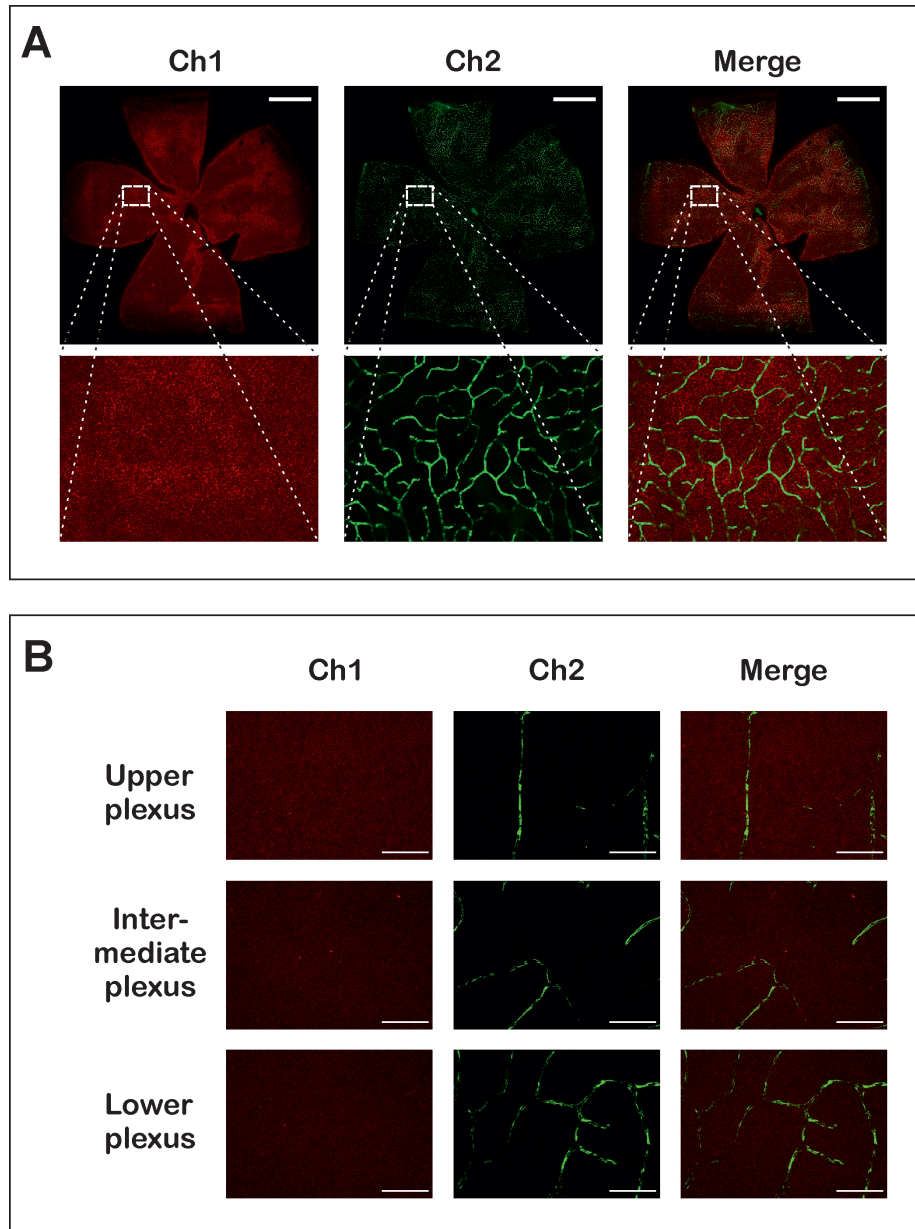


Figure 8.8: Retina flatmounts of 129 mice injected with EXP-NP90 after 2 h incubation interval. **A:** Tile image of complete retina flatmount (scale bar 1000  $\mu$ m) plus 50-fold zoom-in sections. **B:** Selected images of a z-stack (scale bar 50  $\mu$ m).

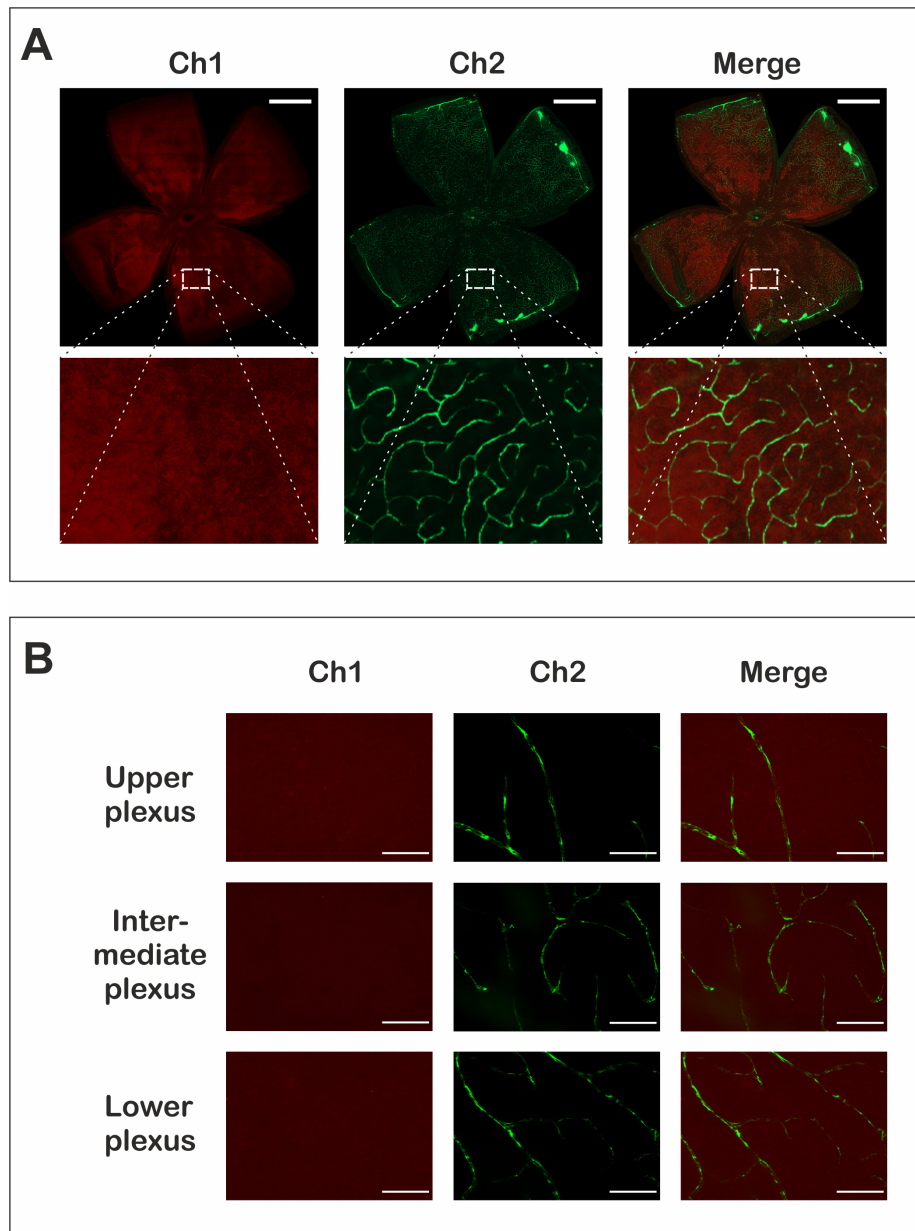


Figure 8.9: Retina flatmounts of 129 mice injected with EXP-NP60<sup>-</sup> after 2 h incubation interval. **A:** Tile image of complete retina flatmount (scale bar 1000  $\mu$ m) plus 50-fold zoom-in sections. **B:** Selected images of a z-stack (scale bar 50  $\mu$ m).

and 8.9. There mice received EXP-NP90 or EXP-NP60<sup>-</sup> and were incubated for two hours. This was the shortest incubation interval. It was not possible to identify a NP-related fluorescence signal. This result was consistent within the whole experiment cohort and all incubation intervals. These data confirmed the biodistribution studies, where a targeting effect for ocular vasculature was not observed. Therefore an *in vivo* targeting effect could not be verified with this experimental setup.

## 8.4 Conclusion and Outlook

These studies provided meaningful data to grasp the *in vivo* fate of the core-shell NPs. It was shown that targeted NPs were able to bind and reside at murine tissue. So the targeted core-shell NPs were determined in the spleen and the kidneys. The targeting of renal tissue with EXP3174 decorated core-shell NPs was already shown by Fleischmann et. al. [40]. They added also cycloRGD-ligands to the NP shell to trigger cellular uptake, which was not intended for this work. Furthermore the core-shell NPs resided within the liver, arguing for a receptor mediated binding. Since EXP3174 is an antagonist for AT1Rs [49], the targeted core-shell NPs were not directly taken up. This behavior was already observed in the *in vitro* studies (refer to section 6.3.3). Furthermore, a renal elimination pathway was identified. That pathway was plausible, since the building blocks of the core-shell NPs were biodegradable polymers (refer to chapter 3). Lastly, the green coloration of the urine of the laboratory animals confirmed that elimination pathway.

However, a targeting effect for the ocular vascular tissue as it was proven by Hennig et. al. [1] could not be proven so far. The reasons therefore are multifactorial:

- 1 Particle size is the most striking difference between the mNPs of Hennig et. al. [1] and the here introduced core-shell NPs. While Hennig et. al. used anorganic Quantum Dots with a hydrodynamic diameter of 15 nm to 21 nm (manufacturer information - prior linkage of EXP3174 ligands), the core-shell NPs were substantially greater ( $105 \pm 13$  nm and  $68 \pm 6$  nm). However, an *in vivo* targeting effect of this kind of core-shell NPs was already evidenced [40, 50]. Nevertheless it could be beneficial to use an microfluidic manufacturing technique in order to further reduce the NP size [51].
- 2 Another aspect was the stability of the core-shell NPs. Here the stability in human plasma was investigated. The vigorous centrifugation step was implemented to remove precipitated plasma proteins for a meaningful DLS measurement. This centrifugation step generated immense mechanical stress for the core-shell NPs. An intact PEG shell was absolutely needed to survive. The NP dispersions were manufactured on the day before the experiment and stored in the fridge. The dispersant was DPBSx0.1. The stability study also indicated that a buffered core-shell NP dispersion was only stable for approximately 24 hours at body temperature. Consequently it must be assumed that the PEG shell was already impaired due to the storage until the start of the experiment. It is highly

recommended to use freshly prepared or freeze-dried core-shell NP dispersions for upcoming experiments. A suitable freeze-drying protocol was already designed (refer to chapter 5).

- 3 Last but not least, the design of the core-shell NPs needs further improvements. The analysis of the PEG shell revealed an intermediate conformation and large average distances between the individual PEG chains (refer to section 4.3.3). A dense brush reduces the opsonization *in vivo* and raises the circulation half-life [52–56]. The enhancement of the PEG brush density could be achieved via reducing the MW of the PLA-block to 10 kDa, which is easily controllable via the synthesis (refer to chapter 3). This approach was already successfully implemented by Maslanka et al. [50] and Fleischmann et al. [40]. The subsequent addition of adhering shorter PEG-chains is another concept to cover free valences for opsonization [57].

Summing up, EXP-NP90 and EXP-NP60<sup>-</sup> were not able to target ocular tissue. But they already showed promising properties for an *in vivo* administration. It is recommended to repeat the *in vivo* studies taking the latter considerations into account. Active drug targeting initially needs a passive targeting effect [58]. This means that the binding of EXP3174 ligands to the target receptors require a spatial proximity to enable receptor-mediated binding. Therefore a dense and intact PEG shell is absolutely needed to enhance the circulation half-life and to refine the core-shell NPs so that they will become an effective pharmacon.

## 8.5 References

- [1] Robert Hennig et al. “Multivalent Nanoparticles Bind the Retinal and Choroidal Vasculature”. In: *Journal of Controlled Release* 220.A (2015), pp. 265–274. DOI: 10.1016/j.jconrel.2015.10.033.
- [2] James Blanchard. “Evaluation of the Relative Efficacy of Various Techniques for Deproteinizing Plasma Samples Prior to High-Performance Liquid Chromatographic Analysis”. In: *Journal of Chromatography B* 226.2 (1981), pp. 455–460. DOI: 10.1016/S0378-4347(00)86080-6.
- [3] Manh Ha Nguyen et al. “Speciation Analysis of Arsenic Compounds by HPLC-ICP-MS: Application for Human Serum and Urine”. In: *Journal of Analytical Methods in Chemistry* 2018 (2018). DOI: 10.1155/2018/9462019.
- [4] Xi Zhou et al. “Development a Simple and Rapid HPLC-ESI-Q-TOF/MS Method for Determination of Short- and Medium- Chain Chlorinated Paraffins in Human Serum”. In: *Journal of Chromatography B* 1126-1127 (2019). DOI: 10.1016/j.jchromb.2019.121722.
- [5] Alexey V. Kozlov et al. “An Improved Extraction Protocol for Therapeutic Dabigatran Monitoring Using HPLC-MS/MS”. In: *Journal of Chromatography B* 1130-1131 (2019). DOI: 10.1016/j.jchromb.2019.121808.

## 8.5. REFERENCES

---

- [6] Nicole Menche and Stephanie Engelhardt. *Biologie, Anatomie, Physiologie: Kompaktes Lehrbuch für Pflegeberufe*. 7. Aufl. Pflege heute. München: Elsevier, Urban & Fischer, 2012.
- [7] Abdul Khader Mohammad and Joshua J. Reineke. "Quantitative Detection of PLGA Nanoparticle Degradation in Tissues Following Intravenous Administration". In: *Molecular Pharmaceutics* 10.6 (2013), pp. 2183–2189. DOI: 10.1021/mp300559v.
- [8] Banu S. Zolnik and Diane J. Burgess. "Effect of Acidic pH on PLGA Microsphere Degradation and Release". In: *Journal of Controlled Release* 122.3 (2007), pp. 338–344. DOI: 10.1016/j.jconrel.2007.05.034.
- [9] Changhui Li, George W. Kattawar, and Ping Yang. "Effects of Surface Roughness on Light Scattering by Small Particles". In: *Journal of Quantitative Spectroscopy & Radiative Transfer* 89.1-4 (2004), pp. 123–131. DOI: 10.1016/j.jqsrt.2004.05.016.
- [10] K. Avgoustakis et al. "PLGA–mPEG Nanoparticles of Cisplatin: In Vitro Nanoparticle Degradation, In Vitro Drug Release and In Vivo Drug Residence in Blood Properties". In: *Journal of Controlled Release* 79.1-3 (2002), pp. 123–135. DOI: 10.1016/S0168-3659(01)00530-2.
- [11] James M. Anderson and Matthew S. Shive. "Biodegradation and Biocompatibility of PLA and PLGA Microspheres". In: *Advanced Drug Delivery Reviews* 64 Supplement (2012), pp. 72–82. DOI: 10.1016/j.addr.2012.09.004.
- [12] Annamalai Pratheep Kumar et al. "Nanoscale Particles for Polymer Degradation and Stabilization - Trends and Future Perspectives". In: *Progress in Polymer Science* 34.6 (2009), pp. 479–515. DOI: 10.1016/j.progpolymsci.2009.01.002.
- [13] Qing Cai et al. "Enzymatic Degradation Behavior and Mechanism of Poly(lactide-co-glycolide) Foams by Trypsin". In: *Biomaterials* 24.4 (2003), pp. 629–638. DOI: 10.1016/S0142-9612(02)00377-0.
- [14] Bin Li et al. "Butyrylcholinesterase, Paraoxonase, and Albumin Esterase, but not Carboxylesterase, are Present in Human Plasma". In: *Biochemical Pharmacology* 70.11 (2005), pp. 1673–1684. DOI: 10.1016/j.bcp.2005.09.002.
- [15] Feng Yang et al. "Effect of Human Serum Albumin on Drug Metabolism: Structural Evidence of Esterase Activity of Human Serum Albumin". In: *Journal of Structural Biology* 157.2 (2007), pp. 348–355. DOI: 10.1016/j.jsb.2006.08.015.
- [16] R. Gref et al. "'Stealth' Corona-Core Nanoparticles Surface Modified by Polyethylene Glycol (PEG): Influences of the Corona (PEG Chain Length and Surface Density) and of the Core Composition on Phagocytic Uptake and Plasma Protein Adsorption". In: *Colloids and Surfaces B: Biointerfaces* 18.3-4 (2000), pp. 301–313. DOI: 10.1016/S0927-7765(99)00156-3.
- [17] Damian Wild et al. "Exendin-4-Based Radiopharmaceuticals for Glucagonlike Peptide-1 Receptor PET/CT and SPECT/CT". In: *Journal of Nuclear Medicine* 51.7 (2010), pp. 1059–1067. DOI: 10.2967/jnumed.110.074914.



## 8.5. REFERENCES

---

- [18] Michal Grzmil et al. "Pharmacological Inhibition of mTORC1 Increases CCKBR-Specific Tumor Uptake of Radiolabeled Minigastrin analogue  $^{177}\text{Lu}$ -PP-F11N". In: *Theranostics* 10.24 (2020), pp. 10861–10873. DOI: 10.7150/thno.45440.
- [19] Tessa Luehmann et al. "Biodistribution of Site-Specific PEGylated Fibroblast Growth Factor-2". In: *ACS Biomaterials Science & Engineering* 6.1 (2020), pp. 425–432. DOI: 10.1021/acsbiomaterials.9b01248.
- [20] Olivia M. Merkel et al. "In Vivo SPECT and Real-Time Gamma Camera Imaging of Biodistribution and Pharmacokinetics of siRNA Delivery Using an Optimized Radiolabeling and Purification Procedure". In: *Bioconjugate Chemistry* 20.1 (2009), pp. 174–182. DOI: 10.1021/bc800408g.
- [21] Mauricio Morais and Michelle T. Ma. "Site-Specific Chelator-Antibody Conjugation for PET and SPECT Imaging with Radiometals". In: *Drug discovery today: Technologies* 30 (2018), pp. 91–104. DOI: 10.1016/j.ddtec.2018.10.002.
- [22] Jingyi Zhu et al. " $^{99\text{mTc}}$ -Labeled Polyethylenimine-Entrapped Gold Nanoparticles with pH-Responsive Charge Conversion Property for Enhanced Dual Mode SPECT/CT Imaging of Cancer Cells". In: *Langmuir* 35.41 (2019), pp. 13405–13412. DOI: 10.1021/acs.langmuir.9b02617.
- [23] Hongbo Gao et al. " $^{99\text{mTc}}$ -Conjugated Manganese-Based Mesoporous Silica Nanoparticles for SPECT, pH-Responsive MRI and Anti-Cancer Drug Delivery". In: *Nanoscale* 8.47 (2016), pp. 19573–19580. DOI: 10.1039/c6nr07062k.
- [24] Teresa Martínez Martínez et al. "Fluorescent DTPA-Silk Fibroin Nanoparticles Radiolabeled with  $^{111}\text{In}$ : A Dual Tool for Biodistribution and Stability Studies". In: *ACS Biomaterials Science & Engineering* 6.6 (2020), pp. 3299–3309. DOI: 10.1021/acsbiomaterials.0c00247.
- [25] Yi-Nan Zhang et al. "Nanoparticle-Liver Interactions: Cellular Uptake and Hepatobiliary Elimination". In: *Journal of Controlled Release* 240 (2016), pp. 332–348. DOI: 10.1016/j.jconrel.2016.01.020.
- [26] Vito Racanelli and Barbara Rehermann. "The Liver as an Immunological Organ". In: *Hepatology* 43.2 Suppl 1 (2006), S54–62. DOI: 10.1002/hep.21060.
- [27] E. Wisse et al. "The Size of Endothelial Fenestrae in Human Liver Sinusoids: Implications for Hepatocyte-Directed Gene Transfer". In: *Gene Therapy* 15.17 (2008), pp. 1193–1199. DOI: 10.1038/gt.2008.60.
- [28] Zohreh Amoozgar and Yoon Yeo. "Recent Advances in Stealth Coating of Nanoparticle Drug Delivery Systems". In: *Wiley Interdisciplinary Reviews Nanomedicine and Nanobiotechnology* 4.2 (2012), pp. 219–233. DOI: 10.1002/wnan.1157.
- [29] Gina Song et al. "Nanoparticles and the Mononuclear Phagocyte System: Pharmacokinetics and Applications for Inflammatory Diseases". In: *Current Rheumatology Reviews* 10.1 (2014), pp. 22–34.

## 8.5. REFERENCES

---

- [30] Chunbai He et al. "Effects of Particle Size and Surface Charge on Cellular Uptake and Biodistribution of Polymeric Nanoparticles". In: *Biomaterials* 31.13 (2010), pp. 3657–3666. DOI: 10.1016/j.biomaterials.2010.01.065.
- [31] Ken-ichi Ogawara et al. "Hepatic Uptake of Polystyrene Microspheres in Rats: Effect of Particle Size on Intrahepatic Distribution". In: *Journal of Controlled Release* 59.1 (1999), pp. 15–22. DOI: 10.1016/S0168-3659(99)00015-2.
- [32] Mahmoud Elsabahy and Karen L. Wooley. "Design of Polymeric Nanoparticles for Biomedical Delivery Applications". In: *Chemical Society Reviews* 41.7 (2012), pp. 2545–2561. DOI: 10.1039/c2cs15327k.
- [33] A. G. Desai and M. L. Thakur. "Radiopharmaceuticals for Spleen and Bone Marrow Studies". In: *Seminars in Nuclear Medicine* 15.3 (1985), pp. 229–238. DOI: 10.1016/S0001-2998(85)80002-7.
- [34] Robert W. Evans and Washington Ogowang. "Interaction of Indium with Transferrin". In: *Biochemical Society Transactions* 16.5 (1988), pp. 833–834. DOI: 10.1042/bst0160833.
- [35] Wesley R. Harris and Luigi Messori. "A Comparative Study of Aluminum(III), Gallium(III), Indium(III), and Thallium(III) Binding to Human Serum Transferrin". In: *Coordination Chemistry Reviews* 228.2 (2002), pp. 237–262. DOI: 10.1016/S0010-8545(02)00037-1.
- [36] John B. Vincent and Sharifa Love. "The Binding and Transport of Alternative Metals by Transferrin". In: *Biochimica et Biophysica Acta* 1820.3 (2012), pp. 362–378. DOI: 10.1016/j.bbagen.2011.07.003.
- [37] Po Sing Leung et al. "Expression and Localization of AT1 Receptors in Hepatic Kupffer Cells: Its Potential Role in Regulating a Fibrogenic Response". In: *Regulatory Peptides* 116.1-3 (2003), pp. 61–69. DOI: 10.1016/S0167-0115(03)00192-7.
- [38] Andrew M. Allen, Jialong Zhuo, and Frederick A. O. Mendelsohn. "Localization and Function of Angiotensin AT1 Receptors". In: *American Journal of Hypertension* 13.S1 (2000), S31–S38. DOI: 10.1016/S0895-7061(99)00249-6.
- [39] Diem T. Dinh et al. "Angiotensin Receptors: Distribution, Signalling and Function". In: *Clinical Science* 100.5 (2001), pp. 481–492. DOI: 10.1042/cs1000481.
- [40] Daniel Fleischmann et al. "Adenovirus-Mimetic Nanoparticles: Sequential Ligand–Receptor Interplay as a Universal Tool for Enhanced In Vitro/In Vivo Cell Identification". In: *ACS Applied Materials & Interfaces* 12.31 (2020), pp. 34689–34702. DOI: 10.1021/acscami.0c10057.
- [41] Filip K. Swirski et al. "Identification of Splenic Reservoir Monocytes and their Deployment to Inflammatory Sites". In: *Science* 325.5940 (2009), pp. 612–616. DOI: 10.1126/science.1175202.
- [42] Marnix A. Lameijer et al. "Monocytes and Macrophages as Nanomedicinal Targets for Improved Diagnosis and Treatment of Disease". In: *Expert Review of Molecular Diagnostics* 13.6 (2013), pp. 567–580. DOI: 10.1586/14737159.2013.819216.

## 8.5. REFERENCES

---

- [43] Zhong Jian Cheng, Heikki Vapaatalo, and Eero Mervaala. "Angiotensin II and Vascular Inflammation". In: *Medical Science Monitor* 11.6 (2005), RA194–205.
- [44] Meixia He et al. "Angiotensin II Induces the Expression of Tissue Factor and its Mechanism in Human Monocytes". In: *Thrombosis Research* 117.5 (2006), pp. 579–590. DOI: 10.1016/j.thromres.2005.04.033.
- [45] Jeannine Guenther et al. "Angiotensin Receptor Type 1 and Endothelin Receptor Type A on Immune Cells Mediate Migration and the Expression of IL-8 and CCL18 when Stimulated by Autoantibodies from Systemic Sclerosis Patients". In: *Arthritis Research & Therapy* 16.R65 (2014), pp. 1–14. DOI: 10.1186/ar4503.
- [46] Benjamin Junglas et al. "Connective Tissue Growth Factor Causes Glaucoma by Modifying the Actin Cytoskeleton of the Trabecular Meshwork". In: *The American Journal of Pathology* 180.6 (2012), pp. 2386–2403. DOI: 10.1016/j.ajpath.2012.02.030.
- [47] Andrea E. Dillinger et al. "CCN2/CTGF Promotor Activity in the Developing and Adult Mouse Eye". In: *Cell and Tissue Research* 384.3 (2021), pp. 625–641. DOI: 10.1007/s00441-020-03332-4.
- [48] Magdalena Schneider et al. "A Novel Ocular Function for Decorin in the Aqueous Humor Outflow". In: *Matrix Biology* 97 (2021), pp. 1–19. DOI: 10.1016/j.matbio.2021.02.002.
- [49] M. de Gasparo et al. "International Union of Pharmacology. XXIII. The Angiotensin II Receptors". In: *Pharmacological Reviews* 52.3 (2000), pp. 415–472.
- [50] Sara Maslanka Figueroa et al. "Nanoparticles Mimicking Viral Cell Recognition Strategies are Superior Transporters into Mesangial Cells". In: *Advanced Science* 7.11 (2020). DOI: 10.1002/advs.201903204.
- [51] Kathrin Abstiens and Achim M. Goepferich. "Microfluidic Manufacturing Improves Polydispersity of Multicomponent Polymeric Nanoparticles". In: *Journal of Drug Delivery Science and Technology* 49 (2019), pp. 433–439. DOI: 10.1016/j.jddst.2018.12.009.
- [52] Donald E. Owens and Nicholas A. Peppas. "Opsonization, Biodistribution, and Pharmacokinetics of Polymeric Nanoparticles". In: *International Journal of Pharmaceutics* 307.1 (2006), pp. 93–102. DOI: 10.1016/j.ijpharm.2005.10.010.
- [53] Shyh-Dar Li and Leaf Huang. "Stealth Nanoparticles: High Density but Sheddable PEG is a Key for Tumor Targeting". In: *Journal of Controlled Release* 145.3 (2010), pp. 178–181. DOI: 10.1016/j.jconrel.2010.03.016.
- [54] Qi Yang et al. "Evading Immune Cell Uptake and Clearance Requires PEG Grafting at Densities Substantially Exceeding the Minimum for Brush Conformation". In: *Molecular Pharmaceutics* 11.4 (2014), pp. 1250–1258. DOI: 10.1021/mp400703d.
- [55] Anisha A. D'souza and Ranjita Shegokar. "Polyethylene Glycol (PEG): A Versatile Polymer for Pharmaceutical Applications". In: *Expert Opinion on Drug Delivery* 13.9 (2016), pp. 1257–1275. DOI: 10.1080/17425247.2016.1182485.

## 8.5. REFERENCES

---

- [56] Nicolas Bertrand et al. "Mechanistic Understanding of In Vivo Protein Corona Formation on Polymeric Nanoparticles and Impact on Pharmacokinetics". In: *Nature Communications* 8.1 (2017). DOI: 10.1038/s41467-017-00600-w.
- [57] Martina Pannuzzo et al. "Overcoming Nanoparticle-Mediated Complement Activation by Surface PEG Pairing". In: *Nano Letters* 20.6 (2020), pp. 4312–4321. DOI: 10.1021/acs.nanolett.0c01011.
- [58] Gregory T. Tietjen et al. "Focus on Fundamentals: Achieving Effective Nanoparticle Targeting". In: *Trends in Molecular Medicine* 24.7 (2018), pp. 598–606. DOI: 10.1016/j.molmed.2018.05.003.

## **Chapter 9**

# **Overall Summary**

It was the major objective of this thesis to establish a nanoparticulate platform technology with the potential to become a therapeutic option for the treatment of wet age-related macular degeneration (AMD) and proliferative diabetic retinopathy (PDR). The implementation of anti-vascular endothelial growth factor (VEGF) therapeutics marked a milestone in the treatment of these neovascular ocular diseases [1]. However, not every patient responds to the anti-VEGF therapy and beyond that, the intravitreal injections bear the risk for severe complications like endophthalmitis [2]. The pathological processes are complex and offer a multitude of further targets for the development of therapeutics (refer to chapter 1). Core-shell nanoparticles (NPs) provide the needed flexibility to tailor their physicochemical properties (e.g. size, surface charge, ligand density and shell architecture) and design specialized therapeutics. Furthermore, a single core-shell NP can be decorated with different ligands [3, 4] and also loaded with therapeutic agents [5].

This work was focussed on the investigation of two candidates: (a) EXP-NP90 and (b) EXP-NP60. Both candidates were decorated with the angiotensin II receptor type 1 (AT1R) antagonist losartan carboxylic acid (EXP3174). The AT1R is an essential part of the ocular Renin-Angiotensin-Aldosterone System (RAAS) that triggers the secretion of growth and transcription factors like VEGF, transforming growth factor beta (TGF- $\beta$ ) and nuclear factor kappa-light-chain-enhancer of activated B-cells (NF- $\kappa$ B) [6]. This means that a selective blocking of ocular AT1Rs could inhibit the VEGF-mediated neovascularization but also additional pathological processes like vascular inflammation or neuronal dysfunction. Moreover, a systemic administration would not bear the risk for endophthalmitis as it is the case for intravitreal injections [2].

**Chapter 3** summarizes the synthesis and analytics of all building blocks needed for the manufacturing of core-shell NPs. Polyethylene glycol (PEG)-polylactic acid (PLA) block-co-polymers were the most essential components. Ring-opening polymerization according to Qian et. al. [7] gave the opportunity to add a PLA block to commercially available PEG-macroinitiators. The resulting polymers had an outstanding narrow polydispersity index (PDI). The following polymers were prepared:

Block-Co-Polymer	End Group	PEG Length	PLA Length	PDI
MeO-PEG <sub>5k</sub> -PLA <sub>20k</sub>	Methoxy	4.8 kDa	17.2 kDa	1.60
MeO-PEG <sub>2k</sub> -PLA <sub>20k</sub>	Methoxy	2.0 kDa	19.2 kDa	1.61
HOOC-PEG <sub>2k</sub> -PLA <sub>20k</sub>	Carboxy	2.1 kDa	19.6 kDa	1.61
NH <sub>2</sub> -PEG <sub>5k</sub> -PLA <sub>20k</sub>	NH <sub>2</sub>	5.0 kDa	19.1 kDa	2.28

In addition, losartan was oxidized with potassium permanganate to receive losartan carboxylic acid (EXP3174). Then, EXP3174 was covalently coupled to NH<sub>2</sub>-PEG-PLA to receive EXP3174-PEG-PLA. This modified block-co-polymer gave the opportunity to tune the resulting ligand density with the manufacturing procedure precisely. Beyond the synthesis of block-co-polymers, acid-terminated poly(lactic-co-glycolic) acid (PLGA) with a molecular weight (MW) of 13.4 kDa was purchased. PLGA was used to stabilize the core-shell-NPs.

Furthermore, PLGA was labeled with the fluorescent dye CF<sup>TM</sup>647 as well as ultra-small gold particles. Hence, the core-shell NPs can be easily tagged and investigated with a multitude of analysis techniques like flow cytometry, confocal laser scanning microscopy (CLSM) or inductively coupled plasma (ICP)-mass spectrometry (MS).

**Chapter 4** described the manufacturing procedure and the physicochemical properties of both candidates. Over all experiments, twenty batches of EXP-NP90 and sixteen EXP-NP60<sup>-</sup> batches were manufactured. The core-shell NPs were prepared via nanoprecipitation as it was basically developed by Fessi et. al. [8]. The block-co-polymers were dissolved in acetonitrile (ACN) (organic phase) and subsequently injected into a vigorously stirred aqueous buffer solution (aqueous phase). The EXP3174 molecules were attached to a 5 kDa PEG chain, while blank PEG chains had a MW of 2 kDa (filling PEG). This means that the targeting molecules stuck out of the NPs. This structural feature caused an affinity gain of three orders of magnitude.

EXP-NP90 had a size of  $105 \pm 13$  nm (PDI  $0.10 \pm 0.01$ ). They were manufactured using a methoxy-terminated PEG-PLA block-co-polymer. EXP-NP60<sup>-</sup> had a size of  $68 \pm 6$  nm (PDI  $0.09 \pm 0.02$ ) only. They were manufactured using a carboxy-terminated PEG-PLA block-co-polymer. This means that both candidates differ solely by the end group of inserted filling PEG, which is also the reason for different  $\zeta$ -potentials:  $-9.2 \pm 0.2$  mV versus  $-12.6 \pm 0.6$  mV.

A milestone of this work was the validation of particle number concentration (PNC) calculation function against nanoparticle tracking analysis (NTA) measurements. The function is:

$$PNC = \frac{TPC}{\rho_{NP} \times \frac{1}{6}\pi (d_H)^3 \times N_A} \quad (9.1)$$

*TPC* is the total polymer content,  $\rho_{NP}$  is the NP density,  $d_h$  is the hydrodynamic diameter and  $N_A$  is the Avogadro constant. The calculation of the PNC was essential to determine the ligand density per NP. The larger EXP3174 decorated NP90 (EXP-NP90) carried  $3500 \pm 1499$  ligands, while smaller EXP3174 decorated NP60<sup>-</sup> (EXP-NP60<sup>-</sup>) carried only  $1017 \pm 382$  ligands. Hence, the average number of targeting ligands was a multiple of the average spike number of viruses. As representative examples, 16 to 22 spikes per virion were determined for the severe acute respiratory syndrome corona virus type 2 (SARS-CoV-2) [9] and 14 for the human immunodeficiency virus (HIV) [10] only.

Apart from that, the conformation of the PEG shell was analyzed. The modeling resulted in an intermediate state between a brush and a mushroom conformation. The average distance between the PEG chains was  $2.06 \pm 0.14$  (EXP-NP90) and  $2.60 \pm 0.11$  (EXP-NP60<sup>-</sup>). Therefore both candidates were moderately vulnerable for protein adsorption and accelerated degradation in vivo [11].

The storage stability of core-shell NPs was investigated in **chapter 5**. PLA as well as PLGA are sensitive to hydrolytic degradation. That's why a dynamic light scattering (DLS)-based stability study was initiated. Even reduced temperature storage (fridge) indicated a limited usability period. The half-life of

large non-targeted NP90 was  $267 \pm 58$  d and  $355 \pm 70$  d for smaller non-targeted NP60<sup>-</sup>. Consequently, a freeze-drying protocol was designed to remove water quantitatively and prevent a hydrolytic degradation. Sucrose (final concentration 10 %) served as exclusive excipient to ensure NP stability. It is worth to mention, that freeze-dried core-shell NPs were not only investigated for the conservation of their size properties, but also for their targeting effect after redispersion. The test dispersions maintained the full AT1R avidity. It is strongly recommended to use freeze-dried core-shell NP for any following experiment. This ensures the long-term stability and provides a suitable formulation for clinical investigations as well as therapeutic application.

**Chapter 6** investigated the *in vitro* binding performance of EXP3174-decorated EXP-NP90 and EXP-NP60<sup>-</sup>. The AT1R-positive rat mesangial cells (rMCs) were chosen for the experiments. It was shown that the mixing of longer EXP3174-decorated PEG-chains (5 kDa) and shorter filling PEG-chains (2 kDa) resulted in a tremendous affinity gain. This means that the targeting ligands stuck out of the NP like spikes of a virus. Such a NP architecture provided a sub-nanomolar avidity, which was another milestone of this work. With respect to Hennig et. al., PEGylation of EXP3174 resulted in an affinity loss that can be counterbalanced by multivalent NPs [12]. But this architecture led to multivalent NPs that even outperformed the affinity of naive EXP3174. The binding performance was double checked with functional calcium mobilization assay (CaA) and a radioligand based radioligand binding experiment (RL-A):

		EXP-NP90	EXP-NP60 <sup>-</sup>
CaA	pIC <sub>50</sub>	$9.60 \pm 0.11$	$9.27 \pm 0.11$
RL-A	pIC <sub>50</sub>	$10.04 \pm 0.23$	$9.34 \pm 0.07$

Therefore, both candidates were able to target and silence the AT1Rs signalling. In addition, the avidity was determined for a rMCs with a 5-fold increased AT1R density. This experiment was intended to mimic the upregulation of AT1Rs under inflammatory circumstances [13, 14]. But the avidity of both candidates remained unchanged:

		EXP-NP90	EXP-NP60 <sup>-</sup>
RL-A	pIC <sub>50</sub>	$9.79 \pm 0.14$	$9.23 \pm 0.14$

Moreover, the targeted core-shell NPs were found to reside on the cell surface. They do not enter their target cells, which was interpreted as a feature of the antagonistic EXP3174 properties. Naive EXP3174 does not trigger endocytosis [15–19]. This observation was really important to interpret the biodistribution study.

A deeper insight into the binding kinetics of core-shell NPs was gained in **chapter 7**. It was emphasized that only 9.2 ligands of gold-tagged EXP-NP90 and 7.7 of gold-tagged EXP-NP60<sup>-</sup> bound to AT1Rs. This means that only less than 1 % of the carried EXP3174 ligands mediated the NP binding and the strong avidity gain. Keeping this in mind, it can be recommended to reduce the amount of treasured EXP3174-PEG-PLA block-co-polymers in the manufacturing procedure.



---

In **chapter 8** both candidates were investigated for their *in vivo* binding performance. Prior to the experiments, non-targeted NP90 and NP60<sup>-</sup> were investigated for their stability in human serum at body temperature. The half-life of larger NP90 was  $32.9 \pm 14.1$  h and only  $3.89 \pm 0.27$  h for NP60<sup>-</sup>. The results gave evidence that core-shell NPs were able to survive for several hours in human serum. This means that *in vivo* binding studies were possible, but concurrently indicate a very fast degradation mechanism.

The core-shell NPs were tagged with radioactive [<sup>111</sup>In]Indium cations. Any other chemical modifications were not needed. It is worth to mention that this work took advantage of three different labeling techniques: (a) fluorescent dyes (CF™647), (b) ultra-small gold particles and (c) radioactive [<sup>111</sup>In]indium cations that provided access to a multitude of analysis techniques. Radioactive EXP-NP60<sup>-</sup> were injected into healthy 129 mice. The majority of the dose was found in the liver. This is typical for NPs, but the EXP3174 decorated core-shell NPs resided there at least for 48 hours. In the same time interval non-targeted NP60<sup>-</sup> were already completely eliminated. It was concluded that the targeted NPs resided on the surface of AT1R-positive cells as it was observed in the *in vitro* binding studies (refer to chapter 6). Beyond that, an accumulation in the kidneys and the spleen was recognized, but this was not the case for ocular tissue.

In another experiment fluorescently labeled EXP-NP90 and EXP-NP60<sup>-</sup> were injected into healthy 129 mice. The elimination half-life was  $1.90 \pm 0.10$  h and  $2.16 \pm 0.14$  h. Thus both candidates circulated only for a few hours within the bloodstream. An enhanced circulation time is an important prerequisite for active drug targeting [20]. It was concluded that core-shell NPs were eliminated via the renal pathway. Finally also an in-depth scanning of the retinal vasculature did not substantiate the binding of EXP3174 decorated core-shell NPs to the ocular vasculature. The NP size, the PEG shell design and stability aspects were identified as plausible root causes.

All in all, it was shown that core-shell NPs are a highly flexible platform technology for the development of new therapeutic options in the treatment of proliferative ocular diseases. The candidates EXP-NP90 and EXP-NP60<sup>-</sup> were not able to verify their outstanding *in vitro* binding performance *in vivo*. Nevertheless, these experiments should be pursued considering the aforementioned refinements.

## References

- [1] Jaimie D. Steinmetz et al. "Causes of Blindness and Vision Impairment in 2020 and Trends over 30 Years, and Prevalence of Avoidable Blindness in Relation to VISION 2020: the Right to Sight: an Analysis for the Global Burden of Disease Study". In: *The Lancet Global Health* 9.2 (2021), E144–E160. DOI: 10.1016/S2214-109X(20)30489-7.
- [2] Anne-Sofie Petri et al. "Intravitreal Injections with Vascular Endothelial Growth Factor Inhibitors: A Practical Approach". In: *Ophthalmology and Therapy* 9.1 (2020), pp. 191–203. DOI: 10.1007/s40123-020-00230-4.

- 
- [3] Daniel Fleischmann et al. "Adenovirus-Mimetic Nanoparticles: Sequential Ligand–Receptor Interplay as a Universal Tool for Enhanced In Vitro/In Vivo Cell Identification". In: *ACS Applied Materials & Interfaces* 12.31 (2020), pp. 34689–34702. DOI: 10.1021/acsami.0c10057.
- [4] Sara Maslanka Figueroa et al. "Nanoparticles Mimicking Viral Cell Recognition Strategies are Superior Transporters into Mesangial Cells". In: *Advanced Science* 7.11 (2020). DOI: 10.1002/advs.201903204.
- [5] Daniel Fleischmann et al. "Targeted Delivery of Soluble Guanylate Cyclase (sGC) Activator Cinaciguat to Renal Mesangial Cells via Virus-Mimetic Nanoparticles Potentiates Anti-Fibrotic Effects by cGMP-Mediated Suppression of the TGF- $\beta$  Pathway". In: *International Journal of Molecular Sciences* 22.5 (2021). DOI: 10.3390/ijms22052557.
- [6] Sadie K. Dierschke and Michael D. Dennis. "Retinal Protein O-GlcNAcylation and the Ocular Renin Angiotensin System: Signaling Cross-Roads in Diabetic Retinopathy". In: *Current Diabetes Reviews* 1.1 (2021), pp. 1–15. DOI: 10.2174/1573399817999210111205933.
- [7] Haitao Qian et al. "A Strategy for Control of "Random" Copolymerization of Lactide and Glycolide: Application to Synthesis of PEG-b-PLGA Block Polymers Having Narrow Dispersity". In: *Macromolecules* 44.18 (2011), pp. 7132–7140. DOI: 10.1021/ma201169z.
- [8] Hatem Fessi et al. "Nanocapsule Formation by Interfacial Polymer Deposition Following Solvent Displacement". In: *International Journal of Pharmaceutics* 55.1 (1989), R1–R4. DOI: 10.1016/0378-5173(89)90281-0.
- [9] Tomasz Wierzbicki et al. "Effect of Receptors on the Resonant and Transient Harmonic Vibrations of Coronavirus". In: *Journal of the Mechanics and Physics of Solids* 150 (2021). DOI: 10.1016/j.jmps.2021.104369.
- [10] Ping Zhu et al. "Distribution and Three-Dimensional Structure of AIDS Virus Envelope Spikes". In: *Nature* 441.7095 (2006), pp. 847–852. DOI: 10.1038/nature04817.
- [11] R. Gref et al. "'Stealth' Corona-Core Nanoparticles Surface Modified by Polyethylene Glycol (PEG): Influences of the Corona (PEG Chain Length and Surface Density) and of the Core Composition on Phagocytic Uptake and Plasma Protein Adsorption". In: *Colloids and Surfaces B: Biointerfaces* 18.3-4 (2000), pp. 301–313. DOI: 10.1016/S0927-7765(99)00156-3.
- [12] Robert Hennig et al. "Nanoparticle Multivalency Counterbalances the Ligand Affinity Loss upon PEGylation". In: *Journal of Controlled Release* 194 (2014), pp. 20–27. DOI: 10.1016/j.jconrel.2014.07.062.
- [13] Georg Nickenig and David G. Harrison. "The AT1-Type Angiotensin Receptor in Oxidative Stress and Atherogenesis: Part II: AT1 Receptor Regulation". In: *Circulation* 105.4 (2002), pp. 530–536. DOI: 10.1161/hc0402.102619.
- [14] Toshihide Kurihara et al. "Neuroprotective Effects of Angiotensin II Type 1 Receptor (AT1R) Blocker, Telmisartan, via Modulating AT1R and AT2R Signaling in Retinal Inflammation". In: *Investigative Ophthalmology & Visual Science* 47.12 (2006), pp. 5545–5552.

- 
- [15] M. de Gasparo et al. "International Union of Pharmacology. XXIII. The Angiotensin II Receptors". In: *Pharmacological Reviews* 52.3 (2000), pp. 415–472.
- [16] Delphine Fessart, May Simaan, and Stéphane A. Laporte. "C-Src Regulates Clathrin Adapter Protein 2 Interaction with Beta-Arrestin and the Angiotensin II Type 1 Receptor During Clathrin-Mediated Endocytosis". In: *Molecular Endocrinology* 19.2 (2005), pp. 491–503. DOI: 10.1210/me.2004-0246.
- [17] Marie-Eve Poupart et al. "ARF6 Regulates Angiotensin II Type 1 Receptor Endocytosis by Controlling the Recruitment of AP-2 and Clathrin". In: *Cellular Signalling* 19.11 (2007), pp. 2370–2378. DOI: 10.1016/j.cellsig.2007.07.015.
- [18] Thomas A. Morinelli et al. "Clathrin-Dependent Internalization of the Angiotensin II AT1A Receptor Links Receptor Internalization to COX-2 Protein Expression in Rat Aortic Vascular Smooth Muscle Cells". In: *European Journal of Pharmacology* 748 (2015), pp. 143–148. DOI: 10.1016/j.ejphar.2014.12.018.
- [19] Manojkumar A. Puthenveedu and Mark von Zastrow. "Cargo Regulates Clathrin-Coated Pit Dynamics". In: *Cell* 127.1 (2006), pp. 113–124. DOI: 10.1016/j.cell.2006.08.035.
- [20] Gregory T. Tietjen et al. "Focus on Fundamentals: Achieving Effective Nanoparticle Targeting". In: *Trends in Molecular Medicine* 24.7 (2018), pp. 598–606. DOI: 10.1016/j.molmed.2018.05.003.



**Part II**

**Supplement**



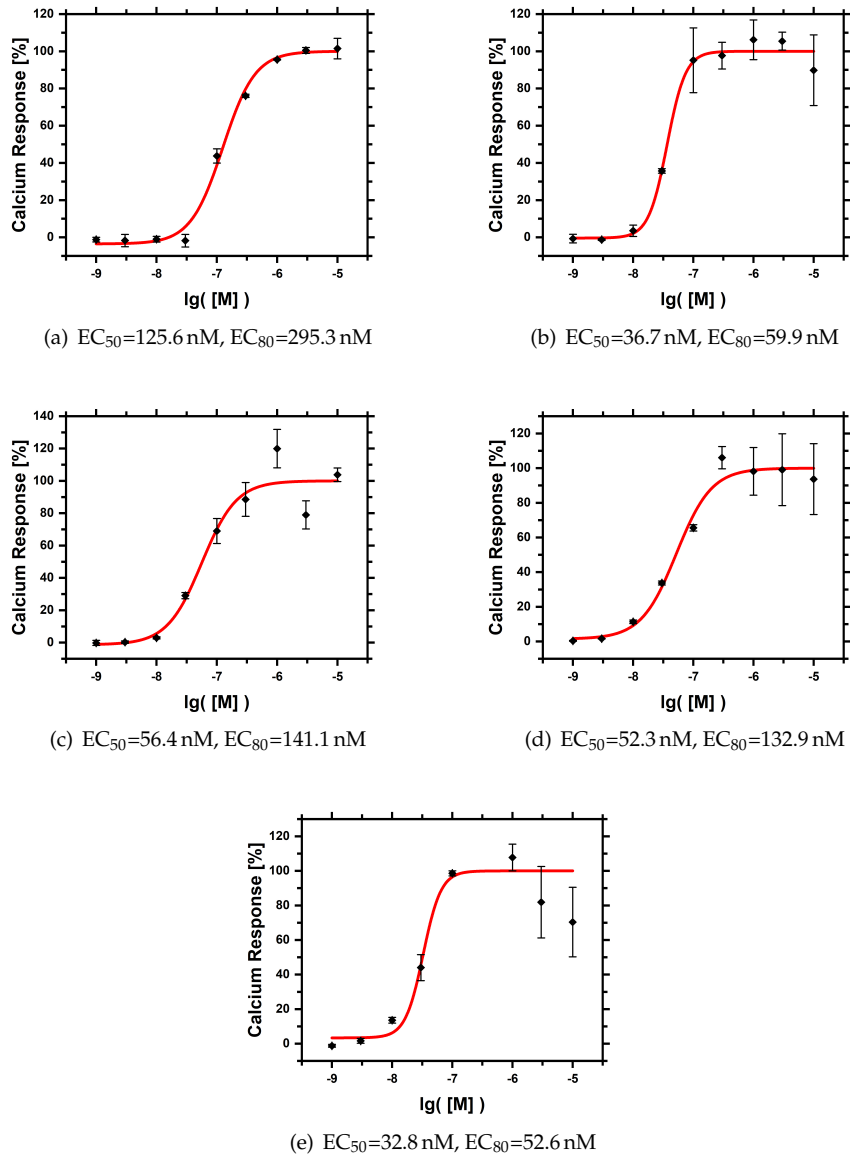
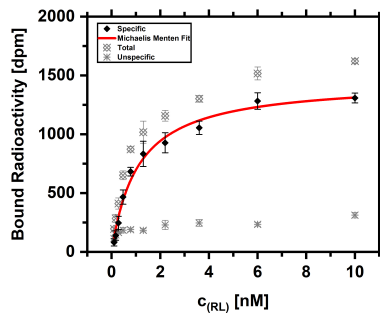
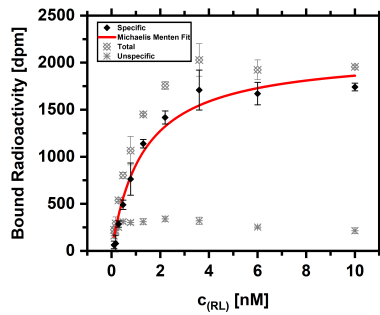


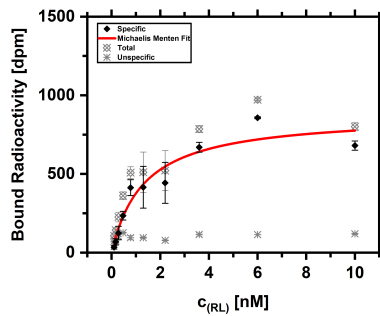
Figure S1: Summary of individual calcium mobilization assays (CaAs). Here rat mesangial cells (rMCs) were incubated with different concentrations of angiotensin II (Ang II) and induce calcium influx. Overall an  $EC_{50}$  of  $60.8 \pm 16.8 \text{ nM}$  and an  $EC_{80}$  of  $136.4 \pm 43.7 \text{ nM}$  were found.



(a) Parameter:  $B_{\max}=1454$  dpm,  $K_d=1.1$  nM; Cell number: 110.000 rMC /well; AT1R: 94.293 receptors /cell



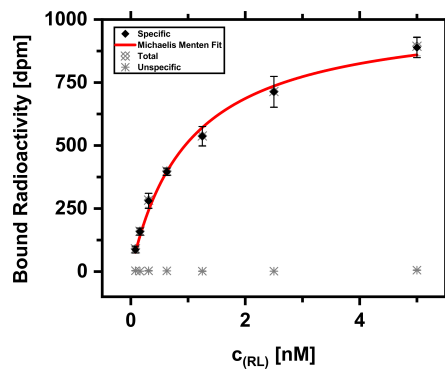
(b) Parameter:  $B_{\max}=2104$  dpm,  $K_d=1.3$  nM; Cell number: 225.000 rMC /well; AT1R: 66.707 receptors /cell



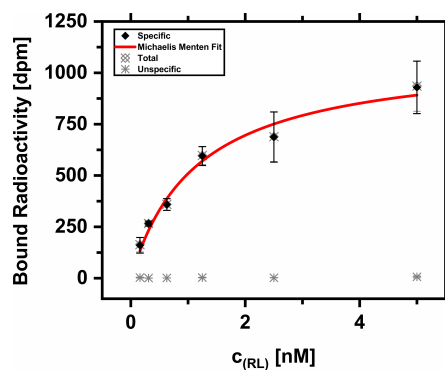
(c) Parameter:  $B_{\max}=879$  dpm,  $K_d=1.3$  nM; Cell number: 106.667 rMC /well; AT1R: 58.774 receptors /cell

Figure S2: Independent saturation binding experiments of rMCs using the tritium labeled angiotensin II derivative radioligand ( $[^3\text{H}]\text{UR-MK292}$ ). Unspecific binding was determined by the addition of Ang II. The rMCs carried  $73\,258 \pm 18\,643$  AT1R/cell. The  $K_d$  accounted  $1.2 \pm 0.1$  nM.

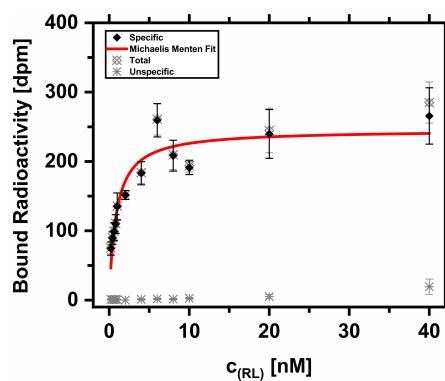




(a) Parameter:  $B_{\max}=1034$  dpm,  $K_d=1.0$  nM;  
Cell number: 42.000 rMC/well; AT1R:  
351.242 receptors /cell

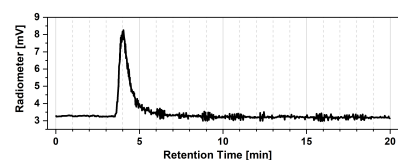


(b) Parameter:  $B_{\max}=1097$  dpm,  $K_d=1.2$  nM;  
Cell number: 42.000 rMC/well; AT1R:  
372.643 receptors /cell

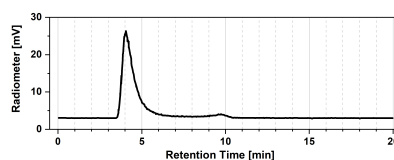


(c) Parameter:  $B_{\max}=246$  dpm,  $K_d=0.9$  nM; Cell  
number: 20.250 rMC/well; AT1R:  
346.638 receptors /cell; For this experiment  
 $[^3\text{H}]\text{UR-MK292}$  was diluted (1/2) with cold  
UR-MK292.

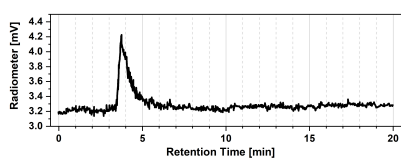
Figure S3: Independent saturation binding experiments of transfected rMCs using the  $[^3\text{H}]\text{UR-MK292}$ . Unspecific binding was determined by the addition of losartan carboxylic acid (EXP3174). The rMCs carried  $356\,841 \pm 13\,877$  AT1R/cell. The  $K_d$  accounted  $1.0 \pm 0.2$  nM.



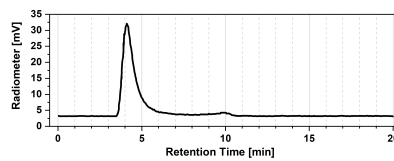
(a)  $^{111}\text{In-NP90}$  ( $t_r = 4.0$  min).



(b)  $^{111}\text{In-NP90}$  pre-incubated with DTPA ( $t_r = 4.0$  min).

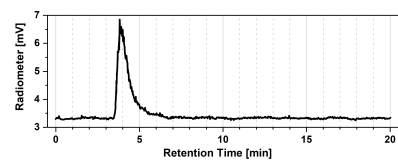


(c)  $^{111}\text{In-EXP-NP90}$  ( $t_r = 3.9$  min)

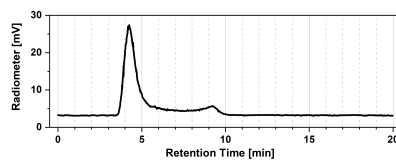


(d)  $^{111}\text{In-EXP-NP90}$  pre-incubated with DTPA ( $t_r = 3.9$  min).

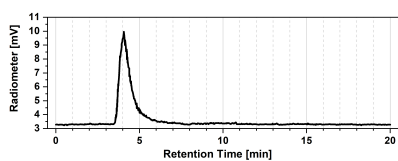
Figure S4: High-performance liquid chromatography (HPLC) chromatograms of  $^{111}\text{In-EXP-NP90}$  and  $^{111}\text{In-NP90}$  pre-incubated with and without DTPA.



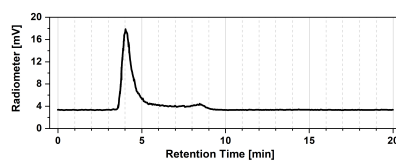
(a)  $^{111}\text{In-NP60}^-$  ( $t_r = 4.0$  min)



(b)  $^{111}\text{In-NP60}^-$  pre-incubated with DTPA ( $t_r = 4.0$  min).

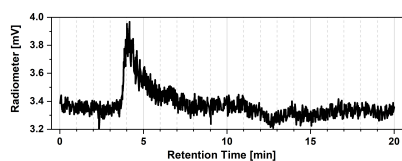


(c)  $^{111}\text{In-EXP-NP60}^-$  ( $t_r = 4.0$  min)

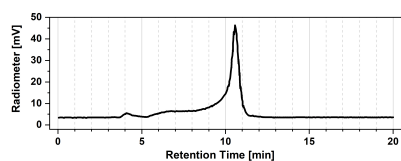


(d)  $^{111}\text{In-EXP-NP60}^-$  pre-incubated with DTPA ( $t_r = 4.0$  min).

Figure S5: HPLC chromatograms of  $^{111}\text{In-EXP-NP60}^-$  and  $^{111}\text{In-NP60}^-$  pre-incubated with and without DTPA.



(a) [ $^{111}\text{In}$ ]InCl<sub>3</sub> dilution ( $t_r = 4.0$  min).



(b) [ $^{111}\text{In}$ ]InCl<sub>3</sub> dilution pre-incubated with DTPA ( $t_r = 10.7$  min).

Figure S6: HPLC chromatograms of references for radiolabeled core-shell NPs (see figure S4 and figure S5).

**Part III**

**Appendix**



# Abbreviations

$\zeta$ -potential	zeta-potential
[ <sup>3</sup> H]UR-MK292	tritium labeled angiotensin II derivative radioligand
$N_A$	Avogadro constant
$R_F$	Flory radius
$T_f$	freezing temperature
$T'_g$	glass transition temperature of the maximal freeze-concentrated dispersion
$T_g$	glass transition temperature
$d_h$	hydrodynamic diameter
$d_{TEM}$	diameter based on transmission electron microscopy images
$w'$	concentration of the maximal freeze-concentrated dispersion
<sup>111</sup> In	<sup>111</sup> indium
ACE	angiotensin converting enzyme
ACN	acetonitrile
AGE	advanced glycosylation endproducts
AMD	age-related macular degeneration
Ang I	angiotensin I
Ang II	angiotensin II
AREDS	Age Related Eye Disease Study
AT1R	angiotensin II receptor type 1
AT2R	angiotensin II receptor type 2
atm	atmospheric pressure
ATP	adenosine triphosphate
Au	aurum
$B_{max}$	maximal number of binding sites
BBB	blood-brain barrier
BlamD	basal laminar deposit
BlinD	basal linear deposit
BM	BRUCH's membrane
BRB	blood-retinal barrier
BSA	bovine serum albumin
BSM	basement membrane

## Abbreviations

---

CaA	calcium mobilization assay
CADASIL	cerebral autosomal dominant arteriopathy with subcortical infarcts and leukoencephalopathy
CDCl <sub>3</sub>	deuterated chloroform
CHCl <sub>3</sub>	chloroform
CI	confidence interval
CLSM	confocal laser scanning microscopy
CML	N-carboxymethyl-lysine
CNS	central nervous system
CoA	Certificate of Analysis
CT	computed tomography
DABCO	<i>IUPAC name</i> 1,4-diazabicyclo[2.2.2]octane
DAD	diode-array detector
DAG	diacyl glycerol
DBU	1,8-diazabicyclo[5.4.0]undec-7-ene
DCC	N,N'-dicyclohexylcarbodiimide
DCM	dichloromethane
DCR	derived count rate
DCU	dicyclohexylurea
DIPEA	N,N-diisopropylamine, Huenig's base
DLS	dynamic light scattering
DME	diabetic macular edema
DMF	dimethylformamide
DMSO	dimethyl sulphoxide
DMSO-d <sub>4</sub>	deuterated dimethyl sulphoxide
DMTMM	4-(4,6-dimethoxy-1,3,5-triazin-2-yl)-4-methylmorpholinium chloride
DNA	desoxyribonucleic acid
DOTA	1,4,7,10-tetraazacyclododecane-1,4,7,10-tetraacetic acid
DPBS	Dulbecco's Phosphate Buffered Saline
DPBSx0.1	diluted Dulbecco's Phosphate Buffered Saline (x0.1)
DR	diabetic retinopathy
DTPA	diethylenetriaminepentaacetic acid
EC	endothelial cell
EC <sub>50</sub>	half maximal effective concentration
EC <sub>80</sub>	concentration inducing 8/10 of the maximum biological effect
ECM	extracellular matrix
EDC	N-(3-dimethylaminopropyl)-N'-ethylcarbodiimide
EDTA	ethylenediaminetetraacetic acid
EGTA	ethylene glycol-bis(2-aminoethylether)-N,N,N',N'-tetraacetic acid
EMA	European Medicines Agency
EXP-NP60 <sup>-</sup>	EXP3174 decorated NP60 <sup>-</sup>



## Abbreviations

---

EXP-NP90	EXP3174 decorated NP90
EXP-NP <sub>5k</sub>	EXP3174-decorated methoxy terminated nanoparticles with a 5 kDa PEG shell
EXP3174	losartan carboxylic acid
F <sub>c</sub>	fraction crystallization domain
FBS	fetal bovine serum
FDA	United States Food and Drug Administration
FITC	fluorescein isothiocyanate
FLD	fluorescence detector
fluram	4-phenylspiro-[furan-2(3H),1-phthalan]-3,3'-dione, fluoresceamine
GA	geographic atrophy
GCP	Good Clinical Practice
GFAT	fructose-6-phosphate-amido transferase
GMP	Good Manufacturing Practice
GPC	gel permeation chromatography
GPCR	G-protein coupled receptor
HCl	hydrochloric acid
HCV	hepatitis C virus
HDL	high density lipoprotein
HIF	hypoxia induced factor
HIV	human immunodeficiency virus
HPLC	high-performance liquid chromatography
HRD-rMC	high-receptor density rat mesangial cellF
iBRB	inner blood-retinal barrier
IC <sub>50</sub>	half maximal inhibitory concentration
ICP	inductively coupled plasma
IDL	intermediate density lipoprotein
IgG	immunoglobulin G
IP <sub>3</sub>	inositole-1,4,5-phosphate
ITS	insulin-transferrin-selenium
K <sub>d</sub>	equilibrium dissociation constant of the ligand-receptor complex
K <sub>i</sub>	equilibrium dissociation constant
KG	body weight
lactide	3,6-dimethyl-1,4-dioxane-2,5-dione
LC	liquid chromatography
LDL	low density lipoprotein
LDL-R	low density lipoprotein receptor
MMP	matrix metalloproteases
mNP	model nanoparticle
MPS	mononuclear phagocyte system
MS	mass spectrometry

## Abbreviations

---

mtDNA	mitochondrial desoxyribonucleic acid
MW	molecular weight
MWCO	molecular weight cut off
NADPH	<i>IUPAC</i> Nicotinamide adenine dinucleotide phosphate
NaOH	sodium hydroxide
NF- $\kappa$ B	nuclear factor kappa-light-chain-enhancer of activated B-cells
NHS	N-hydroxysuccinimide
NMR	nuclear magnetic resonance
NO	nitric oxide
NP	nanoparticle
NP60 <sup>-</sup>	carboxy-terminated nanoparticle
NP90	methoxy-terminated nanoparticle
NPDR	non-proliferative diabetic retinopathy
NTA	nanoparticle tracking analysis
NVU	neurovascular unit
oBRB	outer blood-retinal barrier
OCT	optical coherence tomography
P-gp	P-glycoprotein
PARP1	Poly-ADP-ribose polymerase 1
PC	pericyte
PDGF	platelet derived growth factor
PDGF $\alpha$	platelet derived growth factor alpha
PDGF $\beta$	platelet derived growth factor beta
PDGF-R $\beta$	platelet derived growth factor receptor beta
PDI	polydispersity index
PDR	proliferative diabetic retinopathy
pEC <sub>50</sub>	negative decimal logarithm of EC <sub>50</sub>
PEG	polyethylene glycol
PFA	paraformaldehyde
PGC-1 $\alpha$	peroxisome proliferator-activated receptor gamma coactivator 1-alpha
pIC <sub>50</sub>	negative decimal logarithm of IC <sub>50</sub>
PKC	protein kinase C
PLA	polylactic acid
PLGA	poly(lactic-co-glycolic) acid
PIGF	placental growth factor
PM	plasma membrane
PMMA	poly(methyl methacrylat)
PNC	particle number concentration
PS	polystyrene
PTFE	polytetrafluoroethylene
Q-TOF	quadrupol time-of-flight mass spectrometer
RAAS	Renin-Angiotensin-Aldosterone System

## Abbreviations

---

RAGE	receptors for advanced glycosylation endproducts
RC	regenerated cellulose
RI	refractive index
RL-A	radioligand binding experiment
rMC	rat mesangial cell
RNA	ribonucleic acid
ROI	region of interest
ROS	reactive oxygen species
RP	reversed-phase
RPE	retinal pigment epithelium
RSD	relative standard deviation
RT	room temperature
SARS-CoV-2	severe acute respiratory syndrome corona virus type 2
SD	standard deviation
SEM	standard error of the mean
SPECT	single-photon emission computed tomography
Suc	Sucrose (D(+)-Saccharose)
T1DM	diabetes mellitus type 1
T2DM	diabetes mellitus type 2
$t_r$	retention time
tBoc	tert-butyloxycarbonyl
TCA	trichloroacetic acid
TEM	transmission electron microscopy
TFA	trifluoroacetic acid
TGF- $\beta$	transforming growth factor beta
TMS	tetramethylsilane
TNF- $\alpha$	tumor necrosis factor alpha
TPC	total polymer content
Tre	D(+)-Trehalose
TRIS	tris(hydroxymethyl)aminomethane; <i>IUPAC name</i> 2-amino-2-(hydroxymethyl) propane-1,3-diol
UHPLC	ultra high performance liquid chromatography
VEGF	vascular endothelial growth factor
VEGF-R	vascular endothelial growth factor receptor
VLDL	very low density lipoprotein
WHO	World Health Organization



# Curriculum Vitae

Name: Sebastian Beck  
Date of Birth: 26<sup>th</sup> August, 1990  
Place of Birth: Schleiz (Thuringia/ Germany)  
Nationality: Germany

## Graduations and Certificates

06/24/2019 Specialist in Pharmaceutical Technology  
08/10/2017 Diploma Degree (Dipl.-Pharm.)  
12/18/2015 Licensed Pharmacist, Government of Lower Franconia,  
Wuerzburg  
06/18/2009 University Entrance Qualification

## Professional Carrer

Since 06/2021 Process Expert, Bayer Bitterfeld GmbH, Bitterfeld  
09/2020 - 05/2021 Scientific Batch Record Reviewer, Fraunhofer Institute for  
Cell and Gene Therapy, Leipzig  
04/2016 - 06/2020 Pharmacist, Momentum-Apotheke, Landshut

## Scientific Education

02/2016 - 03/2019 Professional Training in Pharmaceutical Technologies,  
Bavarian Chamber of Pharmacists, Munich  
01/2016 - 12/2019 PhD Candidate, Pharmaceutical Technology, University of  
Regensburg  
05/2015 - 10/2015 Practical Training, Bahnhof-Apotheke, Freilassing  
11/2014 - 04/2015 Diploma Student, Pharmaceutical Technology, Martin-  
Luther-University, Halle-Wittenberg  
10/2010 - 09/2014 Studies of Pharmacy, Friedrich-Alexander-University,  
Erlangen-Nuremburg

## School Education

07/2009 - 07/2010 Military Service, Otto-Lilienthal-Kaserne, Roth  
08/2001 - 06/2009 Grammar School 'Dr. Konrad Duden Gymnasium', Schleiz  
1999 - 2001 Primary School, Tanna  
1997 - 1999 Primary School, Saalburg



# List of Publications

## Poster Presentations

**Sebastian Beck**, Kathrin Abstiens and Achim Goepferich "Multivalent Polymeric Nanoparticles for Targeting the Angiotensin-II-receptor type 1". 11<sup>th</sup> World Meeting on Pharmaceutics, Biopharmaceutics and Pharmaceutical Technology (2018) Granada, Spain.

**Sebastian Beck** and Achim Goepferich "Multivalent Block-Co-Polymer Nanoparticles Bind to Target Cells with high Avidity". DPhG Annual Meeting (2018) Hamburg, Germany.

**Sebastian Beck** and Achim Goepferich "Multivalent Block-Co-Polymer Nanoparticles for the Treatment of wet AMD and DR". 6<sup>th</sup> GALENUS Workshop (2018) Wuerzburg, Germany.

**Sebastian Beck** and Achim Goepferich "Formulation Development for Freeze-Drying of Polymeric Core-Shell Nanoparticles". Controlled Release Society Annual Meeting (2019) Valencia, Spain.

## Short Paper

**Sebastian Beck**, Kathrin Abstiens and Achim Goepferich "Multivalent Polymeric Nanoparticles for Targeting the AT1R". 11<sup>th</sup> World Meeting on Pharmaceutics, Biopharmaceutics and Pharmaceutical Technology (2018) Granada, Spain.

## Peer-Reviewed Publications

Sara Maslanka Figueroa, Anika Veser, Kathrin Abstiens, Daniel Fleischmann, **Sebastian Beck** and Achim Goepferich "Influenza A Mimetic Nanoparticles Trigger Selective Cell Uptake". In: *Proceedings of the National Academy of Science* 116.20 (2019) ISSN: 0027-8424. DOI:10.1073/PNAS.1902563116.

Sara Maslanka Figueroa, Daniel Fleischmann, **Sebastian Beck** and Achim Goepferich "The Effect of Ligand Mobility on the Cellular Interaction of Multivalent Nanoparticles". In: *Macromolecular Bioscience* 20.4 (2020) ISSN: 1616-5195. DOI:10.1002/MABI.201900427.

Sara Maslanka Figueroa, Daniel Fleischmann, **Sebastian Beck** and Achim Goepferich "Thermodynamic, Spatial and Methodological Considerations for the Manufacturing of Therapeutic Polymer Nanoparticles". In: *Pharmaceutical Research* 37.3 (2020) ISSN: 1573-904X. DOI: 10.1007/s11095-020-2783-4.

Sara Maslanka Figueroa, Daniel Fleischmann, **Sebastian Beck**, Philipp Tauber, Ralph Witzgall, Frank Schweda and Achim Goepferich "Nanoparticles Mimicking Viral Cell Recognition Strategies are Superior Transporters into Mesangial Cells". In: *Advanced Science* 7.11 (2020) ISSN: 2198-3844. DOI: 10.1002/ADVS.201903204.

Ajay Kumar Yagati, Arne Behrent, **Sebastian Beck**, Simone Rink, Achim Goepferich, Junhong Min, Min-Ho Lee, Antje Baeumner "Laser-Induced Graphene Interdigitated Electrodes for Label-Free or Nanolabel-Enhanced Highly Sensitive Capacitive Aptamer-Based Biosensors". In: *Biosensors and Bioelectronics* 164 (2020) ISSN: 0956-5663. DOI:10.1016/J.BIOS.2020.112272.

Daniel Fleischmann, Sara Maslanka Figueroa, **Sebastian Beck**, Kathrin Abstiens, Ralph Witzgall, Frank Schweda, Philipp Tauber and Achim Goepferich "Adenovirus-Mimetic Nanoparticles: Sequential Ligand–Receptor Interplay as a Universal Tool for Enhanced In Vitro/In Vivo Cell Identification". In: *ACS Applied Materials and Interfaces* 12.31 (2020) ISSN: 1944-8244. DOI:10.1021/ACSAMI.0C10057.

Christian Ziegler, Moritz Graf, **Sebastian Beck** and Achim Goepferich "A Novel Anhydrous Preparation of PEG Hydrogels Enables High Drug Loading with Biologics for Controlled Release Applications". In: *European Polymer Journal* 147 (2021) ISSN: 0014-3057. DOI: 10.1016/J.EURPOLYMJ.2021.110286.



## Acknowledgments

First and foremost, I would like to express my sincerest gratitude to Prof. Dr. Achim Goepferich who has given me the opportunity to join his research group and to investigate such an outstanding topic. I appreciated the reliance on my work, the productive discussions as well as his valuable and versatile suggestions. I am very grateful to profit from the scientific exchange and the interdisciplinary experiences at several conferences and far-reaching cooperations. Both were so important for the research project and my personal growth. Besides, I am deeply thankful to receive the possibility to become a certified specialist in pharmaceutical technology.

Many thanks go to Prof. Dr. Miriam Breunig and Dr. Ferdinand Brandl for their excellent advices and their support whenever requested.

A very special thank goes to my lab mates Dr. Alexandra Lawrowska and Dr. Sara Maslanka-Figueroa. This includes not only the uncountable scientific conversations, but also the casual and really enjoyable atmosphere inside and outside the lab.

Furthermore, I offer my deepest gratitude to all members of the Department of Pharmaceutical Technology. Thank you so much for the numerous scientific debates, sharing the joy as well as the frustration of research and the fruitful working atmosphere. Beyond that, I am gladly looking back to a memorable time with so many activities like our trip to the ski resort 'Wilder Kaiser', our conference journeys, the hiking tour in the Alps, the visits of the Christmas markets and much more. In particular, I want to thank:

- The 'senior PhD students' for their warm welcome, the introduction to different laboratory techniques and analysis methods especially cell culture and nanoparticle handling. Similarly, I will always remember our common trips to the folk festivals in Regensburg or the climbing/ bouldering experiences.
- Dr. Kathrin Gregoritza for introducing the manufacturing technique of core-shell nanoparticles and her outstanding support especially at the beginning of my research project.
- Dr. Daniel Fleischmann und Dr. Sara Maslanka-Figueroa for the very close collaboration within our research projects. Despite the challenging and time consuming-experiments, I really enjoyed the pleasant mix of focussed research and humorous leisure.

- Dr. Marilena Bohley for the important support of the animal experiments.
- Christian Ziegler not only for the scientific exchange during lunch break, but also for the common lab time, his motivation, the controversial conversations about soccer or the stock market, many cultural evenings and an ongoing friendship.

Additionally, I want to thank Eva Wrobel who was always open for the everyday issues and also beyond. I further thank Silvia Babl, Angelika Beriè, Andrea Blaimer, Stefan Kolb, Renate Liebl and Edith Schindler for their great support.

Moreover, I offer my deepest gratitude to several colleagues of different research groups that provided access to such important analytical techniques:

- Manuel Roesener and Dr. Joerg Tessmar (University Hospital of Wuerzburg/ Germany) for the GPC measurements.
- Dr. Tom Wersig and Prof. Dr. Karsten Maeder (Martin Luther University Halle-Wittenberg/ Germany) for enabling the nanoparticle tracking analysis (NTA) measurements.
- Dr. Max Keller (University of Regensburg) for the provision of the radioligand UR-MK292 and the suggestions about the design of radioligand binding studies.
- Dr. Philipp Tauber, Prof. Dr. Frank Schweda and Prof. Dr. Ralph Witzgall as well as Silvia Babl, Dr. Andrea Dillinger and Prof. Ernst Tamm (University of Regensburg) for the intense collaboration during the *in vivo* experiments.
- Alain Blanc and Dr. Martin Behè (Paul-Scherer Institute/ Villingen/ Switzerland) for the realization of the radiolabeling and the SPECT-based biodistribution studies.

Additional gratitude is owed to the German Research Foundation (DFG) for the financial support.

Beyond that, I want to thank my former teacher of English, Student Council Mr. Thomas Hegner, who reviewed this thesis for linguistic aspects. Thank you for your flexibility, engagement and so many cheerful talks.

Last but not least, I want to offer my heartfelt thanks to my wife Helen and my whole family who encouraged me in every part of my life. Thank you for your persistent motivation and the strong familiar backing. Without your support I would not have been able to make this progress!

## Declaration in Lieu of Oath

I hereby confirm that I have written this thesis on my own and that I have not used any other media or materials the the ones referred to in this thesis.

Leipzig,

\_\_\_\_\_   
Date

\_\_\_\_\_   
Sebastian Beck